

Observation and measurement of the supersymmetric
process $\tilde{\chi}_2^0 \rightarrow \tilde{\chi}_1^0 \ell\ell$
with the CMS experiment at LHC

Candidate: Georgia Karapostoli

A thesis submitted for the degree of
Doctor of Philosophy in Physics
written under the supervision of Prof. Paris Sphicas

Department of Physics
National and Kapodistrian University of Athens
Athens, October 2008

Contents

1	Introduction	3
2	Theoretical overview	5
2.1	The Standard Model	5
2.2	Motivation for New Physics	8
2.3	Supersymmetry	10
2.4	The Minimal Supersymmetric Standard Model	14
2.4.1	Particle content and interactions	14
2.4.2	Soft supersymmetry breaking in the MSSM	17
2.5	Phenomenology of the MSSM	18
2.6	Constraining the MSSM parameter space	21
3	The Compact Muon Solenoid at LHC	25
3.1	The Large Hadron Collider	25
3.2	The CMS detector	27
3.2.1	The inner Tracker	29
3.2.2	The Electromagnetic calorimeter	34
3.2.3	The Hadron calorimeter	37
3.2.4	The superconducting magnet	40
3.2.5	The muon system	40
3.2.6	The Trigger	42
4	Physics objects: reconstruction and selection	45
4.1	Electron reconstruction and selection	45
4.1.1	The PixelMatchGsfElectron algorithm	46
4.1.2	Electron identification	48
4.2	Muon reconstruction	52
4.3	Jet reconstruction	54
4.4	Application to di-lepton analysis	55
4.4.1	Lepton reconstruction and selection efficiencies	55

CONTENTS

4.4.2	Lepton tracker isolation	57
4.4.3	Jet cleaning and lepton-jet separation	63
4.4.4	The recoil missing E_T	64
5	Di-lepton analysis with early data	67
5.1	Signal phenomenology and analysis strategy	67
5.2	Trigger selection	69
5.3	Observability of supersymmetric di-lepton final states	74
5.3.1	Signal versus standard model backgrounds	74
5.3.2	Cuts optimization	75
5.4	Dilepton mass composition and background measurement	78
5.4.1	Flavor-symmetric background	79
5.4.2	Flavor-asymmetric background	81
5.4.3	Background from fake leptons	82
5.5	Di-lepton mass reconstruction	84
5.5.1	Endpoint measurement	84
5.5.2	Fitting procedure	86
5.5.3	Fit results with a toy Monte Carlo study	89
5.6	Systematic uncertainties	89
5.7	Conclusion	93
6	The endpoint technique	95
6.1	Kinematic relations for the endpoints	95
6.1.1	Endpoint in $M_{\ell\ell}$	96
6.1.2	Endpoints in $M_{\ell q}$	97
6.1.3	Endpoints in $M_{\ell\ell q}$	99
6.1.4	Endpoint for the sum $M_{\ell_1 q} + M_{\ell_2 q}$	101
6.2	The mSUGRA LM1 and LM6 benchmark points	102
6.3	Invariant mass distributions at LM1 and LM6	106
6.3.1	Dilepton invariant mass	107
6.3.2	Lepton - quark invariant masses	107

CONTENTS

6.3.3	Dilepton - quark invariant mass	111
6.3.4	The $M_{\ell_1 q} + M_{\ell_2 q}$ invariant mass	115
7	Sparticle mass reconstruction	117
7.1	Event selection	117
7.2	Reconstruction of (di)lepton-jet masses	119
7.2.1	Combinatorial background	119
7.3	Jet calibration performance	124
7.3.1	Lepton - jet mass resolution	125
7.4	Endpoint measurements at LM6	127
7.4.1	Dilepton edge(s)	127
7.4.2	$M_{\ell\ell q}^{\max}$ first measurement	129
7.4.3	$M_{\ell_1 q}^{\max}$ and $M_{\ell_2 q}^{\max}$ measurements	130
7.4.4	The $M_{\ell_2 q}$ fit properties	136
7.4.5	$M_{\ell\ell q}^{\max}$ measurement revisited	139
7.4.6	$(M_{\ell_1 q} + M_{\ell_2 q})^{\max}$ measurement	141
7.5	Endpoint measurements at LM1	142
7.6	The global fit to extract the masses	147
7.7	The Acceptance effect	152
8	Conclusion	159
‘		

1

Introduction

Supersymmetry (SUSY), if it exists and is within the reach of the LHC, predicts a number of spectacular experimental signatures. The high mass of the squarks and gluinos, which are expected to be the primary particles produced in the pp collisions of the LHC, implies numerous final-state decay products with large transverse momenta. Furthermore, if SUSY is to provide the explanation to the dark matter mystery, the lightest supersymmetric particle (LSP) should be stable, very weakly interacting and have significant mass, thus resulting in large missing energy. Whereas this last characteristic of SUSY events can be exploited to separate them from “background” processes from the Standard Model, it also renders the full reconstruction of a sparticle decay impossible. This makes analyses searching for SUSY very intricate, since the traditional “peak” in some invariant mass distribution can no longer be used to establish firmly the existence of a new particle. Establishing the presence of a new particle state is, nevertheless, still possible – and the discovery of the W boson at the CERN Sp \bar{p} S collider is a good example. In the case of SUSY, expectations are that the corresponding analysis will be more difficult due to the higher jet multiplicities expected, but also due to much larger backgrounds (mainly from W/Z and top production) in the relevant kinematic regime. As a result, it is broadly expected that the first signs of SUSY may well be obtained in inclusive signatures (e.g. jets and missing energy) which may provide some information on the mass scale of the decaying (s)particles but no direct evidence for the existence of SUSY itself.

Early signs of SUSY are also expected in the dilepton (especially same-sign) and in the generic jets+missing energy+leptons channels. While the presence of leptons makes these signatures more robust, the lack of a convincing “mass peak” maintains the indirect nature of the observation.

In an attempt to circumvent this problem to the greatest possible extent, the observation of the decay $\tilde{\chi}_2^0 \rightarrow \ell^\pm \ell^\mp \tilde{\chi}_1^0$ has been studied extensively in the past 15 years. With the LSP (the $\tilde{\chi}_1^0$) always missing, the invariant mass spectrum of the two leptons is characterized by a linear rise with mass (indicative of the spin-zero nature of the decay) and an abrupt edge at the kinematic limit (corresponding to the mass difference between the two neutralinos, i.e. the $\tilde{\chi}_2^0$ and the $\tilde{\chi}_1^0$). The observation of this edge has been touted as one of the potential “key” SUSY signatures¹. This decay mode has received a lot of attention in the signature, since the position of the edge can be determined with (a priori) high precision and is an example of “high-precision” SUSY measurements at the LHC. This high precision also probes the properties of SUSY particles since the position of the di-electron and di-muon edges could be found to be different, indicating a

¹In a different region of mSUGRA space the decay to a light higgs boson and a $\tilde{\chi}_1^0$ provides another “key” – though not unique to SUSY – signature for SUSY.

CHAPTER 1. INTRODUCTION

non-degeneracy in the masses of the selectron and smuon [13].

The purpose of this analysis is to study the precision with which one can observe this dilepton edge with a relatively modest amount of integrated luminosity (taken to be 1fb^{-1} here). It is by no means expected that this signature will constitute the first observation of an excess over the Standard Model (SM) expectations, and for this reason the analysis assumes that a general excess over the SM will have already been established. The implication is that the analysis aims at maximizing the precision of the determination of the edge, rather than the significance of the overall SUSY excess over the background processes.

Assuming the discovery of supersymmetry another important objective of the LHC studies comes into play: the measurement of the parameters of the underlying supersymmetric model. On this direction, the present thesis presents an attempt on the measurement of the supersymmetric particle masses using the decay chain involving the $\tilde{\chi}_2^0$. The analysis is placed on a complementary basis to the di-lepton analysis that will serve to the establishment of supersymmetry through the measurement of the properties of the SUSY particles.

According to the expectations that the gluinos and squarks (of the first two generations) must be among the heaviest of sparticles, the signal decay chain of $\tilde{\chi}_2^0 \rightarrow \tilde{\chi}_1^0 \ell \ell$ may arise from sequential decay chains, such as

$$(\tilde{g} \rightarrow) \tilde{q}(q) \rightarrow \tilde{\chi}_2^0 q(q) \rightarrow \tilde{\ell}^\pm \ell^\mp q(q) \rightarrow \tilde{\chi}_1^0 \ell^\pm \ell^\mp q(q)$$

generically referring to the chain as a *cascade* decay of \tilde{g}/\tilde{q} . The longer the decay chain is, the more information is in principle available to the measurement of the masses of the sparticles involved. It has been seen that exploiting the kinematic properties of such decay chains, the reconstruction of four susy masses (namely the $M_{\tilde{\chi}_1^0}$, $M_{\tilde{\ell}}$, $M_{\tilde{\chi}_2^0}$ and $M_{\tilde{q}}$) may be achieved by measuring upper endpoints in the invariant mass distributions of the visible particles (two leptons and a quark). The methodology encountered in this thesis involves the least model-dependent assumptions. However and for the sake of clarity, two models² which assume the enhancement of the signal decay mode will be used as an example in order to illustrate the procedure of the measurements and the extraction of the masses.

Throughout the analysis, a complete overview of the values of the various endpoints of the mass distributions as a function of the sparticle masses will be presented. The problem of how to identify the leptons and jets and how to reduce the combinatorial backgrounds which unavoidably arise from the selection will be addressed. A difficulty is that, depending on the ratios of the sparticle masses, different configurations and hence different formulae can relate the masses to the endpoints in two- and three-body effective mass distributions. It will be shown that the identification of the correct configuration (and corresponding formula) can be based on correlations between different effective mass distributions. Moreover, the applicability of a given formula depends on well defined ratios and only some of them can be valid at any given mass point.

²These points are taken to be the mSUGRA LM1 and LM6.

2

Theoretical overview

2.1 The Standard Model

The Standard Model is a quantum field theory which provides a very elegant and successful theoretical description of the elementary particles and their interactions. The basic concept of the theory is the principle of local gauge invariance under the symmetry group $SU(3) \times SU(2) \times U(1)$, via which the theory describes the strong, weak and electromagnetic interactions via the exchange of spin-1 gauge fields: eight massless gluons and one massless photon, for the strong and electromagnetic interactions respectively, and three massive bosons, W^\pm and Z , for the weak interaction.

The matter particle content of the theory is composed of the known leptons and quarks, which are organized in three families:

$$\begin{bmatrix} \nu_e & u \\ e^- & d' \end{bmatrix}, \quad \begin{bmatrix} \nu_\mu & c \\ \mu^- & s' \end{bmatrix}, \quad \begin{bmatrix} \nu_\tau & t \\ \tau^- & b' \end{bmatrix} \quad (2.1)$$

The strong interactions are described in the context of the gauge theory of **Quantum Chromodynamics (QCD)**. The gauge symmetry group of the theory, $SU(3)_C$, is generated by the local color transformations which leave the Lagrangian invariant. There are three possible color states for the quarks which are assumed to be in the fundamental representation of the group of dimension three. The gauge boson particles which are associated with this gauge symmetry are the gluons; there are eight of them as implied by the number of $SU(3)$ generators. The QCD Lagrangian is built with promoting the global symmetry $SU(3)$ to a local one by replacing the derivative of the quark field in the Dirac equation, by its covariant derivative:

$$D_\mu q \equiv \left(\partial_\mu - ig_s \left(\frac{\lambda_\alpha}{2} \right) A_\mu^\alpha \right) q \quad (2.2)$$

where

$$q = \begin{pmatrix} q_1 \\ q_2 \\ q_3 \end{pmatrix} \quad (2.3)$$

and q_i = quark fields ($i = 1, 2, 3$), g_s = strong coupling constant, $\frac{\lambda_\alpha}{2}$ = $SU(3)$ generators and A_μ^α = gluon fields ($\alpha = 1, \dots, 8$).

CHAPTER 2. THEORETICAL OVERVIEW

The QCD Lagrangian can then be written in terms of the quark fields, including in addition a kinetic term for the gluon fields:

$$\mathcal{L}_{QCD} = \bar{q}(i\cancel{D} - m_q)q - \frac{1}{4}F_{\mu\nu}^\alpha F_\alpha^{\mu\nu} \quad (2.4)$$

The gauge interactions between the quarks and gluons are contained in the $\bar{q}i\cancel{D}q$ term, $\bar{q}g_s \frac{\lambda^\alpha}{2} A_\mu^\alpha \gamma^\mu q$. The gluon field strength is,

$$F_{\mu\nu}^\alpha = \partial_\mu A_\nu^\alpha - \partial_\nu A_\mu^\alpha + g_s f^{\alpha\beta\gamma} A_{\mu\beta} A_{\nu\gamma} \quad (2.5)$$

exhibiting a bilinear term characteristic to the non-Abelian nature of the QCD gauge theory with structure constants $f^{\alpha\beta\gamma}$ ($\alpha, \beta, \gamma = 1, \dots, 8$). The consequence of this term is that the gluons interact not only with the quarks but also among themselves.

The **Electroweak Theory** requires the symmetry of $SU(2)_L \times U(1)_Y$ to be a local symmetry of the electroweak Lagrangian. $SU(2)_L$ is the weak isospin group and acts only on left-handed fermions, while $U(1)_Y$ is the weak hypercharge group. The left-handed fermions transform as doublets under the $SU(2)_L$,

$$f_L = \begin{pmatrix} \nu_L \\ e_L \end{pmatrix}, \begin{pmatrix} u_L \\ d_L \end{pmatrix}, \dots \quad (2.6)$$

whereas the right-handed fermions transform as singlets,

$$f_R = e_R, u_R, d_R, \dots \quad (2.7)$$

The gauge bosons which are associated with the $SU(2)_L \times U(1)_Y$ group are four, three of which are the weak bosons W_μ^i ($i = 1, 2, 3$), corresponding to the three $SU(2)_L$ generators, $T_i = \frac{\sigma_i}{2}$ where σ_i are the Pauli matrices. The fourth one is the hypercharge boson, B_μ , corresponding to the $U(1)_Y$ generator, $\frac{Y}{2}$.

The $SU(2)_L \times U(1)_Y$ symmetry is promoted from global to local using the covariant derivative for a generic fermion field f ,

$$D_\mu f = \left(\partial_\mu - ig\vec{T} \cdot \vec{W}_\mu - ig'\frac{Y}{2}B_\mu \right) f \quad (2.8)$$

where g and g' are the $SU(2)_L$ and $U(1)_Y$ coupling constants respectively. Similarly to the case of QCD, the gauge invariant electroweak interactions are generated from the $\bar{f}i\cancel{D}f$ term.

The total Lagrangian of the Electroweak theory is obtained by including the gauge boson kinetic terms in addition to the fermion ones. The Lagrangian can then be written as:

$$\mathcal{L}_{EW} = \bar{f}i\cancel{D}f - \frac{1}{4}W_{\mu\nu}^i W_i^{\mu\nu} - \frac{1}{4}B_{\mu\nu} B^{\mu\nu} \quad (2.9)$$

with the gauge part written in terms of the field strength tensors $W_{\mu\nu}^i = \partial_\mu W_\nu^i - \partial_\nu W_\mu^i + g\epsilon^{ijk}W_\mu^j W_\nu^k$ and $B_{\mu\nu} = \partial_\mu B_\nu - \partial_\nu B_\mu$. The gauge part of the Lagrangian contains the self-interaction terms among the three W_μ^i , $i = 1, 2, 3$ gauge bosons, as it is expected by the non-abelian nature of the $SU(2)_L$ group.

2.1. THE STANDARD MODEL

The physical states of the gauge bosons are known as W_μ^\pm , Z_μ and A_μ , and are obtained from the electroweak interaction eigenstates by the following expressions,

$$W_\mu^\pm = \frac{1}{\sqrt{2}}(W_\mu^1 \mp iW_\mu^2) \quad (2.10)$$

$$Z_\mu = \cos \theta_w W_\mu^3 - \sin \theta_w B_\mu \quad (2.11)$$

$$A_\mu = \sin \theta_w W_\mu^3 + \cos \theta_w B_\mu \quad (2.12)$$

where the weak (Weinberg) angle, θ_w , determines the rotation in the neutral sector and is equal to

$$\tan \theta_w = g/g' \quad (2.13)$$

It is noted that mass terms for these physical boson states are not present in the Lagrangian up to now, as it is forbidden by gauge invariance. However, the boson masses can be generated in a gauge invariant way by the spontaneous breaking of the $SU(2)_L \times U(1)_Y$ symmetry and the Higgs mechanism. To this subject we come next.

The Electroweak Symmetry Breaking. First, let us write the full standard model Lagrangian for reference

$$\mathcal{L}_{SM} = \bar{q}i\not{D}q + \bar{\ell}i\not{D}\ell - \frac{1}{4}(F_{\mu\nu}^\alpha)^2 \quad (2.14)$$

$$+|D_\mu \phi|^2 - V(\phi) \quad (2.15)$$

$$-(\lambda_u^{ij}\bar{u}_R^i \phi \cdot q_L^j + \lambda_d^{ij}\bar{d}_R^i \phi^* \cdot q_L^j + \lambda_\ell^{ij}\bar{e}_R^i \phi^* \cdot e_L^j + h.c.) \quad (2.16)$$

The line (2.14) is the pure gauge theory as it was discussed in extend previously. This part of the Lagrangian contains only three parameters, the three standard model gauge couplings g_s, g, g' . The line (2.15) corresponds to the electroweak symmetry breaking part and is associated with the Higgs boson field. The standard model introduces one scalar field, a doublet of weak interaction $SU(2)$,

$$\phi = \begin{pmatrix} \phi^+ \\ \phi^0 \end{pmatrix} \quad (2.17)$$

so that its vacuum expectation value can give masses to the W and Z bosons. If we take the potential energy of the Higgs field to be $V(\phi) = -\mu^2\phi^\dagger\phi + \lambda(\phi^\dagger\phi)^2$, this is minimized when $\phi^\dagger\phi = \mu^2/2\lambda$. Therefore, one particular vacuum state is

$$\langle \phi \rangle = \begin{pmatrix} 0 \\ 1/\sqrt{2}v \end{pmatrix} \quad (2.18)$$

where $v^2 = \mu^2/\lambda$. The physical spectrum is built by performing small oscillations around this vacuum. These are parametrized as

$$\phi = e^{i\alpha(x)\tau} \begin{pmatrix} 0 \\ \frac{1}{\sqrt{2}}(v + h(x)) \end{pmatrix} \quad (2.19)$$

with $\alpha^\alpha(x)$ an $SU(2)$ gauge transformation. We note that the field $h(x)$ is the only gauge-invariant degree of freedom and so the symmetry breaking sector gives rise to only one new particle, the Higgs scalar. In contrast to the gauge boson sector, the Higgs boson mass and the Higgs self-coupling λ are completely undetermined in the standard model. They are related at tree level by $m_H^2 = 2\lambda v^2$.

Inserting (2.18) into the kinetic term for ϕ , one finds a mass term for the W and Z ,

$$m_W = g \frac{v}{2}, \quad m_Z = \sqrt{g^2 + g'^2} \frac{v}{2} \quad (2.20)$$

The vacuum expectation value v has been determined experimentally from μ -decay and is equal to $v = (\sqrt{2}G_F)^{-\frac{1}{2}} = 246$ GeV. The line (2.16) gives similarly an origin for the masses of quarks and leptons via their interaction with the Higgs. The parameters λ_{ij} are three complex 3×3 matrices of couplings which are allowed by the gauge symmetry of the standard model, and are known as Yukawa couplings. When the Higgs acquires a vacuum expectation value, these couplings turn into mass terms,

$$m_e = \lambda_e \frac{v}{\sqrt{2}}; \quad m_u = \lambda_u \frac{v}{\sqrt{2}}; \quad m_d = \lambda_d \frac{v}{\sqrt{2}}; \dots \quad (2.21)$$

The Higgs sector is the only sector in the standard model that has not been tested yet. The only relevant information has been derived from indirect constraints and direct searches. However, theoretical arguments exist, providing a favorable region on the Higgs mass, $130 \text{ GeV} \leq m_H \leq 180 \text{ GeV}$ which is consistent with an effective standard model description that survives all the way to the Planck scale¹. On the other hand, the non-observation of clear signals in accelerator experiments like CERN and Fermilab, has only lead to indirect experimental bounds on the Higgs boson mass. The global fit to precision measurements of electroweak observables has resulted in the $\Delta\chi^2 = \chi^2 - \chi^2_{min}$ curve shown in fig. 2.1. At 95% confidence level, it was obtained

$$114.4 \text{ GeV} < m_H < 144 \text{ GeV}. \quad (2.22)$$

2.2 Motivation for New Physics

The standard model has been proved, at least phenomenologically, as a successful theory and has been established experimentally with a precision of 0.1%. Still, it can only be regarded as a low-energy effective theory of the yet-more-fundamental theory. The fact for example that its theoretical framework cannot accommodate gravity which is governed by the Planck scale, $M_P = (8\pi G_{Newton})^{-1/2} = 2.4 \times 10^{18}$ GeV, makes it almost obvious that the standard model needs to be extended to describe physics at higher energies. Several reasons can be listed outlining the problematic theoretical aspects of the standard model, in favor of new physics in the TeV scale: i) the “hierarchy problem”: what is the origin of the masses of the particles, if they are due to the Higgs boson field, and if yes, why are they so small. ii) Unification of the strong and electromagnetic

¹Although the hierarchy problem between the electroweak and a very high energy scale like $\Lambda = M_{Pl}$ (Planck scale) still persists.

2.2. MOTIVATION FOR NEW PHYSICS

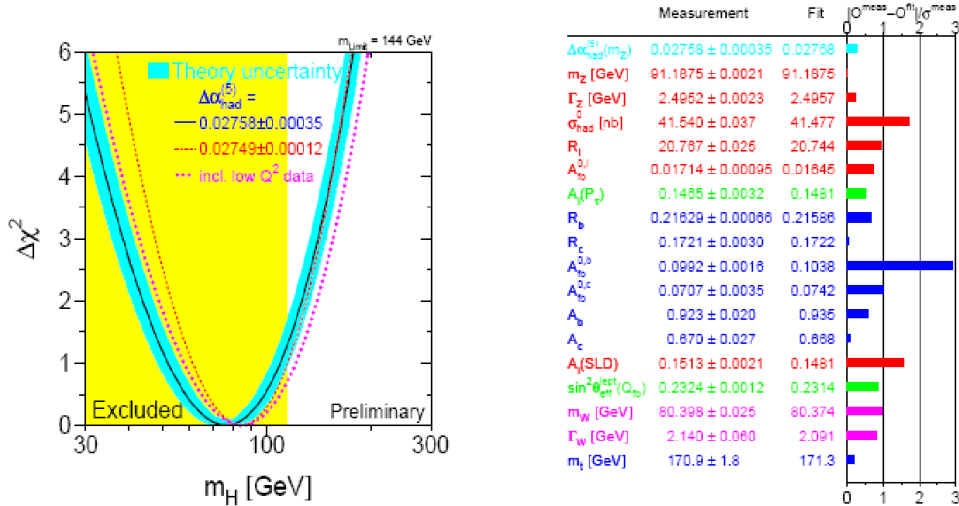


Figure 2.1: Left: $\Delta\chi^2 = \chi^2 - \chi^2_{\text{min}}$ versus m_H , from the global fit to the electroweak data. The vertical band indicates the 95% exclusion limit from direct searches. Right: Comparison between the measurements of the combined analysis of the standard model and the results from the global electroweak fit.

gauge couplings at the Planck scale (or Grand Unified Theory, GUT, scale) does not occur in the standard model. This could only be achieved with the addition of new physics that would modify the running of couplings above the electroweak scale. iii) It does not explain the quantum numbers of the particles like the electric charge Q , the weak isospin I and the hypercharge Y .

Supersymmetry has been proposed in order to solve many of the above problems in the standard model, and most importantly the infamous "hierarchy problem". That is to explain the origin of the large hierarchy of energy scales from the W and Z masses to the Planck scale (*gauge hierarchy*) and protect the stability of this hierarchy in the presence of quantum corrections, the latter being impossible within the standard model.

The hierarchy problem.

The scalar sector of the standard model, the Higgs boson, receives enormous corrections from the virtual effects of every particle that couples, directly or indirectly, to the Higgs field. As an example let us consider the contribution of a loop containing a heavy fermion f with mass m_f to the Higgs self-energy. If the Higgs field couples to f with a term in the Lagrangian $-\lambda_f H \bar{f} f$, then the Feynman diagram in figure 2.2a yields a correction

$$\delta m_H^2 = -\frac{|\lambda_f|^2}{8\pi^2} \Lambda_{UV}^2 + \dots \quad (2.23)$$

where we have introduced an ultraviolet momentum cutoff Λ_{UV} in order to regulate the loop integral; this parameter represents the energy scale at which new physics enters and is comparable with the Planck scale. In this view, this quantum correction to m_H^2 is some 30 orders of magnitude

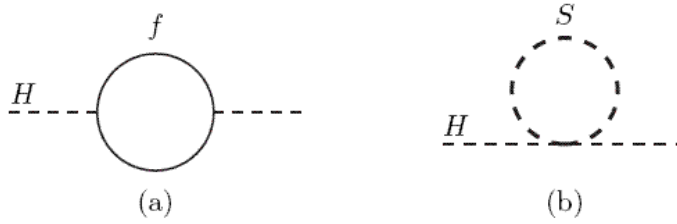


Figure 2.2: *One-loop quantum corrections to the Higgs squared mass parameter m_H^2 , due to (a) a Dirac fermion f , and (b) a scalar S .*

larger than the expected value of the Higgs mass². This is only directly a problem to the stability of the Higgs mass. However, since the fermions and the electroweak bosons W^\pm, Z obtain their masses from $\langle H \rangle$, the entire spectrum of the standard model becomes sensitive to the parameter Λ_{UV} .

If another heavy scalar particle S exists with mass m_S that couples to the Higgs with a Lagrangian term $-\lambda_S |H|^2 |S|^2$, then the Feynman diagram in figure 2.2b gives a correction

$$\delta m_H^2 = \frac{\lambda_S}{16\pi^2} \left[\Lambda_{UV}^2 - 2m_S^2 \ln \left(\frac{\Lambda_{UV}}{m_S} \right) + \dots \right]. \quad (2.24)$$

Comparing eqs. (2.23) and (2.24) strongly suggests that if a new symmetry which relates fermions and bosons exists, then the Λ_{UV}^2 contributions would neatly cancel because of the relative minus sign between fermion loop and boson loop contributions to δm_H^2 . This sort of cancellation also requires that the associated dimensionless couplings should be related by $\lambda_S = |\lambda_f|^2$.

In fact, a theory which guarantees that the quadratic divergences in scalar squared masses vanish to all orders of perturbation theory, exists and is called *Supersymmetry*.

2.3 Supersymmetry

A supersymmetry transformation must turn a bosonic state into a fermionic one, and vice versa. In other words, the generator Q of the symmetry must be an anticommuting spinor, with

$$Q|\text{Boson}\rangle = |\text{Fermion}\rangle, \quad Q|\text{Fermion}\rangle = |\text{Boson}\rangle$$

Spinors are intrinsically complex objects, so Q^\dagger (the hermitian conjugate of Q) is also a symmetry generator. It is obvious that the generators themselves must carry half-integer spin, i.e. are fermionic, and therefore supersymmetry must be a space-time symmetry. These supersymmetry properties can be synthesised in anticommutation and commutation relations forming the supersymmetric algebra:

²Since we know experimentally that $\langle H \rangle$ is approximately 174 GeV, from the weak interaction properties measurements, it must be that m_H^2 is very roughly of order -100 GeV.

$$\{Q, Q\} = \{Q^\dagger, Q^\dagger\} = 0$$

$$\{Q, Q^\dagger\} = P^\mu$$

$$[P^\mu, Q] = [P^\mu, Q^\dagger] = 0$$

where P^μ is the four momentum generator of space-time translations and must appear in the supersymmetry algebra in order to be consistent with Lorentz covariance.

The single-particle states of a supersymmetric theory are organized in *supermultiplets*, which constitute the irreducible representations of the supersymmetry algebra. Each supermultiplet contains both fermionic and bosonic states, which are known as superpartners of each other. Furthermore, the number of bosonic degrees of freedom n_b and the number of fermionic degrees of freedom, n_f , in each supermultiplet are equal,

$$n_b = n_f \quad (2.25)$$

It follows that particles that fall into the same supermultiplet have the following properties: (i) since the squared-mass operator $-P^2$ commutes with the operators Q and Q^\dagger , they must have equal eigenvalues of $-P^2$, and therefore equal masses. (ii) The supersymmetry generators Q, Q^\dagger also commute with the generators of gauge transformations. Therefore particles in the same supermultiplet must also be in the same representation of the gauge group, or else must have the same quantum numbers of electric charge, weak isospin and color.

In every renormalizable field theory, there are two types of supermultiplets: chiral and vector supermultiplets. Their content can be any possible combination of bosonic and fermionic fields which is consistent with eq. (2.25).

Chiral or *matter* or *scalar* supermultiplets have a single Weyl fermion ψ (with two spin helicity states, so $n_f = 2$) and two real scalars (each with $n_b = 1$) which are naturally assembled into a complex scalar field.

The left- and right-handed parts of all the standard model fermions transform differently under the gauge group, and so they must be members of chiral supermultiplets. The names for the spin-0 partners of the quarks and leptons are constructed by prepending an "s", which stands for scalar, and so they are called *squarks* and *sleptons* (or sometimes *sfermions*). The left-handed and right-handed pieces of the quarks and leptons constitute separately a two-component Weyl fermion and therefore each must have its own scalar partner. For example, the left-handed and right-handed parts of the electron Dirac field are called left- and right-handed selectrons, and are denoted \tilde{e}_L and \tilde{e}_R ³. The standard model neutrinos are always left-handed, so the sneutrinos are denoted generically by $\tilde{\nu}$. Finally, a similar scheme applies to the squarks \tilde{q}_L, \tilde{q}_R with $q = u, d, s, c, b, t$.

The Higgs scalar boson also resides in a chiral supermultiplet, since it has spin-0. Actually, for reasons that will be explained later, the structure of supersymmetric theories require two Higgs supermultiplets, one to give mass to the up-type quarks and the other to the down-type quarks.

³The "handedness" here does not refer to the helicity of the selectrons but that of their superpartners.

The fermionic partners of the Higgs scalars are called *higgsinos*.

Vector or *gauge* supermultiplets, consist of a gauge field (spin-1 boson with two helicity states, $n_b = 2$) and its fermionic partner, a Weyl fermion (with $n_f = 2$) which is called *gaugino*. Note that a gauge boson must transform as the adjoint representation of the gauge group, and so its fermionic partner, the gaugino, must also. Since the adjoint representation of a gauge group is always its own conjugate, the gaugino fermion must have the same transformation properties for left-handed and right-handed components. The vector bosons of the standard model clearly must reside in gauge supermultiplets. The fermionic superpartner of the gluon is called \tilde{g} , the *gluino*, and the fermionic partners of the electroweak bosons W 's and Z , are the \tilde{w} (*winos*) and \tilde{z} (*zino*) respectively.

An exact unbroken supersymmetry would predict that a particle and its superpartner have the same mass, so the supersymmetric particles should have been detected long ago together with the observed standard model particles. However, none of the superpartners of the standard model particles has been discovered so far, and so their masses must differ. This may indicate that supersymmetry is broken in the vacuum state chosen by nature. On the other hand, if supersymmetry is to be a solution to the hierarchy problem, then this mass difference between fermions and bosons must be at the weak scale

$$|m_f^2 - m_b^2| \leq 1 \text{ TeV}^2 \quad (2.26)$$

We therefore led to consider "soft" supersymmetry breaking. This means that the effective Lagrangian of the minimal supersymmetric theory can be written in the form

$$\mathcal{L} = \mathcal{L}_{SUSY} + \mathcal{L}_{soft} \quad (2.27)$$

where \mathcal{L}_{SUSY} contains all the gauge and Yukawa interactions and preserves supersymmetry invariance, and \mathcal{L}_{soft} violates supersymmetry but contains only mass terms and coupling parameters with positive mass dimension. The latter is needed in order to ensure that the scalar masses squared are only logarithmically divergent.

Supersymmetric Lagrangians

Let ψ_i , A_i be the fermion and complex scalar fields respectively of a chiral supermultiplet, denoted by the symbol ϕ . Lagrangians for chiral supermultiplets consist of two parts, the Kahler potential and the superpotential. The Kahler potential is just the kinetic terms for the fields and can be written as

$$\mathcal{L}_{kin}^{chiral} = \partial_\mu A_i^* \partial^\mu A_i + \bar{\psi}_i \gamma^\mu \partial_\mu \psi_i + F_i^* F_i \quad (2.28)$$

where F is a non-dynamical, auxiliary, complex field which has been introduced so as to allow the supersymmetry algebra to work off-shell. The superpotential is defined by a holomorphic function $W(\phi)$ of the chiral supermultiplets ϕ_i and therefore it cannot contain their complex conjugates ϕ_i^* ,

$$\mathcal{L} \supset -\frac{1}{2} \frac{\partial^2 W}{\partial \phi_i \partial \phi_j} |_{\phi_i = A_i} \psi_i \psi_j + \frac{\partial W}{\partial \phi_i} |_{\phi_i = A_i} F_i \quad (2.29)$$

2.3. SUPERSYMMETRY

The first term in (2.29), describes the Yukawa couplings between fermionic and bosonic components of the chiral supermultiplets. For what concerns the second term, we can solve for the field F and eliminate it from the Lagrangian, to find instead a potential term

$$V_F = \left| \frac{\partial W}{\partial \phi_i} \right|_{\phi_i=A_i}^2 \quad [2.30]$$

This simple result is called the *F-term* potential. It is minimized by setting all of the F_i equal to zero. If this is possible, we obtain a vacuum expectation value with $\langle H \rangle = 0$ which is also invariant to supersymmetry, otherwise $\langle H \rangle \neq 0$ which implies that supersymmetry is spontaneously broken.

A vector supermultiplet W_α , consisting of the gauge field A_μ and a Weyl fermion λ_α , has the supersymmetric Lagrangian

$$\mathcal{L}_{kin}^{gauge} = -\frac{1}{4}F_{\mu\nu} + \bar{\lambda}^\alpha i\slashed{D}\lambda^\alpha + \frac{1}{2}D^\alpha D^\alpha \quad [2.31]$$

where the field D is a non-dynamical (auxiliary) real scalar field.

Since the vector supermultiplets contain gauge fields, chiral supermultiplets which transform non-trivially under the gauge group should also couple to the vector multiplets to make the Lagrangian gauge invariant. This leads to the following modification of the Kahler potential,

$$\mathcal{L}_{kin} = D_\mu A_i^\dagger D^\mu A_i + \bar{\psi}_i i\gamma^\mu D_\mu \psi_i + F_i^\dagger F_i \quad [2.32]$$

$$-\sqrt{2}(A^\dagger T^\alpha \lambda^\alpha \psi) - g A^\dagger T^\alpha D^\alpha A. \quad [2.33]$$

Using eqs. (2.29, 2.30), one can solve for D^α and eliminate it from the Lagrangian to find a potential term, known as *D-term*

$$V_D = \frac{g^2}{2}(A^\dagger T^\alpha A)^2 \quad [2.34]$$

As with the F-term, the ground state of this potential is obtained by setting all of the D^α equal to zero, if it is possible, to obtain a supersymmetric vacuum state with $\langle H \rangle = 0$.

Using the eqs. (2.33, 2.30, 2.34), we can write down the full supersymmetric generalization of the standard model as

$$\mathcal{L} = \mathcal{L}_{gauge} + \mathcal{L}_{kin} + \mathcal{L}_{Yukawa} + \mathcal{L}_\mu \quad [2.35]$$

The last term is an additional gauge-invariant term that we could add to the superpotential,

$$\Delta W = \mu h_1 h_2 \quad [2.36]$$

This term stands for phenomenological reasons and contributes a supersymmetric mass term to the Higgs field and to their fermion partners. An important notice is that the parameter μ is the only new parameter that we have added so far to the standard model.

Softly broken supersymmetry

We now need to find terms in the Lagrangian which cause supersymmetry to be spontaneously broken. In general, models of supersymmetry breaking are not simple. So most studies of supersymmetry do not invoke the supersymmetry breaking mechanism directly but rather try to treat its consequences phenomenologically. This can be done by adding terms to (2.35) which violate supersymmetry but become negligible at higher energies. An important constraint however is that such terms should not spoil the cancellation of quadratic divergences in the scalar mass terms.

So, the possible soft supersymmetry breaking terms in the Lagrangian of a general theory are

$$\begin{aligned}\mathcal{L}_{soft} = & - \left(\frac{1}{2} M_\alpha \lambda^\alpha \lambda^\alpha + \frac{1}{2} b^{ij} \phi_i \phi_j + \frac{1}{6} \alpha^{ijk} \phi_i \phi_j \phi_k \right) + \text{c.c.} \\ & - (m^2)_j^i \phi^{j*} \phi_i\end{aligned}\quad (2.37)$$

with coefficients that correspond to gaugino masses M_α for each gauge group, scalar squared-mass terms $(m^2)_i^j$ and b^{ij} , and (scalar)³ couplings α^{ijk} . The first term removes the degeneracy between gauginos and gauge bosons. The next two terms are usually called bilinear and trilinear soft breaking terms with parameters b^{ij} and α^{ijk} with mass dimension one. The last term is the masses for scalar components in the chiral supermultiplets, which removes degeneracy between the scalar and spinor components.

We are now ready to build a phenomenological model of supersymmetry by adding in (2.35) the various terms in \mathcal{L}_{soft} with coefficients to be determined by experiment.

2.4 The Minimal Supersymmetric Standard Model

The minimal supersymmetric Standard Model (MSSM) is essentially a straight forward supersymmetrization of the standard model. It is "minimal" in the sense that the number of superfields and interactions are kept as small as possible. As in the standard model, the MSSM is based on the gauge group $SU(3)_C \times SU(2)_L \times U(1)_Y$. It is also a fully realistic supersymmetric model, i.e. a theory with softly broken supersymmetry that satisfies all phenomenological constraints.

2.4.1 Particle content and interactions

We have argued that each of the known fundamental particle must reside in either a chiral or gauge supermultiplet, and have a superpartner with spin differing by 1/2 unit. Since there are no viable candidates to the role of superpartners, the particle spectrum of the MSSM is obtained by doubling the existing particle spectrum of the standard model. We next describe chiral and gauge supermultiplets that make up the particle content of the MSSM.

Table 2.1 summarizes all the chiral superfields of a minimal supersymmetric extension of the standard model. These are classified according to their transformation properties under the gauge group $SU(2)_L \times U(1)_Y$, so that: Q contains the quark and squark $SU(2)_L$ doublets,

$$Q = \begin{pmatrix} u_L \\ d_L \end{pmatrix} \quad \text{and} \quad \tilde{Q} = \begin{pmatrix} \tilde{u}_L \\ \tilde{d}_L \end{pmatrix} \quad (2.38)$$

while the U^c and D^c contain the (s)quark singlets: up-type and down-type left-handed anti-quarks \bar{u}_R and \bar{d}_R , and their scalar partners \tilde{u}_R^* and \tilde{d}_R^* .

2.4. THE MINIMAL SUPERSYMMETRIC STANDARD MODEL

The superfield L contains the lepton and slepton $SU(2)_L$ doublets,

$$L = \begin{pmatrix} \nu_L \\ e_L \end{pmatrix} \quad \text{and} \quad \tilde{L} = \begin{pmatrix} \tilde{\nu}_L \\ \tilde{e}_L \end{pmatrix} \quad (2.39)$$

and E^c contains the (s)lepton singlets: the right-handed anti-electron \bar{e}_R , and its superpartner \tilde{e}_R^* .

Table 2.1: *Chiral supermultiplets in the MSSM.*

Superfield	spin-1/2	spin-0	$SU(3)_C, SU(2)_L, U(1)_Y$
\hat{Q}	(u_L, d_L)	$(\tilde{u}_L, \tilde{d}_L)$	$(3, 2, \frac{1}{6})$
\hat{U}^c	\bar{u}_R	\tilde{u}_R^*	$(\bar{3}, 1, -\frac{2}{3})$
\hat{D}^c	\bar{d}_R	\tilde{d}_R^*	$(\bar{3}, 1, \frac{1}{3})$
\hat{L}	(ν_L, e_L)	$(\tilde{\nu}_L, \tilde{e}_L)$	$(1, 2, -\frac{1}{2})$
\hat{E}^c	\bar{e}_R	\tilde{e}_R^*	$(1, 1, 1)$
H_u	$(\tilde{H}_u^+, \tilde{H}_u^0)$	(H_u^+, H_u^0)	$(1, 2, +\frac{1}{2})$
H_d	$(\tilde{H}_d^0, \tilde{H}_d^-)$	(H_d^0, H_d^-)	$(1, 2, -\frac{1}{2})$

The Higgs boson also resides in a chiral supermultiplet. The Higgs couples to the up-type quarks and generate their masses upon the symmetry breaking. In order to generate down-type quark masses, however, we normally use $i\sigma_2 H^* = (H^+, H^0) = (H^{0*}, -H^-)$. In the supersymmetric fashion of the standard model, this trick does not work because the superpotential is not allowed to include a complex conjugation of this sort. Therefore, we need to introduce another chiral supermultiplet H_d which has the same gauge quantum numbers of $i\sigma_2 H^*$ above⁴. So, the weak isospin components of H_u with $T_3 = (1/2, -1/2)$ have electric charges 1, 0 respectively, and are denoted as

$$H_u = \begin{pmatrix} H_u^+ \\ H_u^0 \end{pmatrix} \quad \text{and} \quad \tilde{H}_u = \begin{pmatrix} \tilde{H}_u^+ \\ \tilde{H}_u^0 \end{pmatrix} \quad (2.40)$$

Similarly, the $SU(2)_L$ -doublet complex scalar H_d has $T_3 = (1/2, -1/2)$ components are denoted as

$$H_d = \begin{pmatrix} H_d^0 \\ H_d^- \end{pmatrix} \quad \text{and} \quad \tilde{H}_d = \begin{pmatrix} \tilde{H}_d^0 \\ \tilde{H}_d^- \end{pmatrix} \quad (2.41)$$

Table 2.2 summarizes the gauge supermultiplets containing the vector bosons of the standard model and their fermionic superpartners, the gauginos. The $SU(3)_C$ gauge bosons, the gluons, are associated with a spin-1/2 color-octet supersymmetric partner, the gluino. The $SU(2)_L \times U(1)_Y$ spin-1 gauge bosons W^+, W^0, W^- and B^0 , are associated with spin-1/2 superpartners $\tilde{W}^+, \tilde{W}^0, \tilde{W}^-$ and \tilde{B}^0 , the winos and bino. After electroweak symmetry breaking, the W^0 and B^0 gauge eigenstates mix to give mass eigenstates Z^0 and γ . The corresponding gaugino mixtures of \tilde{W}^0 and \tilde{B}^0 are called zino (\tilde{Z}^0) and photino ($\tilde{\gamma}$).

⁴Another reason to need both H_u and H_d chiral supermultiplets is to cancel the gauge anomalies arising from their spinor components.

Table 2.2: *Vector supermultiplets in the MSSM.*

Superfield	spin-1/2	spin-1	$SU(3)_C, SU(2)_L, U(1)_Y$
gluino, gluon	\tilde{g}	g	(8, 1, 0)
winos, W bosons	$\tilde{W}^\pm \tilde{W}^0$	$W^\pm W^0$	(1, 3, 0)
bino, B boson	\tilde{B}^0	B^0	(1, 1, 0)

Having specified the field content, we turn to define the interactions that arise from the superpotential of the MSSM Lagrangian. Of course one piece of the superpotential is the gauge field superpotential which produces the kinetic terms for the gauge bosons and gauginos. These terms generate the gauge interactions which are uniquely determined by the choice of the gauge group.

The other piece is the superpotential for the matter and Higgs fields. We shall note at this point that although the gauge symmetries constraint the superpotential, they do not completely fix it. Therefore, we can invoke the principle of minimality and only introduce those terms in the superpotential that are necessary to build a realistic model. This approach leads to the following superpotential:

$$W = \lambda_e^{ij} H L_i E_j^c + \lambda_d^{ij} H Q_i D_j^c + \lambda_u^{ij} \bar{H} Q_i U_j^c + \mu H \bar{H} \quad (2.42)$$

The first three terms correspond to the Yukawa couplings in the standard model (with exactly the same number of parameters). The subscripts i and j are generation indices. The parameter μ has mass dimension one and gives a supersymmetric mass to both fermionic and bosonic components of the chiral supermultiplets H_u and H_d .

However, there are other terms that one can write that are gauge invariant and analytic in the chiral superfields, but are not included in the MSSM because they violate either baryon number (B) or lepton number (L). Such terms are

$$W_{\Delta L=1} = \lambda_e'^{ijk} L_i L_j E_k^c + \lambda_d'^{ijk} L_i Q_j D_k^c + \mu'_i L_i H_u \quad (2.43)$$

$$W_{\Delta B=1} = \lambda_u'^{ijk} D_i^c D_j^c U_k^c \quad (2.44)$$

The terms in eq. (2.43) violate total lepton number by 1 unit and those in eq. (2.44) violate baryon number by 1 unit. The possible existence of such terms seems rather problematic, because there is no experimental evidence for the existence of any B- and L-violating processes. The most obvious experimental constraint comes from the non-observation of proton decay, which would violate both B and L by 1 unit. On the other hand, L- and B-conservation cannot be imposed as a principle: both are known to be violated by non-perturbative electroweak effects, which are negligible at ordinary energies but might be relevant in the early universe.

An alternative symmetry exists instead, which has the effect of eliminating the possibility of B and L violating terms, while allowing the good terms in eq. (2.42). This new symmetry is called "R-parity" or equivalently "matter parity". R-parity is a discrete symmetry which is defined for each particle as

$$R_p = (-1)^{3(B-L)+2s} \quad (2.45)$$

2.4. THE MINIMAL SUPERSYMMETRIC STANDARD MODEL

where s is the spin of the particle. Under R-parity, all standard model particles (matter fermions, Higgs and gauge bosons) carry even parity, while their superpartners odd due to the $(-1)^{2s}$ factor. This leads to the following extremely important phenomenological consequences:

- The lightest supersymmetric particle (LSP) must be absolutely stable. If the LSP is also electrically neutral, it can make an attractive candidate for the non-baryonic dark matter that seems to be required by cosmology.
- The decay products of all other particles must contain an odd number of LSPs (usually just one).
- In accelerator experiments, sparticles can only be produced in pairs.

2.4.2 Soft supersymmetry breaking in the MSSM

Up to now we have presented the supersymmetry conserving part of the MSSM Lagrangian. We saw that the gauge and Yukawa sectors introduce the same number of parameters as in the standard model; the Higgs sector involves the parameter μ which actually replaces two parameters of the standard model.

However, one needs to introduce a very large number of free parameters if it is to describe the supersymmetry breaking sector. Following the general classifications in eq. (2.37), and assuming R-parity conservation, the non-supersymmetric MSSM Lagrangian is given by

$$\begin{aligned} -\mathcal{L}_{soft}^{MSSM} = & \frac{1}{2} \left(M_3 \tilde{g} \tilde{g} + M_2 \tilde{W} \tilde{W} + M_1 \tilde{B} \tilde{B} + \text{c.c.} \right) \\ & + m_Q^{2ij} \tilde{Q}_i^* \tilde{Q}_j + m_U^{2ij} \tilde{U}_i^* \tilde{U}_j + m_D^{2ij} \tilde{D}_i^* \tilde{D}_j + m_L^{2ij} \tilde{L}_i^* \tilde{L}_j + m_E^{2ij} \tilde{E}_i^* \tilde{E}_j \\ & + \left(A_U^{ij} \lambda_u^{ij} \tilde{Q}_i \tilde{U}_j H_u + A_D^{ij} \lambda_d^{ij} \tilde{Q}_i \tilde{D}_j H_d + A_E^{ij} \lambda_e^{ij} \tilde{Q}_i \tilde{E}_j H_d + \text{c.c.} \right) \\ & + m_{H_u}^2 |H_u|^2 + m_{H_d}^2 |H_d|^2 + (B \mu H_u H_d + \text{c.c.}) \end{aligned} \quad (2.46)$$

with the following set of parameters:

- Gaugino majorana masses M_3, M_2, M_1 associated with the $SU(3), SU(2)$ and $U(1)$ subgroups of the standard model.
- Five scalar squared-mass parameters $\mathbf{m_Q^2}, \mathbf{m_U^2}, \mathbf{m_D^2}, \mathbf{m_L^2}, \mathbf{m_E^2}$, for the squarks and sleptons.
- Coefficients $\lambda_u A_U, \lambda_d A_D$ and $\lambda_e A_E$ of the Higgs-sfermion-sfermion trilinear interaction terms.
- Three scalar mass parameters $m_{H_u}^2, m_{H_d}^2$, and $B\mu$, which contribute to the Higgs potential.

The mass-squared parameters of the squarks and sleptons are all three-by-three hermitian matrices, while the trilinear couplings A^{ij} (so-called "A-parameters") and the bilinear coupling B ("B-parameter") are general complex numbers. Surprisingly enough, this results to more than 100 unknown real constants coming from the supersymmetry breaking sector of the MSSM. Fortunately, most processes are affected by only a (small) subset of these new parameters.

2.5 Phenomenology of the MSSM

Since the introduction of weak-scale supersymmetry has been motivated by the (yet hypothetical) existence of elementary Higgs bosons, it seems reasonable to start the discussion of the phenomenology of the MSSM with a treatment of the Higgs sector.

The potential for the Higgs fields have been shown to receive contributions from the term in the superpotential $W = \mu H_u H_d$ in eqs. (2.42), as well as the soft parameters in the last line of eq. (2.46). Altogether we find:

$$\begin{aligned} V_{Higgs} &= (m_{H_u}^2 + \mu^2)|H_u|^2 + (m_2^2 + m_{H_d}^2)|H_d|^2 - B\dot{\mu}(\epsilon_{ij}H_u^i H_d^j + \text{h.c.}) \\ &+ \frac{1}{8}(g^2 + g'^2)(|H_d|^2 - |H_u|^2)^2 + \frac{1}{2}g^2|H_d^{i*} H_u^i|^2 \end{aligned} \quad (2.47)$$

It is always possible to perform a gauge transformation so that the neutral components of the two Higgs doublets acquire a non-zero vacuum expectation value as

$$\langle H_u \rangle = \begin{pmatrix} 0 \\ v_u \end{pmatrix} \quad \text{and} \quad \langle H_d \rangle = \begin{pmatrix} v_d \\ 0 \end{pmatrix} \quad (2.48)$$

The Higgs potential can now be minimized easily by solving the equations $\partial V/\partial v_u = \partial V/\partial v_d = 0$. It is usually more convenient to solve these equations for the three squared-mass parameters in eq. (2.47), rather than for the vevs v_u and v_d . The reason is that the combination of vevs $v_u^2 + v_d^2 = m_W^2/g^2 = (246\text{GeV})^2$, is fixed by the W boson mass and the gauge coupling, whereas the ratio

$$\tan \beta \equiv v_u/v_d \quad (2.49)$$

becomes a free parameter of the model.

Due to the symmetry breaking, three of the eight degrees of freedom in the higgs doublets (two times the four real scalar fields) are absorbed by the the W^+, W^- and Z bosons, and we are left with five physical scalar particles. These are the two CP-even scalars h^0, H^0 , one CP-odd scalar A^0 , and two charged scalars H^+ and H^- . Their masses can be worked out from the minimized potential, resulting in:

$$m_A^2 = 2\mu^2 + m_{H_u}^2 + m_{H_d}^2, \quad m_{H^\pm}^2 = m_W^2 + m_A^2, \quad (2.50)$$

$$m_{h^0}^2, m_{H^0}^2 = \frac{1}{2} \left(m_A^2 + m_Z^2 \pm \sqrt{(m_A^2 + m_Z^2)^2 - 4m_Z^2 m_A^2 \cos^2 2\beta} \right) \quad (2.51)$$

The parameter space of the MSSM Higgs sector can be described by two parameters. This is because the potential in eq. (2.47) contains three independent parameters, $\mu^2 + m_{H_u}^2$, $\mu^2 + m_{H_d}^2$, and μB , while one combination is fixed by the symmetry breaking mechanism and Z -mass constraints. Current experimental constraints on the parameter space are usually presented in the $(m_{h^0}, \tan \beta)$ or $(m_A, \tan \beta)$ plane, as shown for example in fig. 2.3.

Following the $SU(2)_L \times U(1)_Y$ symmetry breaking, any two particles with different $SU(2)_L \times U(1)_Y$ quantum numbers can mix, if they have the same $SU(3)_C \times U(1)_{em}$ quantum numbers. We meet

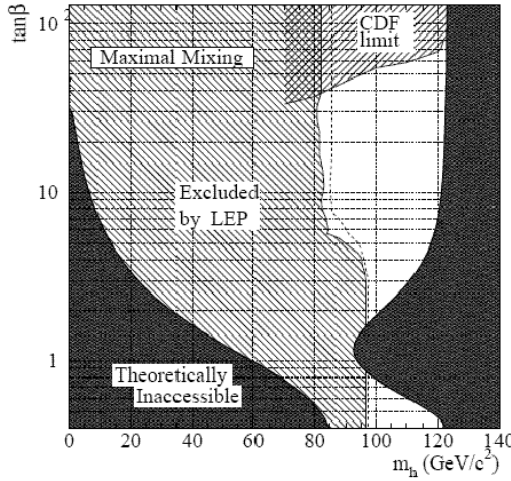


Figure 2.3: Regions in the $(m_{h^0}, \tan \beta)$ plane excluded by the MSSM Higgs boson searches at LEP in data up to 189 GeV, and at CDF in run I data. The regions not allowed by the MSSM for a top mass of 175 GeV, a SUSY scale of 1 TeV and maximal mixing in the stop sector are also indicated. The dotted curve is the LEP expected limit.

such mixing terms already in the standard model quark and lepton masses, since they couple a left-handed $SU(2)$ doublet to a right-handed singlet. A closely related phenomenon occurs in the sfermion sector of the MSSM.

Neglecting for simplicity inter-generational mixing, the spin-0 partners of left- (\tilde{f}_L) and right-handed (\tilde{f}_R) quarks and leptons can mix, and their mixing is described by mass matrices whose elements receive all type of contributions (F-terms, D-terms and SUSY breaking terms) in the scalar potential. These matrices are decomposed in a series of 2×2 matrices of the form

$$\mathcal{M}_f^2 = \begin{pmatrix} m_{\tilde{f}_{LL}}^2 & m_{\tilde{f}_{LR}}^2 \\ m_{\tilde{f}_{RL}}^2 & m_{\tilde{f}_{RR}}^2 \end{pmatrix} \quad (2.52)$$

where

$$m_{\tilde{f}_{LL}}^2 = m_f^2 + m_{\tilde{f}_L}^2 (\text{soft}) + m_{\tilde{f}_L}^2 (\text{D-term}) \quad (2.53)$$

$$m_{\tilde{f}_{RR}}^2 = m_f^2 + m_{\tilde{f}_R}^2 (\text{soft}) + m_{\tilde{f}_R}^2 (\text{D-term}) \quad (2.54)$$

$$m_{\tilde{f}_{LR}}^2 = \begin{cases} m_f(A_f + \mu \tan \beta) & f = e, \mu, \tau, d, s, b \\ m_f(A_f + \mu \cot \beta) & f = u, c, t \end{cases} \quad (2.55)$$

and the D-term contribution is given by

$$m^2 (\text{D-term}) = m_Z^2 \cos 2\beta (T_{3L} - \sin^2 \theta_w Q). \quad (2.56)$$

One therefore expects that the interaction eigenstates (\tilde{f}_L, \tilde{f}_R), differ from the mass eigenstates (\tilde{f}_1, \tilde{f}_2) with increasing the sfermion mass. However, the amount of L-R mixing is proportional

to the mass of the corresponding fermion and is usually considered negligible for the first two generations.

With substituting in eqs. (2.52)-(2.56), for the case of the scalar top we find the mixing matrix (in the $(\tilde{t}_L, \tilde{t}_R)$ basis) as:

$$\mathcal{M}_{\tilde{t}}^2 = \begin{pmatrix} m_t^2 + m_{\tilde{t}_L}^2 + (\frac{1}{2} - \frac{2}{3}s_w^2)c_{2\beta}m_Z^2 & -m_t(A_t + \mu \cot \beta) \\ -m_t(A_t + \mu \cot \beta) & m_t^2 + m_{\tilde{t}_R}^2 + \frac{2}{3}s_w^2c_{2\beta}m_Z^2 \end{pmatrix} \quad (2.57)$$

where $s_w^2 = \sin^2 \theta_w$ and $c_{2\beta} = \cos 2\beta$. Similarly, the mass matrices for the sbottoms and staus in their gauge eigenstates $(\tilde{b}_L, \tilde{b}_R)$ and $(\tilde{\tau}_L, \tilde{\tau}_R)$ basis respectively, are

$$\mathcal{M}_{\tilde{b}}^2 = \begin{pmatrix} m_b^2 + m_{\tilde{b}_L}^2 + (\frac{1}{2} - \frac{2}{3}s_w^2)c_{2\beta}m_Z^2 & -m_b(A_b + \mu \tan \beta) \\ -m_b(A_b + \mu \tan \beta) & m_b^2 + m_{\tilde{b}_R}^2 - \frac{1}{3}s_w^2c_{2\beta}m_Z^2 \end{pmatrix} \quad (2.58)$$

and

$$\mathcal{M}_{\tilde{\tau}}^2 = \begin{pmatrix} m_\tau^2 + m_{\tilde{\tau}_L}^2 - (\frac{1}{2} - s_w^2)c_{2\beta}m_Z^2 & -m_\tau(A_\tau + \mu \tan \beta) \\ -m_\tau(A_\tau + \mu \tan \beta) & m_\tau^2 + m_{\tilde{\tau}_R}^2 - s_w^2c_{2\beta}m_Z^2 \end{pmatrix} \quad (2.59)$$

Both (2.58) and (2.59) have off-diagonal elements which increase with $\tan \beta$. Thus, the sbottom and staus mixing becomes significant at high $\tan \beta$ (in practise this usually means more than about 10 or so).

As for the strongly interacting, spin-1/2, gluinos, they do not mix with each other and their mass is an independent parameter in \mathcal{L}_{soft} .

The electroweak symmetry breaking also leads to mixing between gauginos and higgsinos. The charged higgsinos (\tilde{H}_u^+ and \tilde{H}_d^-) and winos (\tilde{W}^+, \tilde{W}^-) combine to form two mass eigenstates with charge ± 1 called *charginos*. Similarly, the neutral higgsinos (\tilde{H}_u^0 and \tilde{H}_d^0) and the neutral gauginos (\tilde{B}, \tilde{W}^0) can combine to form four mass eigenstates called *neutralinos*. The electroweak gaugino-higgsino mixing results from the last term in eq. (2.32) which can couple a Higgs boson to a gaugino and a higgsino; when the Higgs field is replaced by its vev, these terms generate off-diagonal entries in the "chargino" and "neutralino" mass matrices.

In the gauge-eigenstate basis $(\tilde{W}^+, \tilde{H}_u^+, \tilde{W}^-, \tilde{H}_d^-)$, the chargino mass terms in the Lagrangian are:

$$\mathcal{M}_\pm = \begin{pmatrix} M_2 & \sqrt{2}m_W \sin \beta \\ \sqrt{2}m_W \cos \beta & \mu \end{pmatrix} \quad (2.60)$$

By diagonalizing this mass matrix, we obtain the physical massive fermions, the charginos which are denoted as $\tilde{\chi}_{1,2}^\pm$. They are ordered from lowest to highest mass as

$$m_{\tilde{\chi}_1^\pm} < m_{\tilde{\chi}_2^\pm} \quad (2.61)$$

An important phenomenological consequence is that in the region where $\mu > M_2 \gg m_W$, the $\tilde{\chi}_1^+$ is approximately wino, with mass $M_1 \approx M_2$, while the $\tilde{\chi}_2^+$ is approximately higgsino, with mass $M_2 \approx \mu$. For $M_2 > \mu > m_W$, the content of $\tilde{\chi}_1^+$ and $\tilde{\chi}_2^+$ reverses. Generally, we refer to the region

2.6. CONSTRAINING THE MSSM PARAMETER SPACE

of parameters where the $\tilde{\chi}_1^+$ is mainly wino as the *gaugino* region, and that in which $\tilde{\chi}_1^+$ is mainly higgsino as the *higgsino* region.

The neutralino mass spectrum can be obtained similarly by diagonalizing the following mass matrix written here in the $(\tilde{B}, \tilde{W}^0, \tilde{H}_d^0, \tilde{H}_u^0)$ basis:

$$\mathcal{M}_0 = \begin{pmatrix} M_1 & 0 & -m_Z s_w \cos \beta & m_Z s_w \sin \beta \\ 0 & M_2 & m_Z c_w \cos \beta & -m_Z c_w \sin \beta \\ -m_Z s_w \cos \beta & m_Z c_w \cos \beta & 0 & -\mu \\ m_Z s_w \sin \beta & -m_Z c_w \sin \beta & -\mu & 0 \end{pmatrix} \quad (2.62)$$

where the abbreviations $c_w \equiv \cos \theta_w$, $s_w \equiv \sin \theta_w$ are used. The mass eigenstates of this mass matrix, the neutralinos, are denoted as $\tilde{\chi}_i^0$ ($i = 1, 2, 3, 4$) and are ordered in mass as

$$m_{\tilde{\chi}_1^0} < m_{\tilde{\chi}_2^0} < m_{\tilde{\chi}_3^0} < m_{\tilde{\chi}_4^0} \quad (2.63)$$

The phenomenological properties of the neutralinos follow from arguments similar to those used for the charginos. As an example, in the gaugino region, the $\tilde{\chi}_1^0$ is mainly bino with mass M_1 , and the $\tilde{\chi}_2^0$ is mainly wino (\tilde{w}^3) with mass M_2 . In many MSSM scenarios the lightest neutralino, $\tilde{\chi}_1^0$, is assumed to be the LSP, unless there is a lighter gravitino or unless R-parity is not conserved. This is because it is the only MSSM particle that can make a good dark matter candidate following the cosmological constraints.

2.6 Constraining the MSSM parameter space

Overall the minimal supersymmetric standard model introduces a large number of degrees of freedom, primarily due to the parameters of the soft supersymmetry breaking sector. Indeed we saw that the supersymmetry conserving part involves the three gauge couplings g_i and the Yukawa coupling constants λ_A . The supersymmetry breaking part, according to (2.46), adds to the MSSM many new parameters for which we argued in section 2.3.3 that

$$M_1, M_2, M_3, \mathbf{a_U}, \mathbf{a_D}, \mathbf{a_E} \sim m_{soft}, \quad (2.64)$$

$$\mathbf{m_Q^2}, \mathbf{m_U^2}, \mathbf{m_D^2}, \mathbf{m_L^2}, \mathbf{m_E^2}, m_{H_u}^2, m_{H_d}^2, B\mu \sim m_{soft}^2 \quad (2.65)$$

with a characteristic mass scale m_{soft} that is at the level of 1 TeV.

It is clear that a theory with so many degrees of freedom cannot have much of predictive power. It also adds to the bad picture the fact that many of its phenomenological consequences exhibit new sources of CP violation that are inconsistent with the experimental bounds or unsuppressed flavor-changing neutral currents. Such phenomenological deficiencies could actually rule out almost the entire parameter space of the MSSM. So ultimately a more fundamental theory of supersymmetry breaking is needed, one that would provide a rational set of soft-susy breaking terms and be consistent with “low-energy constraint”.

A way on this direction comes from the fact that the soft parameters, the superpotential parameters as well as the gauge couplings of the theory are not really constants, but they vary with the energy scale at which they are probed. The idea is to impose a particular structure on the soft susy

breaking terms at a common high-energy scale (such as the Planck scale). And the weak-scale MSSM parameters, relevant to collider physics, can then be derived using their *renormalization group equations* (RGE).

The renormalization group equations for the gauge coupling constants g_i are described in term of the so called beta functions b_i , and are given by

$$\frac{d}{d \log Q} g_i(Q) = -\frac{b_i}{(4\pi)^2} g_i^3 \quad (2.66)$$

The b_i are constants which depend on the gauge group and on the matter multiplets to which the gauge bosons couple. For $SU(N)$ theories with matter in the fundamental representation, it is $b_N = (\frac{11}{3}N - \frac{1}{3}n_f - \frac{1}{6}n_s)$, where n_f is the number of chiral (left-handed) fermions and n_s is the number of complex scalars which couple to the gauge bosons. Figure 2.4 compares the RG evolution of the inverse gauge couplings $\alpha_i = g_i^2/4\pi$, in the standard model (dashed lines) and the MSSM (solid lines). Unlike the standard model, the MSSM includes just the right particle content to ensure that the gauge couplings can unify, at a scale $M_U \sim 2 \times 10^{16}$ GeV.

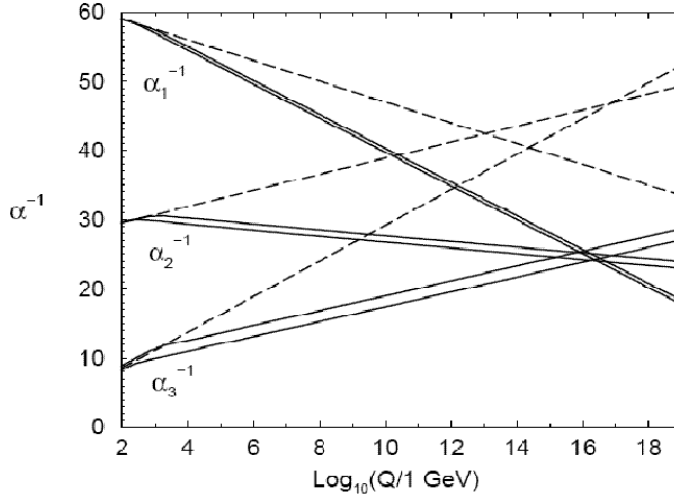


Figure 2.4: Renormalization group evolution of the inverse gauge couplings $\alpha_i^{-1}(Q)$ in the standard model (dashed lines) and the MSSM (solid lines).

The renormalization group equation for a gaugino mass M_i is

$$\frac{d}{d \log Q} M_i = -\frac{1}{(4\pi)^2} 2b_i M_i \quad (2.67)$$

Comparing the eqs. (2.66) and (2.67), we find that $M_i(Q)$ and $\alpha_i(Q) = g_i^2(Q)/4\pi$ have the same RGE, and so their ratio is constant as a function of Q . This relation is often written as $M_i(Q)/\alpha_i(Q) = m_{1/2}/\alpha_U$, where α_U is the unification value of the coupling constant ($\alpha_U = 24$), and $m_{1/2}$ is the underlying soft mass parameter. In other words the gaugino masses also unify at the grand unification scale (GUT), at a value equal to $m_{1/2}$:

$$M_1(M_{\text{GUT}}) = M_2(M_{\text{GUT}}) = M_3(M_{\text{GUT}}) \equiv m_{1/2} \quad (2.68)$$

2.6. CONSTRAINING THE MSSM PARAMETER SPACE

As a consequence, the effective gaugino mass parameters at the weak scale are related as

$$M_1 : M_2 : M_3 = g_1^2 : g_2^2 : g_3^2 \simeq 1 : 2 : 6 \quad (2.69)$$

The above relation actually reveals the tendency of the colored particle, in that case being the gluino, to be much heavier than the uncolored ones (wino and bino here). This turns out to be a rather model independent conclusion.

Let us now turn to our original problem of understanding the underlying susy-breaking mechanism and how it is possible to deduct the very large number of parameters to a manageable level. The most appealing explanations of the supersymmetry breaking assume that it occurs in a "hidden sector" of particles that have no direct couplings to the "visible sector" chiral supermultiplets of the MSSM. However, the two sectors do share some interactions that are responsible for mediating supersymmetry breaking from the hidden sector to the visible sector, resulting in the MSSM soft terms.

There are two main scenarios for what the mediating interactions might be. The first, and most popular one, suggests that the interactions are gravitational or more precisely that are associated with new physics including gravity. This is the so called "gravity-mediated" scenario. The other one assumes that the flavor-blinding mediating interactions are the ordinary electroweak and QCD gauge interactions, and is thus called "gauge-mediated supersymmetry breaking" (GMSB) scenario. The phenomenological predictions among the various models, in general, depend on their different boundary conditions of the renormalization group equations. We will next only outline the characteristics of the first model which is the one assumed in the next chapters.

Gravity-mediated models in their simplest version are known as "minimal supergravity" or mSUGRA. The mSUGRA model assumes that the soft susy-breaking parameters at the renormalization scale $Q \approx M_P$ take the simple form

$$\begin{aligned} \mathbf{m}_Q^2 &= \mathbf{m}_U^2 = \mathbf{m}_D^2 = \mathbf{m}_L^2 = \mathbf{m}_E^2 = m_0^2 \mathbf{1} \\ m_{H_u}^2 &= m_{H_d}^2 = m_0^2 \\ A_U &= A_D = A_E = A_0 \mathbf{1} \end{aligned} \quad (2.70)$$

in which the scalar squared masses and the A-parameters are flavor-diagonal and universal. The new symbols introduced refer to the *universal scalar mass* m_0 , and the *universal scalar coupling* A_0 .

Equations (2.68), (2.70) have the virtue of being highly predictive, when they are imposed as boundary conditions to the RGEs at the Planck scale. The RG evolution of the soft parameters down to the electroweak scale allows us then to predict the entire MSSM spectrum in terms of just five parameters m_0 , $m_{1/2}$, A_0 , $\tan \beta$ and μ (plus the already-measured gauge and Yukawa couplings of the MSSM). Typical mSUGRA models often express their phenomenological results in terms of m_0 and $m_{1/2}$ only, while the other parameters are kept fixed, since most of the soft parameters are only slightly depending on them.

3

The Compact Muon Solenoid at LHC

3.1 The Large Hadron Collider

The Large Hadron Collider (LHC) is a particle accelerator which is being built at CERN, the European Organization of Nuclear Research, in Geneva (Switzerland). The collider is contained in a circular 27-km long tunnel which used to host CERN's Electron Positron (LEP) collider, at a depth about 100m underground. The design operation of the LHC is the acceleration of two separate proton beams which will be brought to head-on collisions at four interaction points. The proton collisions are meant to reach a center-of-mass energy of 14 TeV, an energy which is seven times higher than any other hadron collider to date.

The main purpose of the LHC is to study the physics at an energy scale of 1 TeV. The LHC is conceived to explore the validity and limitations of the Standard Model, which has been well tested by previous experiments like LEP in the past, but in the absence of the Higgs boson turns out to break down at certain high energy scales, that is of the order of ~ 1 TeV. It is therefore, foremost, a machine to look for possible physics Beyond the Standard Model (BSM). Experiments at the LHC will search for new physics phenomena at the TeV scale such as supersymmetry or extra dimensions.

The key parameters of the LHC accelerator machine in order to serve over this wide range of physics program are the energy of the colliding beams and the luminosity. The rate of physics events produced in an accelerator is given by the relation

$$\mathcal{R} = \sigma \mathcal{L} \quad (3.1)$$

where σ is the cross section of the physical process and \mathcal{L} is the luminosity. In order to maintain an equally effective physics programme at a higher given energy E , the luminosity of a collider must increase in proportion to E^2 . This is because the cross-section of parton-parton scattering decreases by that amount ($\sigma \propto 1/E^2$). In addition, for a hadron collider the situation gets more complex if one takes into account the structure functions of the partons, which decrease rapidly with increasing x (the variable x measures the fraction of the proton momentum which is carried by the parton). Such limiting factors have led to the design operation of LHC at luminosity of $\mathcal{L} = 10^{34} \text{ cm}^{-2} \text{ s}^{-1}$.

The luminosity of an accelerator colliding two bunches of particles n_1, n_2 with a frequency f is

given by

$$\mathcal{L} = f \frac{n_1 n_2}{(4\pi\sigma_x\sigma_y)} \quad [3.2]$$

where σ_x, σ_y are the gaussian transverse profiles of the beam. The design luminosity of LHC therefore requires high collision frequency of the proton bunches as well as a large number of protons per bunch.

The number of protons in each bunch at LHC will be 10^{11} . Due to this high number, the average number of inelastic collisions between protons (minimum bias events) per bunch crossing will be high, and will reach ~ 20 . This leads to an increased difficulty in the experimental conditions, since the rare interesting events which are possible to occur in a bunch crossing, will be overlapping (piled-up) with this 20 minimum bias events. A way to eliminate the number of these pile-up events while keeping the same luminosity is to operate the accelerator with a high collision frequency. This frequency is chosen as of 40 MHz for LHC, resulting in a time interval between two collisions of 25 ns.

In order to reach the energy of 7 TeV per beam, the protons are initially prepared by several LHC accelerator components that successively increase their energy. First, the linear accelerator Linac 2 is used to generate 50 MeV protons. The protons are then fed into the Proton Synchotron Booster (PSB) and in turn the Proton Synchrotron (PS) so that they are accelerated up to a total energy of 26 GeV. The Super Proton Synchrotron (SPS) will finally increase their energy to 450 GeV before they are inserted into the main LHC ring. The proton beams circulate inside the ring in vacuum tubes (beam pipes) in order to avoid their collisions with normal matter (like air molecules). Inside the pipe, their acceleration is achieved by electric fields which are provided by Radio-Frequency (RF) cavities. The LHC will use eight cavities per beam, each delivering 2 MV, an accelerating field of 5 MV/m, at 400 MHz. A large variety of magnets are used to direct the beams around the ring and maximize the probability for head-on collisions between the protons. There are 1232 dipole magnets (“bending magnets”) which will be used to keep the beams on their circular path, and an additional 392 quadrupole magnets that will focus the beams to stay inside the vacuum chambers (“focusing magnets”). In total some 1600 superconducting magnets will be used that need to operate at a temperature of $T = 1.9K$.

Figure 3.1 shows a schematic view of the LHC and the component accelerators, while table 3.1 summarizes the parameters of the machine’s operation.

The LHC will also be used to collide lead (Pb) ions with design luminosity $\mathcal{L} = 10^{27}\text{cm}^{-2}\text{s}^{-1}$ and centre-of-mass energy of 1312 GeV, allowing in addition heavy-ion experiments. Four detectors are installed at the LHC in order to analyze the collisions at the interaction points. Two of them, the ATLAS experiment and the Compact Muon Solenoid (CMS) are large, “multipurpose” detectors, which are designed to cover the widest possible range of physics at LHC. The other two, are more specialized detectors: the Large Ion Collider Experiment (ALICE) will study properties of the quark-gluon plasma in heavy ion collisions, and LHCb, CP violation phenomena in the interactions of B-particles.

3.2. THE CMS DETECTOR

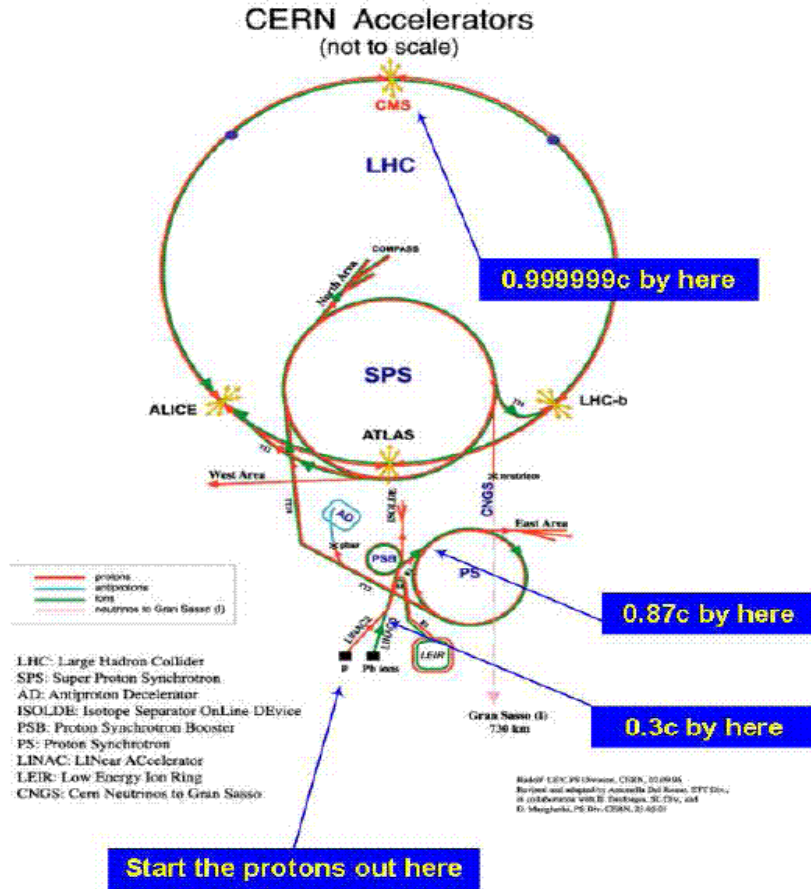


Figure 3.1: *Schematic view of the Large Hadron Collider.*

Parameter	symbol	pp	HI	unit
Energy at collision	E	7	2.76	TeV
Dipole field at 7TeV	B	8.33	8.33	T
Design Luminosity	\mathcal{L}	10^{34}	10^{27}	$cm^{-2}s^{-1}$
Luminosity lifetime	$\tau_{\mathcal{L}}$	15	6	hr
Protons per bunch	n_b	$1.15 \cdot 10^{11}$	$7.0 \cdot 10^7$	-
Bunches per beam		2808	592	-
Bunch spacing		25	100	ns

Table 3.1: *Nominal parameters of the LHC operation.*

3.2 The CMS detector

In general, a collider detector should be designed as a perfect sphere around the interaction point to be able to detect all particles produced in the collisions. However, this would be extremely

difficult from the technical point of view, and therefore a cylindrical shape has been chosen. For the CMS detector, the overall design is mainly determined by the solenoidal shape of the magnet and the requirement to provide the best possible geometrical coverage. As every modern detector in accelerator experiments, CMS is composed by several sub-detectors which are placed in concentric layers one around the other, while each of them is dedicated to perform different and complementary measurements.

In order to accomplish the physics goals of LHC, the detector components of CMS should meet the following requirements:

1. A precise and efficient muon system, that allows good identification of muons and measurement of their momenta, and the ability to trigger on them online.
2. A high performance electromagnetic calorimeter, for the accurate measurement of the energy and the position of electrons and photons.
3. A high quality central tracker compatible with (1) and (2), for measuring the momentum of charged particles from their bending in the magnetic field and also for the identification of the primary interaction vertex and secondary vertices.
4. A hadronic calorimeter with large hermetic coverage, in order to measure the energy of neutral or charged hadronic particles as well as any overall imbalance of escaping weakly interacting particles.

The detection of muons is among the highest priorities for CMS because they constitute a very clean signature for many of the interesting processes that will be searched for and studied at LHC. The choice of the magnetic field configuration is a crucial issue for measuring the muon momentum. CMS will use a powerful solenoid magnet which will produce magnetic field along the direction of the beam and therefore will bend the charged particles in the transverse plane. It can easily be shown that the muon momentum is reconstructed with a precision which depends on the magnetic field strength B and its length L , through the following relation:

$$\frac{\sigma_{p_T}}{p_T} = \frac{\sigma_s}{s} = \sigma_s \frac{8p_T}{0.3BL^2} \quad (3.3)$$

where p_T is the particle's transverse momentum and s is the sagitta, or amount of bending, of the particle's track inside the magnetic field. This simple result shows that the precision of the momentum measurement is proportional to BL^2 . CMS has chosen a high field strength of 4 Tesla along with a compact configuration of the detector¹.

Overall, the CMS detector has a total length of 24m, a diameter of 14.6m and weighs approximately 14500 tonnes. As per the mechanical structure, the detector is subdivided in three main areas: the *barrel* and the two *end-caps*. The barrel is the cylindrical part of the detector, concentric to the beam line. The end-caps are placed perpendicular to the beam direction, at the two sides of the barrel. Basically, the barrel covers the pseudorapidity range $|\eta| \leq 1.5$ and the end-caps cover the region $1.5 \leq |\eta| \leq 3.0$.

¹Opposed to ATLAS choice of a big size detector with a rather moderate magnetic field.

3.2. THE CMS DETECTOR

In the following sections, the various sub-detector systems are described in detail. The main distinguishing features are (see figure 3.2): a full-silicon-based tracking system in the innermost layers of CMS, surrounded by a homogenous scintillating-crystal electromagnetic calorimeter. The latter is itself surrounded by a sampling hadronic calorimeter. In the heart of CMS sits the solenoid magnet which is large enough to accomodate both the tracker and calorimetry inside. The large muon detector systems are inside the return yoke of the magnet.

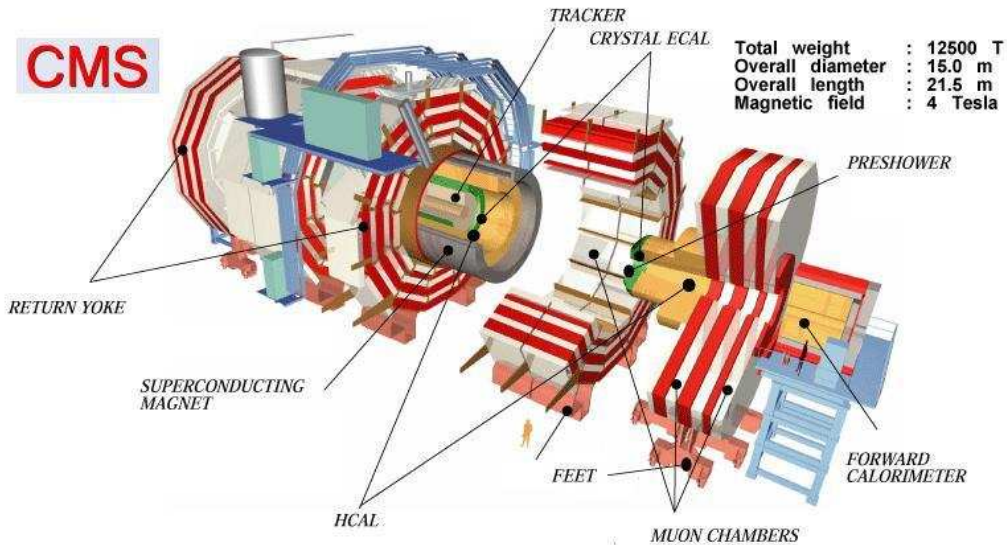


Figure 3.2: *The CMS detector set up in the various sub-detector systems.*

The CMS coordinate system adopted is defined as follows: the z-axis is parallel to the beam axis and the magnetic field of the solenoid, and the polar angle is defined with respect to it. The azimuthal angle around the z-axis is denoted by the symbol ϕ , and the pseudorapidity $-\log(\tan \theta/2)$ is denoted by the symbol η . The symbol p_T is used to denote the component of momentum transverse to the beam axis.

3.2.1 The inner Tracker

The tracking system is placed at the first layer of CMS, the closest to the interaction point. The role of the tracker is to provide a precise and efficient measurement of the trajectories of charged particles but also reconstruction of the position of their vertex. Embedded inside the strong magnetic field of the solenoid, the tracker allows the reconstruction of high-pT muons, electrons and hadrons with high momentum resolution in the pseudorapidity region $|\eta| < 2.5$. Moreover, vertex finding in the tracker allows the identification of heavy flavor hadrons (jet flavor tagging), like b -jets and τ -jets.

The detector technology has been driven by the challenging experimental conditions of the tracker

operation. Given the high design luminosity of LHC, in each bunch crossing there will be around 20 overlapping minimum bias events expected to produce on average more than 1000 charged particles inside the tracker acceptance. To accomodate with high particle densities, the detectors must have high granularity and fast response, so that the tracks are reliably identified and attributed to the correct bunch crossing. Moreover they should be robust enough to stand the harsh radiation environment. On the other hand, the detector implementation implied would lead essentially to an increased density of the on-detector support electronics. This is not desirable because the material budget of the detector should be minimized as possible in order to limit secondary phenomena from multiple scattering, bremsstrahlung, photon conversions and nuclear interactions.

In order to find a compromise, two kind of technologies have been employed based in an all-silicon configuration. A silicon pixel detector is placed in the inner regions of the tracker, extended up to radius $r \approx 10$ cm, where the occupancy is highest. This is because particles emerging from min. bias events are usually low p_T particles with small-radius helical tracks due to the magnetic field, resulting in lower occupancy at larger radii. Silicon microstrips detectors are then adequate to handle medium and low occupancy regions (of $r > 20$ cm). Both detectors' segmentation is such that channel occupancies are kept at or below the level of $\sim 1\%$ in all radii. Overall, track reconstruction can be reliably performed based on relatively small number of measurement layers, each being able to provide clean and precise coordinate determination.

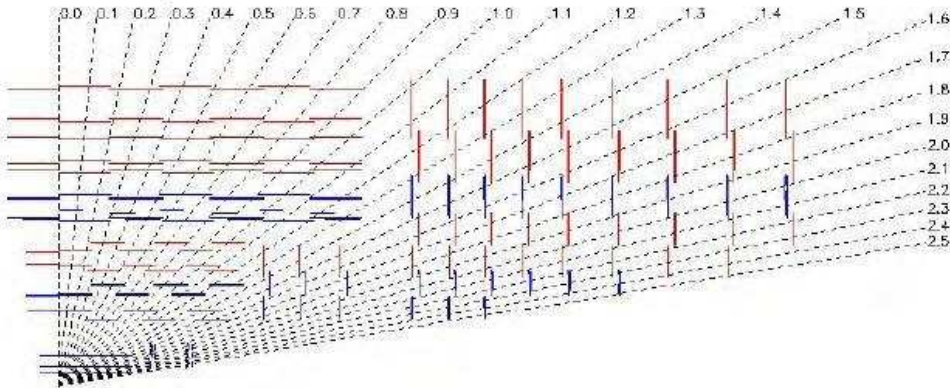


Figure 3.3: $r - z$ view of a quarter of the CMS tracker showing the pseudorapidity coverage. Segments correspond to detector modules, lighter ones are single-sided modules and darker ones double-sided.

A layout of the CMS tracker is shown in figure 3.3. The outer radius of the CMS tracker extends up to nearly 110 cm, while its total length is approximately 540 cm. The pseudorapidity coverage corresponds to $|\eta| < 2.5$.

The pixel detector

The pixel detector of CMS consists of three barrel layers (BPix) with two end-cap disks (FPix) on

each side. The BPix layers are placed at a mean radii 4.4, 7.3 and 10.2 cm respectively and will be 53 cm long. The FPix, extending from ≈ 6 to 15 cm in radius, will be placed on each side at $z = \pm 34.5$ and $z = \pm 46.5$ cm. At the initial low luminosity runs of LHC, the pixel detector will be limited to two BPix and one FPix only. The arrangement of the three(two) barrel layers and the forward pixel disks on each side define three (two) measurement layers, i.e. three (two) possible points (hits) for each track measurement, over almost the full η -coverage of the tracker ($|\eta| < 2.5$). Figure 3.4 shows the geometrical arrangement of the pixel detector and the hit coverage as a function of the pseudorapidity for the cases of low and high luminosity runs supersimposed.

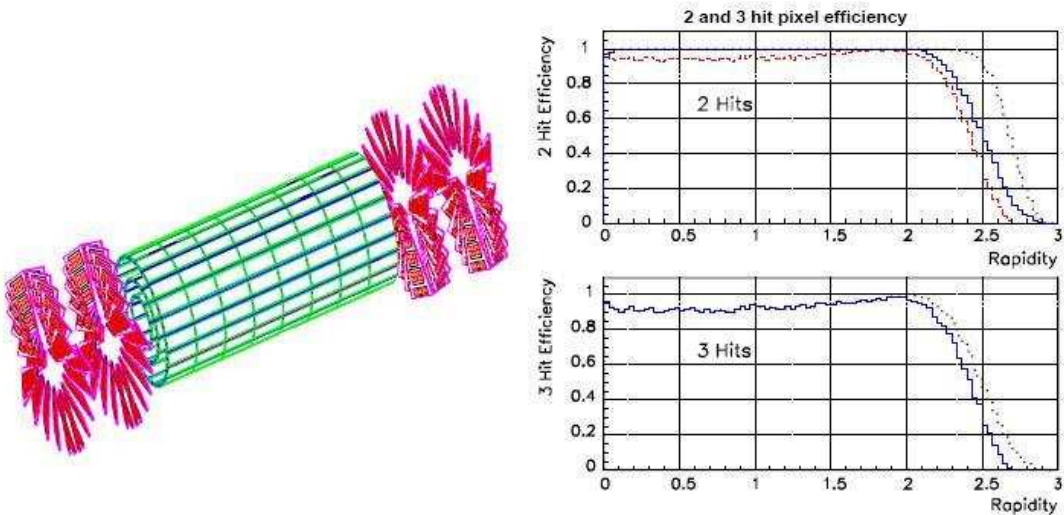


Figure 3.4: *Layout of the CMS pixel detector (left) and its hit coverage as a function of pseudorapidity (right).*

The pixel layers have a modular architecture where each detector unit consists of a thin, segmented sensor plate with highly integrated readout chips connected to it. The whole pixel system comprises more than 1400 pixel modules, corresponding to about $6 \cdot 10^7$ pixel units. The pixel shape is “almost” square with a size of $100 \times 150 \mu\text{m}^2$. The finest granularity of the pixel detector results to low levels of occupancy of about 10^{-4} per pixel per LHC crossing.

The dimensions of a unit pixel are subject to an optimal vertex position resolution in both the (r, ϕ) and z coordinates. The (r, ϕ) resolution is however further improved by taking into advantage the Lorentz effect: the pixels are n-on-n devices so that their response is strongly affected by the Lorentz drift of electrons inside the 4T magnetic field. In the barrel, the Lorentz angle is large (34°), and the pixels are deliberately arranged so that the charge induced is spread over more than one cell. The forward detectors are tilted by 20° to allow similarly charge-sharing between adjacent cells. With the pixel read-out, an analogue signal interpolation allows to achieve a spatial resolution in the range of $15 - 20 \mu\text{m}$.

The Silicon Strip detector

The Silicon Strip detectors are divided into four main areas: the inner barrel (TIB), the inner disks (TID), the outer barrel (TOB) and the end-caps (TEC) (see figure 3.3). The TIB and TOB systems are made respectively of four and six concentric layers which are assembled in shells. The TID system is composed of three small disks, each divided in three concentric rings, while the TEC is composed of nine disks on each side, each made of four to seven rings. The whole inner tracker will be contained in a cylindrical support tube with a diameter of 2.4 m and a total length of 5.4 m.

The silicon sensors of the tracker are based on the microstrips technology and are organized in modules of different shape and size. All of the sub-systems (TIB, TOB, TID, TEC) comprise together 15148 modules. Each module contains one or two silicon sensors, for a total of 24244 sensors. The pitches and the strip length of the sensors are determined from the spatial resolution requirements in the different areas of the system.

The modules of the TIB and TID have a single sensor with a thickness of 320 microns. The strip pitch ranges from 80 to 120 microns for the TIB, and from 100 to 145 microns for the TID. The outer modules of the TOB and the three outer TEC rings, hold two sensors. As the radiation is lower in that region, the strips can be larger and the pitch width varies from 80 to 185 microns. Due to the resulting increased noise, the signal-to-noise ratio can be kept at good levels by using thicker sensors than the normal $300 \mu\text{m}$ sensors. The sensor thickness is chosen at 500 microns for both the TOB and the TEC, except for the three innermost rings of the latter.

Almost half of the modules in the tracker layout are double-sided modules. These are made of two independent single modules glued together back-to-back with a relative rotation of 100 mrad with respect to each other. In this arrangement, the tracker layers of double-sided modules can provide a measurement in both the z coordinate in the barrel modules, and the r coordinate in the disks, i.e. a three-dimensional measurement. The double-sided modules are mounted in the first two layers of the TIB and TOB, in the first two TID rings, and in the first, second and fifth ring of the TEC. The resulting single-point resolution is $23\text{-}24 \mu\text{m}$ (for inner layers) and $35\text{-}52$ (for outer layers) μm in the (r, ϕ) direction and of $230 \mu\text{m}$ and $530 \mu\text{m}$, for TIB and TOB layers respectively, in z .

The CMS silicon strip tracker has a total of 9.3 million strips which corresponds to 198 m^2 of active silicon area. Overall, the tracker layout defines a set of measurement layers which varies in η . As shown in figure 3.5, there are at least ≈ 9 hits in the silicon strip tracker, with at least 4 of them being two-dimensional measurements, over the full range of $|\eta| < 2.4$.

Material Budget

Apart from the sensitive detector volumes, the Tracker includes much of non-active material, such as support structures, electrical supply cables and cooling services. In the pseudorapidity range between 1.2 and 2.1, the material budget can be extended up to more than one radiation lengths, as shown in figure 3.6. The same figure also shows the material budget in units of interaction length. The amount of material in the Tracker should be kept as low as possible in order to limit

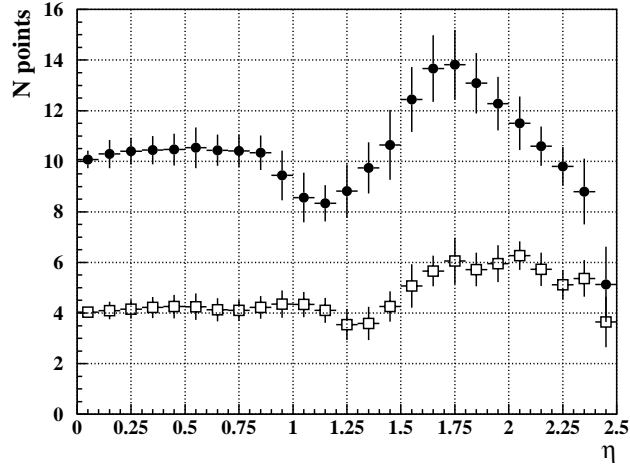


Figure 3.5: *Hit coverage of the CMS strip tracker as a function of the pseudorapidity η . Filled circles correspond to the total number of measurement points while open squares to points from stereo layers only.*

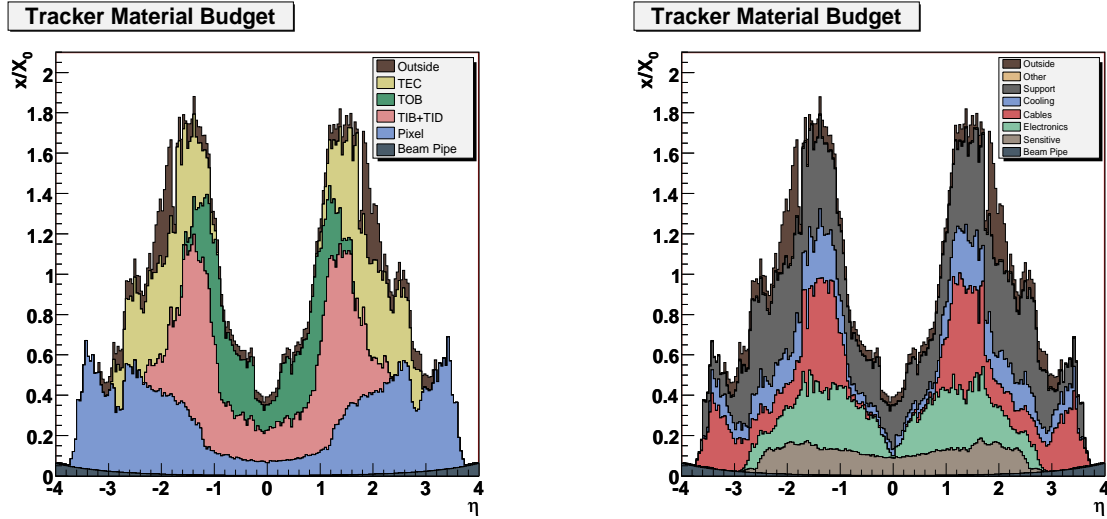


Figure 3.6: *Material budget in units of radiation length as a function of the pseudorapidity η , decomposed in the active (left) and the non-active contributions (right).*

secondary phenomena like multiple scattering, bremsstrahlung and photon conversions which could distort the role of the electromagnetic calorimeter. Therefore, a proper balance between the number of hits per track measurement (i.e. the number of active layers) and the amount of tracker material, is crucial for an efficient track reconstruction.

Performance of the tracker

The global track reconstruction performance is illustrated in figure 3.7, where the expected reconstruction efficiency for muons and pions is plotted as a function of pseudorapidity. For muons, the efficiency is mainly flat at 99% over most of the acceptance, whereas in $\eta \approx 0$ is slightly decreased due to gaps between the ladders of the pixel detector at $z \approx 0$. Due to the reduced coverage of the forward pixel disks, the efficiency is also dropped at high η . For the case of pions and hadrons in general, the efficiency is lower because of the interactions with the tracker material.

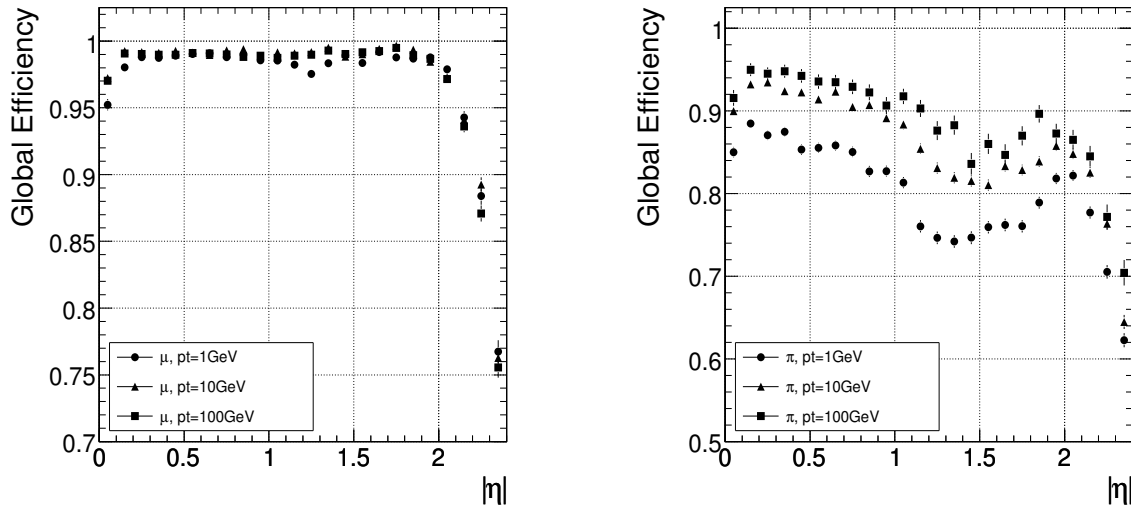


Figure 3.7: *Global track reconstruction efficiency as a function of pseudorapidity, for muons (left) and pions (right).*

3.2.2 The Electromagnetic calorimeter

The CMS electromagnetic calorimeter (ECAL) lies at the second layer of the CMS detector, surrounding the Tracker. Its role is the measurement of the energy of electrons and photons, and in conjunction with the hadronic calorimeter, the measurement of hadronic jets.

The design concept of the ECAL has been based on the requirement to provide excellent resolution in the measurement of the invariant mass of two photons coming from the decay of the Higgs $H \rightarrow \gamma\gamma$, which is the main channel to the discovery of the Higgs boson for $m_H \leq 130$ GeV. In this mass region, the width of the Higgs is small, and therefore the observed signal width will all be due to instrumental effects, i.e. resolution. Since for the measurement the signal lies over a high irreducible background, high resolution is crucial. Moreover, a good angular resolution between the two photons as well as π^0/γ separation is needed to suppress the reducible background coming from π^0 's. Therefore, a calorimeter with fine segmentation is needed.

CMS has deployed a hermetic and homogeneous calorimeter. Scintillating crystals made of lead tungstate (PbWO_4), constitute the active medium of the calorimeter. The material PbWO_4 was chosen because of its high density (8.28g/cm^3) and short radiation ($X_0 = 0.89$ cm) and Moliere

($R_m = 2.2$ cm) lengths, allowing for a very compact calorimeter system with high granularity. An intense R&D program has been developed in the recent years which has progressively improved several other properties and qualities of the crystals, so as to make them suitable in the challenging LHC environment. Some of the important aspects in the development of the crystals is to have a fast response and be radiation resistant.

Indeed, lead tungstate is a fast scintillating crystal: the scintillation decay time is comparable with the LHC bunch crossing time, since almost 80% of the crystal's light is emitted within 25ns. However a drawback is that it has a relatively low light yield. For this reason, the scintillation light is collected and amplified by photodetectors with intrinsic gain, that can operate in a 4T magnetic field. In the barrel, silicon avalanche photodiodes (ADPs) are used. In the endcaps, the higher radiation levels and the approximately axial magnetic field suggested the use of vacuum photo-triodes (VPTs).

The crystals have been optimized so to withstand the high radiation dose rates during the LHC operation. R&D studies have shown that radiation affects the transparency of the crystals through the formation of color centers and the transport of light is changed by self-absorption of the crystals. CMS has designed a light-injection system that will continuously monitor the wave-length dependent loss of light and measure the optical transmission, so that to correct the crystal's response accordingly.

A preshower system is installed in front of the endcap ECAL for π^0 rejection. It is designed to detect the slightly-overlapping pair of photons from a π^0 decay and to distinguish these from the single shower produced from a single photon interacting with the calorimeter material .

The general structure

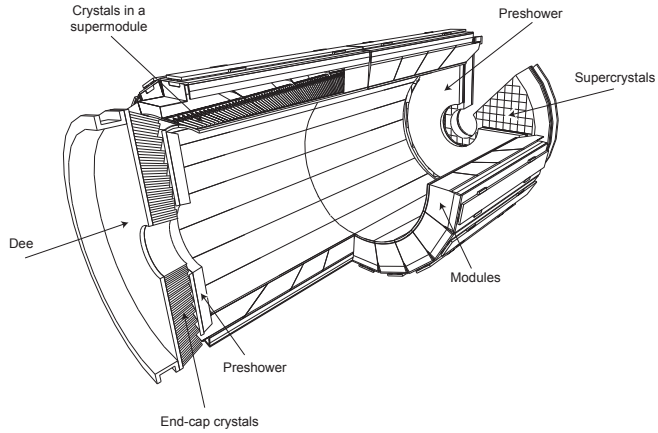


Figure 3.8: Layout of the CMS electromagnetic calorimeter showing the arrangement of crystal modules, supermodules and endcaps, with the preshower in front.

The barrel part of the ECAL (EB) covers the pseudorapidity range of $|\eta| < 1.479$. The EB is

structured in 36 identical “supermodules”, each covering half the barrel length and 20 degrees in ϕ . A supermodule is composed of 4 modules, of 500 crystals in the first module and 400 crystals in the rest modules, resulting in a total of 61200 crystals. The crystals are arranged in a quasi-projective geometry, with their axes tilted at 3° with respect to the line from the nominal vertex, so as to avoid cracks aligned with particle trajectories. As per the dimensions of a barrel crystal: its cross section corresponds to 0.0174×0.0174 in $\eta - \phi$, or $22 \times 22\text{mm}^2$ at the front face of the crystal. The crystal’s length is 230 mm corresponding to $25.8 X_0$. The barrel crystal volume is 8.14 mm^3 and the weight is 67.4 t.

The ECAL endcaps (EE) cover the pseudorapidity range $1.479 < |\eta| < 3$. Each EE is structured as 2 “Dees”, consisting of semi-circular plates in which mechanical units of 5×5 crystals, known as “supercrystals” or SCs, are mounted. In total, 7324 crystals are contained in each end-cap. The end-cap crystals, like the barrel crystals, off point from the nominal vertex position but with angles varying from 2 to 8 degrees. The endcap crystal dimensions are slightly different than the barrel ones: they have a front face cross section of $28.62 \times 28.62\text{mm}^2$ and a length of 220mm($24.7X_0$). The endcaps crystal volume is 2.90mm^3 and the weight is 24.0 t.

The energy resolution

For energies below about 500 GeV, where shower leakage from the rear of the calorimeter starts to become significant, the energy resolution can be parametrized as a function of the energy with the following formula:

$$\left(\frac{\sigma_E}{E}\right)^2 = \left(\frac{S}{\sqrt{E}}\right)^2 + \left(\frac{N}{E}\right)^2 + C^2 \quad (3.4)$$

where S is the stochastic term, N the noise term, and C the constant term. The individual contributions for each term are summarised in the following:

- The stochastic term S , is relevant with the event-to-event fluctuations in the lateral shower containment and the photostatistics. The first contribution is expected to be about 1.5% when the energy is reconstructed by summing an array of 5×5 crystals, and about 2% when using 3×3 crystals. The photostatistics contribution involves the ability of light emission of the crystals, the efficiency in light collection on the face of the photodetectors as well as the quantum efficiency of the photodetectors. It is expected to contribute to the stochastic term by $\approx 2.1\%$ for both the barrel and the end-cap regions.
- The noise term N , is relevant with every instrumental effect that can distort the measurement of the energy deposited, independently of the energy itself (e.g. noise from the electronics, digitization or the pile-up events). The expected contribution is equivalent to 8 MeV/channel after one year of operation at $\mathcal{L} = 10^{33}\text{cm}^{-2}s^{-1}$, and 30 MeV/channel at the end of the first year of operation at $\mathcal{L} = 10^{34}\text{cm}^{-2}s^{-1}$.
- The constant term C , determines the energy resolution in higher energies and comprises of contributions from various phenomena (non-uniformity of the longitudinal light collection, intercalibration errors, leakage of energy from the back of the crystal etc).

The full energy resolution of the ECAL, for incident electrons measured in a test beam, is shown in figure 3.9; the values of the stochastic, noise, and constant terms are extracted by fitting the measured points with formula (3.4).

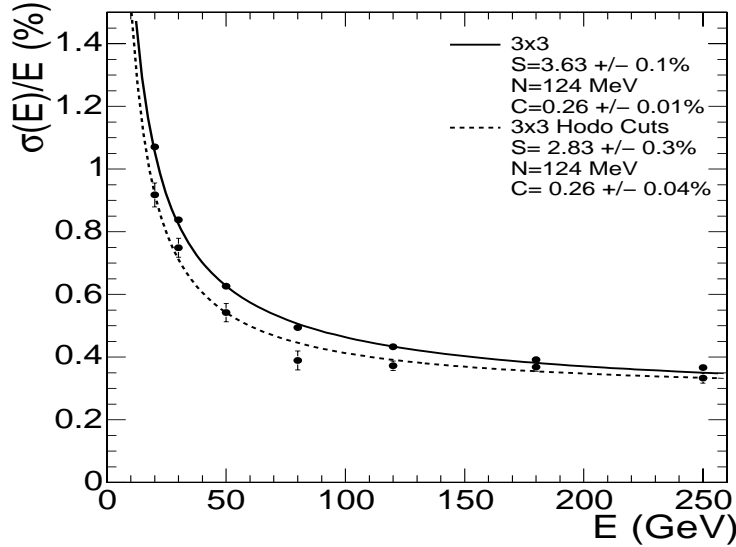


Figure 3.9: *The ECAL energy resolution as a function of electron energy, measured from a test beam. The energy was measured by summing an array of 3×3 crystals with an electron impacting the central crystal.*

3.2.3 The Hadron calorimeter

The CMS hadronic calorimeter (HCAL) surrounds the ECAL and is used in conjunction with the latter for the measurement of the energy and direction of jets, as well as the missing transverse energy flow in events. The important requirements imposed for the deployment of the HCAL are:

- to provide good energy resolution up to jet energies of 1 TeV, and therefore HCAL must ensure the best possible containment of the hadronic showers (approximately 11 interaction lengths λ_I are needed).
- provide hermeticity, so as not to spoil the missing transverse energy calculations (a coverage of $|\eta| < 5$ is needed).

The design of the HCAL has been essentially influenced by the choice of magnet parameters since most of the CMS calorimetry is located inside the magnet coil. Figure 3.10 shows a longitudinal view of the CMS detector and the placement of the HCAL components in the η direction. The central hadron calorimeter (barrel and two end-caps) covers the pseudorapidity region $|\eta| < 3$. The hadron calorimeter barrel is radially restricted between the outer surface of the electromagnetic calorimeter ($R = 1.77\text{m}$) and the inner surface of the magnet coil ($R = 2.95\text{m}$). This constraints the total amount of material which can be put in to sample adequately the hadronic showers.

An outer hadron calorimeter is therefore placed outside the solenoid complementing the barrel calorimeter.

Beyond $|\eta| = 3$, forward hadron calorimeters are placed at 11.2 m from the interaction point, in order to extend the pseudorapidity coverage down to $|\eta| = 5.2$. Besides the measurement of the missing transverse energy, the HF also serves in the identification of high- p_T jets in the forward region.

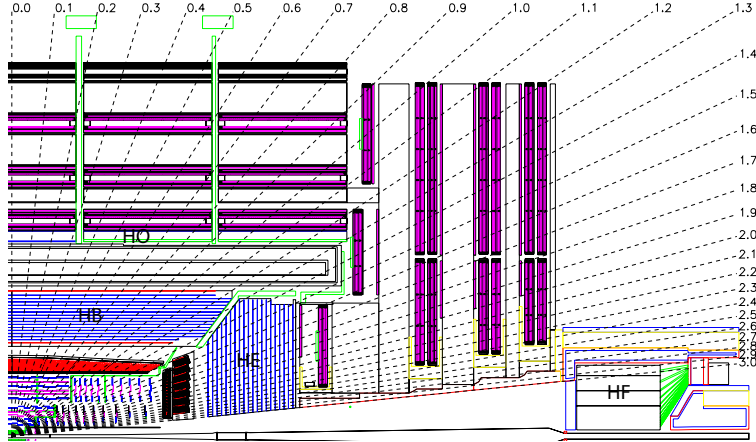


Figure 3.10: Longitudinal view of the CMS detector showing the locations of the HCAL components: the barrel (HB), outer barrel (HO), end-cap (HE) and forward calorimeter (HF).

The central hadron calorimeter is divided in the barrel hadron part (HB) covering the region $|\eta| < 1.3$, and the two end-cap parts (HE) covering $1.3 < |\eta| < 3$. Both HB and HE are located inside the magnet coil. They are sampling calorimeters which use dense layers of absorbing medium interleaved with thinner layers of scintillator detectors. Brass is chosen as the absorber material because its main constituent is copper, which is non-magnetic material and easy to machine inside the strong magnetic field. Plastic scintillators constitute the active medium of the calorimeters. The scintillation light is read by wave-length shifting fibres and the use of photodetectors (hybrid photodiodes, or HPDs) that can provide gain and operate in high axial magnetic fields. The scintillator layers are organised in tiles (towers) with a segmentation that is to assure a good separation between two-jet combinations. The $\eta - \phi$ granularity of the central calorimeter is 0.087×0.087 for $|\eta| < 1.6$ and $\approx 0.17 \times 0.17$ for $|\eta| \geq 1.6$. The longitudinal segmentation for HB is one unit while for HE, varies from one to three. The overall assembly of the absorber and tile structures enables a configuration that contains no uninstrumented cracks or projective dead areas over the full pseudorapidity coverage.

At $|\eta| = 0$ the central calorimeter has a depth corresponding to about 7 interaction lengths. This depth is not adequate to contain the hadron shower (and can give rise to non-Gaussian tails in the energy resolution of low energy jets and to missing transverse energy mismeasurements). For this reason, an outer hadronic calorimeter is situated outside the magnet coil and covering the region $-1.26 < |\eta| < 1.26$, to measure the HB energy leakage. This system is called HO or “tail-catcher” and assures that the hadronic showers are sampled with at least 10 interaction lengths over the

3.2. THE CMS DETECTOR

whole η coverage. Test beam results have shown that HO improves the energy resolution for 300 GeV pions by 10%.

Two hadron forward (HF) calorimeters are installed after the HEs, one at each end of the CMS detector, extending the pseudorapidity coverage of the HCAL up to $|\eta| = 5$. The forward calorimeters are subject to a severe irradiation environment with particle fluxes reaching the 760 GeV of deposited energies per proton-proton interaction, compared to only 100 GeV in the rest of the detector. Therefore, instead of the conventional scintillator and wave-shifter materials, the HF uses radiation-resistant quartz-fibres interleaved with absorber plates made of steel. The cherenkov light emitted by the fibres is channeled by photomultipliers.

In contrast to the ECAL, the performance requirements on the energy resolution of the HCAL are less constrained by the physics processes. In fact, the calorimeter jet energy resolution is compromised by effects such as the jet-finding algorithm, the fragmentation process, the magnetic field and energy pile-up at the high luminosity runs of LHC.

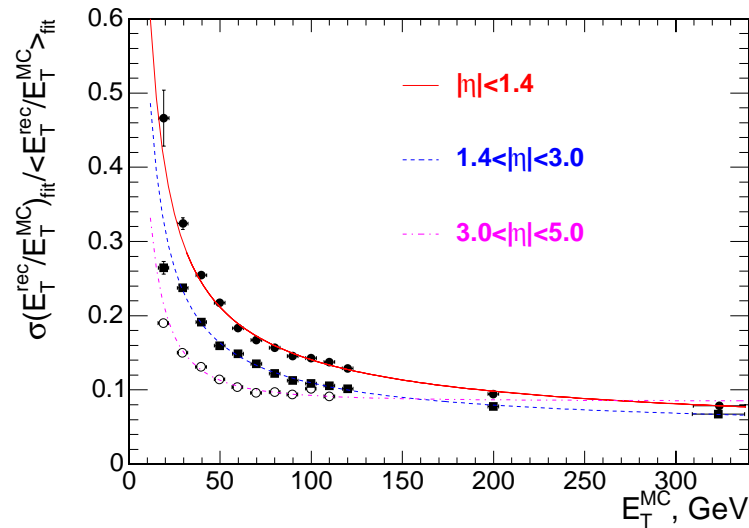


Figure 3.11: The jet transverse energy resolution as a function of the jet transverse energy for barrel jets ($|\eta| < 1.4$), end-cap jets ($1.4 < |\eta| < 3.0$) and forward jets ($3.0 < |\eta| < 5.0$). The jets are reconstructed with the iterative cone algorithm (with cone radius of 0.5).

Due to the above reasons, the CMS calorimetry is “non compensating”: the response to the electromagnetic part of the hadron shower is different from the response to the hadronic part ($e/h \sim 1.4$). The non-compensation effects, which degrade both the linearity and energy resolution of the calorimeter, can be reduced by the usage of energy-dependent ECAL and HCAL weights. To further improve the jet energy resolution CMS is studying particle flow algorithms which measure charged particles in the tracker, photons in the ECAL and long-lived neutral hadrons in the HCAL.

3.2.4 The superconducting magnet

The driving aspect of the CMS detector design is the choice of the magnetic field configuration to serve in a precise measurement of the momentum of muons. According to (3.3), the precision of the measurement of the momentum of charged particles inside a magnetic field is proportional to p/BR^2 . For an optimal momentum resolution, CMS has drawn the attention to the importance of the large bending power needed compensating for a modestly-sized magnet system.

CMS uses a large superconducting solenoid ($L = 13\text{m}$) coaxial to the beam, to produce a strong magnetic field of 4T. With an inner radius at 5.9m, the magnet coil is large enough to allow the tracker and calorimetry sub-systems to be fully integrated inside. The magnetic flux of the field is returned via a 1.5m thick saturated iron yoke instrumented with four stations of muon chambers. In this configuration, the magnetic field provides the appropriate bending power for the efficient triggering on muons and the accurate reconstruction of their tracks in the region up to $|\eta| < 2.5$.

3.2.5 The muon system

The muon system lies in the outermost layer of the CMS detector. Its main goals are the identification of muons, thanks to their large life-time and penetrating power, and the precise measurement of their momentum when additional information from the inner tracker is combined. The muon system also serves for triggering purposes due to its featuring capability to provide fast information for muon identification online.

The muon system consists of four stations which are interleaved with the iron return yoke plates of the magnet system. This allows for about 25000 m^2 of active detection planes to be covered whereas the various radiation environments have lead to the deployment of three different detector technologies: drift tubes, cathode strip chambers and resistive plate chambers. The drift tubes and the cathode strip chambers provide excellent spatial resolution while the resistive plate chambers provide complementary good timing measurements. The geometrical arrangement of the muon system is shown in figure 3.12. The barrel part of the muon system extends with $|\eta| < 1.2$ and the two end-caps as of $0.9 < |\eta| < 2.4$.

The **drift tube chambers (DTs)** are placed in the barrel region where the expected particle flux is low ($< 10 \text{ particles/s} \cdot \text{cm}^2$) and the residual magnetic field in the chambers is low. The drift tube system is segmented in 5 iron wheels along the beam axis, with chambers organized in 4 stations at different radii (MB1-MB4) within each wheel. DT chambers use rectangular drift cells with a cross section of $13 \times 42\text{mm}^2$. A drift cell consists of a stainless steel anode wire which is closed between two alluminium plates of parallel I-beams; two copper strip electrodes, which are glued to the alluminium plates in front of the wire, work as cathodes and improve the shaping of the electric field. In the presence of gas mixture (85% Ar and 15% CO₂), the distance of a track from the wire is measured by the drift time of the ionization electrons through a linear relationship. The transverse dimension of the drift cell, i.e. the maximum drift length has been chosen to be 21 mm which results to a single point resolution of $\approx 200\mu\text{m}$. Four layers of drift cells staggered by half a cell are grouped together to form a superlayer (SL). A single DT chamber is composed of three such SLs: the two outer SLs measure the muon coordinate in the ($r - \phi$) bending plane and the central one measures the z position along the beam line. In each muon station the DT

3.2. THE CMS DETECTOR

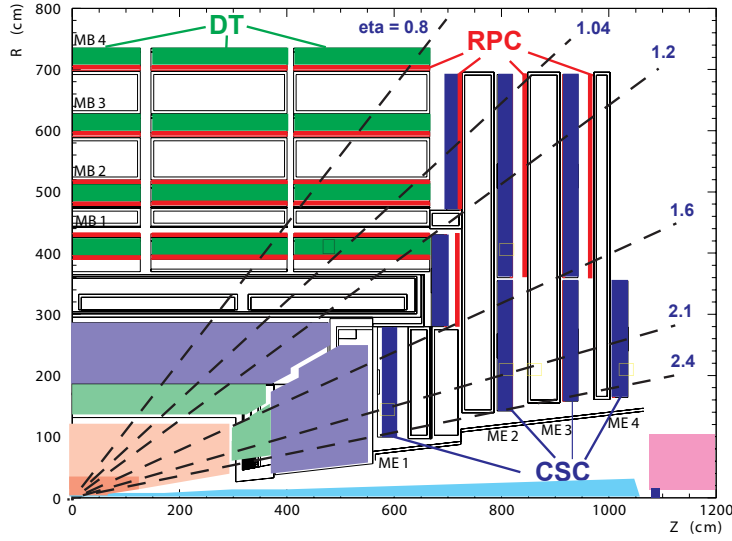


Figure 3.12: Geometrical arrangement of the muon detectors in the $r - z$ plane.

chambers are separated as much as possible to achieve an angular resolution of $1\mu\text{rad}$ in ϕ .

The **cathode strip chambers (CSCs)** are placed in the two end-cap regions in order to provide high precision position measurements in the presence of large and non-uniform magnetic field. Their fast response and the finer segmentation allows the CSCs to operate in high radiation environment (of up to $1\text{ kHz}/\text{cm}^2$). The cathode strip chamber system contains 4 stations (ME1-ME4) of chambers which are mounted on three iron disks perpendicular to the beam line on each end of the detector. A CSC is a multiwire proportional chamber and consists of six active gas layers (filled with $\text{Ar} - \text{CO}_2 - \text{CF}_4$), each layer having a plane of radial cathode strips and a plane of anode wires aligned in the orthogonal direction to the strips. The gas ionization and the subsequent electron avalanche close to the wires, caused by a particle traversing each plane of a chamber, induces a charge on several strips of the cathode plane. A precise position measurement, with a resolution of about $\approx 200\mu\text{m}$ (ϕ measurement), is obtained by determining the centre-of-gravity of the charge distribution on the strips. The signal of the wires gives the radial coordinate but with a coarser resolution, of about 5mm.

The **resistive plate chambers (RPCs)** are placed both in the barrel and end-cap regions, complementing the DT and CSC systems and providing fast information for triggering purposes. RPCs are gaseous parallel-plate detectors, operated in avalanche mode to ensure good operation at high rates. They have a thin gap (2 mm between two plates) and high gain so that can tag an ionizing event in much shorter time than the 25 ns between two LHC crossings. With their fast response and good time resolution, RPCs form a dedicated trigger system with sharp p_T thresholds over a large portion of the rapidity range ($|\eta| < 1.6$) of the muon system. The resistive plate chamber system in the barrel has six radial stations placed within the same five wheels as the DT system (two RPC chambers in both the MB1 and MB2 stations, and one chamber each for MB3 and

MB4). The arrangement is such that a high- p_T muon will cross up to 6 RPCs and 4 DT chambers, producing up to 44 measured points in the DT system from which a muon track candidate can be built. In the end-caps, the RPC system shares the same four stations as the CSC system and helps to solve ambiguities in the CSCs.

The configuration of the muon system ensures the efficiency of muon track reconstruction to be above 90%, for 100 GeV muons in the whole pseudorapidity range. The momentum resolution of tracks measured by the muon system generally depends on the η region, since for $|\eta| > 1.5$ the bending of the muon tracks is smaller. Figure 3.13 shows the transverse-momentum resolution as a function of the transverse-momentum for muons measured in the “muon-system only”, the “inner tracker only” and both (“full system”). Overall the best performance is obtained by the full system with the momentum resolution varying between 0.8% and 1.5% for 10 GeV muons, and between 4% and 6% for 1 TeV muons over the full range $|\eta| < 2.4$.

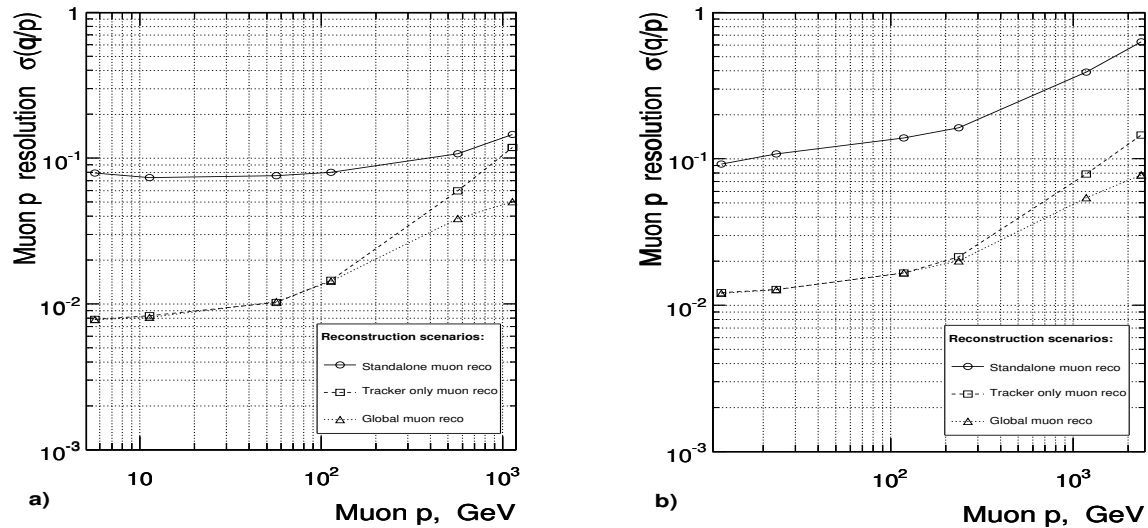


Figure 3.13: *Muon momentum resolution as a function of the muon momentum using the muon-system only (“standalone muon”), the inner tracker only, and both (“global muon”). Left panel corresponds to $|\eta| < 0.8$ and right panel to $1.2 < |\eta| < 2.4$.*

3.2.6 The Trigger

At the nominal LHC operating conditions, the detector is expected to observe an event rate of approximately 10^9 Hz. The associated amount of data generated by the millions of detector electronics channels, with a typical size of 1 MB per event (zero-suppressed), would thus be of order 100 TeraByte per second. Since it is impossible to record all this information, the rate has to be reduced. A triggering system has been developed with the task to perform a reduction down to 10^2 Hz, which is the maximum rate for storing events and processing offline. As already mentioned, the rate input rate of 40 MHz is dominated by events with low transverse momentum. The trigger must therefore provide a high reduction factor and at the same time must maintain a high selection

efficiency on interesting events. This functionality is performed in two steps.

The Level-1 trigger

The output rate for the L1 trigger is designed to reach the 50 (100) kHz for the low (high) luminosity phase of LHC. The functionality of the L1 trigger is crucial because it has to analyze every bunch crossing in a deadtime-free operation². The size of the LHC detectors and the underground caverns imposes a minimum transit time for the signals from the detector front-end electronics to reach the L1 trigger services and back. The total time allocated for the transit and for the L1 processing, is 3.2 μ s. During this time, the detector data are pipelined in buffers while the L1 has to reach a decision to keep or discard data from a given bunch crossing. Of the total latency, the time allocated to the L1 trigger calculations is less than 1 μ s. When the L1 accepts the event, the data are moved to be processed by the HLT.

The L1 trigger operates on custom-designed, largely programmable hardware which is placed onto the detector in order to avoid data transfers. Due to the time available for the L1 to reach a decision upon a given bunch crossing, which is too short to read all the data coming from all parts of the detector, L1 trigger uses information only from the calorimeters and the muon system. The L1 system is therefore organised in a Calorimeter trigger and a Muon trigger, whose task is to determine highest-rank calorimeter and muon objects; the relevant information is then transferred to the Global trigger which has to take the global decision to reject an event or accept it for further evaluation by the HLT. The Calorimeter trigger is subdivided in trigger towers, which match with the segmentation of the calorimeters (5×5 crystals or HCAL towers). The Calorimeter trigger uses regions of 4×4 trigger towers to identify the best candidates out of four categories: electrons and photons, central jets, forward jets and τ -jets. The information from these objects is then passed to the Global trigger along with measurement of the missing transverse energy. The Muon trigger analyzes information for the three detectors of the muon system separately; the information is combined and similarly passed to the Global trigger. The decision of the Global trigger is finally received for every trigger object according to algorithm calculations implemented on programmable logic devices.

The High-Level Trigger

The High-Level trigger of CMS will reduce the output rate from the Level-1 trigger down to 100 Hz. The HLT is a software system similar with that of the offline analysis and is implemented on a filter farm of about one thousand of commercial processors. The idea behind the HLT is the regional reconstruction *on demand*, that is that only the objects found in useful regions are reconstructed whereas the non-interesting events should be rejected as soon as possible. This has led to the development of three logical levels. At the first one, only the information from the calorimeters and the muon system is used; at the second level, information from the pixel detectors of the tracker is also added when finally, at the third level, the full event information is available.

²In reality, due to technical limitations, the laser firing the synchronous signal, to accept an event, to all the front-ends, cannot operate on two successive bunch crossings. This implies an efficiency loss of 0.1% at a L1 accept rate of 100 kHz.

4

Physics objects: reconstruction and selection

The present analysis uses data samples that were produced with the Computing, Software and Analysis challenge performed in the Fall 2007 (CSA07) [27]. It is targeting to 1fb^{-1} of statistics and therefore the data samples have been re-reconstructed with calibration and alignment constants based on the understanding of the detector obtained with 100pb^{-1} of data (referred to as “ 100 pb^{-1} samples”). The samples were generated with the CMS software Framework CMSSW, using the `1.4_X` series for simulation/digitization and `1.6_X` for reconstruction. The official package “SusyAnalyzer” [28] was used to access and analyze the data.

4.1 Electron reconstruction and selection

The electron reconstruction of CMS focuses in the identification and the four-momentum measurement of electrons originating from the primary (interaction) vertex. The electron reconstruction flow uses information from both the silicon tracker and the electromagnetic calorimeter, forming electron objects by the combination of a track emerging from the primary vertex and the associated clustered energy in the ECAL. It is obvious that reconstruction of electrons can be done in the angular range $|\eta| < 2.5$ as viewed from the nominal vertex.

The challenging issue featuring the electron reconstruction is the effect of bremsstrahlung radiation of electrons inside the tracker material. An electron traversing the silicon layers of the pixel and inner tracker detectors radiates bremsstrahlung photons; in the presence of the B field, the energy reaching up the surface of the ECAL can be significantly spread in the ϕ -direction. The bremsstrahlung emission pattern and the integral amount of radiation along the electron trajectory depend on average on the amount of tracker material distributed in front of the ECAL (see figure 3.6) which varies strongly with η . Furthermore, the situation is complicated by subsequent photon conversions which are likely to occur. The secondary low-momentum electrons from e^+e^- pairs are trapped by the magnetic field and this might additionally lead to substantial loss of the electron’s initial energy inside the tracker region. In order to cope better with these effects, sophisticated clustering algorithms and track reconstruction methods have been developed by CMS and these are described next.

CHAPTER 4. PHYSICS OBJECTS: RECONSTRUCTION AND SELECTION

4.1.1 The PixelMatchGsfElectron algorithm

The PixelMatchGsfElectrons

The electron reconstruction is initiated by the presence of electromagnetic super-clusters. Super-cluster (SC) objects are built during the ECAL regional reconstruction; they are clusters of clustered crystals whose main purpose is the recovery of the electron energy spread in ϕ caused by the bremsstrahlung photons.

CMS has developed two types of dedicated clustering algorithms which are called “hybrid” and “island”, and are used for electrons in the ECAL barrel and end-caps respectively. The hybrid algorithm uses the energy sums in fixed size arrays of crystals (3 or 5 crystals in η) and searches dynamically for separated energy in the ϕ direction; the supercluster is formed when no other collections of arrays with energy sum above 100 MeV is found. The island algorithm is instead using energy sums of crystals collected dynamically starting from a seed crystal with an energy above a certain threshold; the supercluster is formed by clusters of such clusters inside a very narrow η -window and a much wider ϕ -window. The super-cluster building parameters, such as the cluster seed E_T thresholds or the maximal η/ϕ -window, are optimized in both cases so that to minimize the super-cluster containment variations which basically influence the electron energy measurements.

The ECAL super-clusters are used to drive the finding of pixel “seeds” for the reconstruction of primary electron tracks. The building of electron tracks follows the lines of the CMS track reconstruction strategies; this is done in four main steps.

Firstly, the *Seed Generator* looks for initial tracks called seeds in the pixel detector. In the case of electrons the search is restricted in a region which is compatible with a super-sluster in the ECAL. The method takes into advantage of the fact that the energy weighted mean position of the super-cluster (assuming an adequate collection of photons) coincides with the position in the ECAL that a non-radiating electron of the same initial momentum would have impacted. By propagating this point backwards through the magnetic field under both charge hypotheses, a track hit is looked for in the innermost layer of the pixel detector. Search windows are adapted in both the ϕ - and z -directions according to the uncertainty of the ϕ_{sc} measurement and the spread of the interaction vertex, respectively. When a first compatible hit is found, the z coordinate of the primary track vertex is re-estimated by combining the pixel hit found and calorimetry information in the Rz plane. The predicted trajectory is then propagated to look for a second pixel hit in the next pixel layers.

Two pixel hits are then used to seed the building of an electron track in the silicon tracker detectors. This is the purpose of the *Trajectory Builder*, which constructs outwards all the possible trajectories from the given pixel seeds. The default track reconstruction method in CMS relies on a simple Kalman Filter (KF) algorithm; in the case of electrons, the Gaussian Sum Filter (GSF) approach is used instead for the building process which takes into account the non-gaussian fluctuations of the track parameters due to material effects such as multiple scattering etc. In the GSF method, the distributions of the state vectors and errors are treated as Gaussian mixtures, with weights of the gaussian components that depend on the measurements. The track building process starts with compatible hits in the first silicon layers and an extrapolation is performed using a Bethe

4.1. ELECTRON RECONSTRUCTION AND SELECTION

Heitler modeling of the electron energy losses up to the end of the tracking volume. The electron track hits are collected in successive silicon layers with a tolerance of 1 layer without hits. On the other hand, if more than one hit is found on a given silicon layer then many candidate trajectories are built in parallel. The *Trajectory Cleaner* then serves in keeping the best two of them based on the smallest χ^2 . Finally, the *Trajectory Smoother* is used to fit the tracks; at this step the track parameters and errors are made available for each tracker layer through a backward fit of the trajectories.

The facts that electron track hits can be efficiently collected through the tracker volume as well as that meaningful track parameters and errors are available at both the inner (vertex) and outer (ECAL surface) tracker layers, are great benefits from using the GSF tracks. They give the possibility not only to improve the matching between the tracker and the calorimeter but also to have a good estimate of the amount of bremsstrahlung radiated by the track using the tracker information only. This finds major applications in distinguishing various electron patterns and improve the electron energy measurement as well as the electron identification performance.

Electron classification

The electron reconstruction algorithm described above provides several calorimeter and tracking observables which are in one way or another sensitive to the effects of bremsstrahlung radiation and the energy lost in the tracker material. Such observables are used to define quality criteria and separate the electron population in different classes in order to better disentangle the non-gaussian sources of fluctuations of the ECAL super-cluster energy containment and the tracker momentum measurement. Among the useful quantities used to define the various classes are:

- the relative difference between the momentum measured at the outermost state (p_{out}) of the electron track and the momentum measured at the origin (p_{in}), $f_{\text{brem}} = (p_{\text{in}} - p_{\text{out}})/p_{\text{in}}$. This quantity is linearly dependent with the amount of bremsstrahlung radiated along the electron trajectory.
- the matching in ϕ between the reconstructed track and the super-cluster ($\Delta\phi_{\text{out}} = \phi_{\text{sc}} - \phi_{\text{trk}}^{\text{extrap.}}$) is furthermore sensitive to the bremsstrahlung collection in the ECAL.
- the matching between the total energy E_{sc} collected by the super-cluster and the momentum measurement obtained at the track origin is sensitive to the energy lost in the tracker material. This is often expressed with the ratio of the relevant quantities, $E_{\text{sc}}/p_{\text{in}}$.

There are four classes to qualify electrons: i) the **golden electrons** are the most precisely measured electrons. They are shown less affected by radiation emission ($f_{\text{brem}} < 0.2$), they have a reconstructed track well matched the super-cluster ($|\Delta\phi_{\text{out}}| < 0.15$) and a well behaved super-cluster pattern ($E_{\text{sc}}/p_{\text{in}} > 0.9$). ii) The **big brem electrons** are also very well measured although they have significantly radiated ($f_{\text{brem}} > 0.5$); they have a good energy-momentum matching between the super-cluster and the electron track at the origin and no evidence for energy lost ($0.9 < E_{\text{sc}}/p_{\text{in}} < 1.1$). Electrons that fall in this category are indicative of having radiated all the bremsstrahlung in a single step, either very early or very late when crossing the silicon layers. iii) The **narrow electrons** are complementing the previous two classes; they still have a

CHAPTER 4. PHYSICS OBJECTS: RECONSTRUCTION AND SELECTION

good energy-momentum matching but due to their big bremsstrahlung, they show a relaxed geometrical matching between the track and the super-cluster (outside the range of golden and big brem electrons). iv) the **showering electrons** are finally the remaining, “badly” measured electrons. This is most likely electrons which suffer from secondary conversions of some early radiated bremsstrahlung, and are thus observed with a bad energy-momentum E/p matching.

Overall the different kind of electrons falling into the above classes are characterized by different energy-momentum measurement variations; this makes it obvious that “well measured” and “badly measured” electrons need to enter with different weights at the physics analysis level. This is the purpose of the electron identification, which applies as an intermediate functionality between the electron reconstruction and the usage of electron candidates in a particular physics analysis scenario.

4.1.2 Electron identification

The electron identification uses estimators, characterizing the electron “quality”, to provide a set of selection criteria that will allow primarily well behaved electrons (that is according to expectations from single electrons) to enter the analysis level. However, well measured and badly measured electrons are furthermore expected to be differently affected by the possible background electron sources and especially those which involve “fake” electrons. Such electrons for example can arise from hadron overlaps in jet (QCD) events. The performance (efficiency, rejection power, purity) of the identification procedure is obviously dependent on the nature of the background considered and should therefore be determined with respect to that.

Figure 5.7 shows some typical distributions of electron identification variables plotted against different electron classes. They are all shown using a sample of real electrons, for the golden and showering entries, and a sample of QCD di-jet events to account for the fake electrons. Considering the different behavior of the distributions among the electron classes, the following conclusions on the usage of the identification variables can be drawn:

- the H/E , defined as the ratio of the energy deposited in the HCAL tower just behind the electromagnetic seed cluster over the energy of the seed cluster, is discriminating for all classes, with a slight loss of discriminating power for showering electrons; the same holds for the $\Delta\eta_{\text{in}}$ and $\Delta\phi_{\text{in}}$ variables calculated with track parameters at the vertex when extrapolated to the surface of the ECAL.
- the Σ_9/Σ_{25} variable, calculated from the ratio of the energy sums over 3×3 and 5×5 crystal matrices centered on the highest energy crystal of the seed cluster, gives discriminating power for all but showering electrons;
- the $\Delta\phi_{\text{out}}$, with track momentum from the outermost track position and energy from the electron seed-cluster, is discriminating only for golden electrons;
- the E/p_{in} with track parameters at the vertex and using super-cluster energy and E/p_{out} with track at the outermost state and energy from the electron sub-cluster, are more discriminating for the showering class.

4.1. ELECTRON RECONSTRUCTION AND SELECTION

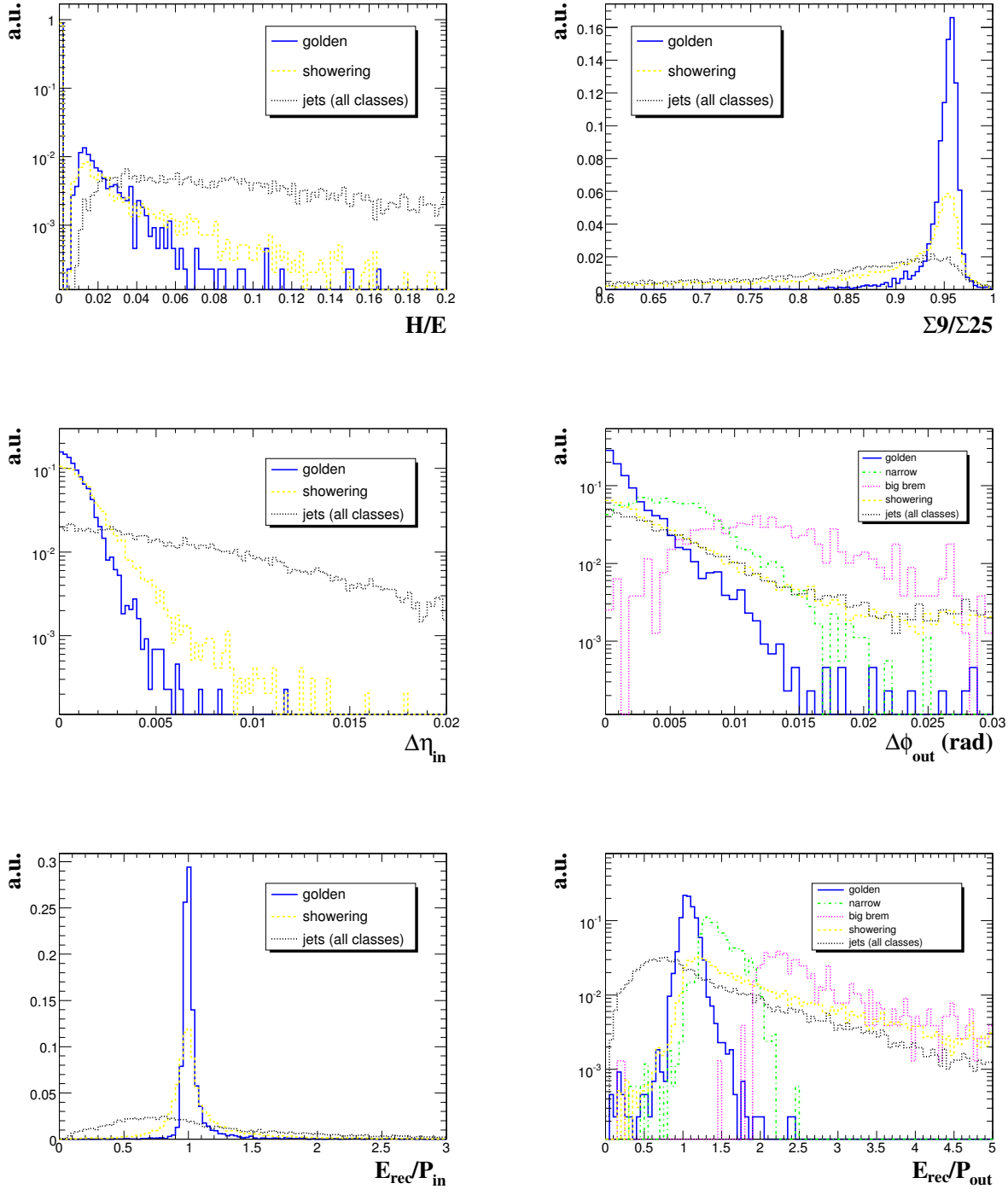


Figure 4.1: Electron identification variables and their distributions among the different electron classes; the plots demonstrate the behavior of real electrons uniformly distributed in the p_T^e range between 5 and 50 GeV/c compared to “fake” electron candidates found in jets from a QCD di-jet background generated in the range $25 < \hat{p}_T < 170$ GeV/c.

CHAPTER 4. PHYSICS OBJECTS: RECONSTRUCTION AND SELECTION

In a physics analysis sample, the electrons found by the electron reconstruction algorithm are, obviously, not all real: the size of the electron collection is in principle larger than that of the real electrons. Several cleanup tools to refine the collection according to electron quality requirements, and discriminate between fake and real electrons exist. Each of them uses a selected set of quality variables which are combined to perform an electron Identification (ID), using cuts, or multivariate techniques such as a likelihood or neural net. Three different kinds of cut-based electron ID algorithms have been developed, namely the “robust”, “loose” and “tight”. The ”robust” selection¹ uses a very simple loose electron ID suitable for start-up conditions. The selection is based on four cut variables which are basically independent of the measured bremsstrahlung fraction and insensitive to tracker misalignment:

$$\sigma_{\eta}, \quad \Delta\eta_{\text{in}}, \quad \Delta\phi_{\text{in}}, \quad H/E \quad (4.1)$$

applying different cut values for the barrel and end-cap regions.

The “loose” and “tight” types use a more sophisticated selection method making use of the electron classification depending on the amount of bremsstrahlung radiation along the electron trajectory. Three categories are defined as regions in the E/p versus f_{brem} plane, characterized by:

- Category 1: high f_{brem} and energy-momentum matching as $0.8 < E/p < 1.1$.
- Category 2: low bremsstrahlung fraction with $f_{\text{brem}} < 0.6$ in the barrel and $f_{\text{brem}} < 0.1$ in the end-caps.
- Category 3: E/p matching not close to 1.

The 1st category is dominated by real electrons and therefore loose cuts are only applied. Category 2 includes mainly fakes and tighter cuts are chosen, whereas category 3 includes mostly fakes but also real electrons with a bad E/p matching. Electrons that appear both in bad E/p and f_{brem} fraction ($E/p < 0.8$ and $f_{\text{brem}} < 0.2$) are directly rejected. The “tight” selection follows the lines of the “loose” selection but with tighter cuts in all ID variables and a larger region in the E/p versus f_{brem} plane,

$$E/p < 0.9 \cdot (1 - f_{\text{brem}}) \quad (4.2)$$

being rejected. Both types have been optimized in order to provide good rejection of fake electrons.

Reference plots for comparing the performance of the above three selection types are shown on figure 4.2. The reconstruction and identification efficiencies are plotted as a function of the generated electron p_T and η using a sample with $Z \rightarrow ee$ events (2 electrons final state). The efficiency is defined as the number of generated electrons that matched with reconstructed electrons passing the reconstruction/selection criteria, divided by the number of all generated electrons. The electron fake rate provided by the electron reconstruction and identification strategies is also shown on figure 4.3. The electron fake rate is defined here as the number of reconstructed jets that matched

¹A more appropriate name for this selection, that would better reflect the nature of the selection, might be “very loose”. The word “robust” is used to indicate “robustness” against the early conditions of the CMS detector.

4.1. ELECTRON RECONSTRUCTION AND SELECTION

with a reconstructed and identified electron divided by the number of all the reconstructed jets. The plots show the fake rate as function of the reconstructed jet E_T and η using a sample of QCD jets, with jets reconstructed with the iterative cone algorithm.

Overall the robust and loose identification methods provide an efficiency of almost 98% with respect to the reconstruction, for electrons with $p_T > 5$ GeV and $|\eta| < 2.5$. The fake rates appear as of 4.1% for the robust and of 1.5% for the loose identification. For what concerns the tight selection, it yields a 3% lower efficiency in selecting real electrons compared to the other two selections, to profit from a factor 2 decrease in the electron fake rate.

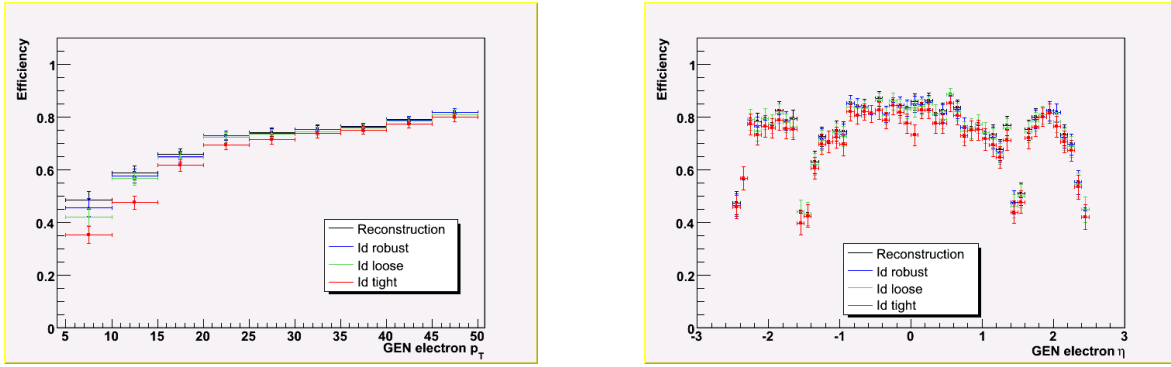


Figure 4.2: Reconstruction and identification efficiency as a function of the generated electron p_T (left) and η (right), after reconstruction and the application of three cut-based selection settings. The plots refer to events with two electrons in the final state ($Z \rightarrow ee$).

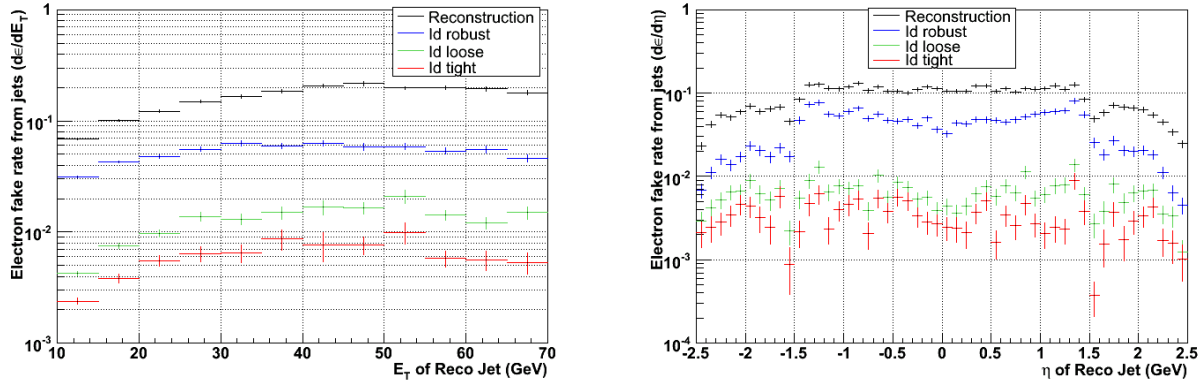


Figure 4.3: Electron fake rate as a function of the reconstructed jet p_T (left) and η (right), after reconstruction and the application of three cut-based selection settings. The plots refer to a sample of QCD jet events generated in the range $20 < \hat{p}_T < 120$ GeV/c – jets are reconstructed with the iterative cone algorithm; no jet energy corrections have been applied.

4.2 Muon reconstruction

The reconstruction of muon objects in CMS is performed using information from both the muon system and the silicon tracker. The muon reconstruction related software has been designed based on the concept of *regional reconstruction*; that is only that parts of a given detector are used that fall into some region of interest (seeding region). As an example, reconstruction of a muon track in the silicon tracker involves only the parts of the tracker where charged particle tracks found compatible with hits in the muon chambers. This obviously saves significant CPU power compared to reconstruction employment in the total tracker data volume. Muon reconstruction in general is performed in 3 steps: i) local reconstruction (local pattern recognition), ii) standalone reconstruction where only the muon system is used and iii) global reconstruction where also the silicon tracker is used.

The muon reconstruction algorithms run both during the High-Level-Trigger (online event selection) and for offline use. In the context of the analysis presented in the next chapters, the offline muon reconstruction method will be described here in more detail. The muon reconstruction chain starts with the “local reconstruction”, i.e. the reconstruction of hit positions in the muon system alone. The DT and CSC tracking detectors as well as the RPCs participate in the reconstruction. Despite the coarser spatial resolution of the RPCs, their role is to complement the tracking chambers, especially in the barrel-endcap transition region where the geometrical coverage is problematic. Hits within each DT and CSC chamber are matched to form “segments” which are used to generate seeds, consisting of a position and direction and an estimate of the muon transverse momentum. This initial estimate is used as a seed for the actual track fit, which results in the so called **standalone muon**.

Initial state vectors are obtained from the segments found in the innermost chambers of the muon system; they are propagated in the outward direction using the Kalman-filter technique. At each measurement surface, the predicted state vectors are compared with previous measurements and updated accordingly. Their propagation from one station to another takes into account muon energy loss in the material, the effect of multiple scattering and the non-uniform magnetic field in the muon system. When the outermost measurement surface is reached, a backward Kalman-Filter fit defines the track parameters at the innermost muon surface. The final track is extrapolated to the nominal interaction point (determined by the beam-spot size: $\sigma_{xy} = 15\mu\text{m}$ and $\sigma_z = 5.3\text{cm}$) and a vertex-constrained fit is performed.

In the subsequent step the standalone muon tracks are matched with the charged-particle tracks reconstructed in the silicon tracker to generate **global muon** candidates. The global muon reconstruction starts with extrapolating the muon trajectory from the innermost muon station to the outer tracker surface taking into account material effects. Silicon layers compatible with the muon trajectory are then used to determine a region of interest in which to perform regional track reconstruction. The determination of the region of interest is based on the track parameters and their estimated uncertainties and this has a strong impact on the reconstruction, fake rate and CPU reconstruction time. In general, well measured muons are reconstructed faster and with higher efficiency than poorly measured ones.

Inside the region of interest, combinations of exactly two hits coming from different tracker layers

4.2. MUON RECONSTRUCTION

are looked for in order to build initial candidate tracks (regional seeds). The procedure involves all the combinations of compatible pixel and double-sided silicon strip layers so that to enhance the final tracking efficiency. As soon as the regional seeds are formed a track reconstruction algorithm runs, using the Kalman-Filter technique. As a first step, the trajectory builder transforms each seed into a set of trajectories working from inside-out. Track parameters are updated at each tracker layer with compatible measurements found on the same layer. In the second step, the trajectory cleaner resolves ambiguities between multiple trajectories arising from the same seed, according to hit multiplicity and χ^2 tests. In the final step, all reconstructed tracks are fitted globally; i.e. using the hits on the muon chambers from the original standalone reconstruction and the hits on the silicon tracker. Final muon candidates are selected on the basis of a χ^2 test.

Reconstruction performance

Figure 4.4 shows the muon reconstruction efficiency as a function of the pseudorapidity for different values of the muon p_T . The results are obtained using single muon event samples simulated with “ideal conditions”, i.e. without taking into account effects from misalignment, miscalibration, neutron background or pile-up. Overall the reconstruction efficiency shows typical values of 95-99%, except in the pseudorapidity regions around $|\eta| = 0.2$ and $|\eta| = 0.8$ - corresponding to the regions between two DT wheels - and around $|\eta| = 1.2$ - the transition region between the DT and CSC systems - where the efficiency drops. The behavior clearly reflects the geometrical structure of the muon system (see figure 3.12).

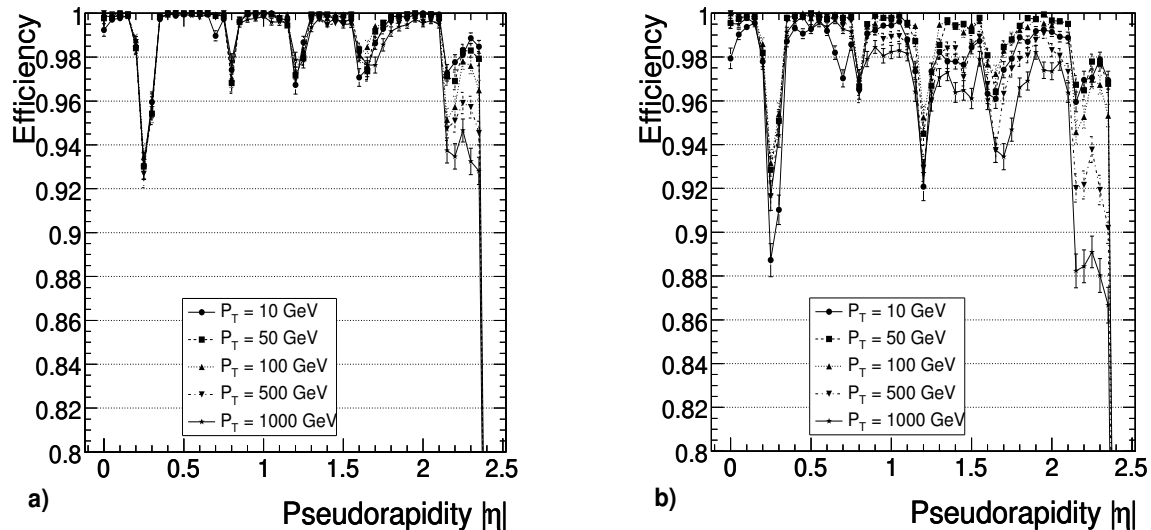


Figure 4.4: *Muon reconstruction efficiency as a function of the pseudorapidity for different muon p_T values: a) obtained with the standalone reconstruction and b) obtained with the global reconstruction.*

4.3 Jet reconstruction

At LHC, physics processes involving quarks or gluons in the final state are expected to dominate high- p_T physics events. Because of QCD confinement, quarks and gluons cannot be observed directly but instead undergo a fragmentation (soft QCD radiation) and a hadronization (formation of hadrons) phase, before they are detected by the tracking and calorimeter systems. The experimentally observed objects associated with the quarks and gluons emitted during the hard scattering process, are called “jets”.

Jet reconstruction uses energy deposits in the calorimeters in order to form collimated objects of stable particles (hadrons). The jet algorithms use as inputs calorimeter towers (“CaloTowers”) which combine ECAL and HCAL cells according to the HCAL granularity. In the barrel, projective towers are formed by a single HCAL cell and 5×5 ECAL crystals, whereas in the end-cap regions they follow a more complex association. For the purpose of jet clustering, the calorimeter towers are defined with an energy given by the tower energy itself and a direction determined by the interaction point and the centre of the tower. The standard jet reconstruction applies energy thresholds to calorimeter cells in order to suppress the contribution from the calorimeter noise. The most commonly used approach applies an overall tower threshold of $E_T > 0.5$ GeV. Among the popular jet clustering algorithms that are supported by CMS, there are:

- the iterative cone algorithm, uses input objects from a list of calorimeter towers or particles with $E_T > 1$ GeV which are ordered in energy. For each object, an iterative procedure starts by looking for input particles that fall into a predefined cone-size of $\Delta R = \sqrt{\Delta\eta^2 + \Delta\phi^2}$ around the direction of the given object. The objects inside the cone are used to calculate a “proto-jet” direction and energy according to the E_T scheme. A proto-jet is considered stable, once its energy changes by less than 1% between iterations and its direction changes by $\Delta R < 0.01$. The objects in the proto-jet are then removed from the list of input objects and the proto-jet is added to the list of jets. The procedure is repeated until the original list is empty.
- the midpoint cone algorithm, is based on an iterative procedure to find stable cones as well. A difference from the iterative cone is that, at a first step, no object is removed from the list. This can result in overlapping proto-jets and a second iteration is performed upon them. For every pair of proto-jets which are closer than twice the cone radius R , a *midpoint* is calculated from the direction of the combined momentum. Midpoints are then used as additional seeds for finding more proto-jets. A splitting and merging procedure is applied finally to ensure that each input object appears in one jet only.
- the inclusive k_T algorithm is a cluster-based jet algorithm. In contrast to the other two algorithms, at each iteration step, pairs of input objects (i, j) that found with the smallest distance $d_{ij} = \min(E_{T,i}^2, E_{T,j}^2) \Delta R_{ij}^2$, are merged and kept in the list as a possible final jet. New jet quantities (energy and direction of the jet) are calculated directly during the clustering, and objects with the smallest radius $D = (E_{T,i}^2 R^2)$ are added successively in the list of final jets.

The iterative cone is simpler and faster and commonly used by CMS on-line during the HLT; the rest, are widely used for offline analysis. The algorithms produce massless jets when the

4.4. APPLICATION TO DI-LEPTON ANALYSIS

so-called “ E_T recombination scheme” is used. This is achieved by equating the jet transverse momentum to the $\sum E_T$ of the tower constituents and then fixing the direction of the jet by the angle $\sin \theta = \sum E_T/E$ where E is the jet energy.

4.4 Application to di-lepton analysis

The analysis to be presented in the next chapters studies di-lepton final states arising from supersymmetric as well as standard model processes. It is for the purpose of this analysis that only electrons or muons with $p_T > 10$ GeV and $|\eta| < 2.4$ are selected. These initial acceptance cuts on the leptons are considered throughout the following studies.

4.4.1 Lepton reconstruction and selection efficiencies

Electrons and muons are reconstructed with the *PixelMatchGsfElectrons* and *GlobalMuonReconstructor* algorithms respectively. It is a feature of the algorithms that multiple electrons coming from more than one electron tracks matching the same super-cluster in the calorimeter appear in the electron candidate list; and similarly there are ghost muons duplicating some of the offline muon candidates. Such electrons or muons are found very close in ΔR causing a peak at zero and are eliminated by applying offline the following clean-up tests²:

Electron duplication: whether multiple electron tracks are associated with the same-supercluster, or inversely one track is associated to several super-clusters, only the best candidate is kept based on the E/p quality criterio.

Muon duplication: multiplication of the muon tracks is removed by choosing the best one, based on the $\Delta p/p$ criterio, where p is the global muon track momentum and Δp the associated measurement error, if several tracks have the same charge and are within a cone of $\Delta R = 0.1$.

A second stage of lepton clean-up follows based on quality requirements on the electron and muon candidates. The analysis applies the “tight” electron identification method which was shown to have the best rejection power on the electron-fakes, despite a small cost in the electron efficiency. A clean-up on the combined muon tracks is performed using the variables $\Delta p/p$, number of hits and χ^2 of the track. The muon track quality is verified, and the muon is kept in the final collection, if

$$\Delta p/p < 0.5, \quad N_{hits} > 8, \quad \chi^2 < 10. \quad \boxed{4.3}$$

The performance of the selection has been studied using a sample of supersymmetric events from the mSUGRA benchmark scenario LM1, from the official CSA07 production. Among the leptons found in the supersymmetric sample, primary leptons as well as background leptons are identified and studied separately due to their different performance when imposing the reconstruction and selection requirements. Primary leptons are identified as prompt leptons coming from the decays

²This is employed internally by the official package “SusyAnalyzer” after the accessing of the electron and muon candidate collections.

CHAPTER 4. PHYSICS OBJECTS: RECONSTRUCTION AND SELECTION

of a heavy susy particle, a W/Z or τ particle. Background leptons are considered coming from the prompt decays of a heavy flavor b or c quark and are called here for simplicity “hadron leptons”.

A matching between the reconstructed and selected as previously defined lepton candidates and the MC truth electrons and muons is initially performed. For every generated electron or muon with $p_T^\ell > 10$ GeV and $|\eta^\ell| < 2.4$, an offline electron or muon candidate is looked for within a pre-defined cone size ΔR . If more than one candidates match the same generated lepton then a “best match” method is applied based on the smallest relative momentum difference, $\Delta p_T/p_T$, between the reconstructed and generated lepton pair. For the matching of electron objects a $\Delta R_{\text{electron pairs}} < 0.4$ is required, whereas for muon objects a narrower cone of $\Delta R_{\text{muon pairs}} < 0.2$ is adequate. In both cases however, the quantity $\Delta p_T/p_T$ should not exceed a certain value (of 4 for electrons and 3 for muons) so that to obtain reasonable pairs of generated leptons and well reconstructed candidates. Figure 4.5 shows the two-dimensional distribution of the ΔR versus the relative momentum difference between pairs of generated leptons and best-matched reconstructed leptons, for electrons and muons separately. As can be seen, electron pairs tend to be broader in the $\Delta p_T/p_T$ than muon pairs, which is expected due to the bremsstrahlung emission and energy loss affecting the electron reconstruction measurements.

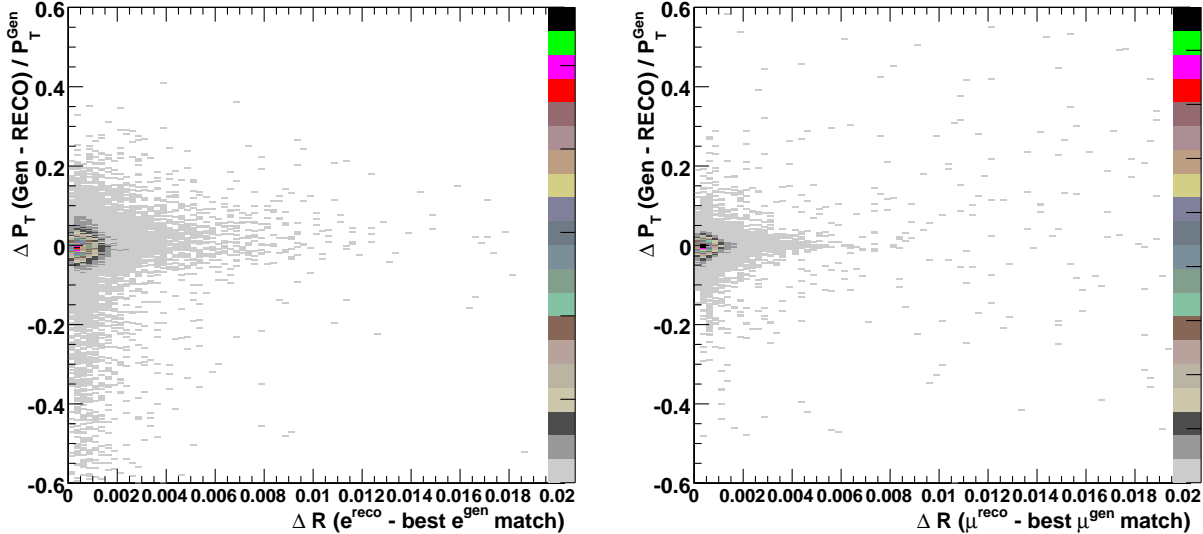


Figure 4.5: *The matching between the MC truth leptons and the reconstructed candidate leptons, for electrons on the left and muons on the right. Plots show the ΔR distance between the reconstructed lepton and the best-matched generated lepton, versus the relative momentum difference $\Delta p_T/p_T$, of the lepton pair. The “best-match” is defined as the generated lepton found within a cone ΔR^{\max} having the smallest $\Delta p_T/p_T$ among multiple matched generated leptons.*

Figures 4.6 and 4.7 show the reconstruction and selection efficiencies as a function of the lepton p_T and η respectively, for electrons and muons separately. For a generated prompt lepton with $p_T^{\text{gen}} > 10$ GeV and $|\eta^{\text{gen}}| < 2.4$, the efficiency to find an offline prompt-lepton candidate with $p_T^{\text{reco}} > 10$ GeV and $|\eta^{\text{reco}}| < 2.4$ is $\sim 79\%$ for electrons and $\sim 97\%$ for muons. The same

4.4. APPLICATION TO DI-LEPTON ANALYSIS

figures show superimposed the corresponding efficiencies for hadron electrons and muons. In this case, the reconstruction and selection performances are shown worse especially for electrons. The tight electron identification requirements are proved quite restrictive in selecting electrons coming from secondary decays of the heavy flavor quarks, with only $\sim 11\%$ of the original hadron electrons surviving in the offline electron candidate list. The most effective cut is coming from the H/E cut applied; this is a cut on the longitudinal shower shape which has a large impact on rejecting electrons with hadron tracks passing within the H/E calculation cone. On the contrary, hadron muons passing the global muon reconstruction, survive with $\sim 94\%$ efficiency. Nevertheless, both hadron electrons and hadron muons are expected to be significantly reduced when imposing additional lepton isolation requirements. The isolation definition and performance on selecting primary leptons are presented next.

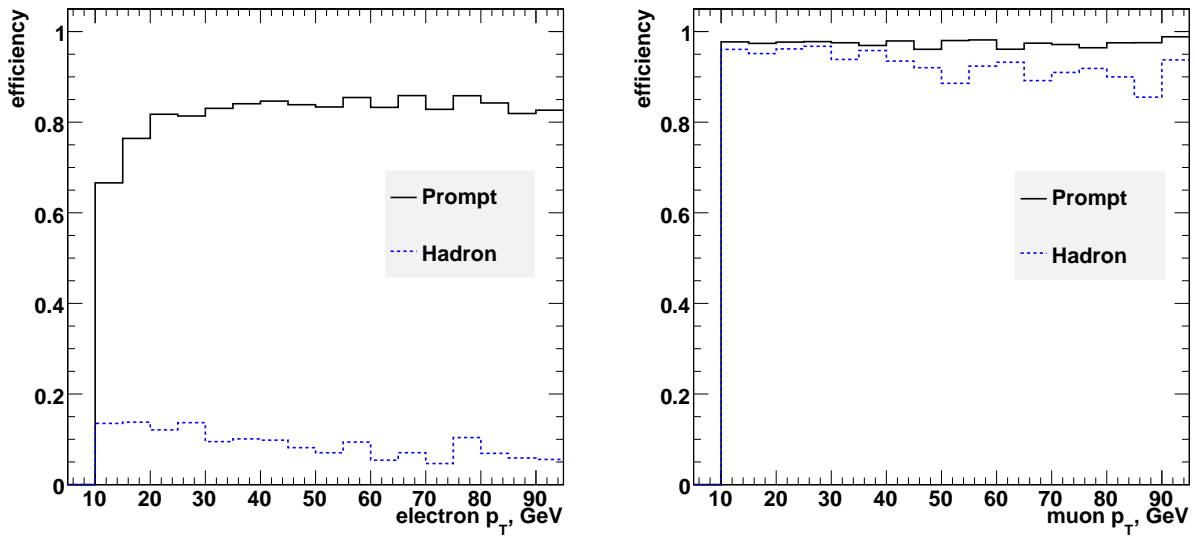


Figure 4.6: *Electron (left) and muon (right) reconstruction and selection efficiency as a function of the generated electron/muon p_T . Leptons are decomposed into “prompt leptons”, coming from a susy, a W/Z or τ particle, and “hadron leptons” arising from the decays of heavy flavor quarks (b or c quarks). The efficiency is defined as the number of generated leptons that matched a reconstructed lepton divided by all generated electrons.*

4.4.2 Lepton tracker isolation

Up to this point, lepton identification has utilized criteria which are largely independent of the physics process under study, even though a small bias towards isolated leptons is built into the algorithms (arising from the mere observation of the objects, e.g. superclusters, charged-particle tracks involved in the selection). Isolation is a key tool in distinguishing leptons from high- p_T processes and fake leptons or leptons coming from heavy-flavor quarks (b/c decays).

The isolation algorithm selected for this analysis is tracker-based and was defined and applied in an identical manner for electrons and muons [30]. This is necessary because a key element of

CHAPTER 4. PHYSICS OBJECTS: RECONSTRUCTION AND SELECTION

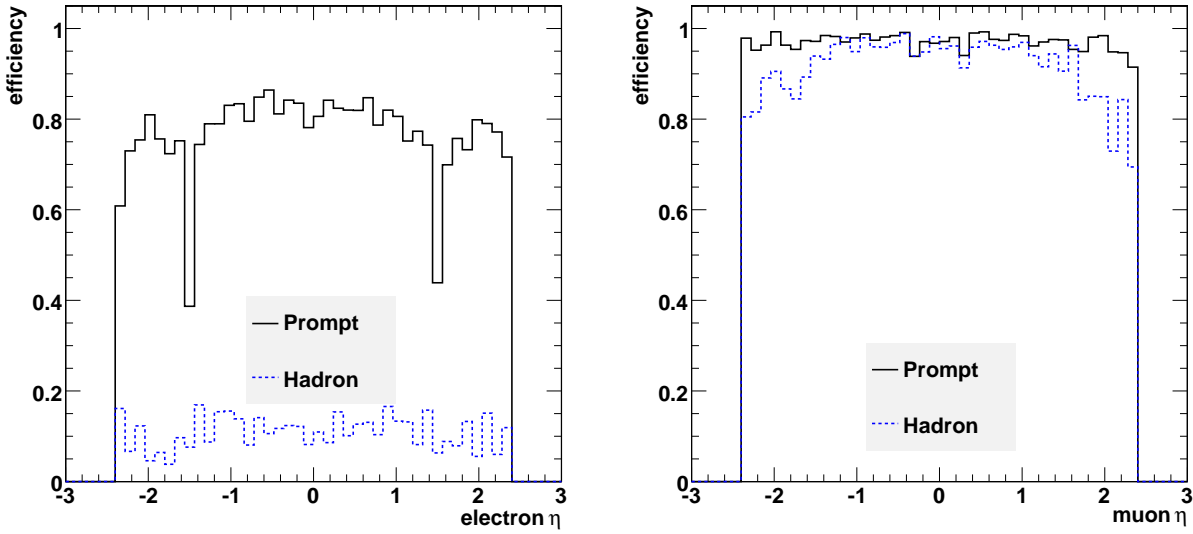


Figure 4.7: Electron (left) and muon (right) reconstruction and selection efficiency as a function of the generated electron/muon η . Leptons are decomposed into “prompt leptons”, coming from a susy, a W/Z or τ particle, and “hadron leptons” arising from the decays of heavy flavor quarks (b or c quarks).

the analysis is the usage of the different-flavor ($e\mu$) data to estimate the same-flavor (ee and $\mu\mu$) backgrounds. It is desirable to apply a correction (for the two lepton reconstruction efficiencies) that does not depend on the environment of the lepton vs the lepton type. The isolation algorithm uses the sum of transverse momenta, p_T , of all charged-particle tracks within a cone in $\eta - \phi$ space (of opening $\Delta R = \sqrt{\Delta\eta^2 + \Delta\phi^2}$) around the lepton candidate, while vetoing tracks within a smaller (inner) cone to remove the charged-particle track of the lepton itself. Only good-quality tracks are considered in calculating the sum of the transverse momenta. The track quality criteria employed include the number of hits assigned to the track and the compatibility of the track with the primary vertex. The complete set of track quality cuts are displayed in table 4.1.

The performance of possible isolation criteria was studied in SUSY (LM1) and $t\bar{t}$ +jets, and is presented in figure 4.8. The isolation distribution is shown separately for three different types of leptons: i) “prompt leptons”, coming from susy particles or a $W/Z/\tau$ decay, ii) “hadron leptons”, coming from the decays of heavy flavor (b, c) quarks and iii) “fake leptons”, typically found inside jets. The prompt lepton efficiency as a function of the isolation cut is shown in figure 4.9, for electrons and muons superimposed, in order to compare the behavior of the isolation requirement on electrons and muons. The isolation requirement applied was chosen to be

$$\sum p_T^{trks} / p_T^{lep} < 0.2 \quad 4.4$$

inside the $\eta - \phi$ region identified by $0.015 < \Delta R < 0.2$. This corresponds to an efficiency of 93% for both electrons and muons, with respect to the reconstruction and selection efficiencies.

In order to justify the choice of the inner ΔR_{in} and outer cone ΔR_{out} sizes in the definition of the lepton tracker isolation above, an optimization procedure has been followed. Four different

4.4. APPLICATION TO DI-LEPTON ANALYSIS

Table 4.1: *Summary of the quality cuts applied on the tracks entering the sum in the definition of the lepton Tracker based isolation, depending on their number of hits.*

Variable	Quality cut		
Number of hits	≥ 10	[8, 9]	[5, 7]
p_T (GeV)	> 1	> 1	> 1
$d0$ (cm)	< 1	< 0.2	< 0.04
dZ (cm)	< 5	< 2.0	< 0.5
$d0/\delta(d0)$	-	< 10	< 7
$dZ/\delta(dZ)$	-	< 10	< 7

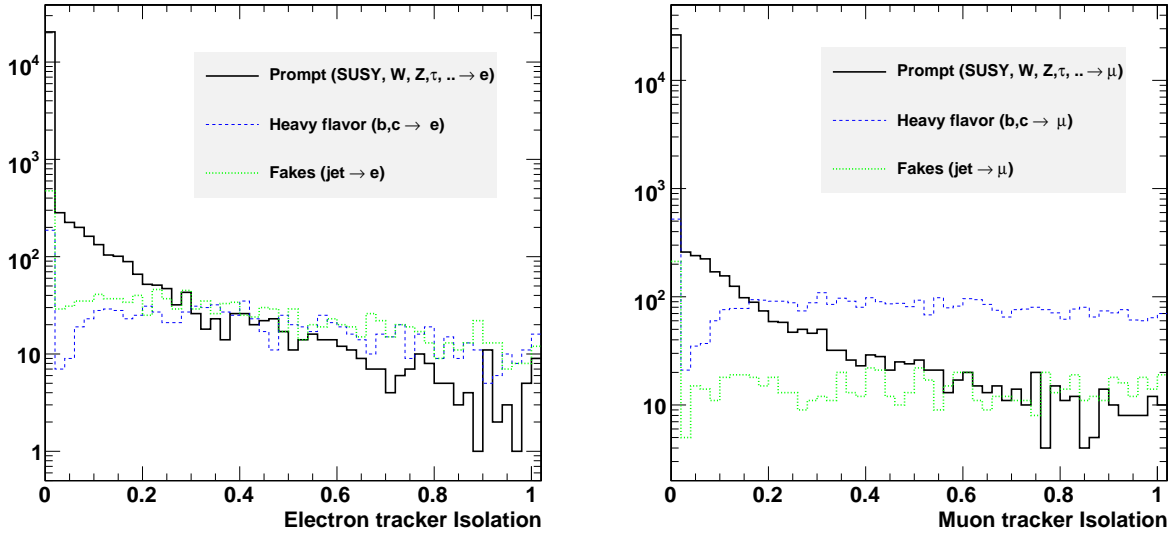


Figure 4.8: *Tracker isolation distributions for electrons (left) and muons (right), in the SUSY (LM1) and $t\bar{t}+jets$ environment. Leptons are distinguished in 3 types : i) Prompt leptons (black), coming from SUSY particles or $W/Z/\tau$ decays, ii) Hadron leptons (blue), coming from decays of heavy flavor hadrons (b, c) and iii) Fake leptons (green) from jets.*

values of the ΔR_{in} (0.01, 0.015, 0.02 and 0.03) have been considered, each for two different values of the ΔR_{out} (0.2 and 0.3), for both electrons and muons isolation. In principle, we expect that a somewhat narrower inner cone should be suitable for including a muon track than an electron

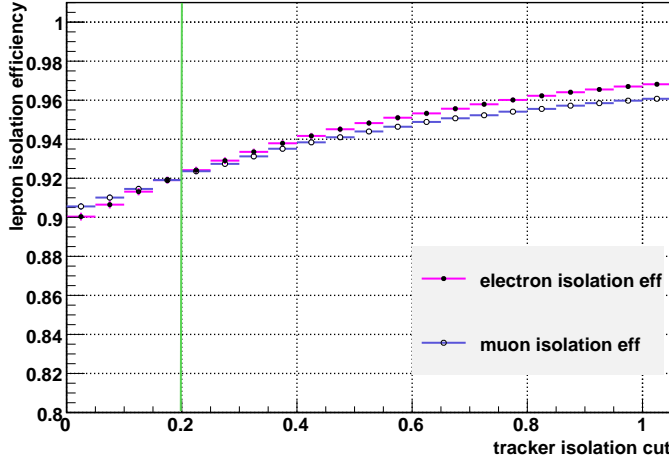


Figure 4.9: *Prompt-lepton isolation efficiency as a function of the tracker isolation cut, for electrons (pink) and muons (blue) superimposed.*

one; however, the choice of the same inner cone for electrons and muons was investigated.

Figure 4.10 and 4.11 shows the isolation efficiencies for prompt electrons and muons versus the rejection over hadron and fake leptons separately, for different values of the isolation cut. Such curves are shown superimposed each corresponding to a different combination of the inner and outer cone sizes. The optimal value of $\Delta R_{\text{out}} = 0.2$ for both electron and muon isolation cones can be noticed immediately. Concerning the inner cone ΔR_{in} , the choice of values in the range $0.01 - 0.03$ does not show to have a significant impact in terms of the lepton efficiencies. A tendency to higher values (~ 0.02) for the optimal electron inner cone and to lower values (~ 0.01) for the case of muons is only slightly visible. Nevertheless, the common choice of $\Delta R_{\text{in}} = 0.015$ can still stand as a good compromise of the two.

It follows from the same plots that the isolation cut at 0.2 accepts primary electrons with 97% efficiency, while rejects $\approx 65\%$ of the fake electrons. For muons, the same isolation requirement accepts primary muons with 96% efficiency and rejects $\approx 93\%$ of the fake muons.

In order to summarize the electron and muon selection (reconstruction, identification and isolation) procedure, and their effect on the actual di-lepton analysis, the opposite-sign and isolated di-electrons or di-muons pairs found among the two highest- p_T leptons of the LM1 susy sample, are selected. Tables 4.2 and 4.3 present the number of di-electron and di-muon events for various lepton-type combinations, as extracted before and after the isolation requirement. The number of events correspond to $\sim 2.5\text{fb}^{-1}$ of integrated luminosity. Overall, the selection retains a good efficiency for the signal di-lepton combinations (prompt-prompt lepton pairs) whereas a significant suppression of di-lepton pairs containing at least one background (hadron or fake) lepton is achieved after the isolation requirement is applied.

4.4. APPLICATION TO DI-LEPTON ANALYSIS

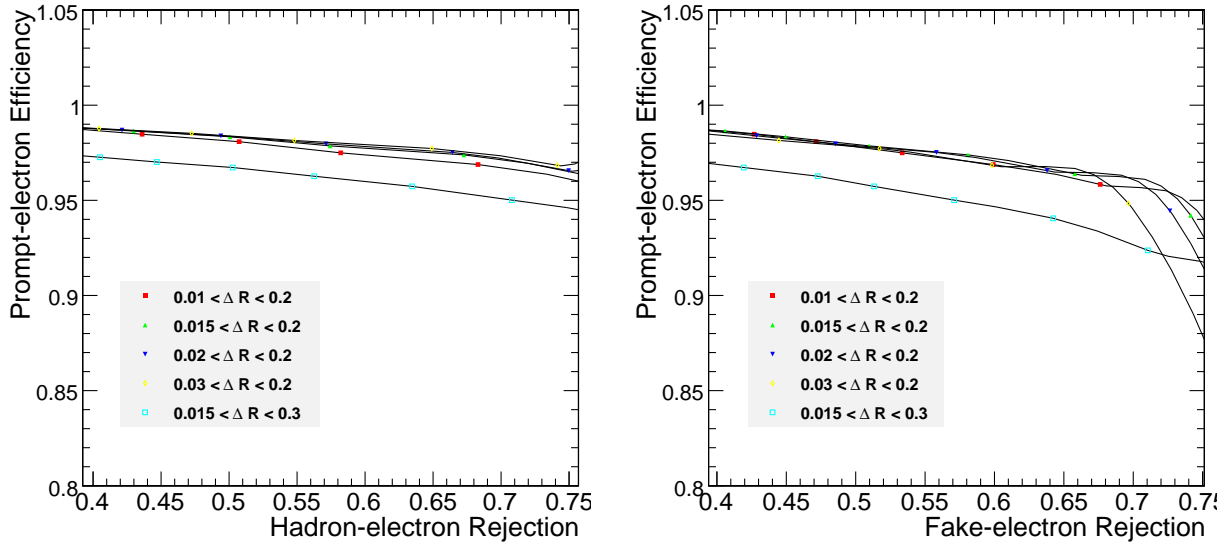


Figure 4.10: Efficiency for selecting primary electrons (left) and muons (right) as a function of the rejection against fakes, for different isolation cone sizes.

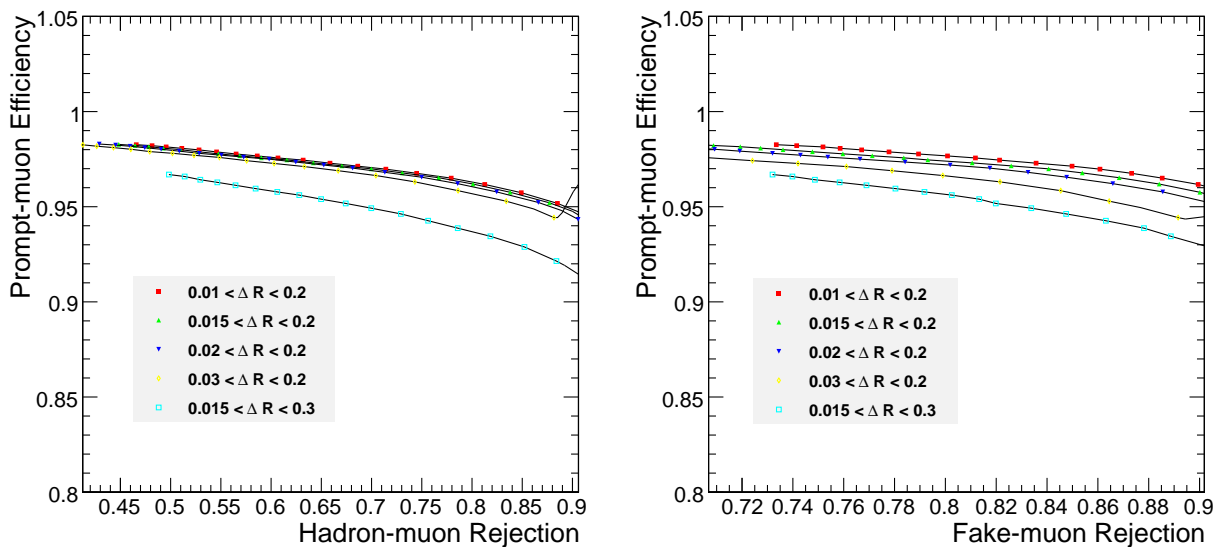


Figure 4.11: Efficiency for selecting primary muons as a function of the rejection against hadron muons (left) and fake muons (right), for different isolation cone sizes.

CHAPTER 4. PHYSICS OBJECTS: RECONSTRUCTION AND SELECTION

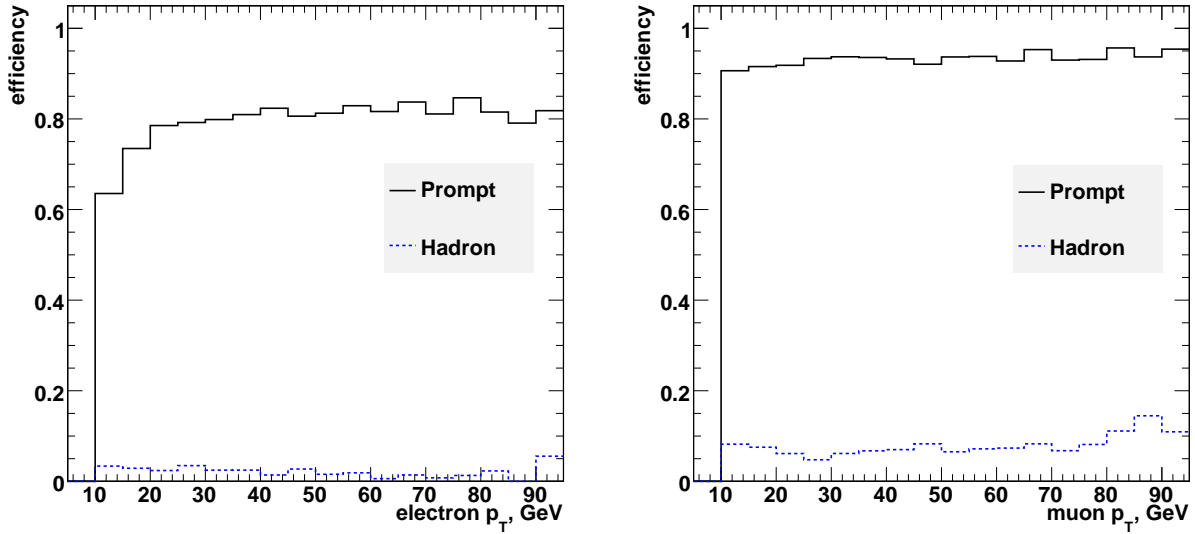


Figure 4.12: Electron (left) and muon (right) efficiency after the isolation requirement imposed, as a function of the generated electron/muon p_T . Leptons are decomposed into “prompt leptons”, coming from a susy, a W/Z or τ particle, and “hadron leptons” arising from the decays of heavy flavor quarks (b or c quarks). The efficiency is defined as the number of generated leptons that matched a reconstructed and isolated lepton divided by all generated electrons.

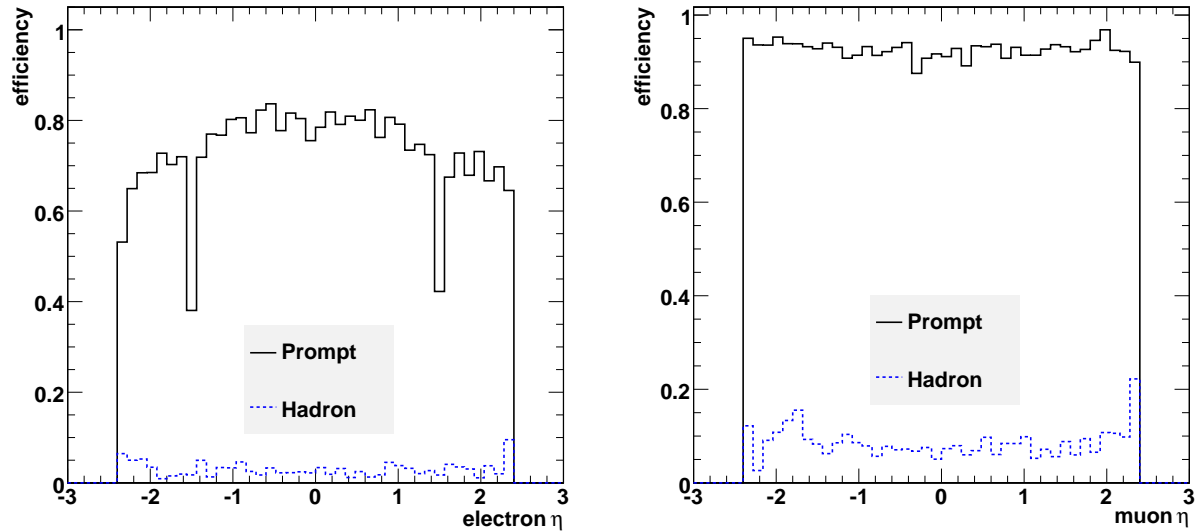


Figure 4.13: Electron (left) and muon (right) efficiency after the isolation requirement imposed, as a function of the generated electron/muon η .

4.4. APPLICATION TO DI-LEPTON ANALYSIS

Table 4.2: *Number of events for combinations of two opposite sign reconstructed electrons, corresponding to 2.5fb^{-1} of integrated luminosity (P: Prompt, H: Hadron, F: Fake).*

Requirement	$e_P^{\pm}e_P^{\mp}$	$e_P^{\pm}e_H^{\mp}$	$e_H^{\pm}e_H^{\mp}$	$e_F^{\pm}e_P^{\mp}$	$e_F^{\pm}e_H^{\mp}$	$e_F^{\pm}e_F^{\mp}$
Reconstruction/selection	2027	75	8	125	8	5
Isolation	2011	20	-	52	2	-

Table 4.3: *Number of events for combinations of two opposite sign reconstructed muons, corresponding to 2.5fb^{-1} of integrated luminosity (P: Prompt, H: Hadron, F: Fake).*

Requirement	$\mu_P^{\pm}\mu_P^{\mp}$	$\mu_P^{\pm}\mu_H^{\mp}$	$\mu_H^{\pm}\mu_H^{\mp}$	$\mu_F^{\pm}\mu_P^{\mp}$	$\mu_F^{\pm}\mu_H^{\mp}$	$\mu_F^{\pm}\mu_F^{\mp}$
Reconstruction/selection	2773	768	337	202	68	37
Isolation	2703	70	4	26	-	-

4.4.3 Jet cleaning and lepton-jet separation

Jets were reconstructed with the iterative cone 0.5 “CaloJet” algorithm [32] and required to have an uncorrected transverse energy $E_T > 15 \text{ GeV}$ and $|\eta| < 3$.

Immediately after the isolation value has been calculated for each lepton, a cleaning stage is performed to check whether the lepton (electron or muon) is also part of a jet. For every non-isolated or isolated lepton, the nearest jet in $\eta - \phi$ space is looked for within a $\Delta R < 0.6$. Three cases are distinguished and checked:

- The lepton is isolated and inside its nearest jet: then the lepton is assumed that fakes the jet. The shared energy-momentum between the lepton and the jet is subtracted from the jet.
- The lepton is part of the nearest jet and it is not isolated: it is the jet assumed that fakes the lepton. The difference between the lepton’s energy-momentum and the shared energy is added to the jet.
- The lepton is not part of the nearest jet and it is also not isolated: the lepton is assumed to be fake and it is fully added to the jet.

The jet clean-up is performed next: the refinement of the reconstructed jet collection is based on the electromagnetic and charged energy fraction of the jet. The charged energy fraction is based

CHAPTER 4. PHYSICS OBJECTS: RECONSTRUCTION AND SELECTION

on the sum of p_T of all tracks associated to the jet and should be > 0.005 . In addition, electron-jet separation is applied in order to veto jets made from electrons. This is done with the following test: for every isolated electron within a $\Delta R(e - \text{jet}) < 0.5$, the ratio of the shared energy between the electron and the jet divided by the energy of the jet, must be below 0.7. The shared energy is calculated by the shared calorimeter towers belonging to the electron and jet objects.

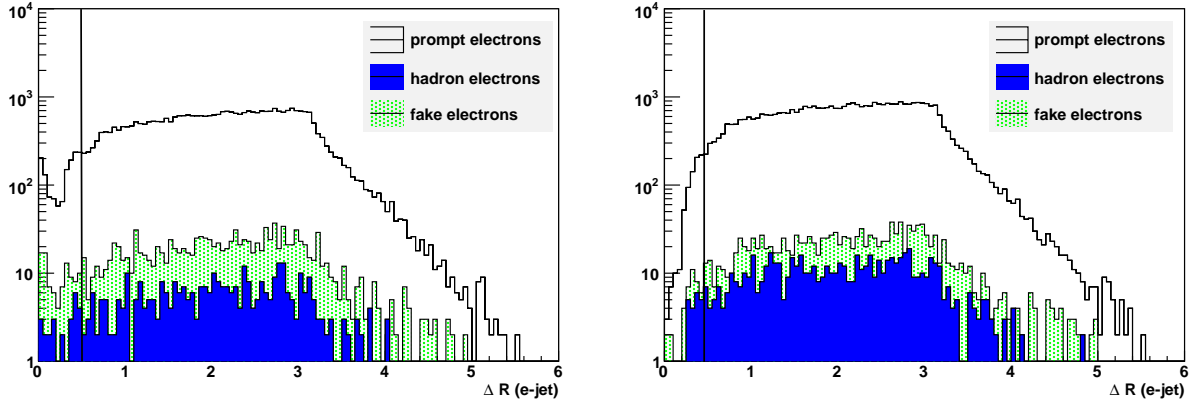


Figure 4.14: Jet - electron separation in $\eta - \phi$ space, for the cases where the electron was tagged as prompt, hadron or fake. Left plot shows the separation before the jet clean-up and right plot after the clean-up has been applied.

The performance of the clean-up of jets has been studied by looking at the ΔR between each jet and its closest isolated electron, for the three cases where the electron was tagged as prompt, hadron or fake separately. The distributions are plotted in figures 4.14 before and after the clean-up is applied. A peak at zero ΔR can be noticed on the plot on the left, coming mainly from prompt electrons faking a jet. This is corrected on the right plot where the fake jets have been identified and removed from the jet collection.

Energy corrections of the reconstructed jets were taken into account using the “MCJet” calibration method³ [33]. This is a particle-level calibration and corrects the energy of the reconstructed jet back to the particle (Generated Jet), taking into account detector effects. The goal of these corrections is to achieve a flat response versus the Jet E_T and η .

4.4.4 The recoil missing E_T

The missing transverse energy in the event E_T is calculated from the recoil of all isolated leptons (electrons or muons) with $p_T^\ell > 10$ GeV and $|\eta^\ell| < 2.4$ and all jets with corrected $E_T^{jet} > 30$ GeV. The transverse components of the momenta of all these objects are summed vectorially to form the transverse components of the missing E_T object,

$$\vec{E}_T = - \sum \vec{p}_T^{jet} - \sum \vec{p}_T^e - \sum \vec{p}_T^\mu \quad (4.5)$$

³Namely, the factorized L2/L3 corrections which have been developed to suit the CSA07 samples

4.4. APPLICATION TO DI-LEPTON ANALYSIS

The jets are required to be separated from electrons as described above. Figure 4.15, left, shows the missing E_T calculated from the calorimeter towers in comparison with the recoil missing E_T , on the right, for di-electron (in color) and di-muon (error bars) events superimposed. The distributions were plotted using a Z to $ee/\mu\mu$ sample, and demonstrate the fact that the recoil MET corrects for the fake missing E_T created in muon events and recovers the dielectron versus dimuon shape, and thus the ratio of events as well. The recoil missing E_T object is subject to systematic uncertainties due to the jet energy scale and will be discussed later.

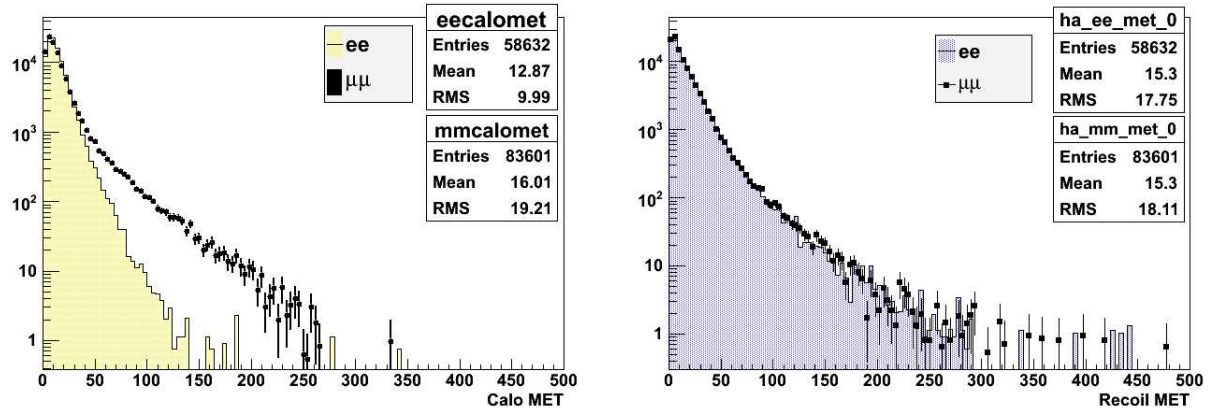


Figure 4.15: Calorimeter missing E_T (left) and recoil missing E_T (right) for dielectron , in color, and dimuon events, in error bars, superimposed. The histograms are normalized to each other.

5

Di-lepton analysis with early data

The analysis presented here is a general-purpose search for the dilepton edge in events which contain (in addition to the two leptons) jets and large missing transverse energy. For a more concrete application of the search but also for the evaluation of systematic uncertainties, we use the mSUGRA “LM1” benchmark point from the CMS Physics TDR [21]. LM1 point is defined by the following five parameters in the mSUGRA ($m_o, m_{1/2}$) plane:

$$m_o = 60\text{GeV}/c^2, \quad m_{1/2} = 250\text{GeV}/c^2, \quad A_o = 0, \quad \tan \beta = 10, \quad \mu > 0 \quad (5.1)$$

5.1 Signal phenomenology and analysis strategy

LM1 is a very favorable point for this analysis: at LM1 the inclusive production cross section is 43.5 pb – and comes mainly from the production of $\tilde{q}\tilde{g}$ (38%), $\tilde{q}\tilde{q}$ (45%) and $\tilde{g}\tilde{g}$ (6.8%) pairs. One of the major characteristics of LM1 is that $m_{\tilde{g}} > m_{\tilde{q}}$ which implies that the \tilde{g} ’s decay in $q\tilde{q}$ pairs; the contribution of the $\tilde{g}\tilde{g}$ pair production to the total squark/gluino production is small compared to $\tilde{q}\tilde{q}/\tilde{g}\tilde{g}$ production. Furthermore, at LM1 $m_{\tilde{\chi}_2^0} > m_{\tilde{\ell}}$ and $m_{\tilde{\chi}_1^\pm} > m_{\tilde{\nu}}$ and hence both the $\tilde{\chi}_2^0$ as well as the $\tilde{\chi}_1^\pm$ are allowed to decay leptonically leading to a number of leptons in the final states. Tables 5.1 and 6.3 summarize the mass spectrum and the production cross sections of SUSY final states at LM1 respectively.

Table 5.1: Supersymmetric particle masses at LM1 benchmark point calculated with PYTHIA [34] interfaced with SOFTSUSY [GeV] [35].

gluino /	\tilde{g}	\tilde{d}_L	\tilde{d}_R	\tilde{u}_L	\tilde{u}_R	\tilde{b}_2	\tilde{b}_1	\tilde{t}_2	\tilde{t}_1
squarks :	603.5	559.6	536.1	552.1	540.1	535.6	510.1	580.3	407.3
sleptons :	\tilde{e}_L	\tilde{e}_R	$\tilde{\tau}_2$	$\tilde{\tau}_1$	$\tilde{\nu}_{eL}$	$\tilde{\nu}_{\tau L}$	higgses :	H^\pm	A
	186.4	119.9	190.3	110.8	167.4	166.9		380.8	371.8
gauginos :	$\tilde{\chi}_4^0$	$\tilde{\chi}_3^0$	$\tilde{\chi}_2^0$	$\tilde{\chi}_1^0$	$\tilde{\chi}_2^\pm$	$\tilde{\chi}_1^\pm$	higgses :	H	h
	362.9	344.1	177.9	96.4	360.2	178.5		372.3	109.3

The SUSY dilepton signature under study arises from the two-body decay of the $\tilde{\chi}_2^0$, $\tilde{\chi}_2^0 \rightarrow \tilde{\ell}^\pm \ell^\mp \rightarrow \ell^\pm \ell^\mp \tilde{\chi}_1^0$ with a BR at 12.7%. Other (SUSY) sources of leptons are also significant and consist in

Table 5.2: Production cross sections of supersymmetric final states at LM1 calculated with PYTHIA interfaced with SOFTSUSY [pb].

$\sigma(\text{SUSY})$	$\sigma(\tilde{g}\tilde{g})$	$\sigma(\tilde{g}\tilde{q}_L)$	$\sigma(\tilde{g}\tilde{q}_R)$	$\sigma(\tilde{q}_L\tilde{q}_L)$	$\sigma(\tilde{q}_L\tilde{q}_R)$	$\sigma(\tilde{q}_R\tilde{q}_R)$	$\sigma(\tilde{b}\tilde{q}_R)$	$\sigma(\tilde{b}\tilde{g})$	$\sigma(\tilde{b}\tilde{b})$
43.5	2.9	8.0	8.5	6.2	6.6	6.8	0.45	0.19	0.24

the decays of the lightest chargino, $\tilde{\chi}_1^\pm \rightarrow \tilde{\nu}\ell$ with a BR at 34.8%, and the decays of W 's and τ 's abundantly produced in gaugino decays.

The leptonic signature from the $\tilde{\chi}_2^0$ decays can be identified with the characteristic sharp edge in the dilepton mass distribution which is due to the undetectable $\tilde{\chi}_1^0$. The important decay chains at LM1 that can be used for such an analysis, together with their branching ratios, are listed below:

$$\tilde{q}_L \xrightarrow{31\%} \tilde{\chi}_2^0 q \xrightarrow{12.7\%} \tilde{\ell}_R^\pm \ell^\mp q \xrightarrow{100\%} \ell^\pm \ell^\mp \tilde{\chi}_1^0 q \quad (5.2)$$

$$\tilde{g} \xrightarrow{22.4\%} \tilde{q}_L q \xrightarrow{31\%} \tilde{\chi}_2^0 q \xrightarrow{12.7\%} \tilde{\ell}_R^\pm \ell^\mp q \xrightarrow{100\%} \ell^\pm \ell^\mp \tilde{\chi}_1^0 q \quad (5.3)$$

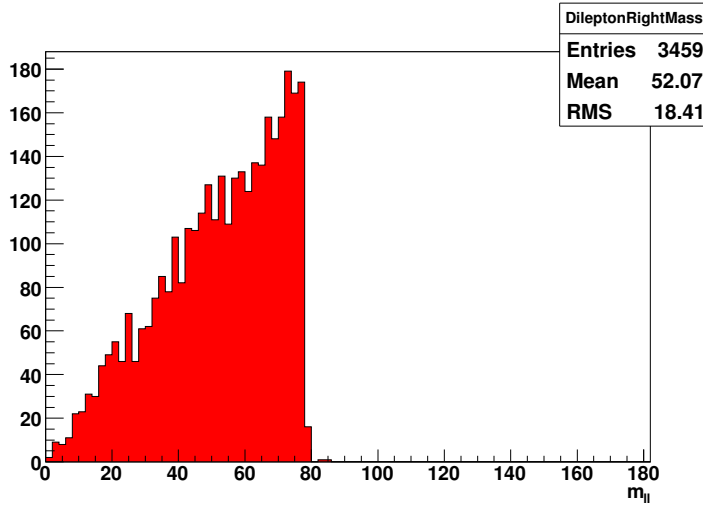


Figure 5.1: Invariant mass of the two opposite-sign same-flavor leptons arising from the two-body decay of the $\tilde{\chi}_2^0$. The distribution shows a characteristic sharp edge with an endpoint value equal to 78.15 GeV.

The basic signature is that of large missing energy (E_T), hard jets and certainly two opposite-sign leptons. This signature has large backgrounds from the usual “high- p_T ” SM processes of $t\bar{t}$, diboson (WW, WZ and Z) and associated production of W/Z bosons and jets. The strategy adopted here is the use of different-flavor ($e\mu$) lepton combinations to estimate the background to the ee and $\mu\mu$ combinations. This is found to work well for all the backgrounds that are flavor-symmetric, whereas a flavor asymmetry is expected in dileptons where one or two of the leptons are either fake or come from heavy-flavor (b/c) decays. Luckily, these backgrounds are much smaller than

5.2. TRIGGER SELECTION

those from the “high- p_T ” SM processes, and their effect on the observation and extraction of the dilepton edge is small.

The edge is extracted from an unbinned maximum-likelihood fit to the invariant mass distribution of the two leptons (ee and $\mu\mu$ separately) with components describing the background and a simple SUSY model. It is found that the position of the edge is quite robust. The methods employed by the analysis are “data-driven” in the sense that they can all be employed with real data – even if for the sake of brevity in the analysis short-cuts were employed. As an example, the ratio of electron to muon reconstruction and identification efficiencies in the real data can be easily determined from Z leptonic decays, where one lepton (tag) satisfies strict identification criteria and the second lepton (probe) has only loose identification criteria applied. Applying the tight identification criteria on the second lepton as well and counting the number of Z candidates with the loose and tight criteria results in a direct measurement of the lepton efficiency from the data. This has already been demonstrated by CMS for both electrons and muons: the “measured” efficiencies are in excellent agreement with the actual efficiencies obtained from using the Monte Carlo (generator) information. Armed with this result, this analysis has not attempted to reproduce this measurement of the efficiency, but rather assumes that such a measurement will be available at the time the analysis will be carried out – and thus the Monte-Carlo efficiency ratio was used.

The data samples

In the CSA07 production, the data has been split up in various Primary Datasets (PD) depending on the Physics content. They are further distinguished in Signals, which refer to specific Physics groups requirements, as well as SM backgrounds which have been mixed up in big datasets (colloquially referred to as “soups”). The latter type of data consists of three Soups, namely the Chowder, containing the ALPGEN $t\bar{t}, W, Z + N_{jets}$ processes, the Stew, containing the lepton enriched QCD, bottomonia and charmonia, and the Gumbo Soup, containing the higher \hat{p}_T QCD bins, photon + Jets as well as Minimum Bias events. The signal samples are only available with the $100 pb^{-1}$ calibration scenario, while for the SM soups all luminosity scenarios have been generated.

Subsets of the SM background soups have also been designed, the so-called skims, which were formed with running over a PD and selecting only the interesting events. In the context of the CMS SUSY group, there have been used the skims denoted as SUSYBSMJetMET_HLT that include the events satisfying the HLT requirement of the logical “or” of all the hadronic triggers. SM backgrounds that have been used from such skims include the $t\bar{t} + N_{jets}$ and the $W/Z + N_{jets}$ with $\hat{p}_T < 300$ GeV. For the W/Z processes, the $\hat{p}_T > 300$ bins were part of the signals samples. The same goes for the diboson samples. Table 5.3 summarizes the data samples used for the di-lepton analysis.

5.2 Trigger selection

Tables 5.4 and 5.5 summarize the major trigger paths that were used in the CSA07 Trigger Menu (with CMSSW_1_6_X), their technical names and their parameters (trigger thresholds) and finally the efficiencies to the SUSY signal.

CHAPTER 5. DI-LEPTON ANALYSIS WITH EARLY DATA

Table 5.3: *Data samples used throughout the analysis, their technical name, skimming status and number of events processed; they were officially produced during CSA07.*

Physics process	Dataset details	Soup	Events
SUSY LM1	LM1_sftsdkpyt	Signal	120624
$t\bar{t} + N_{jets}, N = 1, \dots 4$	CSA07JetMET / ReReco-100pb	Chowder	1651598
$Z + N_{jets}, N = 1, \dots 5$ $p_T(Z) < 300 \text{ GeV}$	CSA07JetMET / ReReco-100pb	Chowder	1651598
$W + N_{jets}, N = 1, \dots 5$ $p_T(W) < 300 \text{ GeV}$	CSA07JetMET / ReReco-100pb	Chowder	1651598
QCD, photon + Jets Minimum bias	CSA07JetMET / Re-Reco-100pb	Gumbo	6142602
lepton enriched QCD, bottomonia/charmonia	CSA07JetMET / ReReco-startup	Stew	1169128
$Z + N_{jets}, N = 1, \dots 5$ $300 < p_T(Z) < 3200 \text{ GeV}$	z_ptzX_alpgen	Signal	299147
$W + N_{jets}, N = 1, \dots 5$ $300 < p_T(W) < 3200 \text{ GeV}$	w_ptwX_alpgen	Signal	462962
Dibosons ($W/Z \rightarrow \text{Inclusive}$)	WW_incl / WZ_incl / ZZ_incl	Signal	1249665
tW (single top)	tW_inclusive	Signal	438791

As will be seen later, the signature employed includes multiple jets, a large missing transverse energy (RecoilMET) and two leptons. In determining the optimal trigger strategy, and in practical terms “trigger path”, it is imperative to compare the various possibilities with respect to the final analysis cuts¹. This can be estimated by the efficiency numbers ϵ_1 and ϵ_2 which are shown on the tables above. The efficiency ϵ_1 for a given trigger path, is defined as the ratio of number of events that are found with the corresponding trigger bit on, divided by the number of all events, while the efficiency ϵ_2 is defined as the ratio of number of events that pass the analysis cuts and found with the corresponding trigger bit on, divided by the number of all events that pass the final analysis cuts.

The hadronic paths, and particularly the ones related with MET, appear to be more efficient in selecting SUSY events than the corresponding leptonic triggers. This is found to arise because of two reasons. The first issue is the recovery of low- p_T SUSY leptons below the leptonic trigger thresholds. This is important because the leptons from the SUSY signal are not very high in transverse momentum, and thus the lepton p_T to be applied should be as low as possible. The second reason is the unavoidable lepton selection inefficiency present in the leptonic trigger paths. Both issues are illustrated with the plots in figures 5.2 where the leptonic and hadronic MET paths efficiencies are plotted as a function of the two highest- p_T electrons and muons respectively. The

¹Assuming that the offline selection cuts are not looser than the online selection criteria, the Trigger path to be applied in the di-lepton analysis should be chosen so that it has the highest efficiency to the SUSY di-lepton final states selected after all cuts.

5.2. TRIGGER SELECTION

Table 5.4: *L1/HLT efficiencies for the leptonic related trigger streams applied to the LM1 SUSY events.*

HLT path	Thres. (GeV)	Technical Name	ϵ_1	ϵ_2
single μ	11	HLT1MuonIso	12.9%	59.1%
single μ (rel.)	16	HLT1MuonNonIso	14.4%	60.1%
double μ	(3, 3)	CandHLT2MuonIso	5.2%	42.8%
double μ (rel.)	(3, 3)	HLT2MuonNonIso	6.2%	44.8%
single e	15	HLT1Electron	10.3%	41.8%
single e (rel.)	17	HLT1ElectronRelaxed	9.7%	40.5%
double e	10	HLT2Electron	2.2%	26.5%
double e (rel.)	12	HLT2ElectronRelaxed	2.9%	29.0%
e + μ	(8, 7)	HLTXElectronMuon	1.8%	14.8%
e + μ (rel.)	(10, 10)	HLTXElectronMuonRelaxed	2.4%	19.0%

Table 5.5: *L1/HLT efficiencies for the JetMET related trigger streams applied to the LM1 SUSY events.*

HLT path	Thres. (GeV)	Technical Name	ϵ_1	ϵ_2
single-jet	200	HLT1Jet	79.6%	89.6%
double-jet	150	HLT2Jet	60.0%	72.4%
triple-jet	85	HLT3Jet	50.3%	77.5%
quad-jet	60	HLT4Jet	41.1%	71.0%
MET	65	HLT1MET	89.5%	98.1%
Acopl. double-jet	125	HLT2JetAco	47.8%	68.7%
single-jet + MET	(180, 60)	HLT1Jet1MET	80.7%	92.2%
double-jet + MET	(125, 60)	HLT2Jet1MET	67.2%	84.4%
triple-jet + MET	(60, 60)	HLT3Jet1MET	64.0%	90.4%
quad-jet + MET	(35, 60)	HLT4Jet1MET	63.8%	92.1%
HT + MET	(350, 65)	HLT1MET1HT	87.1%	98.4%
Sum ET	120	CandHLT1SumMET	95.8%	100%
SUSY 2-jet + MET	(80, 20, 60)	HLTS2jet1METNV	72.1%	85.1%
Acopl. double-jet + MET	(60, 60)	HLTS2jet1METAco	70.9%	89.4%
SUSY Acopl. single-jet + MET	(60, 70)	CandHLTSjet1-MET1Aco	56.3%	67.1%
SUSY Acopl. double-jet + MET	(50, 50, 70)	CandHLTSjet2-MET1Aco	72.5%	90.3%
SUSY Acopl. double-jet	(40, 40, 70)	CandHLTS2jetAco	66.0%	81.9%

efficiencies versus the second lepton p_T threshold are calculated with respect to events with at least two isolated leptons. In both cases, the leptons are matched to prompt leptons, i.e. hadron and fake leptons are excluded. The efficiency is plotted for the hadronic MET and HT+MET paths, as well as for the single-electron, single-muon and double-electron, double-muon paths. The total leptonic path curve is defined as the union of all four leptonic triggers (and is also displayed as the red line).

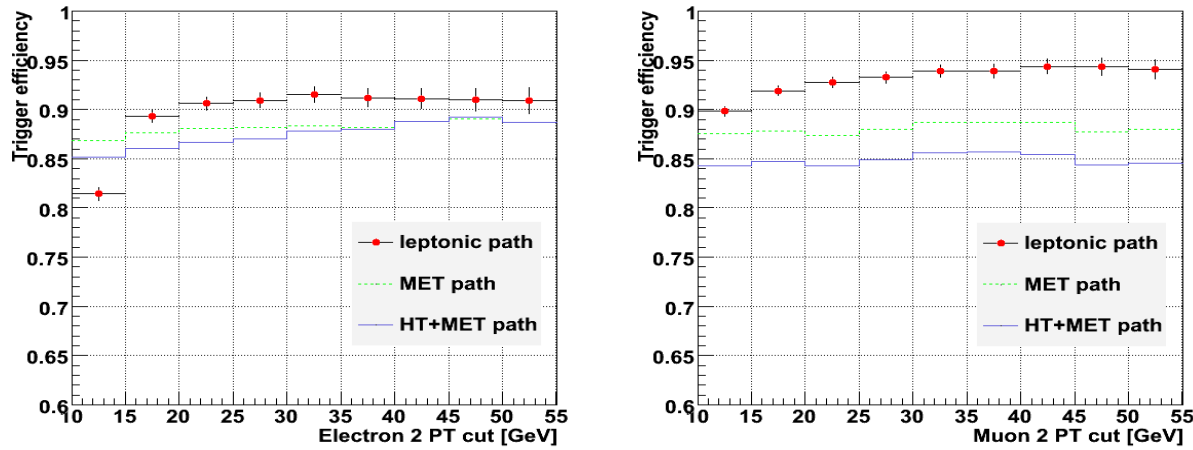


Figure 5.2: Hadronic versus leptonic trigger paths efficiencies as a function of the second electron p_T threshold (left) and the second muon p_T threshold (right).

The efficiency of MET-related paths in selecting events with leptons is essentially independent of the lepton p_T cuts chosen offline. A small correlation is observed between the electron p_T and the MET; this is probably due to the electron contributing to the MET. On the other hand, the leptonic trigger paths reach the plateau of their efficiency curves for offline p_T leptons above 20 GeV. Even in this p_T region, however, the efficiencies of the MET paths are higher because they do not include the efficiency loss at the plateau (i.e. the online lepton selection inefficiency). This picture gets more pronounced when one adds also the Jet and MET offline cuts in the event-selection criteria. For example, figure 5.3 shows the efficiencies of the different trigger paths for events with at least two isolated leptons with $p_T > 10$ GeV, as a function of the offline MET cut. The hadronic MET paths become fully efficient above the online MET threshold (65 GeV), to be compared to the leptonic paths which (as expected) remain constant in efficiency versus the MET cut (and the value indicates the online selection inefficiency).

Next, figures 5.4 show the efficiencies of the trigger paths as a function of the second highest- p_T electrons and muons, after applying an offline MET (RecoilMET) cut at 200 GeV. This value is chosen as the value at which the online MET requirement is fully efficient (actually reaches its maximum value – the corresponding plateau). It can be shown that with respect to the final analysis cuts, the MET paths are about 3% higher in efficiency than the leptonic triggers (averaged for electrons and muons above 20 GeV; the difference is larger for a 10 GeV cut).

The trigger path chosen for this analysis is the HT+MET path which has an efficiency at 98% with respect to the offline cuts. Compared to the MET-only path, the HT+MET path, which is

5.2. TRIGGER SELECTION

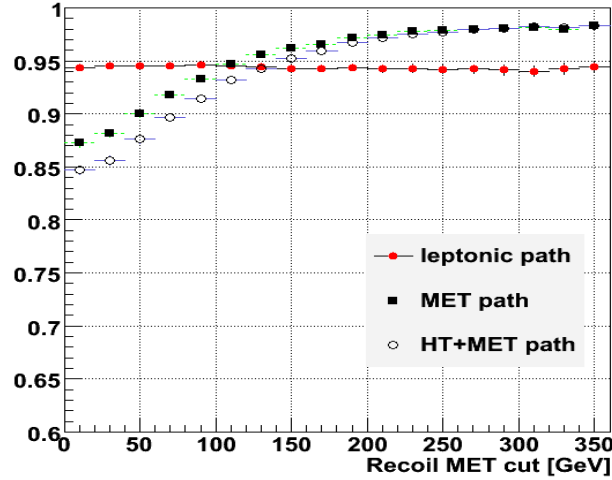


Figure 5.3: Hadronic versus leptonic trigger paths efficiencies, with respect to events with at least 2 isolated leptons with $p_T > 10$ GeV, as a function of the Recoil MET cut. MET trigger paths become fully efficient above the online MET threshold (65 GeV).

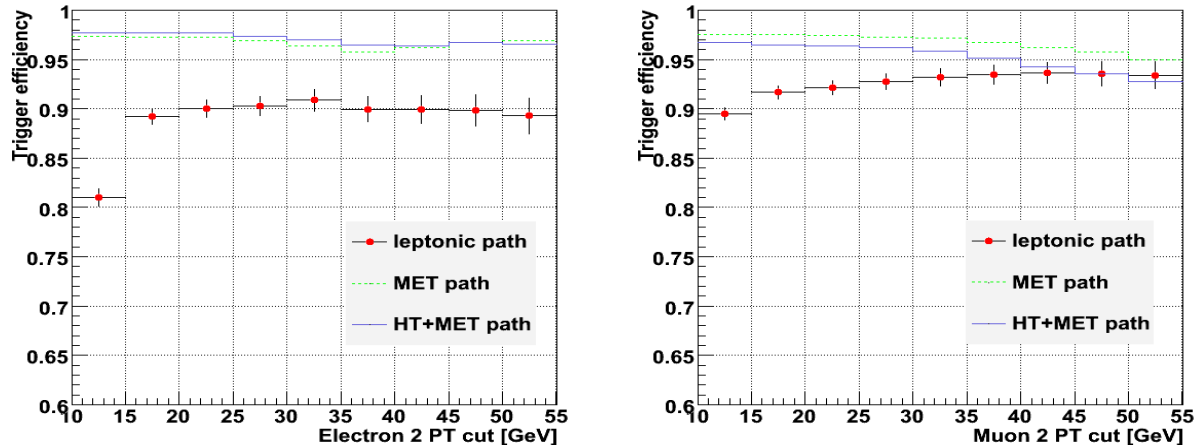


Figure 5.4: Hadronic versus leptonic trigger paths efficiencies as a function of the second electron p_T threshold (left) and the second muon p_T threshold (right). An offline MET cut at 200 GeV has been applied.

based also on jet information, is preferred as a more robust choice, especially for a 1 fb^{-1} analysis.

5.3 Observability of supersymmetric di-lepton final states

The SUSY cross section at LHC is dominated by the production of squarks/gluinos pairs which decay sequentially in q, g , charginos, neutralinos, W, Z and higgses up to the Lightest Supersymmetric Particle (LSP), as follows from the assumption of an R-parity conserving mSUGRA scenario. The stable LSP is weakly interacting and escapes detection giving rise to large missing E_T due to its large mass. In each step in the squark/gluino cascade decay there is a standard model particle produced which gives rise to either a jet or a charged (and isolated) lepton in the event. In general, jets are produced in the initial states of the cascades through the strong interaction, where the differences in masses of the supersymmetric particles are larger. On the other hand, leptons are produced in the final states of the cascades and they loose much of the energy of the initially decayed sparticle. Therefore, the jet spectrum is characterised on average by higher energies than that of the lepton spectrum.

The supersymmetric signature under study is characterized by two Opposite Sign (OS) leptons + jets + E_T^{miss} . Next the full topology of SUSY events is exploited in order to eliminate the Standard Model background over the SUSY signal.

5.3.1 Signal versus standard model backgrounds

Standard Model background processes leading to missing transverse energy, hard jets and isolated leptons constitute a background to the SUSY signal. The missing transverse energy in this case is coming from high- p_T neutrinos and high- p_T particles outside the detector acceptance. Such Standard Model processes are: $t\bar{t}$ (inclusive), $Z + \text{jets}$ with $Z \rightarrow ee/\mu\mu/\tau\tau$, $W + \text{jets}$ with W decaying leptonically and a second fake lepton, $WW/WZ/ZZ + \text{jets}$ as well as QCD processes. The main characteristics that discriminate the SUSY events from the SM processes are their large missing E_T due to the presence of $\tilde{\chi}_1^0$ in the final states, and the high multiplicity of jets.

Most of the SM processes used in the analysis were produced with the ALPGEN generator [36] following the official summer07 CMS production. ALPGEN is a matrix-element MC generator dedicated to the production of multi-parton hard processes in hadronic collisions. It has been used widely for the calculation of the parton-level matrix elements of the processes, interfaced with PYTHIA to handle the partonic evolution (parton shower). The cross section evaluation of the SM processes was provided by ALPGEN depending on the input parton multiplicity, the PDF parameterization and factorization scale, as well as a set of preselected kinematic configurations.

We next compare the event characteristics of the SUSY sample with the corresponding event characteristics of the SM background samples. In all cases, the observables are only compared in shape, i.e. the corresponding distributions are normalized to one. Fig. 5.5 shows the p_T distribution of the two highest- p_T leptons for the SUSY and SM processes superimposed. The average lepton p_T 's for the SUSY and SM samples are quite close to each other as expected, and are thus not indicated for signal discrimination.

In fig.5.6 the jet multiplicity is plotted for the SUSY and SM samples defined as the the number of jets with $E_T > 30$ GeV produced per event. The average jet multiplicity in supersymmetric events is comparable with the one from the $t\bar{t}$ background (~ 3.2). It should be noticed however that the

5.3. OBSERVABILITY OF SUPERSYMMETRIC DI-LEPTON FINAL STATES

Table 5.6: *ALPGEN parameters used in the CSA07 production of SM processes and their cross-sections (in pb). The PDF was set to CTEQ5L ($\alpha_s = 0.127$) and the factorization scale is $\sqrt{\sum (m_V)^2 + \sum (p_{T,photons}^2 + p_{T,jet}^2)}$. For each sample the last jet multiplicity bin is generated with inclusive parton-shower matching.*

Process	Kinematic configuration	x-section (pb)					
		+0jets	+1jets	+2jets	+3jets	+4jets	+5jets
tt + Jets	$p_T^j > 70 \text{ GeV}$ $ \eta^j < 5$ $\Delta R_{jj} > 0.7$	334.5	95.4	18.2	3.2	0.8	-
Z + jets $\hat{p}_T < 300 \text{ GeV}$	$p_T^j > 20 \text{ GeV}$ $ \eta^j < 5$ $\Delta R_{jj} > 0.7$	4400	970	298	81	18.3	13.8
Z + jets $\hat{p}_T > 300 \text{ GeV}$	$p_T^j > 20 \text{ GeV}$ $ \eta^j < 5$ $\Delta R_{jj} > 0.7$	-	0.36	0.55	0.40	0.20	0.46
W + jets $\hat{p}_T < 300 \text{ GeV}$	$p_T^j > 20 \text{ GeV}$ $ \eta^j < 5$ $\Delta R_{jj} > 0.7$	45300	9496	2765	695	161.7	123.9
W + jets $\hat{p}_T > 300 \text{ GeV}$	$p_T^j > 20 \text{ GeV}$ $ \eta^j < 5$ $\Delta R_{jj} > 0.7$	-	2.93	4.07	3.10	1.58	3.09

two samples come from two different MC generators (PYTHIA and ALPGEN for the SUSY and $t\bar{t}$ samples respectively), and the result is biased towards a higher jet multiplicity prediction for the standard model sample case. Nevertheless, a discriminating power of this observable is expected to show up when also the “two-lepton” requirement is applied on the analysis. We note that in SUSY events there is always at least 1 hard jet produced per event. Jets were then ordered in descending order in E_T . The E_T distribution of the two hardest jets is presented in figures 5.7 where we can notice that the average E_T of the leading jet is almost 200 GeV higher for SUSY events than for the standard model samples. The recoil missing E_T distribution is plotted in fig 5.6 (right) for the SUSY and total standard model background processes before any analysis requirement is applied. As can be seen, this variable at the SUSY LM1 events is on average ~ 200 GeV higher than in the standard model processes.

5.3.2 Cuts optimization

The optimization method chosen in order to eliminate the SM background processes in favor of the di-lepton SUSY signal uses the criteria of the signal-to-background ratio (S/B) and significance ($S/\sqrt{S+B}$). These quantities are studied as a function of several cut variables, such as the Jet multiplicity and the E_T of the hardest Jets, and are finally used to define regions of cut values. However, one should keep in mind that the leptonic analysis under study assumes the earlier discovery of supersymmetry , most likely from the inclusive (jet plus missing energy) channels, and

CHAPTER 5. DI-LEPTON ANALYSIS WITH EARLY DATA

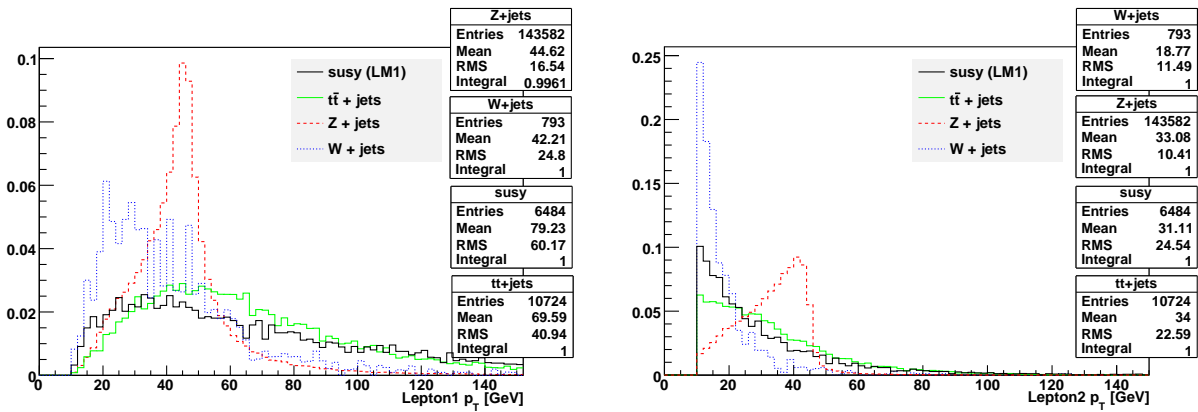


Figure 5.5: Two highest leptons p_T distributions in supersymmetric events (in black) and the major standard model backgrounds ($t\bar{t} + \text{jets}$, $W/Z + \text{jets}$). The distributions are normalized to one.

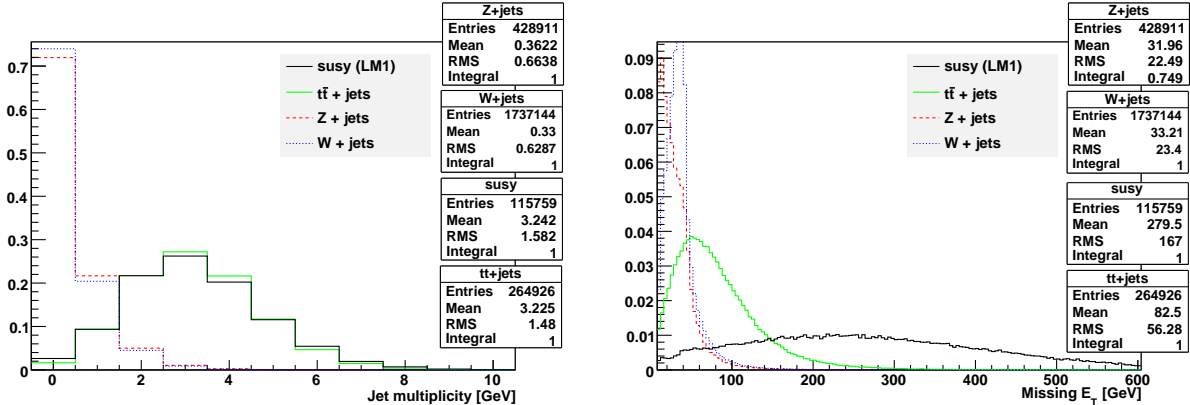


Figure 5.6: Jet multiplicity (left) and missing E_T (right) distributions in supersymmetric events (in black) and the major standard model backgrounds ($t\bar{t} + \text{jets}$, $W/Z + \text{jets}$).

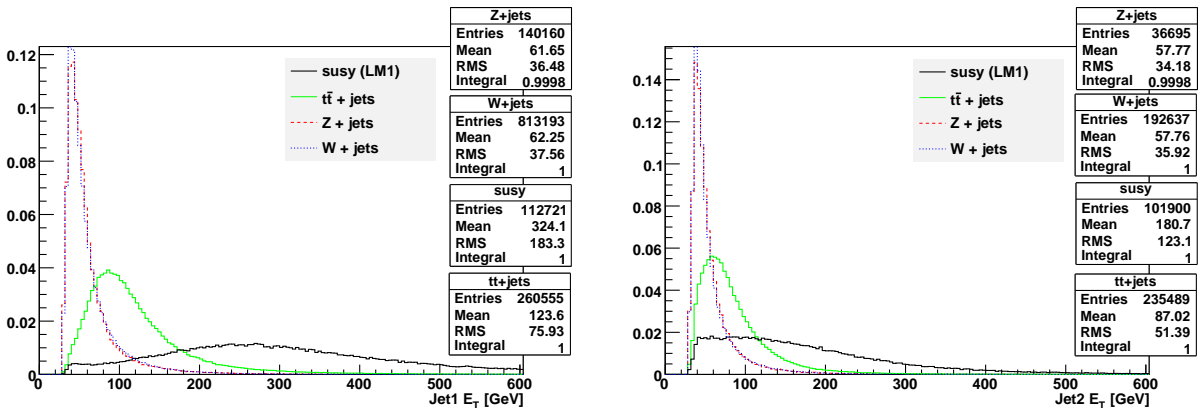


Figure 5.7: Two highest jets E_T distributions in supersymmetric events (in black) and the major standard model backgrounds ($t\bar{t} + \text{jets}$, $W/Z + \text{jets}$).

5.3. OBSERVABILITY OF SUPERSYMMETRIC DI-LEPTON FINAL STATES

is targeting in the best extraction of other SUSY mass parameters and constraints. It is therefore more desirable to look for a reasonable set of cut values that will allow mass measurements, rather than the best optimization of the significance level.

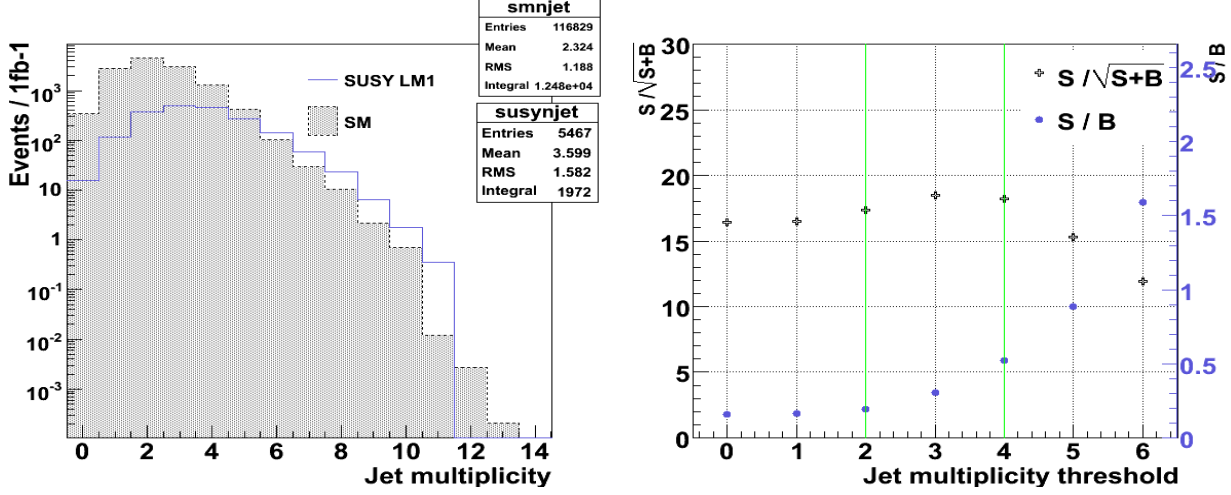


Figure 5.8: Left: Jet multiplicity in the LM1 SUSY (blue) and total SM background (grey) superimposed – jets are required to have $E_T^{cor} > 30$ GeV. Right: Significance and S/B as a function of the jet multiplicity cut value.

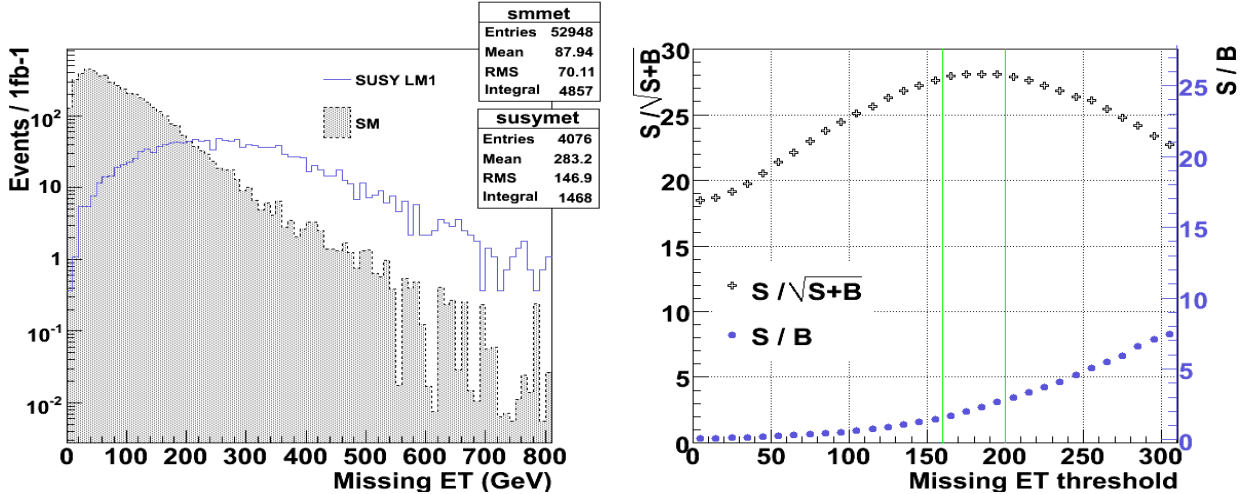


Figure 5.9: Left: Missing E_T distribution in the LM1 SUSY (blue) and total SM background (grey) superimposed. Right: Significance and S/B as a function of the missing E_T threshold.

During the optimization procedure, the SM processes are summed according to their cross-section and total distributions for all background contributions are considered. A preselection on the signal plus SM background event samples has been applied, consisting of the requirement of the HLT path which was chosen to be the HT+MET, as well as the requirement of at least two opposite-sign same-flavor and isolated leptons with $p_T^\ell > 10$ GeV and $|\eta^\ell| < 2.4$. Following the preselection, we look at the jet multiplicity variable which is shown in figure 5.8. The significance function is maximized for a jet multiplicity cut region [2,4], with $E_T^{jet} > 30$ GeV. We choose to cut at 3

jets with the argument that it must suppress significant fraction of the background but not reject major fraction of signal statistics.

Applying the jet multiplicity requirement, we next looked at the E_T of the three leading jets and the missing E_T through an iterative process of studying the effectiveness of their cut when each of them is placed last. Table 5.7 shows the $S/\sqrt{S+B}$ and S/B (in parenthesis) values obtained for a region [100, 150] GeV in E_T^{j1} cut values and a region [160, 200] GeV in missing E_T , chosen as the most favorable ones.

Table 5.7: $S/\sqrt{S+B}$ and S/B (in parenthesis) values obtained for a region [100, 150] GeV in E_T^{j1} cut values and a region [160, 200] GeV in missing E_T .

E_T^{j1} cut	$E_T^{j2} > 80$	$\cancel{E}_T > 160$	$\cancel{E}_T > 180$	$\cancel{E}_T > 200$
$E_T^{j1} > 100$ GeV	20.2 (0.5)	27.3 (2.4)	27.3 (3.1)	27.0 (3.8)
$E_T^{j1} > 120$ GeV	20.5 (0.5)	27.4 (2.5)	27.3 (3.2)	26.9 (3.9)
$E_T^{j1} > 150$ GeV	21.1 (0.6)	27.1 (2.7)	27.0 (3.4)	26.6 (4.1)

The complete set of requirements imposed in the analysis is:

1. At least 2 Opposite Sign (OS) and isolated leptons (e^+e^- or $\mu^+\mu^-$) with $p_T^\ell > 10$ GeV and $|\eta^\ell| < 2.4$.
2. At least 3 jets with $E_T^{jet} > 30$ GeV and $|\eta^{jet}| < 3$.
3. Two hardest jets cut: $E_T^{j1} > 120$ GeV and $E_T^{j2} > 80$ GeV.
4. Missing E_T cut: $E_T^{miss} > 200$ GeV.

5.4 Dilepton mass composition and background measurement

The two OS leptons in signal events arise from the decays of the $\tilde{\chi}_2^0$ and only e^+e^- or $\mu^+\mu^-$ pairs are considered. The “dilepton background” refers to the sum of all sources of two OSSF leptons which are present either in supersymmetric events and do not originate from the $\tilde{\chi}_2^0$ or in SM processes ($t\bar{t}$, decays of the heavy bosons W/Z, heavy flavors and QCD).

When selecting the two highest- p_T leptons in the inclusive SUSY sample, contributions from leptons coming from internal SUSY background sources appear with significant fraction. Such uncorrelated leptons may originate from events with at least one lepton coming from the τ -lepton, the W boson or the leptonic decays of the $\tilde{\chi}_1^\pm$. The first type of leptons are produced mainly in

5.4. DILEPTON MASS COMPOSITION AND BACKGROUND MEASUREMENT

Table 5.8: *Number of events expected for 1fb^{-1} of integrated luminosity for the SUSY signal at LM1 and the major SM backgrounds.*

Process	cross section	$\mathbf{N}(ee/\mu\mu)$	$\mathbf{N}(e\mu)$
<hr/>			
SUSY LM1	43.5 pb	699	211
$t\bar{t} + \text{Jets}$	452.1 pb	98	92
$Z + \text{Jets}$	5.78×10^3 pb	28	3
$W + \text{Jets}$	58.17×10^3 pb	3.4	2
$\text{Dibosons} + \text{Jets}$	179 pb	1.3	1
tW (Single top)	62.5 pb	0.4	0.7
QCD (Gumbo/Stew)		1	1

the decays $\tilde{\chi}_2^0 \rightarrow \tilde{\tau}_1 \tau \rightarrow \tau \tau \tilde{\chi}_1^0$ or $\tilde{\chi}_1^\pm \rightarrow \tilde{\tau} \nu_\tau$. The latter type come from the following sources: W' s from t -quarks coming from the decay $\tilde{b}_{1,2} \rightarrow \tilde{t}_1 W$ or W' s from decays of the t -quarks from \tilde{t} decays.

We discriminate the background in three categories depending on the origin of the dilepton: i) Flavor-symmetric background, which comes in equal amounts of SF and DF leptons ($ee/\mu\mu$ vs $e\mu$), ii) Flavor-asymmetric background producing only SF dileptons and iii) background from fake leptons. They are illustrated in fig. 5.10 as a function of the OSSF dilepton invariant mass which is decomposed in signal and all kind of backgrounds.

In the following, we look at the three sources of backgrounds separately and discuss methods for measuring their size and shape from data.

5.4.1 Flavor-symmetric background

This is the dominant dilepton background coming from flavor symmetric processes such as $t\bar{t}$, WW etc, as well as SUSY cascades with leptons originating from uncorrelated sources. This type of background produces $ee/\mu\mu$ and $e\mu$ final states with equal probability and is shown in figures 5.10 in blue ². One can therefore use the OSSF di-lepton data so as to model the OSSF (ee and $\mu\mu$) background components. In the real data the number of SF ($ee/\mu\mu$) events are expected to be:

$$N(ee) = \frac{1}{2} \times \frac{\epsilon^e}{\epsilon^\mu} \times N(e\mu), \quad N(\mu\mu) = \frac{1}{2} \times \frac{\epsilon^\mu}{\epsilon^e} \times N(e\mu) \quad (5.4)$$

where ϵ^e, ϵ^μ are the electron and muon efficiencies respectively. Thus, one can predict the size as well as the shape of $ee/\mu\mu$ distributions using the $e\mu$ mass distributions if the ratio of electron to muon efficiencies are known. In the real data, this ratio will be measured from Z events with the tag-and-probe method which has already been proven to work. It is not the purpose of this

²Of course, if smuons and selectrons do not have the same mass, this flavor symmetry is not present. In what follows we assume that we can use this symmetry even for the SUSY background.

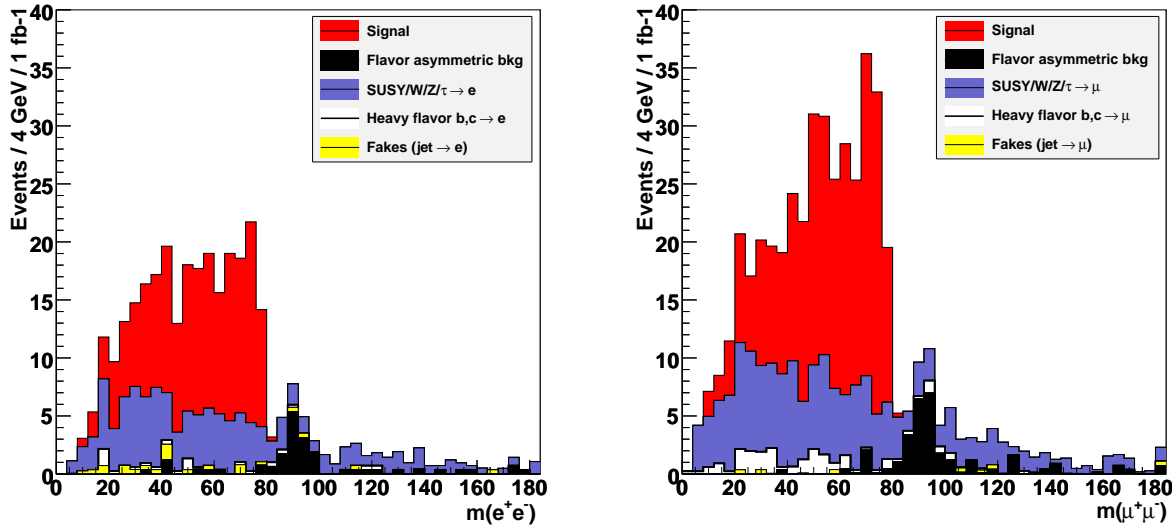


Figure 5.10: *Opposite-Sign dielectron (left) and dimuon (right) mass decomposition in the signal part (red), a flavor-symmetric component (blue), a flavor-asymmetric component (black) and fakes (yellow).*

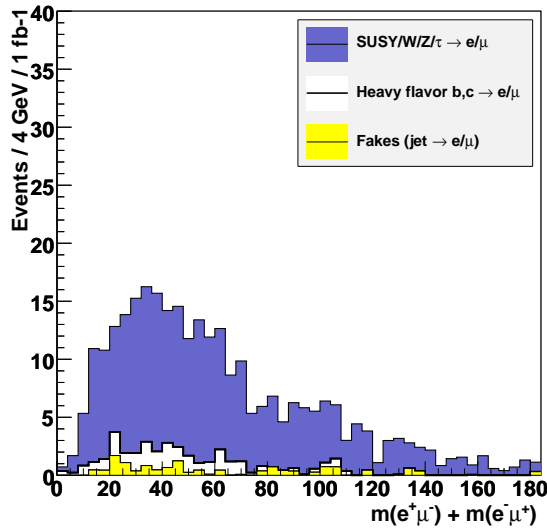


Figure 5.11: *Opposite-Sign $e\mu$ mass decomposition in a flavor-symmetric component (blue) and fakes (yellow).*

analysis to present the method, so here we simply use the ratios as taken from the Monte Carlo. The lepton efficiencies are p_T -dependent, and so is their ratio as shown in fig. 5.12 using leptons from Z events.

5.4. DILEPTON MASS COMPOSITION AND BACKGROUND MEASUREMENT

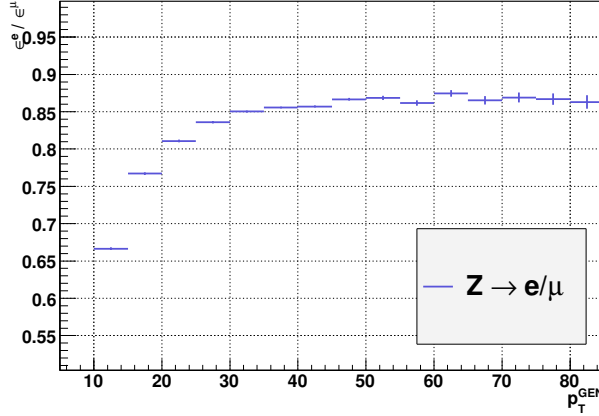


Figure 5.12: Ratio of electron and muon efficiencies as a function of the generated lepton p_T , using Z events decaying to leptons.

The flavor-symmetric background component, for ee or $\mu\mu$ events can then be derived from the convolution of the $e\mu$ data with the p_T -dependent efficiency ratio as:

$$\frac{d\sigma}{dm_{ee}} = \frac{1}{2} \times \int_0^\infty \frac{d^2\sigma}{dm_{e\mu} dp_T}(p_T) R(p_T) dp_T \quad (5.5)$$

where $R = \epsilon^e/\epsilon^\mu$; and similarly for the $\mu\mu$ case. The procedure has been followed by numerically convoluting the $e\mu$ mass and lepton p_T observables. The $e\mu$ mass data are split in mass bins, each being associated with an electron and muon p_T spectrum. The $ee/\mu\mu$ mass data are then calculated in mass bins according to the formula above, in one to one correspondence with the $e\mu$ mass bins. Following this method, fig. 5.13 presents the closure test of the SF $ee/\mu\mu$ background components derivation from the $e\mu$ data. The figures display the distributions “predicted” from the $e\mu$ data and the actual background distribution plotted using Monte Carlo information.

5.4.2 Flavor-asymmetric background

There are other sources rather than the leptonically decayed $\tilde{\chi}_2^0$, which results only in SF dilepton. Such correlated sources are:

- Heavier gauginos ($\tilde{\chi}_3^0, \tilde{\chi}_4^0$) decaying to a Z boson : $\tilde{\chi}_3^0 \rightarrow Z\tilde{\chi}_2^0$, $\tilde{\chi}_3^0 \rightarrow Z\tilde{\chi}_1^0$, $\tilde{\chi}_4^0 \rightarrow Z\tilde{\chi}_2^0$, $\tilde{\chi}_4^0 \rightarrow Z\tilde{\chi}_1^0$
- Leptonic two-body decays of heavier gauginos: $\tilde{\chi}_3^0 \rightarrow \tilde{\ell}^\pm \ell^\mp$, $\tilde{\chi}_4^0 \rightarrow \tilde{\ell}^\pm \ell^\mp$.
- Direct slepton-slepton production : $pp \rightarrow \tilde{\ell}^\pm \tilde{\ell}^\mp$.

The Z -boson decays can be accounted for by including a term (into the final likelihood fit) describing the Z peak (the size will be a fit parameter). The flavor-asymmetric background from

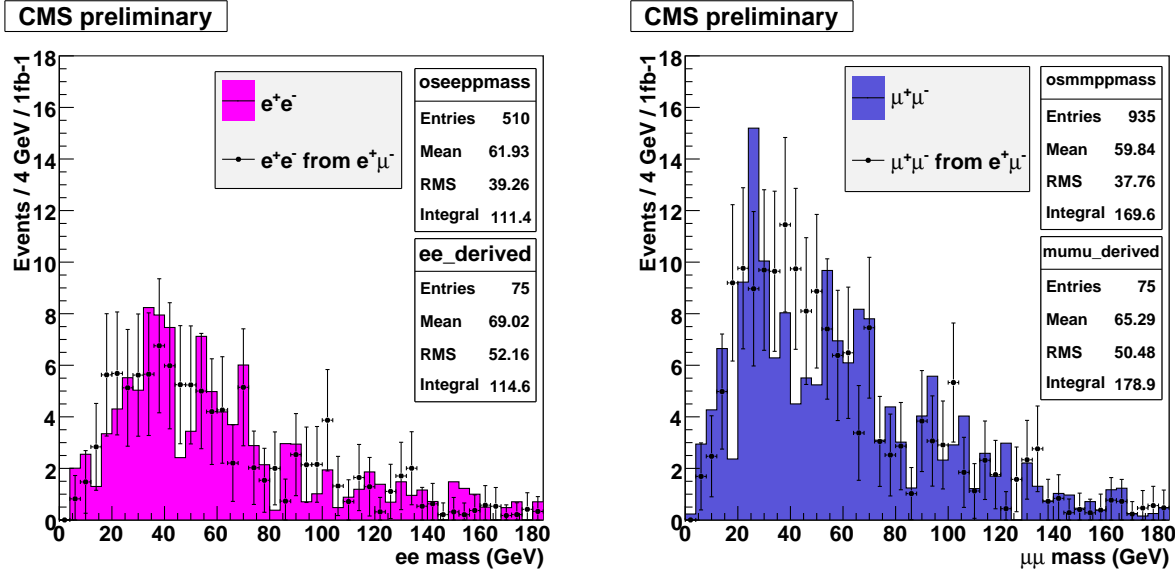


Figure 5.13: *Closure test in flavor-symmetric background measurement: dielectron (left) and dimuon (right) background components matched with MC (histogram) and derived by the $e\mu$ data (errors).*

decays of heavier gauginos, apart from the Z, is fairly small because of the reduced branching ratio compared to the SUSY signal chain. It also typically produces a flat background along the mass spectrum, as shown in black in fig. 5.10. Obviously, there is very little that can be done to estimate this background even after the first observation of SUSY. Moreover, it is very difficult to disentangle additional contributions such as this one (to the OSSF dilepton spectrum) until the statistics is large enough to enable quantitative comparisons to SUSY models (and also until a rough measurement of the sparticle masses is made).

5.4.3 Background from fake leptons

In addition to the previous two irreducible backgrounds, the case where at least one or both of the selected leptons are fake is also studied. This background results in flavor-asymmetric dilepton final states since the probability for fake e's and μ 's is different. This background is more significant in the dielectron final state. It is illustrated in figure 5.10 where the fake di-e / di- μ and $e\mu$ mass distributions are shown in yellow.

We already know that the size of the fake background is small as illustrated on the tables 4.2 and 4.3, where the number of OS dilepton background events are calculated using MC information. The fake background component constitutes 7% of the dielectron events and 1.5% of the dimuon events. We decompose the events with “fake leptons” into three categories: i) fake - prompt, ii) fake - hadron and iii) fake - fake lepton pair combinations. The fake-prompt combinations are the dominant ones and we would like to measure/model it from data. One possibility is to use the Same-Sign (SS) dilepton distributions expecting that, to first order, this background should be sign-symmetric (i.e. OS fakes = SS fakes). If the SS distributions were dominated entirely by the fake leptons combinations, then we could simply model the OS fake di-electron component with

5.4. DILEPTON MASS COMPOSITION AND BACKGROUND MEASUREMENT

the SS dielectrons. In reality, the SS dileptons are dominated from SUSY plus flavor-symmetric SM processes, which come in lower rates than the OS ones. This is illustrated in table 5.9 which lists the numbers of like-sign ee , $\mu\mu$ and $e\mu$ events and in figure 20 , which displays the respective mass distributions. Therefore, unfortunately, SS events cannot be used to predict the number of OS fake dilepton events.

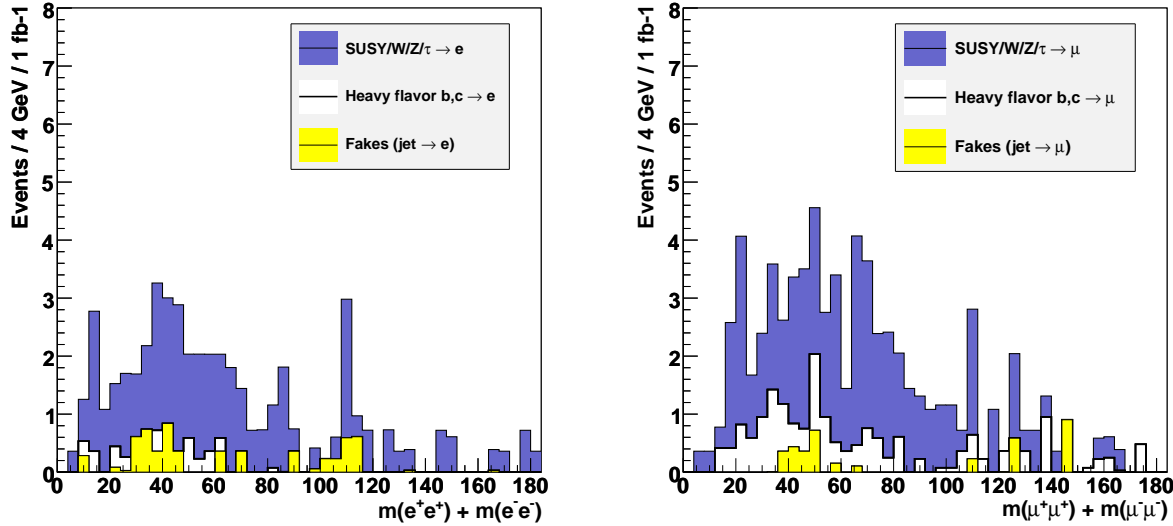


Figure 5.14: *Same-Sign dielectron (left) and dimuon (right) mass decomposition in a flavor-symmetric component (blue) and fakes (yellow).*

Table 5.9: Number of Same-Sign flavor-symmetric background dilepton events, decomposed in pairs of prompt-prompt (P-P) leptons, hadron-prompt (H-P) leptons and fakes-X (F-X) leptons , corresponding to $1fb^{-1}$.

	$e^+e^+ + e^-e^-$	$\mu^+\mu^+ + \mu^-\mu^-$	$e^+\mu^+ + e^-\mu^-$
P-P pairs	41.8	56.5	80.8
H-P / H-H pairs	3.0	17.0	24.5
F-X pairs	6.5	4.2	9.4

It is interesting to note that the ee and $\mu\mu$ background estimates (using the $e\mu$ data) work quite well despite applying electron and muon *efficiencies* (instead of fake rates for the fake lepton component) to estimate these backgrounds. We therefore estimate the correction necessary to account for this effect. We compare, for example, the $\mu\mu$ shape estimated by the $e\mu$ data including the fake/hadron component, with the $\mu\mu$ shape using the prompt $e\mu$ pairs plus the hadron/fake component from the MC. Figure 5.15, left, shows the two shapes superimposed, while the figure on the right presents their ratio which comes out in good agreement with a flat line at 1. We therefore include no correction for this effect but consider the overall effect in the systematic studies as part of the $e\mu$ uncertainty. It will be seen that the overall effect is negligible.

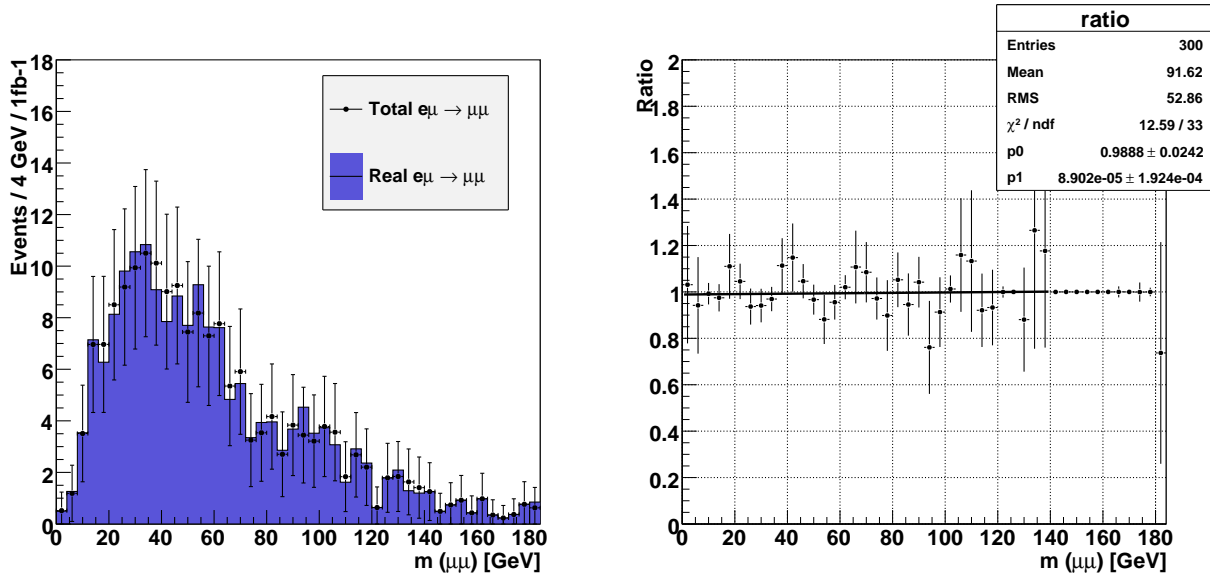


Figure 5.15: *Left:* Comparison of the $\mu\mu$ background shape as estimated by the $e\mu$ including the fake/hadron pairs, with the $\mu\mu$ shape using the $e\mu$ from the prompt dilepton plus the MC hadron/fake component. *Right:* ratio of the two shapes.

5.5 Di-lepton mass reconstruction

The simplest signature of supersymmetric events involving leptons is the dilepton coming from the decay chain $\tilde{\chi}_2^0 \rightarrow \tilde{\ell}_{L,R}\ell \rightarrow \ell\ell\tilde{\chi}_1^0$. The $\tilde{\chi}_2^0$ undergoes two sequential two-body decays and one of its final decay products is the invisible $\tilde{\chi}_1^0$. Consequently the construction of the invariant mass distribution of the other observed decay products (two charged leptons) shows a characteristic endpoint rather than a mass peak. The theoretical shape of the distribution is a triangle with the parametric form $d\Gamma/dm = 2/m_{\ell\ell}^{max,2}m$ where $m_{\ell\ell}^{max}$ is the endpoint value which can be expressed as a function of the mass of the sparticles involved in the signal decay chain, by the formula:

$$m_{\ell\ell}^{max} = m_{\tilde{\chi}_2^0} \sqrt{1 - \frac{m_{\tilde{\ell}_R}^2}{m_{\tilde{\chi}_2^0}^2}} \sqrt{1 - \frac{m_{\tilde{\chi}_1^0}^2}{m_{\tilde{\ell}_R}^2}} \quad (5.6)$$

The endpoint measurement can thus provide a first constraint towards supersymmetric mass reconstruction studies.

5.5.1 Endpoint measurement

In the present analysis, we follow the approach of fitting the whole range of the dilepton invariant mass distribution, and not just the region around the edge, using the shape formula implied by the kinematics of the decay under study. The mass distribution is fitted using the RooFit package [38]. RooFit is a tool for modeling the expected distribution of events in a physics analysis, specialized to perform likelihood fits of the data. It supports the extended likelihood formalism technique,

5.5. DI-LEPTON MASS RECONSTRUCTION

and thus allows the determination of the signal and background events separately. The model function used throughout the fitting process is a composite model of the form:

$$F(m) = N_{sig}S(m) + N_{bkg}B(m) + N_Z Z(m) \quad (5.7)$$

where N_{sig} , N_{bkg} and N_Z are the expected number of events for the three data cases respectively and

- $S(m)$ is the signal model which consists of the convolution of the signal theory shape with a Resolution Model used to describe the di-electron/muon mass resolutions. The signal term is intended to fit for the endpoint value $m_{\ell\ell}^{max}$ (eq.6) and the number of signal events N_{sig} .
- $B(m)$ is used to describe the flavor-symmetric background part as mentioned in section 4.3.1. It is modeled by the $e\mu$ data whose shape is then kept fixed in the total fit and the term is used to extract the expected number of background N_{bkg} events.
- $Z(m)$ is used to model the Z-peak. It consists basically of the convolution of a Breit-Wigner PDF with a Gaussian (Voigtian PDF) whose Z-mass and Z-width parameters are kept fixed. The Z-term also provides the expected number of Z events, which are the sum of SM Z events and Z events coming from SUSY cascades. If the standard model bkg can be totally suppressed, the extraction of N_Z will provide a measurement towards the Z production rate in supersymmetric events.

Several studies in the past have been following the approach of subtracting the DF dilepton mass distribution by the total SF distribution and then fitting the remaining one with the signal PDF. Here we put the background B(m) model in the model PDF and fit for the signal-plus-background data in order to extract number of background events as well. The Z-peak is also included in the fit: although it lies beyond the SUSY dilepton endpoint, it is close enough to affect its measurement.

Dilepton mass resolution. First, the mass resolution model entering the convolution of the signal model has to be determined. In this case, the resolution is extracted from the monte carlo, using the actual SUSY events with relaxed jet and missing E_T cuts so as to maintain as much statistics as possible.

The dimuon and dielectron mass resolutions are in principle different as illustrated in fig. 5.16 and typically they depend on the dielectron/dimuon mass region. Since we are interested in fitting the whole region of the dilepton mass, we need a resolution model to be parametrized as a function of the mass. For this reason, the δm distributions are looked at 4 different regions in mass: i) 0-20 GeV, ii) 20-40 GeV, iii) 40-60 GeV and iv) 60-80 GeV. The last region corresponds to the masses around the dilepton endpoint and is thus highly populated by statistics.

An attempt to parameterize the resolution as a function of the di-lepton mass is presented in figures 5.17 and 5.18. In each of the four mass bins, the invariant mass distributions of the di-electron and di-muon pairs are fitted with the a single gaussian for the muon- and the sum of two gaussians for the electron-events case. The parameters of the gaussian models are extracted from a χ^2 fit and plotted as a function of the dilepton mass. The quality of the fits is tested with the χ^2 value shown as a function of the mass in the same figures.

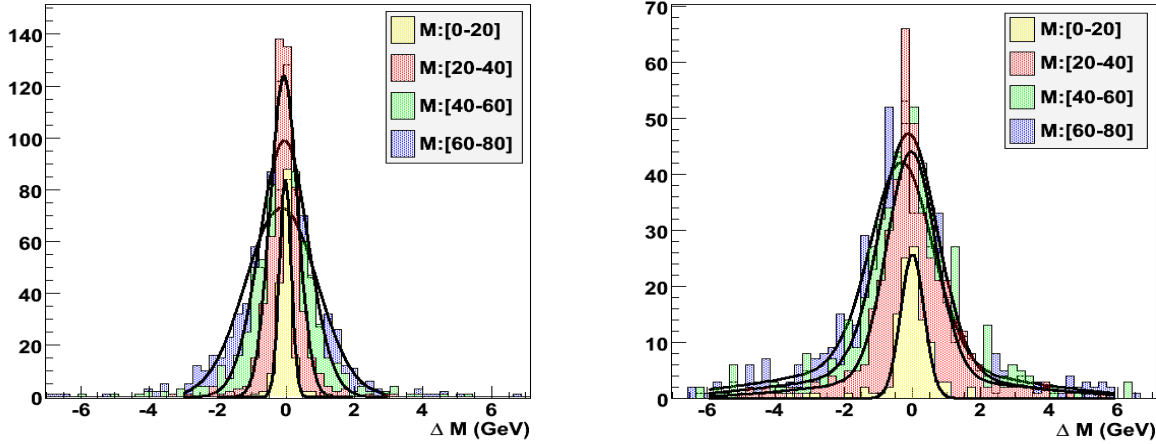


Figure 5.16: $\Delta m(\mu\mu)$ (left) and $\Delta m(ee)$ (right) distributions in four mass bins: i) $m: 20-40 \text{ GeV}$, ii) $m: 40-60 \text{ GeV}$, iii) $m: 60-80 \text{ GeV}$ (from left to right). The distributions are fitted with a Gaussian (di-muon case) or the sum of two Gaussians (di-electron case).

The dimuon mass resolution can be expressed with a Gaussian of non-constant sigma σ as:

$$\text{ResModel}(m_{\mu\mu}) = \text{Gauss}(m; m', \sigma = \beta \cdot m + c) \quad (5.8)$$

with $\mu = 0$ and $\sigma = 0.012 \cdot m + 0.10$, following the fit of the di-muon resolution model parameters as a function of the mass as shown in fig. 5.17. The dielectron resolution model is expressed as the sum of two gaussians, in order to account for the tails in the Δm_{ee} distributions. The two gaussians are distinguished as the one with minimum sigma (σ_{min}) and the other with the maximum sigma (σ_{max}). The resolution model can then be written as:

$$\begin{aligned} \text{ResModel}(m_{ee}) &= \alpha \cdot \text{Gauss}_1(m; m', \sigma_{min} = \beta \cdot m + c_1) \\ &+ (1 - \alpha) \cdot \text{Gauss}_2(m; m', \sigma_{max} = c_2) \end{aligned} \quad (5.9)$$

with $\alpha = 0.66$, $\mu_1 = -0.13$, $\mu_2 = -0.04$, $\sigma_{min} = 0.006 \cdot m + 0.5$ and $\sigma_{max} = 4$, as follows from fig. 5.18. A significant shift of the first Gaussian from zero can be noticed.

The resolution model is meant to be known precisely when measured from data (Z events) and can thus be kept fixed in the fit.

5.5.2 Fitting procedure

The fitting procedure starts with the parameterization of the $B(m)$ background component. The $B(m)$ shape is extracted by fitting the ee and $\mu\mu$ distributions as estimated from the $e\mu$ data, using the functional form $B(m) = \sum_i m^{\alpha_i} \exp^{-\kappa\beta_i m}$, with 4 parameters ($i=2$). The Z -peak PDF is then determined with a Voigtian of fixed central Z mass and width.

Fitting the di-muon and di-electron mass distributions separately results in figures 5.19. For an integrated luminosity of $1fb^{-1}$, the endpoint measurement is:

$$m_{\mu\mu}^{max} = 78.03 \pm 0.56(stat) \text{ GeV}/c^2 \quad (5.10)$$

5.5. DI-LEPTON MASS RECONSTRUCTION

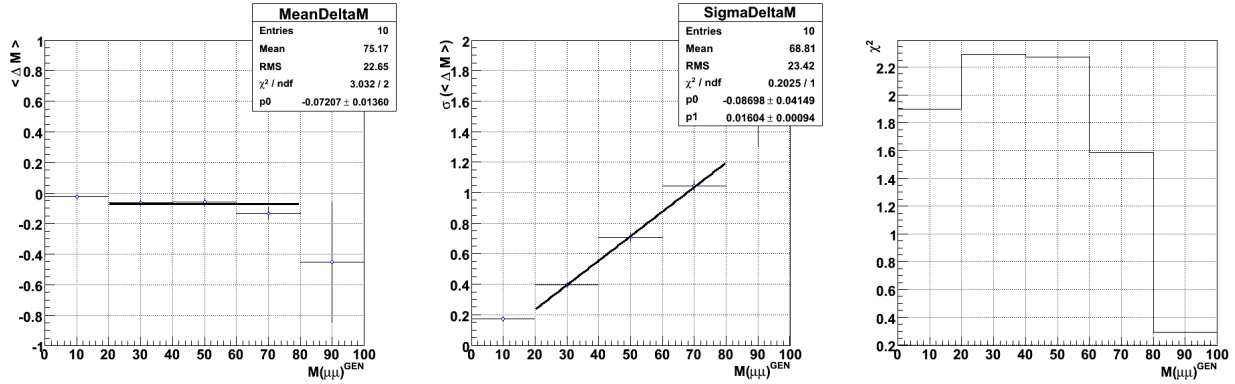


Figure 5.17: Dimuon mass Resolution model as a function of the dimuon $m(\mu\mu)$ mass. Left: Gaussian mean, right: Gaussian sigma.

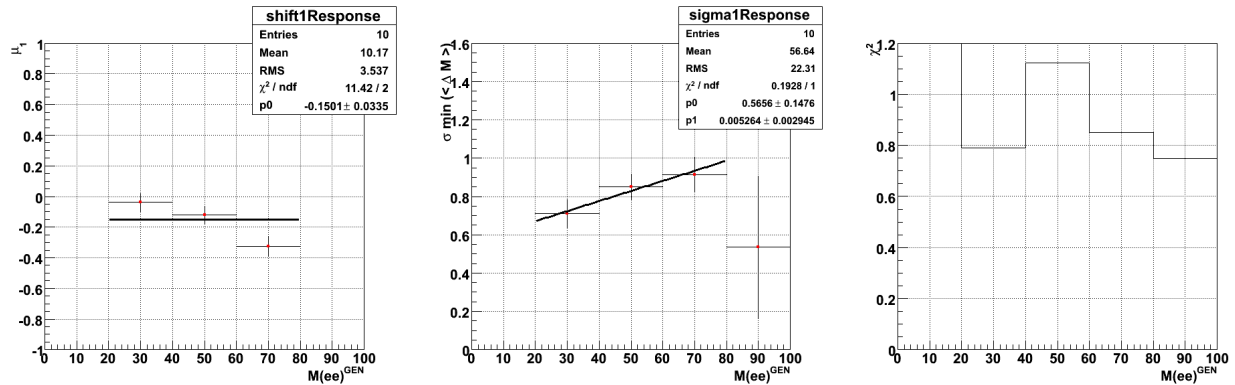


Figure 5.18: Dielectron mass Resolution model as a function of the dielectron $m(ee)$ mass. Left: mean of Gaussian with min σ , right: minimum σ .

$$m_{ee}^{max} = 77.90 \pm 1.00(stat) \text{ GeV}/c^2 \quad (5.11)$$

to be compared with the theoretical value of $m_{\ell\ell}^{max}(TH) = 78.15 \text{ GeV}/c^2$.

Finally, the dielectron and dimuon events are fitted simultaneously, in order to obtain a combined fit result for the endpoint value and its error. The parameters of the simultaneous fit consist in : i) one parameter for the endpoint and ii) six parameters for the number of signal, background and Z events entering in the dielectron and dimuon mass distributions. The fit results are shown in figure 5.20. The combined endpoint value comes at $m_{\ell\ell}^{max} = 78.00 \pm 0.49$, with an error consistent with the separate fits results according to the equation:

$$\frac{1}{\delta m_{\ell\ell}^{max}} = \sqrt{\frac{1}{(\delta m_{ee}^{max})^2} + \frac{1}{(\delta m_{\mu\mu}^{max})^2}} \quad (5.12)$$

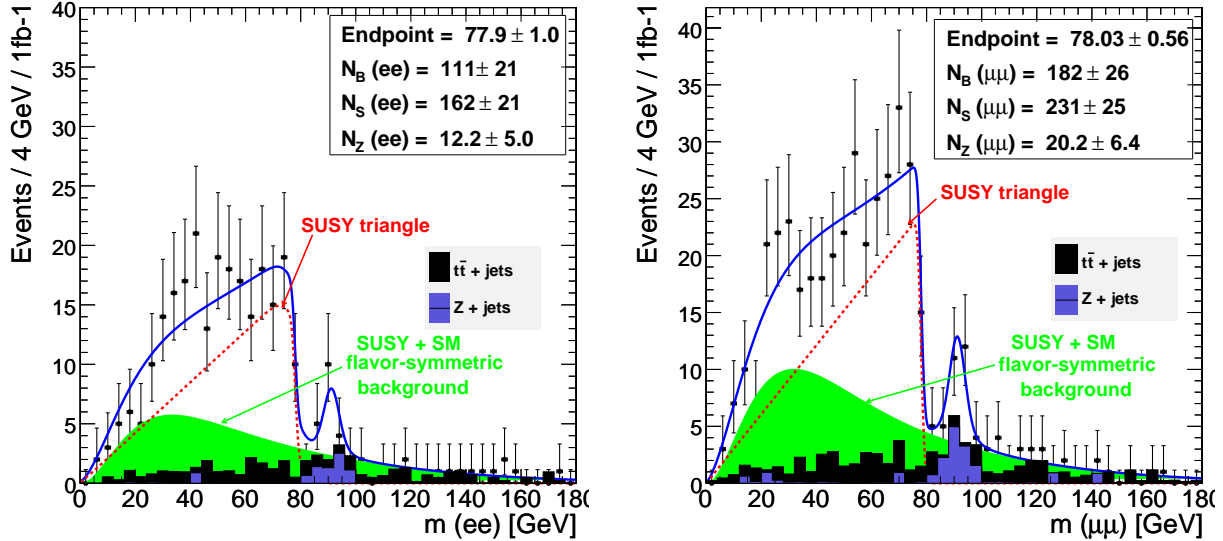


Figure 5.19: *Unbinned likelihood fit of the dielectron (left) and dimuon (right) masses for 1fb^{-1} of integrated luminosity; the signal PDF (red) and the flavor-symmetric background PDF (green) components are shown superimposed, as extracted from the fit.*

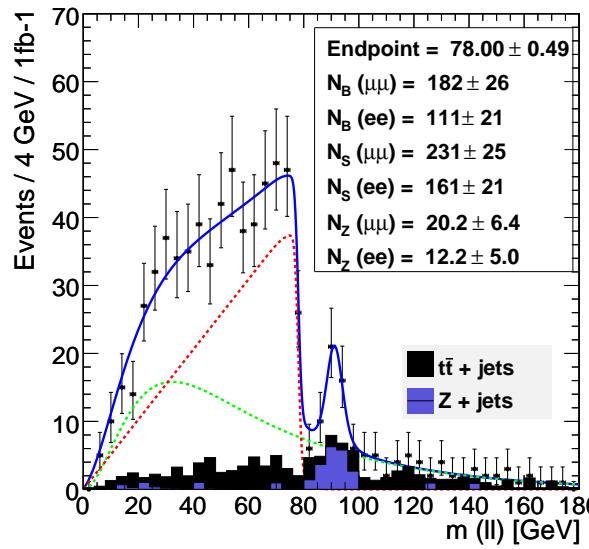


Figure 5.20: *Simultaneous fit of the dielectron and dimuon masses for 1fb^{-1} of integrated luminosity; the signal PDF (red) and the flavor-symmetric background PDF (green) components are shown superimposed, as extracted from the fit.*

5.6. SYSTEMATIC UNCERTAINTIES

5.5.3 Fit results with a toy Monte Carlo study

The demonstration of the fitting procedure, so far, only represents one fit to one pseudo-experiment. However, it is necessary to perform thousands of fits to thousands of pseudo-experiments and use these fit results to extract the final statistical uncertainty on the endpoint parameter. First, the model PDF and its properties is described in more detail. We have already presented the flavor-symmetric $B(m)$ as well as the Z-peak PDF $Z(m)$ parts of the model. We focus here on the signal PDF since it is the one to affect the endpoint extraction. The signal PDF $S(m)$ involves the convolution of the theoretical shape of the dilepton mass, a triangle $T(m)$, with the Resolution model chosen for the di-muon or di-electron masses (a Gaussian or the sum of two Gaussians). The convolution is made by numerical integration as:

$$S(m) = \sum_i T(m_i) \times \exp\left(-\frac{1}{2} \left(\frac{m - m_i}{\sigma(m_i)}\right)^2\right) \quad (5.13)$$

where the limits of the integration are restricted between an $m_{low} = 0$ and $m_{high} = m_{\ell\ell}^{max}$, emphasizing the fact that the upper limit corresponds to the true endpoint value itself and it is a parameter in the fit. The step size of the integration is determined by the number of convolution steps (N_{conv}) and is equal to $(m_{high} - m_{low})/N_{conv}$. We have chosen this number to be 300, resulting to a step size of around 0.25 GeV.

Next, we have run a Monte Carlo generator which was capable of producing toy datasets, sampled according to the model PDF described above. Repeating for 1000 experiments and generating events for the signal plus background cases corresponding to $1fb^{-1}$ of statistics, the datasets were fitted with the generator PDF. The fit results were inspected as per the distributions of the parameters , their errors and their pulls of mean. The relevant plots are shown in Appendix A. We conclude that the final statistical uncertainties on the endpoint(s) should be calculated by the average value on the distributions of the errors and are thus quoted as:

$$\Delta m_{ee}^{max}(stat.) = \pm 1.07 GeV/c^2 \quad (5.14)$$

$$\Delta m_{\mu\mu}^{max}(stat.) = \pm 0.75 GeV/c^2 \quad (5.15)$$

5.6 Systematic uncertainties

Several sources of systematic errors affecting the endpoint(s), but also the number of signal and background events, measurements have been studied. The following effects have been considered: the fitting procedure itself (fitting model construction, fit range), the mass resolution model imposed, the Electron and Jet Energy Scales, the $e\mu$ shape uncertainty due to fake dileptons, and finally the acceptance issue³. The fitting model and fit range uncertainties will not be considered as conventional systematic errors and will not be included in the calculation of the total systematic uncertainty. However, we include a short study on their (possible) effect on the endpoint extraction due to the rather complex construction of the model PDF and ensure that any possible bias is negligible.

³In view of a possible 20 GeV lepton p_T cut

Fitting model. A study of the model used for fitting the di-electron/muon masses has been made with the toy MC study described in the previous chapter. Figure 5.21 shows the pull distributions for the endpoint parameters, in the cases of the di-electron and di-muon toy MC studies respectively. The pull distributions refer to the distribution of the variable $(m_{\ell\ell}^{max}(th) - m_{\ell\ell,i}^{max}(exp)) / \delta m_{\ell\ell,i}^{max}$, which must be consistent with a Gaussian of mean 0 and $\sigma = 1$. A possible bias on the endpoint values due to the fit model are found to be compatible with zero: i) $\delta m_{ee}^{max} = -0.09 \pm 0.04$ GeV and ii) $\delta m_{\mu\mu}^{max} = -0.06 \pm 0.03$ GeV.

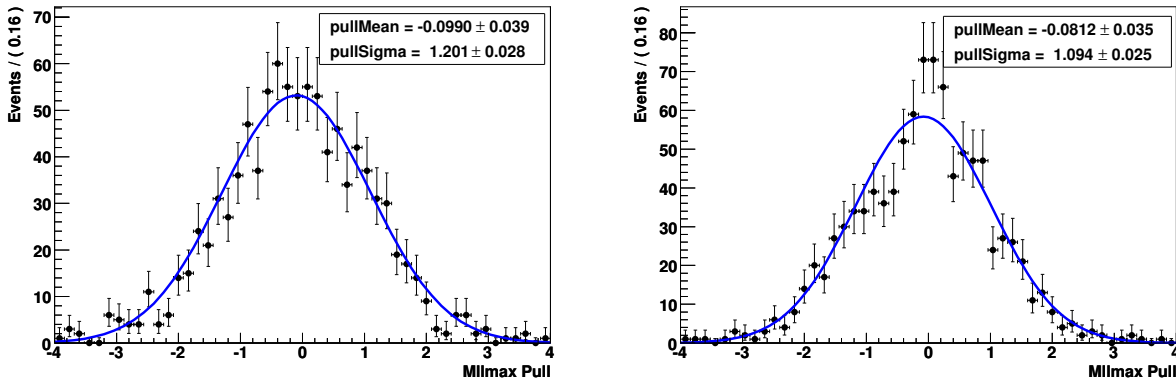


Figure 5.21: Pull distributions of the dielectron (left) and dimuon (right) endpoints fit results, extracted with a Toy MC generation.

Fit range variation. Its effect on the endpoint extraction has also been estimated. The lower limit of the fitting range of the dilepton mass distributions has been varied from 0 to 60 GeV (the 70 GeV case has been excluded as being too close with the endpoint value to be fitted). Figure 5.22 shows the di-electron and di-muon endpoint fit values as a function of the lower limit of the fit Range. The largest shift of the endpoint from its central fit Value, is considered as the largest bias that may be introduced due to the fit Range chosen, and comes equal to: i) $\delta m_{ee}^{max} = 0.10$ GeV and ii) $\delta m_{\mu\mu}^{max} = 0.05$ GeV.

Mass resolution model uncertainty. The uncertainty induced on the endpoint measurement due to the resolution model is looked at next. This is studied by varying the parameters of the resolution model as indicated by the statistical uncertainty with which these parameters have been determined. In data, the resolution model will be entirely adjusted to the Z events resolution measured with $1fb^{-1}$ of data. In the present analysis, the resolution model has been extracted from the MC and is thus determined with the statistical accuracy available from the MC. Tables 5.10 and 5.11 show the actual Resolution model parameters variation ranges, and the estimated bias on the endpoint(s) fit value, for the dielectron and dimuon Resolution model respectively. The largest shift from the central fit values are: i) $\delta m_{ee}^{max} = 0.13$ GeV, mainly due to the minimum σ (σ_{min}) parameter variation, and ii) $\delta m_{\mu\mu}^{max} = 0.06$ GeV. However, the dielectron and dimuon endpoint shifts are kept at a level well below the statistical uncertainties, therefore their estimation is expected to have been interfered with statistical fluctuations.

5.6. SYSTEMATIC UNCERTAINTIES

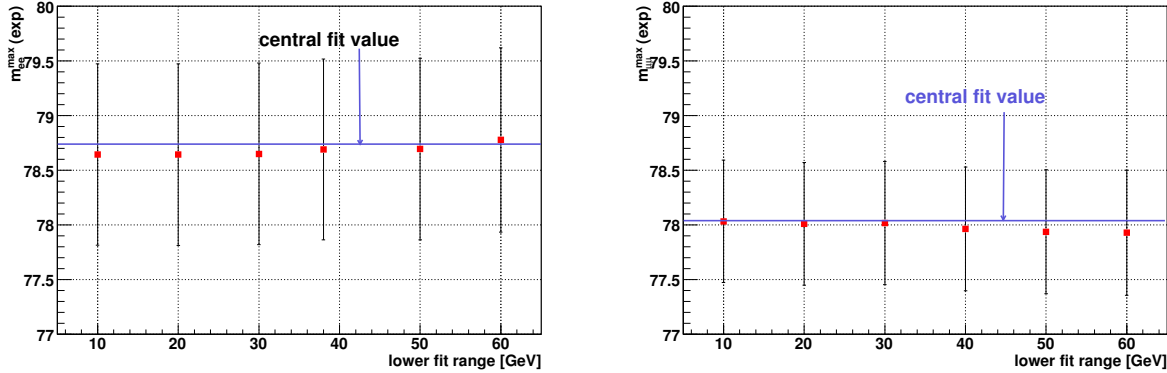


Figure 5.22: Bias on the dielectron (left) and dimuon (right) endpoints introduced due to variation of the fit range.

Table 5.10: Di-electron resolution model uncertainty and induced bias on the endpoint.

Dielectron resolution model parameters variation	m_{ee}^{max} bias [GeV]
$\alpha = 0.66 \pm 0.03$	0.03
$\mu_1 = -0.13 \pm 0.03$	0.03
$\mu_2 = -0.08 \pm 0.34$	0.05
$\beta = 0.006 \pm 0.002$,	
$c = 0.5 \pm 0.2$	0.13
$\sigma_{max} = 4 \pm 1$	-

Table 5.11: Di-muon resolution model uncertainty and induced bias on the endpoint.

Dimuon resolution model parameters variation	$m_{\mu\mu}^{max}$ bias [GeV]
$\mu = -0.09 \pm 0.02$	0.05
$\beta = 0.012 \pm 0.001$	0.02
$c = 0.10 \pm 0.02$	0.06

Electron and Jet Energy Scale. The effect of the Electron and Jet Energy Scale uncertainty upon the extraction of the endpoint as well as the number of signal and background events has also been considered. It has been studied using the full statistics available for the SUSY signal, which

CHAPTER 5. DI-LEPTON ANALYSIS WITH EARLY DATA

correspond to about $2.5 fb^{-1}$ of integrated luminosity, so as to minimize as possible the statistical uncertainty.

We have assumed an uncertainty of $\delta = 0.25\%$ on the absolute Electron Energy Scale (ElecES) for $1 fb^{-1}$ of data. The electron energy has been varied and the dielectron mass fits repeated, resulting to a shift in the position of the dielectron endpoint to about ± 0.20 GeV. The shifts to the number of events come out negligible as expected. The overall results are summarized in table 5.12.

Table 5.12: Electron Energy Scale (ElecES) uncertainty effect: estimated biases on the measurement of the dielectron endpoint and the number of signal and background events.

ElecES	m_{ee}^{max}	$N_{sig}(ee)$	$N_{bkg}(ee)$	$N_Z(ee)$
Fit Value	78.73 ± 0.83	168 ± 22	138 ± 23	9.8 ± 5.1
+0.0025	+0.14	-	+1	-
-0.0025	-0.26	-	-	-

Next, the uncertainty on the JES has been assumed to 5%. The samples have been varied accordingly taking into account propagation to the Recoil MET calculation. No significant effect on the endpoint extraction is expected but rather a variation on the number of total events. Indeed, in the case of the dielectron events are varied as of $-8\% \div +4\%$ for the number of signal events and of $-11\% \div +11\%$ for the number of background events. Similarly, the number of dimuon signal events give a variation of $-7\% \div +5\%$ and the number of background events $-9\% \div +8\%$. The complete set of results are presented on table 5.13.

Table 5.13: Jet Energy Scale (JES) uncertainty effect on the measurement of the dielectron endpoint and the number of signal and background events.

JES	m_{ee}^{max}	$N_{sig}(ee)$	$N_{bkg}(ee)$	$N_Z(ee)$
+0.05	78.64 ± 0.80	174	155	11
± 0.00	78.73 ± 0.83	168	138	9.8
-0.05	78.21 ± 0.94	155	123	8.6

JES	$m_{\mu\mu}^{max}$	$N_{sig}(\mu\mu)$	$N_{bkg}(\mu\mu)$	$N_Z(\mu\mu)$
+0.05	78.07 ± 0.56	272	221	20.7
± 0.00	78.03 ± 0.56	257	202	15.8
-0.05	77.89 ± 0.60	239	184	15

Acceptance. The effect of the lepton p_T cuts in the dilepton endpoint measurement has been studied. Indeed the lepton PT cuts imposed in the 2 highest-PT leptons of the analysis may distort the shape of the dilepton mass which is a straight line of specific slope (triangle). Depending on

5.7. CONCLUSION

the particular mass hierarchy of the mSUGRA model under study, the p_T of the leptons involved in the signal decay chain ($\tilde{\chi}_2^0 \rightarrow \tilde{\chi}_1^0 \ell\ell$) can reach up to relatively low values. For LM1, the influence of the p_T lepton cuts start to show up for lepton $p_T > 10$ GeV and becomes prominent for $p_T > 20$ GeV. For this purpose we have run a toy MC SUSY generator which is capable of producing the kinematics of the $\tilde{\chi}_2^0$ decay chain given the four-vector of the initial squark in the lab frame. The squark p_T and η distributions are taken from the PYTHIA LM1 generation and sampled accordingly to generate events with $\tilde{\chi}_2^0 \rightarrow \tilde{\chi}_1^0 \ell\ell$.

Raising the lepton p_T cuts at 20 GeV, the dielectron and dimuon fits were repeated as shown on figure 5.23 left. A slight asymmetry between the fit function and the data around the mass region at 40 GeV can be noticed which is due to the Acceptance effect. The fits have been repeated including an acceptance correction function in the signal PDF part and the results are shown on the right plot of fig. 5.23, exhibiting a small shift in the dielectron/dimuon endpoint fit value. This shift will be considered as a possible systematic error. Nevertheless, the acceptance does not affect significantly the endpoint extraction.

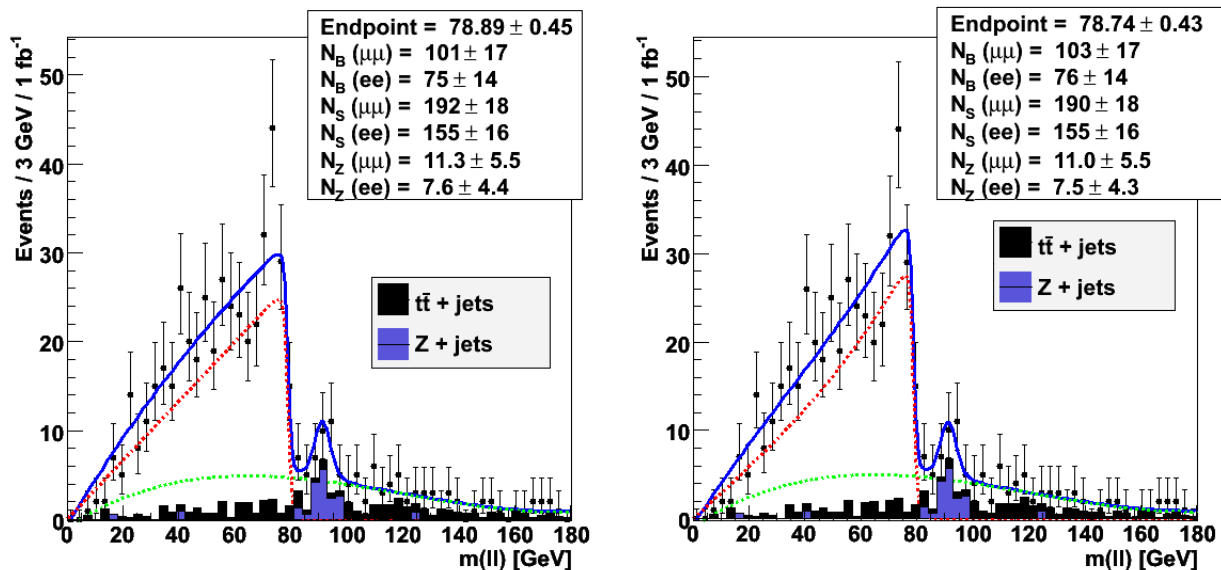


Figure 5.23: Simultaneous fit of the dielectron and dimuon masses for 1 fb^{-1} of integrated luminosity; the lepton p_T cuts are raised to 20 GeV. The acceptance correction function is included in the fit on the bottom plot.

The overall results of the systematic uncertainties are summarized in table 5.14.

5.7 Conclusion

A search for the observation of a dilepton edge from the decay $\tilde{\chi}_2^0 \rightarrow \tilde{\ell}^\pm \ell^\mp \rightarrow \tilde{\chi}_1^0 \ell^\pm \ell^\mp$ has been presented. The analysis assumes 1 fb^{-1} of integrated luminosity with the 100 pb^{-1} calibra-

CHAPTER 5. DI-LEPTON ANALYSIS WITH EARLY DATA

Table 5.14: Summary of dielectron/dimuon endpoint(s) systematic errors.

	m_{ee}^{max} [GeV]	$m_{\mu\mu}^{max}$ [GeV]
Fit value	77.90	78.03
Statistical error	1.07	0.75
ElecES error	0.20	-
JES error	0.22	0.09
Fit Model error	0.09	0.06
Fit Range error	0.10	0.05
Res Model error	0.13	0.06
Acceptance error	0.15	0.14
$e\mu$ shape error	0.02	0.02
Total syst. error	0.36	0.18

tion/alignment knowledge. The selection is optimized for the measurement of the edge, assuming an overall excess of “SUSY” over the SM expectations has been observed. We expect the dilepton endpoint value $m_{\ell\ell}^{max}$ to be determined with a statistical uncertainty of 0.62 GeV. A number of systematic uncertainties have been considered. Overall, the extraction of $m_{\ell\ell}^{max}$ is quite robust: the total systematic uncertainty is expected to be 0.36 GeV for the dielectron, and 0.18 GeV for the dimuon endpoint:

$$\Delta m_{ee}^{max} = \pm 1.07 \text{ (stat.)} \pm 0.36 \text{ (syst.)} \text{ GeV/c}^2 \quad 5.16$$

$$\Delta m_{\mu\mu}^{max} = \pm 0.75 \text{ (stat.)} \pm 0.18 \text{ (syst.)} \text{ GeV/c}^2 \quad 5.17$$

The number of events extracted cannot be used for a cross section measurement due to the unknown masses, and therefore the acceptances. They will, however, be a useful input for further measurements of supersymmetric signatures.

6

The endpoint technique

Supersymmetry studies at the LHC have two major distinct goals. The first one is the discovery of supersymmetric signals, which can be achieved through an excess of events over the standard model expectations. This is primarily the objective of inclusive analyses based on large missing transverse energy and high jet multiplicity to characterize the topology of signal events. Alternatively, one can use supersymmetric signatures involving leptons in a more robust method to discover supersymmetry, much like the analysis presented in the fourth chapter of the thesis.

The second major goal is to extract information on supersymmetric particle properties and ultimately to measure the supersymmetry model parameters. This is the objective of the present chapter of the thesis, where an attempt to measure the supersymmetric particle masses involved in the decay chain relevant to a leptonically decayed $\tilde{\chi}_2^0$:

$$\tilde{q} \rightarrow q\tilde{\chi}_2^0, \quad \tilde{\chi}_2^0 \rightarrow \ell_1 + \tilde{\ell}, \quad \tilde{\ell} \rightarrow \ell_2 + \tilde{\chi}_1^0 \quad (6.1)$$

is presented.

6.1 Kinematic relations for the endpoints

In this section, the basic kinematic characteristics of the supersymmetric decay chain 6.1 are presented. For this purpose one needs to exploit the entire chain. The visible decay products of the decay (two leptons and a quark) can be used to extract useful information when forming the invariant masses of the possible combinations between the leptons and the quark. However, because of the undetectable LSP, the traditional measurement of masses from resonant peaks is impossible and one turns to measure kinematical endpoints (minima/maxima) in the effective mass distributions. A method has been developed and it is known as the endpoint technique.

The endpoint technique is based on the fact that the maxima/minima of the mass distribution of the different combinations of visible particles are related to the masses of the super-partners in the decay chain through a resolved system of equations. Once the endpoints of the distributions are measured, the masses of the SUSY particles can then be extracted. If the measured endpoints are at least as many as the unknown masses, then the endpoint expressions above may be inverted analytically to provide an explicit formula for the masses in terms of the endpoints.

The supersymmetric decay chain under study is a three-step sequential two-body decays which

CHAPTER 6. THE ENDPOINT TECHNIQUE

can be written in the general form:

$$Q \rightarrow X c \rightarrow R b c \rightarrow O a b c \quad (6.2)$$

The application of the endpoint technique is studied in the supersymmetric decay chain 6.1, illustrated in figure 6.1. The particles O, R, X and Q are massive and satisfy the relations:

$$M_Q > M_X > M_R > M_O \quad (6.3)$$

whereas the particles a, b, and c are considered to be massless. The aim is to extract the values of the masses of particles Q, X, R and O from the measurement of kinematic upper endpoints in the invariant mass distributions between the visible particles a, b and c. There are four available (observable) mass combinations: M_{ba} , M_{cb} , M_{ca} and M_{cba} . The maxima of these distributions are reached for specific kinematic configurations of the particles involved.

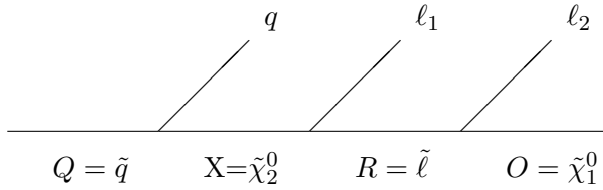


Figure 6.1: Schematic representation of the supersymmetric decay chain involving the two-body decay of the $\tilde{\chi}_2^0$. Particles Q, X, R, O are considered to be massive, with $M_Q > M_X > M_R > M_O$ - whereas the (experimentally visible) particles q, ℓ_1, ℓ_2 are taken to be massless.

In the following, the kinematic formulae of the four mass combinations are presented, assuming that O is a $\tilde{\chi}_1^0$ with mass M_O , R is an intermediate state with mass M_R and particle Q is a \tilde{q} with mass M_Q .

6.1.1 Endpoint in $M_{\ell\ell}$

The invariant mass distribution of the two leptons is calculated in a simple way in the rest frame of $X = \tilde{\chi}_2^0$. If we take the angle between the $\tilde{\ell}$ and the ℓ_2 to be θ^* , it can be shown that the effective mass takes the form:

$$M_{\ell\ell}^2 = \frac{(M_X^2 - M_R^2)(M_R^2 - M_O^2)}{2M_R^2}(1 + \cos \theta^*) \quad (6.4)$$

The upper endpoint of the di-lepton mass is obtained when $\cos \theta^* = 1$, which corresponds to the collinear configuration of the two leptons emitted opposite to each other in the rest frame of X . The di-lepton endpoint formula is then given by:

$$M_{\ell\ell}^{\max} = M_X \sqrt{\left(1 - \frac{M_R^2}{M_X^2}\right) \left(1 - \frac{M_O^2}{M_R^2}\right)} \quad (6.5)$$

6.1. KINEMATIC RELATIONS FOR THE ENDPOINTS

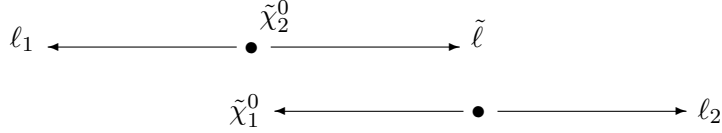


Figure 6.2: Kinematic configuration leading to the maximum of the $(\ell\ell)$ mass.

The shape of the distribution can be obtained easily taking into account the spin-0 nature of the $R = \tilde{\ell}$. For an isotropic decay of R , relation (6.4) implies that the distribution of $M_{\ell\ell}^2$ should be flat and therefore the differential decay width should increase linearly with $M_{\ell\ell}$. That is:

$$\frac{1}{\Gamma} \frac{d\Gamma}{dM_{\ell\ell}} dM_{\ell\ell} = \frac{2}{(M_{\ell\ell}^{\max})^2} M_{\ell\ell} dM_{\ell\ell} \quad (6.6)$$

6.1.2 Endpoints in $M_{\ell q}$

We now turn to the invariant mass distributions involving in addition the quark to combine with the two leptons. The endpoints of the two-particle invariant masses $(\ell_1 q)$ and $(\ell_2 q)$ are reached in collinear configurations of the two leptons and the quark, except the one in which all particles are in the same direction (resulting in zero mass).

The $(\ell_1 q)$ mass. The upper endpoint in the $(\ell_1 q)$ mass can be formed in the configuration where the quark and the ℓ_1 are emitted back-to-back in the rest frame of the $X = \tilde{\chi}_2^0$ (see fig. 6.3). The kinematics describing the configuration are similar to the dilepton case, and the largest value of the $M_{\ell_1 q}^{\max}$ is reached when $R = \tilde{\ell}$ is at rest in the $Q = \tilde{q}$ rest frame. The corresponding formula in this case is written as:

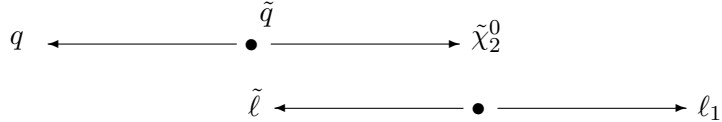


Figure 6.3: Kinematic configuration leading to the maximum of the $(\ell_1 q)$ mass.

$$M_{\ell_1 q}^{\max} = M_Q \sqrt{\left(1 - \frac{M_X^2}{M_Q^2}\right) \left(1 - \frac{M_R^2}{M_X^2}\right)} \quad (6.7)$$

The $(\ell_1 q)$ distribution is affected by spin effects because of the spin-1/2 nature of the $X = \tilde{\chi}_2^0$. A charge asymmetry should be visible between the distinguished cases of $(\ell^+ q)$ and $(\ell^- q)$ distributions. However, if no particular sign selection is required for the ℓ_1 , the asymmetry is cancelled. Therefore the total $(\ell_1 q)$ distribution can also in this case be described by a triangular shape:

$$\frac{1}{\Gamma} \frac{d\Gamma}{dM_{\ell_1 q}} = \frac{2}{(M_{\ell_1 q}^{\max})^2} M_{\ell_1 q} \quad (6.8)$$

CHAPTER 6. THE ENDPOINT TECHNIQUE

The $\ell_2 q$ mass. The configuration leading to the maximum for the $(\ell_2 q)$ mass is shown in fig. 6.4. The configuration is drawn in the rest frame of $Q = \tilde{q}$, whereas the ℓ_2 is in the opposite direction to the quark. It is noted that the ℓ_2 is also in the opposite direction to the ℓ_1 and as a result the $(\ell_2 q)$ mass is maximized together with the $(\ell \ell)$ mass.

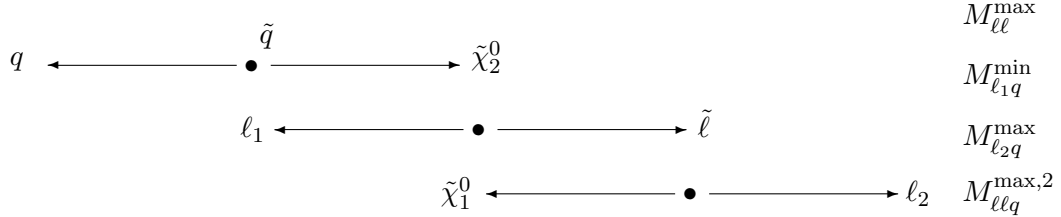


Figure 6.4: Kinematic configuration leading to the maximum of the $(\ell_2 q)$ mass.

The endpoint formula for the $(\ell_2 q)$ system is given by

$$M_{\ell_2 q}^{\max} = M_Q \sqrt{\left(1 - \frac{M_X^2}{M_Q^2}\right) \left(1 - \frac{M_O^2}{M_R^2}\right)} \quad (6.9)$$

Comparing the endpoint formulae between the $(\ell_1 q)$ and $(\ell_2 q)$ distributions, a certain condition of supersymmetric mass ratios allows the $(\ell_2 q)^{\max}$ to be either higher or lower than $(\ell_1 q)^{\max}$. It can be shown that $((\ell_2 q)^{\max})^2 > ((\ell_1 q)^{\max})^2$ in the cases where

$$1 - \frac{M_O^2}{M_R^2} > 1 - \frac{M_R^2}{M_X^2} \Rightarrow M_R^2 > M_X M_O \quad (6.10)$$

An analytic formula of the differential decay width of the $(\ell_2 q)$ system has been calculated in [49] to be:

$$\begin{aligned} \frac{1}{\Gamma} \frac{d\Gamma}{dM_{\ell_2 q}} &= \frac{4M_{\ell_2 q}}{(M_{\ell_2 q}^{\max})^2 \left(1 - \frac{M_R^2}{M_X^2}\right)} \ln \frac{M_X}{M_R} \quad \text{for} \quad 0 \leq M_{\ell_2 q} \leq \frac{M_R}{M_X} \\ &= \frac{4M_{\ell_2 q}}{(M_{\ell_2 q}^{\max})^2 \left(1 - \frac{M_R^2}{M_X^2}\right)} \ln \frac{M_{\ell_2 q}^{\max}}{M_{\ell_2 q}} \quad \text{for} \quad \frac{M_R}{M_X} \leq M_{\ell_2 q} \leq M_{\ell_2 q}^{\max} \end{aligned} \quad (6.11)$$

Similarly to the $(\ell_1 q)$ case, the above formula is valid when the $(\ell_2^+ q)$ and $(\ell_2^- q)$ distributions are merged.

An interesting kinematic feature of the $(\ell_2 q)$ system is the formation of a secondary endpoint in the invariant mass spectrum. This can be obtained by flipping the direction of the decay products of $X = \tilde{\chi}_2^0$, as shown in the configuration of fig. 6.5.

This leads to a maximum mass of

$$\begin{aligned} (M_{\ell_2 q}^{\max, 2})^2 &= \frac{M_R^2}{M_X^2} M_Q^2 \left(1 - \frac{M_X^2}{M_Q^2}\right) \left(1 - \frac{M_O^2}{M_R^2}\right) \\ &= \frac{M_R^2}{M_X^2} (M_{\ell_2 q}^{\max})^2 \end{aligned} \quad (6.12)$$

6.1. KINEMATIC RELATIONS FOR THE ENDPOINTS

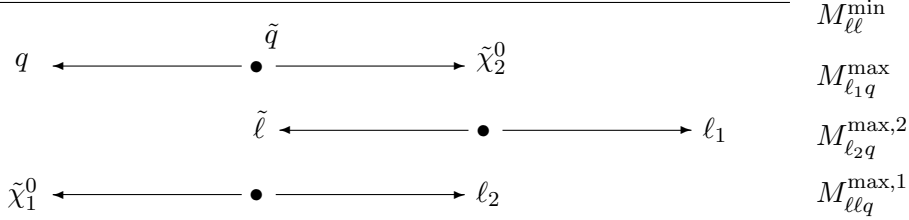


Figure 6.5: Kinematic configuration leading to the secondary maximum of the $(\ell_2 q)$ mass.

Since M_R must be smaller than M_X (otherwise the decay chain is kinematically forbidden), the secondary endpoint of the $(\ell_2 q)$ system can never be larger than the one in (6.9). A difficulty with the experimental observation of this edge is that it is located in a region where there are only a few events. This can be understood by the fact that it is reached for low values of $M_{\ell\ell}$ (ℓ_1 and ℓ_2 are in parallel direction in the maximizing configuration). Nevertheless, one can still draw a conclusion on whether this endpoint is larger than $M_{\ell_1 q}^{\max}$. It can be shown that this is true if the following relation is satisfied

$$2M_R^2 > M_X^2 + M_0^2 \quad (6.13)$$

Distinguishing upper endpoints in $M(\ell_1 q)$ and $M(\ell_2 q)$ distributions. The observation of the $\ell_1 q$ and $\ell_2 q$ endpoints is not a straightforward task. This is originally hampered by the fact that the two leptons (ℓ_1 and ℓ_2) coming from the $\tilde{\chi}_2^0$ decay, cannot be distinguished experimentally. The consequence is that the $(\ell_1 q)$ and $(\ell_2 q)$ distributions cannot be plotted separately in a way to allow the direct measurement of their maxima. Several studies made by the ATLAS collaboration have been following the approach of separating the distributions by plotting the largest and the lowest $M(\ell q)$ combinations [50]. However, although this approach is experimentally clear, it has as a drawback a more complicated system of equations for the derivation of the sparticle masses from the measured endpoints.

In the scope of this thesis, an alternative approach is presented based on correlations between effective masses [54]. As an example, we may notice that the maximum mass of the $\ell_2 q$ system is reached in the configuration maximizing also the $(\ell\ell)$ system. On the contrary, the maximum $(\ell_1 q)$ mass is reached for any value of $M(\ell\ell)$. This can be viewed in the two-dimensional plot of the $M(\ell\ell)$ spectrum versus $M(\ell q)$ for both the two lepton combinations. By selecting larger values of $M(\ell\ell)$, the $M(\ell_2 q)$ endpoint becomes more prominent, allowing its identification in a model independent way.

6.1.3 Endpoints in $M_{\ell\ell q}$

The kinematics of the dilepton - quark system predict various configurations leading to a number of maxima of the $(\ell\ell q)$ invariant mass. The applicability of the different endpoint formulae which correspond to these configurations, depends in principle on the sparticle masses.

In general, an absolute maximum of the $M(\ell\ell q)$ is reached in the non-collinear configuration shown in fig. 6.6. The largest value of the three-particle mass in this case is:

CHAPTER 6. THE ENDPOINT TECHNIQUE

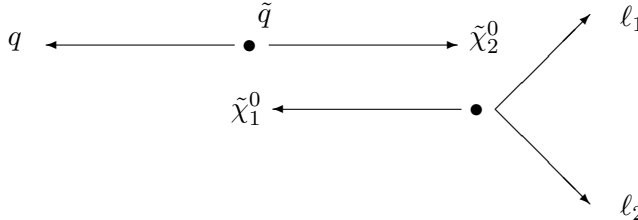


Figure 6.6: Kinematic configuration leading to the absolute maximum of the $(\ell\ell q)$ mass.

$$M_{\ell\ell q}^{\max} = M_Q - M_O \quad (6.14)$$

which corresponds to $O = \tilde{\chi}_1^0$ being at rest in the rest frame of $Q = \tilde{q}$. However, depending on the masses of the supersymmetric particles, this situation may not be kinematically accessible.

Considering the collinear configurations of the dilepton-quark system, three other kinematic endpoints may be reached. A first collinear endpoint is obtained in the configuration depicted in fig. 6.5. In this scheme, the two leptons form a zero-mass object recoiling in the rest frame of $R = \tilde{\ell}$ against the $\tilde{\chi}_1^0$. The corresponding maximum is given by the formula

$$M_{\ell\ell q}^{\max,1} = M_Q \sqrt{\left(1 - \frac{M_X^2}{M_Q^2}\right) \left(1 - \frac{M_O^2}{M_X^2}\right)} \quad (6.15)$$

A second maximum is obtained by flipping the direction of $R = \tilde{\ell}$ decay products in the $\tilde{\chi}_2^0$ decay. The relevant configuration is shown in fig. 6.4, leading to the formula

$$M_{\ell\ell q}^{\max,2} = M_Q \sqrt{\left(1 - \frac{M_R^2}{M_Q^2}\right) \left(1 - \frac{M_O^2}{M_R^2}\right)} \quad (6.16)$$

This endpoint, however, is not independent of the previous endpoints presented as it can be written in the form

$$(M_{\ell\ell q}^{\max,2})^2 = (M_{\ell\ell q}^{\max})^2 + (M_{\ell\ell}^{\max})^2 \quad (6.17)$$

Finally, a third collinear endpoint is realised in the configuration shown in fig. 6.7, obtained by flipping the direction of the $R = \tilde{\ell}$ decay products.

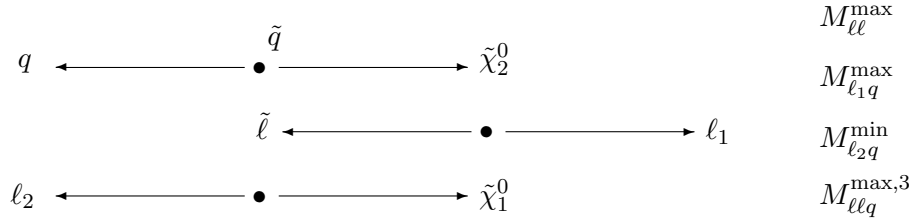


Figure 6.7: Kinematic collinear configuration leading to the third maximum of the $(\ell\ell q)$ mass.

In this case, the endpoint formula is:

$$M_{\ell\ell q}^{\max,3} = M_Q \sqrt{\left(1 - \frac{M_R^2}{M_X^2}\right) \left(1 - \frac{(M_X M_O)^2}{(M_Q M_R)^2}\right)} \quad (6.18)$$

6.1. KINEMATIC RELATIONS FOR THE ENDPOINTS

and it can be easily verified that

$$(M_{\ell\ell q}^{\max,3})^2 = (M_{\ell_1 q}^{\max})^2 + (M_{\ell\ell}^{\max})^2 \quad (6.19)$$

As in the case of the $M_{\ell\ell q}^{\max,2}$, the third endpoint of the $(\ell\ell q)$ mass, $M_{\ell\ell q}^{\max,3}$, is neither independent of the previous endpoints.

Which of the three endpoints (plus the non-collinear) is going to be the “true” endpoint in the $M(\ell\ell q)$ distribution, which is meant to be used later in the determination of the sparticle masses, is unfortunately an issue of the sparticle mass relations which cannot be known in advance. A model-independent approach towards the identification of the true endpoint can be obtained by studying correlations between $M(\ell\ell q)$ near its upper edge and $M(\ell\ell)$, $M(\ell_1 q)$ and $M(\ell_2 q)$. The idea is based on conclusions that can be drawn by inspecting the following regions in sparticle masses:

- $\frac{M_X}{M_Q} \leq \frac{M_R}{M_X} \frac{M_Q}{M_R}$: the true endpoint is given by $M(\ell\ell q)^{\max,1}$. This maximum is reached in the collinear configuration of fig. 6.5 and is characterized by small values of $M(\ell\ell)$.
- $\frac{M_Q}{M_R} \leq \frac{M_R}{M_X} \frac{M_X}{M_Q}$: the true endpoint is given by $M(\ell\ell q)^{\max,2}$. It corresponds to the collinear configuration of fig. 6.4 which is characterised by near maximum values of $M(\ell\ell)$ and of $M(\ell_2 q)$. Additionally in this case, the true endpoint of the $M(\ell q)$ distribution is given by $M(\ell_2 q)^{\max}$.
- $\frac{M_R}{M_X} \leq \frac{M_Q}{M_R} \frac{M_X}{M_Q}$: the true endpoint is given by $M(\ell\ell q)^{\max,3}$. It corresponds to the collinear configuration of fig. 6.7 and is characterised by large values of $M(\ell\ell)$ and of $M(\ell_1 q)$. In this range, the true endpoint of $M(\ell q)$ is given by $M(\ell_1 q)^{\max}$.

Not all endpoint solutions for (ℓq) and $(\ell\ell q)$ can be simultaneously true endpoints. For the case where the $(\ell_1 q)$ is the true endpoint of $M_{\ell q}$, then the endpoint of $M(\ell\ell q)$ can be either $M(\ell\ell q)^{\max,1}$, $M(\ell\ell q)^{\max,3}$ or a non-collinear configuration. If on the other hand the $(\ell_2 q)$ is the true endpoint of $M_{\ell q}$ then the endpoint of $M(\ell\ell q)$ can be either $M(\ell\ell q)^{\max,1}$, $M(\ell\ell q)^{\max,2}$ or a non-collinear configuration.

6.1.4 Endpoint for the sum $M_{\ell_1 q} + M_{\ell_2 q}$

A complete set of observed endpoints in the $(\ell\ell)$, (ℓq) and $(\ell\ell q)$ distributions is in principle adequate for the determination of the four unknown sparticle masses, if the measurements include:

$$M_{\ell\ell}^{\max}, M_{\ell_1 q}^{\max}, M_{\ell_2 q}^{\max} \text{ and } M_{\ell\ell q}^{\max,1} \quad (6.20)$$

However, this is feasible only when the measured endpoint of the $(\ell\ell q)$ mass distribution, corresponds to $M_{\ell\ell q}^{\max,1}$. In other cases, depending on the mass hierarchy of the four new particles, the true endpoint can be $M_{\ell\ell q}^{\max,2}$ or $M_{\ell\ell q}^{\max,3}$, and an additional measurement is required in order to constrain the sparticle masses.

A variable that offers an additional constraint to the endpoint technique is the sum of the $(\ell_1 q)$ and $(\ell_2 q)$ masses. The endpoint of the distribution of this variable does not correspond to the

sum of the maxima of the separate distributions of $(\ell_1 q)$ and $(\ell_2 q)$, since these two maxima are reached in different kinematic configurations. The endpoint of this sum is instead reached in the configuration where the two leptons are emitted opposite to the quark, in the $Q = \tilde{q}$ rest frame, as depicted in fig. 6.5. In this case, it is $M(\ell_1 q) = M(\ell_1 q)^{\max}$ and $M(\ell_2 q) = M(\ell_2 q)^{\max,2}$, and therefore the endpoint of the sum is calculated as

$$\begin{aligned} (M_{\ell_1 q} + M_{\ell_2 q})^{\max} &= M_{\ell_1 q}^{\max} + \frac{M_R}{M_X} M_{\ell_2 q}^{\max} \\ &= M_Q \sqrt{\left(1 - \frac{M_X^2}{M_Q^2}\right)} \left[\sqrt{\left(1 - \frac{M_R^2}{M_X^2}\right)} + \frac{M_R}{M_X} \sqrt{\left(1 - \frac{M_O^2}{M_R^2}\right)} \right] \end{aligned} \quad (6.21)$$

With some algebra, the above relation can also be written in terms of the $(\ell_1 q)$ and $(\ell \ell q)$ endpoints as

$$(M_{\ell_1 q} + M_{\ell_2 q})^{\max} = M_{\ell_1 q}^{\max} + \sqrt{(M_{\ell \ell q}^{\max,1})^2 - (M_{\ell_1 q}^{\max})^2} \quad (6.22)$$

As can be seen in eq.(6.22), the endpoint of this variable provides direct information on the desired maximum (the “first one”) of the $(\ell \ell q)$ distribution.

6.2 The mSUGRA LM1 and LM6 benchmark points

In this thesis, the endpoint technique is applied using the realisation of two different supersymmetric models each defined by a set of parameters within the theoretical framework of mSUGRA. The parameters of the models are chosen among pre-defined test points which have been widely used for studying the sensitivity of SUSY signals just beyond the expected of the Tevatron experiments reach. These test points have been designed to cover as widely as possible the different experimental signatures of supersymmetry. They have been categorized in: i) the Low Mass (LM) SUSY points, which are more relevant to the early period of the LHC data taking and ii) the High Mass (HM) test points relevant to the ultimate reach of LHC. The location of the benchmark points in the $(m_0, m_{1/2})$ plane is shown in figure 6.8.

The working points of the thesis belong to the first category of the LM benchmark points, and are taken to be LM1 and LM6. These points are compatible with WMAP Cold Dark Matter limits in a strict mSUGRA scenario, and are the same as the post-WMAP benchmark points B’ (for LM1) and C’ (for LM6), that can be found in reference [40].

The LM1 point lies in the region of the mSUGRA plane where

$$\text{LM1 : } m_0 = 60 \text{ GeV}/c^2, \quad m_{1/2} = 250 \text{ GeV}/c^2 \quad (6.23)$$

whereas for LM6, the corresponding parameters are

$$\text{LM6 : } m_0 = 85 \text{ GeV}/c^2, \quad m_{1/2} = 400 \text{ GeV}/c^2 \quad (6.24)$$

Both points assume that $A_o = 0$, $\tan \beta = 10$, $\mu > 0$. The higher values of m_0 and $m_{1/2}$ in the LM6 case leads on average to heavier supersymmetric particles. As a result, the LM6 cross-section is small, $\sigma^{\text{LM6}}(\text{LO}) = 4\text{pb}$, approximately one order of magnitude smaller than that of LM1 ($\sim 40\text{pb}$).

6.2. THE MSUGRA LM1 AND LM6 BENCHMARK POINTS

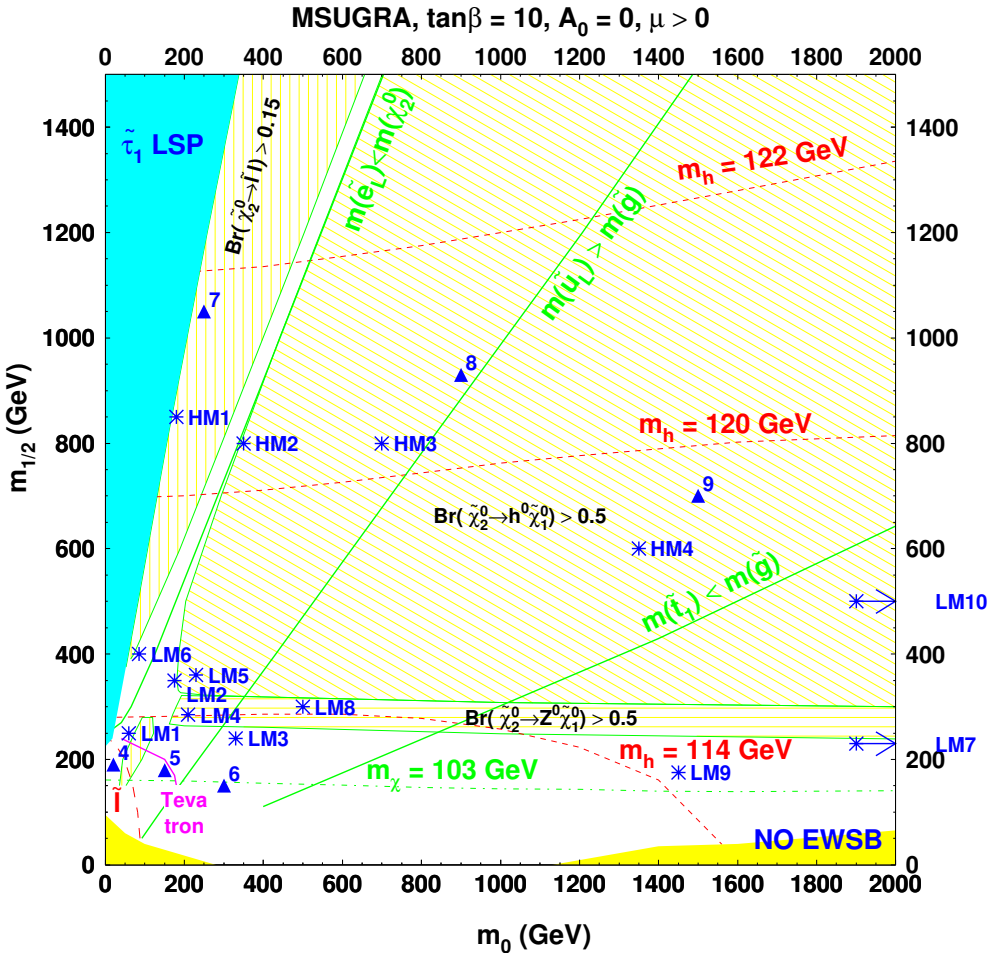


Figure 6.8: The m SUGRA ($m_0, m_{1/2}$) plane showing the position of the test points. Also shown: the expected reach of Tevatron as well as limits from LEP on $m_h > 114$ GeV, chargino and selectron masses. The regions where the $\tilde{\chi}_2^0$ decays dominantly in $\tilde{\chi}_2^0 \rightarrow h^0 \tilde{\chi}_1^0, Z^0 \tilde{\chi}_1^0$ or $\ell^+ \ell^- \tilde{\chi}_1^0$, are distinguished in shaded yellow fill.

LM1 and LM6 points were chosen because of their significant branching ratio to the signal decay chain under study (6.1). The characteristics relevant to an enhancement of this decay can be realised from the particular mass spectrum of their model and their branching ratios to the various supersymmetric decays. Tables 6.1 and 6.2 show the supersymmetric particle masses at points LM1 and LM6 respectively, as calculated with ISAJET 7.69. The same generator used to calculate the branching ratios; the most significant of them are shown on table 6.4.

One of the common features of the two points is that they are both located in the region of the mSUGRA where the gluinos are heavier than the squarks and therefore the gluinos decay dominantly in $q\tilde{q}$ pairs. Because of the mSUGRA assumptions, the lightest two neutralinos are the $\tilde{\chi}_1^0$, which is mostly bino-like, and $\tilde{\chi}_2^0$, which is mostly wino-like. For this reason, the right-handed squark (\tilde{q}_R) decays almost exclusively directly into $q\tilde{\chi}_1^0$. On the other hand, the left-handed squark (\tilde{q}_L) has a non-negligible branching ratio to decay via the $\tilde{\chi}_2^0$ or $\tilde{\chi}_1^\pm$.

CHAPTER 6. THE ENDPOINT TECHNIQUE

Table 6.1: *Supersymmetric particle masses at LM1 benchmark point calculated with ISAJET 7.69 [GeV].*

gluino / squarks :	\tilde{g} 611.3	\tilde{d}_L 564.	\tilde{d}_R 541.2	\tilde{u}_L 558.	\tilde{u}_R 541.5	\tilde{b}_2 535.	\tilde{b}_1 514.2	\tilde{t}_2 575.8	\tilde{t}_1 411.9
sleptons :	\tilde{e}_L 188.6	\tilde{e}_R 118.8	$\tilde{\tau}_2$ 191.7	$\tilde{\tau}_1$ 110.5	$\tilde{\nu}_{eL}$ 168.	$\tilde{\nu}_{\tau L}$ 168.	higgses :	H^\pm 382.2	A 373.
gauginos :	$\tilde{\chi}_4^0$ 361.8	$\tilde{\chi}_3^0$ 341.3	$\tilde{\chi}_2^0$ 179.6	$\tilde{\chi}_1^0$ 94.9	$\tilde{\chi}_2^\pm$ 361.	$\tilde{\chi}_1^\pm$ 179.5	higgses :	H 374.2	h 112.9

Table 6.2: *Supersymmetric particle masses at LM6 benchmark point calculated with ISAJET 7.69 [GeV].*

gluino / squarks :	\tilde{g} 939.8	\tilde{d}_L 863.9	\tilde{d}_R 828.3	\tilde{u}_L 859.9	\tilde{u}_R 830.9	\tilde{b}_2 815.9	\tilde{b}_1 789.5	\tilde{t}_2 836.9	\tilde{t}_1 652.6
sleptons :	\tilde{e}_L 291	\tilde{e}_R 176.7	$\tilde{\tau}_2$ 292.4	$\tilde{\tau}_1$ 169.5	$\tilde{\nu}_{eL}$ 275.5	$\tilde{\nu}_{\tau L}$ 274.9	higgses :	H^\pm 588.8	A 579.6
gauginos :	$\tilde{\chi}_4^0$ 533.8	$\tilde{\chi}_3^0$ 518.2	$\tilde{\chi}_2^0$ 304.8	$\tilde{\chi}_1^0$ 158.1	$\tilde{\chi}_2^\pm$ 533.2	$\tilde{\chi}_1^\pm$ 305.3	higgses :	H 583.6	h 116.8

Furthermore, the masses of the second neutralino ($\tilde{\chi}_2^0$) are larger than at least one of the right-handed or left-handed sleptons ($\tilde{\ell}_{L/R}$), allowing for the leptonic two-body decays of the $\tilde{\chi}_2^0$ to be open and dominant over all other possible decay modes

$$\tilde{\chi}_2^0 \rightarrow h^0 \tilde{\chi}_1^0, Z^0 \tilde{\chi}_1^0, \ell^+ \ell^- \tilde{\chi}_1^0 \quad (6.25)$$

At LM1, the leptonic decays of $\tilde{\chi}_2^0$ are only viable through a right-handed slepton and a lepton ($\tilde{\ell}_R \ell$) with a branching ratio at 11.2%. A significant branching ratio appears also for the $\tilde{\tau}_1 \tau$ mode, at 46%, which is expected to give rise to a substantial background from two opposite-sign same flavor dilepton coming from τ 's in the dilepton signal. A moderate branching ratio of the decay $\tilde{\chi}_1^\pm \rightarrow \tilde{\nu}_\ell \ell^\pm$ at 36%, will also give a source of lepton background (still symmetric in flavor) to the signal $\tilde{\chi}_2^0$ decay chain.

Table 6.3: Production cross sections of supersymmetric final states at LM1 and LM6, calculated with PYTHIA interfaced with ISAJET 7.69 [pb].

σ (pb)	$\sigma(\tilde{g}\tilde{g})$	$\sigma(\tilde{g}\tilde{q}_L)$	$\sigma(\tilde{g}\tilde{q}_R)$	$\sigma(\tilde{q}_L\tilde{q}_L)$	$\sigma(\tilde{q}_L\tilde{q}_R)$	$\sigma(\tilde{q}_R\tilde{q}_R)$	$\sigma(\tilde{b}\tilde{q}_R)$	$\sigma(\tilde{b}\tilde{g})$	$\sigma(\tilde{b}\tilde{b})$
LM1: 40	4.4	9.2	10	2.8	4	3.2	0.24	0.36	0.4
LM6: 4	0.24	0.78	0.87	0.36	0.5	0.44	0.02	0.03	0.04

6.2. THE MSUGRA LM1 AND LM6 BENCHMARK POINTS

At LM6, the $\tilde{\chi}_2^0$ decays to a left-handed slepton and a lepton ($\tilde{\ell}_L \ell$) with a rate of 11%. The decay can proceed as well via a right-handed slepton but the branching ratio is quite reduced: $\text{BR}(\tilde{\chi}_2^0 \rightarrow \tilde{\ell}_R^\pm \ell^\mp) = 1.9\%$. This is in general the case for the regions of the mSUGRA parameter space where the $m_{\tilde{\chi}_2^0} > m_{\tilde{\ell}_L}$, since the right-handed sleptons ($\tilde{\ell}_R$) are always lighter than the left-handed sleptons ($\tilde{\ell}_L$). The rates of the $\tilde{\tau}\tau$ decay modes of $\tilde{\chi}_2^0$ are at a lower level ($\sim 14\%$) than at LM1, whereas the leptonic decays of the $\tilde{\chi}_1^\pm$ are enhanced (44%) here, resulting in a more involved di-lepton background.

In short, the supersymmetric decay chain for which the measurement of the endpoints in invariant mass distributions of leptons and quarks will be investigated in the following sections, appear in the two benchmark points as:

$$\text{LM1 : } (\tilde{g} \xrightarrow{21.6\%} \tilde{q}_L \xrightarrow{31\%} \tilde{\chi}_2^0 q \xrightarrow{11.2\%} \tilde{\ell}_R^\pm \ell^\mp q \xrightarrow{100\%} \ell^\pm \ell^\mp \tilde{\chi}_1^0 q) \quad [6.26]$$

$$\text{LM6 : } (\tilde{g} \xrightarrow{18.4\%} \tilde{q}_L \xrightarrow{31.8\%} \tilde{\chi}_2^0 q \xrightarrow{11\%} \tilde{\ell}_L^\pm \ell^\mp q \xrightarrow{100\%} \ell^\pm \ell^\mp \tilde{\chi}_1^0 q) \quad [6.27]$$

Table 6.4: *Branching ratios of characteristic decays at LM1 and LM6.*

SUSY decay	LM1	LM6
$\text{BR}(\tilde{g} \rightarrow q\tilde{q}_L)$	21.6%	18.4%
$\text{BR}(\tilde{g} \rightarrow q\tilde{q}_R)$	40.9%	35.6%
$\text{BR}(\tilde{q}_L \rightarrow q\tilde{\chi}_2^0)$	31%	31.8%
$\text{BR}(\tilde{q}_L \rightarrow q\tilde{\chi}_1^\pm)$	47.4%	63.0%
$\text{BR}(\tilde{q}_R \rightarrow q\tilde{\chi}_1^0)$	98.4%	99.6%
$\text{BR}(\tilde{\chi}_2^0 \rightarrow \tilde{\ell}_R \ell)$	11.2%	1.9%
$\text{BR}(\tilde{\chi}_2^0 \rightarrow \tilde{\ell}_L \ell)$	-	11%
$\text{BR}(\tilde{\chi}_2^0 \rightarrow \tilde{\tau}_1 \tau)$	46.4%	14%
$\text{BR}(\tilde{\chi}_3^0 \rightarrow Z\tilde{\chi}_1^0)$	12.2%	10.7%
$\text{BR}(\tilde{\chi}_3^0 \rightarrow Z\tilde{\chi}_2^0)$	19.6%	23.4%
$\text{BR}(\tilde{\chi}_1^\pm \rightarrow \tilde{\nu} \ell)$	36.3%	43.6%
$\text{BR}(\tilde{\chi}_1^\pm \rightarrow \tilde{\ell}_L \nu)$	-	10%

6.3 Invariant mass distributions at LM1 and LM6

In this section, the invariant mass distributions of the various combinations between leptons and quarks coming from the decay chain (6.1) are illustrated for the two models presented in the previous section. The correlations between different mass distributions are demonstrated and at the same time methods to identify particular endpoints versus others are discussed. The aim of the study is to highlight methods on the observability of the endpoints without introducing model dependent assumptions.

The mSUGRA LM1 and LM6 points have been generated with ISAJET 7.69 which was interfaced with PYTHIA for the parton shower evolution. Monte Carlo samples in the form of ROOT trees were obtained containing information on both the generated as well as the simulated/reconstructed quantities of particles. The statistics available for these samples correspond to 300fb^{-1} of integrated luminosity. In this section, invariant mass distributions of leptons and quarks are plotted at the generator level and only partons from the PYTHIA documentation particle list, i.e. before the final state radiation (FSR), are used. In order to tag the events containing the desired supersymmetric decay chain, an identification of all particles belonging to the chain must be made. Using the PYTHIA mother-daughter relations, events with two opposite-sign and same-flavor leptons and a quark coming from the same signal squark were selected. The squark was allowed to be any of the left-handed up-type and down-type squark or a right-handed squark. In addition, only squarks of the first two families were taken into account. Although, a right-handed squark is primarily decayed into $q\tilde{\chi}_1^0$ (with almost 98% branching ratio), a small but non-negligible fraction of events were tagged to contain the signal chain coming from a \tilde{q}_R decaying to $q\tilde{\chi}_2^0$.

The effective mass distributions between combinations of the two leptons with the quark were plotted for the events described above at generator level. This level of analysis will allow for a study of the mass distributions which are free of any FSR or detector effects upon the expected shape of the distributions. However, it was noticed that the finite decay width of heavy supersymmetric particles can be considerably large, resulting in a smearing of the distributions. Figures 6.9 show as an example the distributions of the squark masses for the cases of an up-type or down-type \tilde{q}_L and a \tilde{q}_R . The distributions reflect the shape of a Breit-Wigner distribution for each squark as built in ISAJET which is used to generate the mass spectrum of the particles. The variation of the effective mass shapes due to the width of sparticles does not affect the actual endpoint values whatsoever.

The endpoints of the mass distributions have been calculated from the centre mass values of the supersymmetric particles involved in the signal decay chain, according to the formulae presented in the previous section. An overview of the endpoint values for all distributions in the LM1 and LM6 points are shown in table 6.5. The values assume the mass of the squark of the first two families, $Q = \tilde{q}$, in the endpoint formulae. The differences in the endpoint values which are obtained by an up- or down-type squark are found close, varying by $\sim 0.5\%$. The effect is smeared out in the simulated (or real data) distributions where the detector effects dominate and therefore will not be taken into account in the subsequent sections.

6.3. INVARIANT MASS DISTRIBUTIONS AT LM1 AND LM6

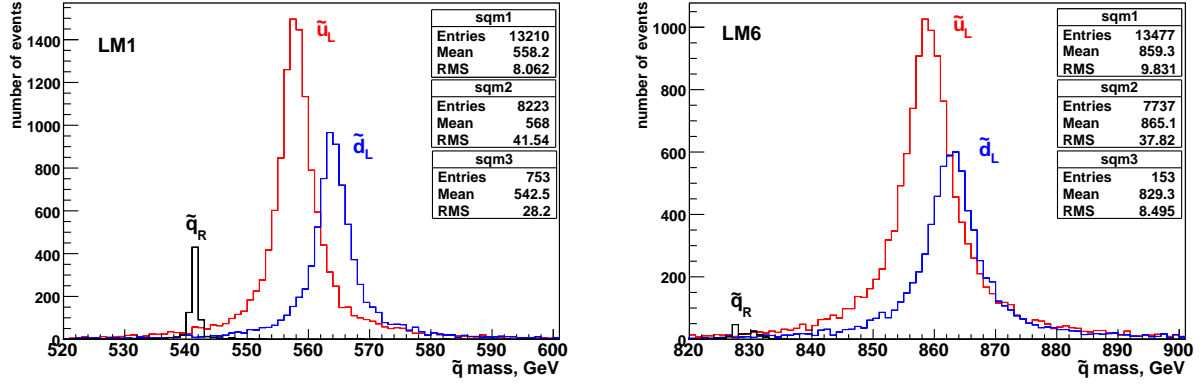


Figure 6.9: Distributions of the mass for up-type, down-type left-handed squarks (\tilde{u}_L and \tilde{d}_L) and right-handed squarks (\tilde{q}_R) generated by ISAJET. The shape of the distributions reflect the form of a Breit-Wigner which was used to account for the finite decay width of the squarks.

6.3.1 Dilepton invariant mass

The invariant mass distributions of the dilepton system is illustrated separately for the LM1 and LM6 cases in fig. 6.10. A characteristic triangular shape is shown in the distributions, with an endpoint value at $81\text{GeV}/c^2$ for LM1 and at $76.1\text{GeV}/c^2$ for LM6. In the latter case, the distribution of a second triangle is superimposed corresponding to the case where the two-body decay of the $\tilde{\chi}_2^0$ is mediated by a right-handed slepton. Due to the reduced branching ratio of the decay, the question of whether it can be observed experimentally remains open.

6.3.2 Lepton - quark invariant masses

The lepton - quark invariant masses are plotted next, for the $(\ell_1 q)$ and $(\ell_2 q)$ combinations superimposed. $M_{\ell_1 q}$ forms a triangular shape in red and $M_{\ell_2 q}$, in blue, shows a triangular shape up to $M_{\ell_2 q} = M_{\ell_2 q}^{\max,2}$ and a logarithmically falling part up to $M_{\ell_2 q} = M_{\ell_2 q}^{\max}$. The endpoint $M_{\ell_2 q}^{\max}$ is greater than $M_{\ell_1 q}^{\max}$ in the case of LM6, as it can be verified by the condition given in (6.13). The situation is reversed in the case of LM1.

CHAPTER 6. THE ENDPOINT TECHNIQUE

Table 6.5: *The upper endpoint values in the effective mass distributions involving the two leptons and the quarks, at the LM1 and LM6 benchmark points.*

Endpoint	LM1 value (GeV/c²)	LM6 value (GeV/c²)	formula
$M_{\ell\ell}^{\max}$	81.0	76.1	(6.4)
$M_{\ell_1 q}^{\max}$ from \tilde{u}_L	396.5	239.1	(6.7)
$M_{\ell_1 q}^{\max}$ from \tilde{d}_L	400.7	240.5	(6.7)
$M_{\ell_2 q}^{\max}$ from \tilde{u}_L	318.5	675.0	(6.9)
$M_{\ell_2 q}^{\max}$ from \tilde{d}_L	322.1	678.6	(6.9)
$M_{\ell_2 q}^{\max,2}$ from \tilde{u}_L	210.8	644.5	(6.12)
$M_{\ell_2 q}^{\max,2}$ from \tilde{d}_L	213.2	647.9	(6.12)
$M_{\ell \ell q}^{\max,1}$ from \tilde{u}_L	449.1	687.4	(6.15)
$M_{\ell \ell q}^{\max,1}$ from \tilde{d}_L	453.9	691.1	(6.15)
$M_{\ell \ell q}^{\max,2}$ from \tilde{u}_L	329.6	679.2	(6.16)
$M_{\ell \ell q}^{\max,2}$ from \tilde{d}_L	332.2	682.9	(6.16)
$M_{\ell \ell q}^{\max,3}$ from \tilde{u}_L	404.7	250.9	(6.18)
$M_{\ell \ell q}^{\max,3}$ from \tilde{d}_L	408.8	252.2	(6.18)
$(M_{\ell_1 q} + M_{\ell_2 q})^{\max}$ from \tilde{u}_L	610.0	883.6	(6.22)
$(M_{\ell_1 q} + M_{\ell_2 q})^{\max}$ from \tilde{d}_L	613.9	888.4	(6.22)

6.3. INVARIANT MASS DISTRIBUTIONS AT LM1 AND LM6

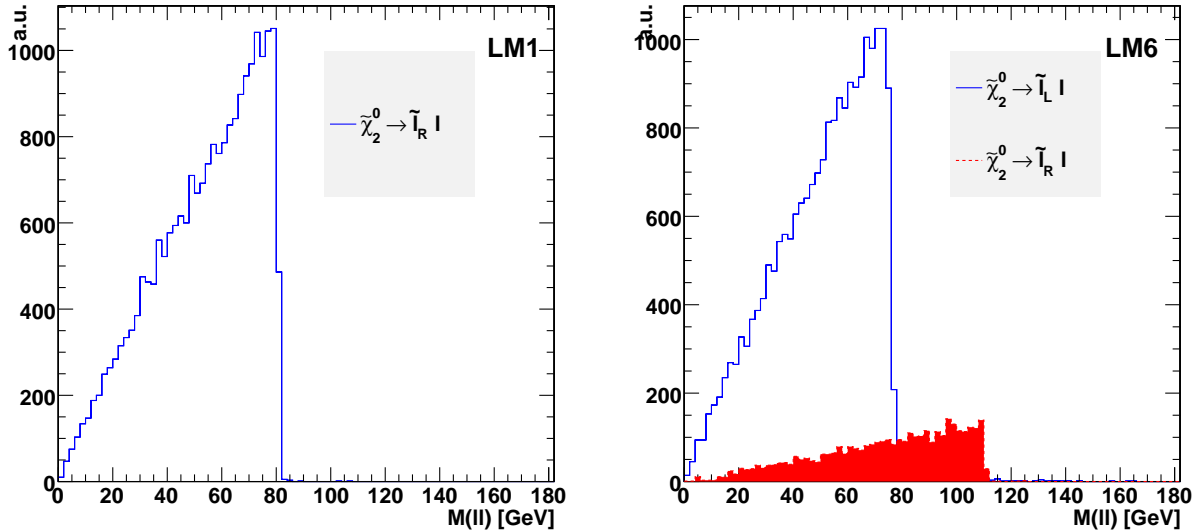


Figure 6.10: $M_{\ell\ell}$ distributions showing a characteristic triangular shape, for the LM1 (left) and LM6 (right) benchmark points. In the LM6 case, a second edge also appears coming from the \tilde{l}_R - mediated two-body decay of the $\tilde{\chi}_2^0$.

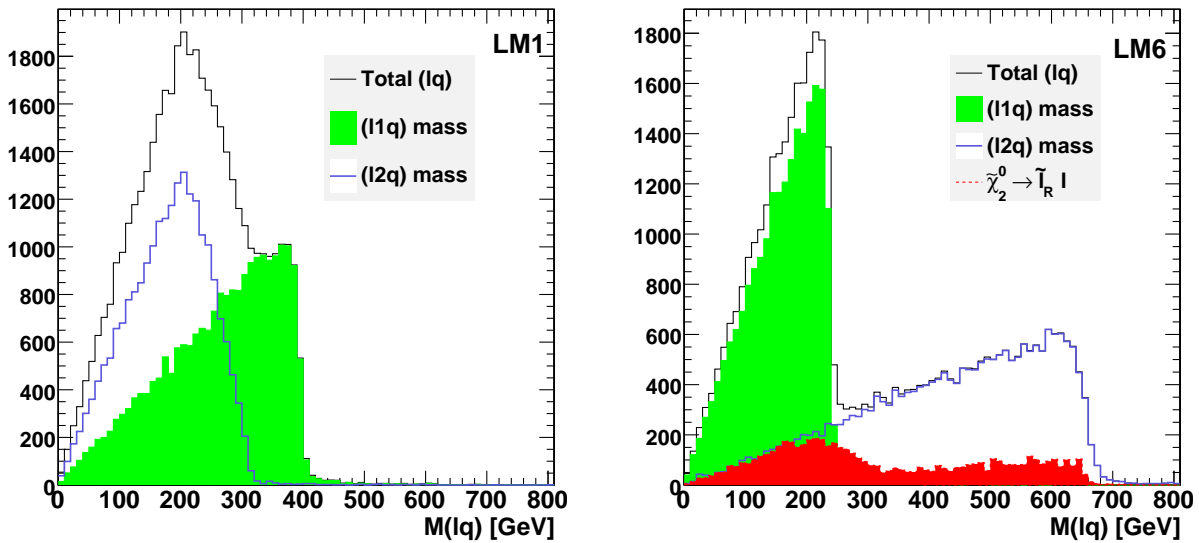


Figure 6.11: M_{lq} distributions for the LM1 (left) and LM6 (right) benchmark points. The $(\ell_1 q)$ and $(\ell_2 q)$ distributions are plotted superimposed in green and blue respectively.

CHAPTER 6. THE ENDPOINT TECHNIQUE

In the scope of this thesis, an attempt to measure the two endpoints in $M_{\ell q}$ directly using the total distribution will be presented. This however requires the earlier identification of the $(\ell_1 q)$ and $(\ell_2 q)$ distributions, in order to unambiguously assign the correct formula, either (6.7) or (6.9), to each of them. This will be shown to be feasible and work well in the case of clearly separated $(\ell_1 q)$ and $(\ell_2 q)$ distributions (LM6 case), whereas in the case of overlapping distributions (LM1 case), it can become tricky.

In both cases the correlation of $M_{\ell q}$ versus the $M_{\ell\ell}$ could aid the attempt. For the example of LM6, figures 6.12 show the corresponding two-dimensional plots for the $(\ell_1 q)$ and $(\ell_2 q)$ distributions separately. As shown in section 5.1.2, the $M_{\ell_1 q}$ distribution can attain its maximum for any value of $M_{\ell\ell}$, whereas the $M_{\ell_2 q}$ distribution is maximized when $M_{\ell\ell} = M_{\ell\ell}^{\max}$. The same picture has also been observed in the correlation plots for LM1. Therefore, a plot of the total $M_{\ell q}$ distribution for high values of $M_{\ell\ell}$ should enhance the $M_{\ell_2 q}$ distribution against the $M_{\ell_1 q}$ one, so that a distinction between the two can be made¹. The effectiveness of the method is investigated already at the generator level. Figures 6.13 show the (ℓq) distributions after a cut on the dilepton mass at $70\text{GeV}/c^2$ has been applied.

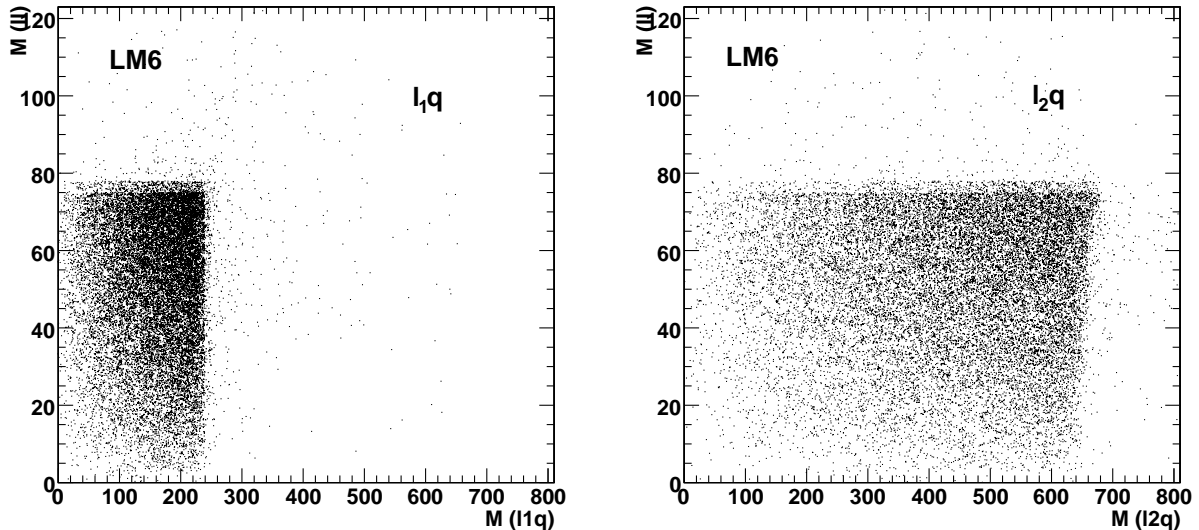


Figure 6.12: The correlation of $M_{\ell_1 q}$ (left) and $M_{\ell_2 q}$ (right) distributions with the $M_{\ell\ell}$ mass.

The endpoint values in the LM6 $M_{\ell q}$ distribution are, $M_{\ell_1 q}^{\max} = 239.1\text{GeV}/c^2$, $M_{\ell_2 q}^{\max} = 675.\text{GeV}/c^2$ and $M_{\ell_2 q}^{\max,2} = 644.5\text{GeV}/c^2$. The measurement of the position of the endpoints corresponding to the signal decay chain ($\tilde{\ell}_L$ - mediated), is however affected by the interference of the distributions coming from the $\tilde{\ell}_R$ - mediated decay. The sample can be cleaned from these secondary events by applying an upper cut $M_{\ell\ell} < M_{\ell\ell}^{\max}$, as soon as the dilepton endpoint has been measured.

¹Due to the large difference of the LM6 edge positions, the $M_{\ell\ell}$ cut has only a marginal effect in the LM6 distributions.

6.3. INVARIANT MASS DISTRIBUTIONS AT LM1 AND LM6

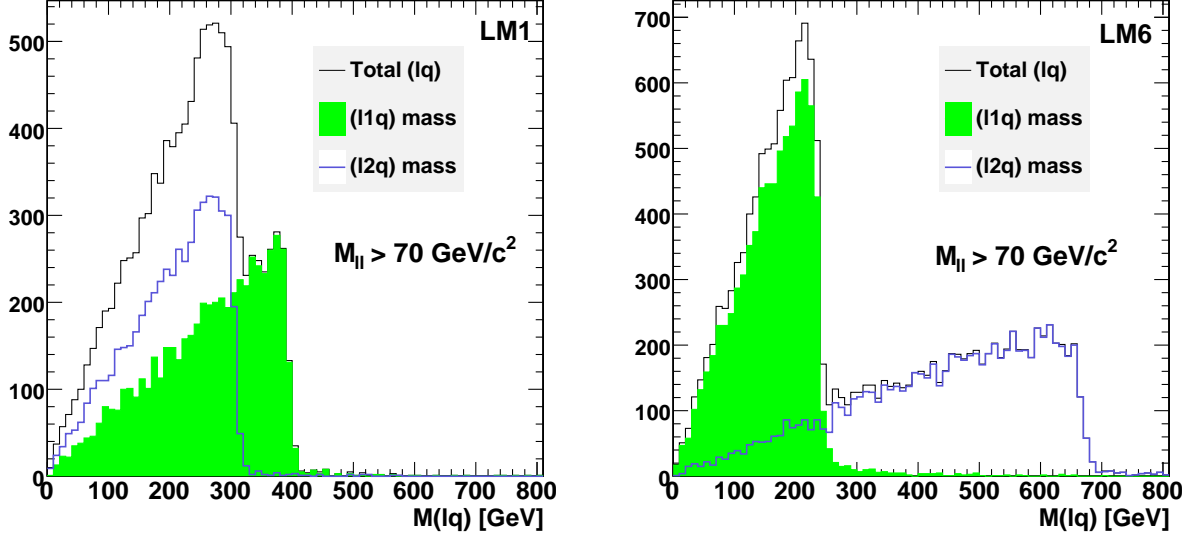


Figure 6.13: $M_{\ell q}$ distributions for the LM1 (left) and LM6 (right) benchmark points, after a cut on the dilepton mass $M_{ll} > 70 \text{ GeV}/c^2$. The $(\ell_1 q)$ and $(\ell_2 q)$ distributions are plotted superimposed in green and blue respectively.

6.3.3 Dilepton - quark invariant mass

The invariant mass distributions of the dilepton-quark system are shown next (see fig. 6.14). The identification of the true endpoint in the distribution is investigated as follows:

The plot of $M_{\ell\ell q}$ versus $M_{\ell\ell}$ is considered first. The correlation plots (see fig. 6.15) indicate a true endpoint of $M_{\ell\ell q}$ at the minimum values of $M_{\ell\ell}$ for both the LM1 and LM6 distributions. This means that $M_{\ell\ell q}^{\max} = M_{\ell\ell q}^{\max,1}$. However, the endpoint appears in the region where there are few events and its observation is ambiguous. An alternative approach is to look for the true endpoint $M_{\ell\ell q}$ using its correlation with $M_{\ell q}$ mass. Figures 6.16 show the corresponding two-dimensional plots for the $(\ell_1 q)$ and $(\ell_2 q)$ distributions separately. The illustration will refer to the LM6 distributions, for the sake of simplicity.

$M(\ell\ell q)$ vs $M(\ell 1 q)$

From the $(\ell_1 q)$ versus $(\ell\ell q)$ correlation, it can be seen that the maximum $M_{\ell_1 q}^{\max}$ is reached for a wide range of values in $M_{\ell\ell q}$. It is clear that the maximum is also reached for the true maximum of $M_{\ell\ell q}$. The $M_{\ell_1 q}$ is maximized in the two configurations in figures 6.5 and 6.7, which are associated also with the $M_{\ell\ell q}^{\max,1}$ and $M_{\ell\ell q}^{\max,3}$ endpoints respectively. It should be noted that $M_{\ell\ell q}^{\max,3}$ cannot be a true maximum since it is coming together with $M_{\ell_2 q}^{\min}$, and therefore at lower values of $M_{\ell\ell q}$ as indicated on the right of fig. 6.16. It can be verified from table 6.5 that indeed $M_{\ell\ell q}^{\max,3} = 250.9 \text{ GeV}/c^2$ is smaller than $M_{\ell\ell q}^{\max,1} = 687.4 \text{ GeV}/c^2$.

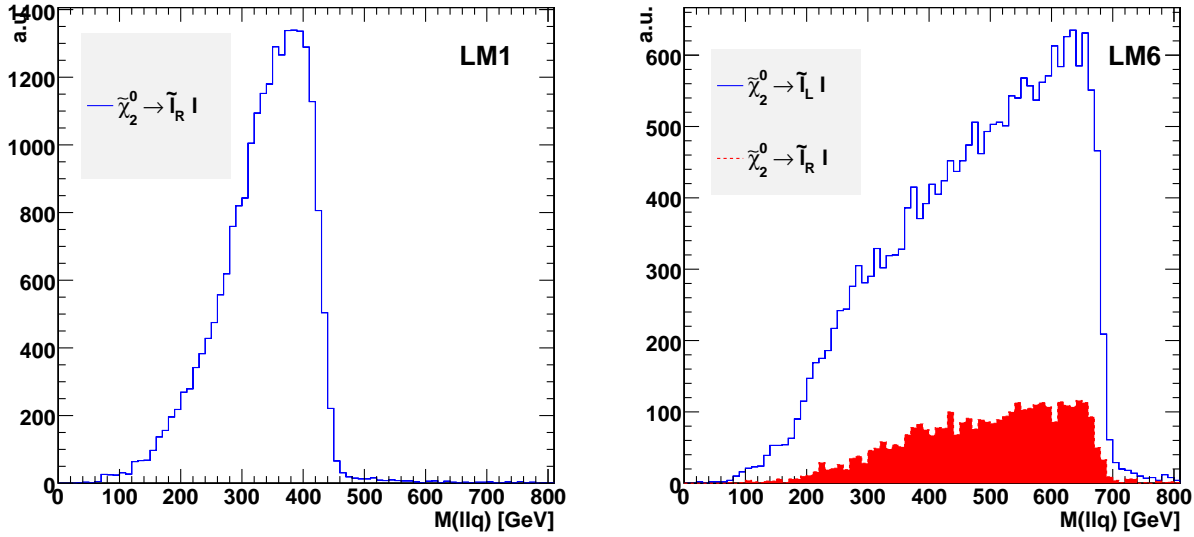


Figure 6.14: $M_{\ell\ell q}$ distributions for the LM1 (left) and LM6 (right) benchmark points.

$M(\text{llq})$ vs $M(\text{l2q})$

For what is seen in the $(\ell_2 q)$ versus $(\ell\ell q)$ correlation plot, the maximum $M_{\ell_2 q}^{\max}$ corresponds to an endpoint in the $M_{\ell\ell q}$ distribution. This is compatible with the fact that there is only one configuration (fig. labelled 6.4) leading to the maximum for $M_{\ell_2 q}$. Therefore, the corresponding $M_{\ell\ell q}$ endpoint is $M_{\ell\ell q}^{\max,2}$; its value is $M_{\ell\ell q}^{\max,2} = 679.2 \text{ GeV}/c^2$. Another endpoint however is visible which is associated with the secondary endpoint of $M_{\ell_2 q}$, $M_{\ell_2 q}^{\max,2}$. As implied by the configuration in figure 6.5, this endpoint corresponds to $M_{\ell\ell q}^{\max,1}$. Also in this picture, $M_{\ell\ell q}^{\max,2}$ can be excluded from being a true maximum since it minimizes $M_{\ell_1 q}$ (see figure 6.16, left). The true endpoint can therefore be assigned to $M_{\ell\ell q}^{\max,1}$.

In some cases, even if a correlation plot is able to reveal the indicating structure, it will be questionable which of the two endpoints ($M_{\ell\ell q}^{\max,1}$ or $M_{\ell\ell q}^{\max,2}$) is the actual true endpoint of $M_{\ell\ell q}$. The effect is pronounced in SUSY scenarios where the two endpoints $M_{\ell\ell q}^{\max,1}$ and $M_{\ell\ell q}^{\max,2}$, or equivalently the endpoints $M_{\ell_2 q}^{\max}$ and $M_{\ell_2 q}^{\max,2}$, are very close to each other².

Experimentally, the above conclusions cannot be drawn unless a distinction between $M_{\ell_1 q}$ and $M_{\ell_2 q}$ distributions can be established. A possible approach for this has been presented in the previous subsection, when one studies the correlations of $M_{\ell q}$ with $M_{\ell\ell}$. If however no direct evidence can be obtained in this way, the correlation of $M_{\ell q}$ with $M_{\ell\ell q}$ can be used instead. The idea behind this approach is to identify the conditions under which $M_{\ell_1 q}^{\max}$ or $M_{\ell_2 q}^{\max}$ can be obtained. Reversing the ordering of the conclusions above, $M_{\ell_1 q}^{\max}$ must lie between two endpoint values of $M_{\ell\ell q}$, whereas $M_{\ell_2 q}^{\max}$ must coincide with exactly one endpoint (that is the $M_{\ell\ell q}^{\max,2}$ endpoint).

²This is exactly the case at LM6 benchmark point.

6.3. INVARIANT MASS DISTRIBUTIONS AT LM1 AND LM6

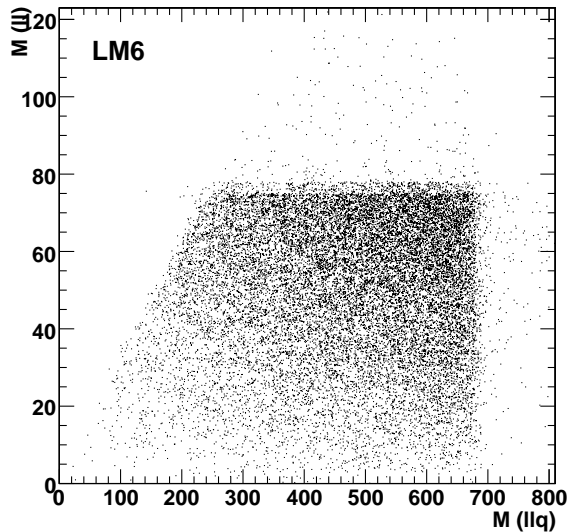


Figure 6.15: *The correlation of $M_{\ell\ell q}$ distribution with $M_{\ell\ell}$.*

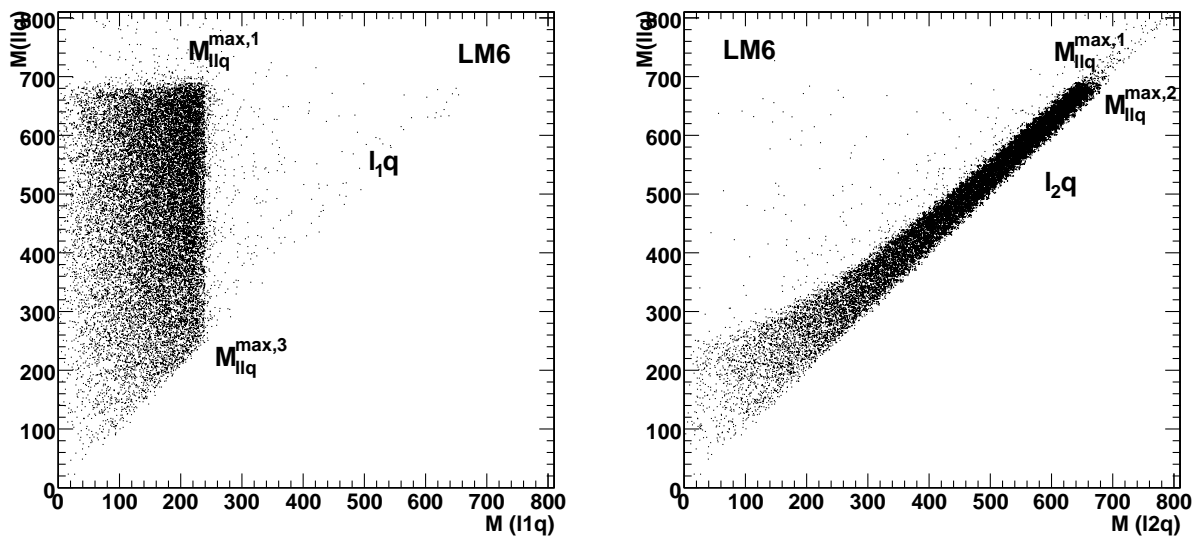


Figure 6.16: *The correlation of $M_{\ell 1q}$ (left) and $M_{\ell 2q}$ (right) distributions with $M_{\ell\ell q}$.*

CHAPTER 6. THE ENDPOINT TECHNIQUE

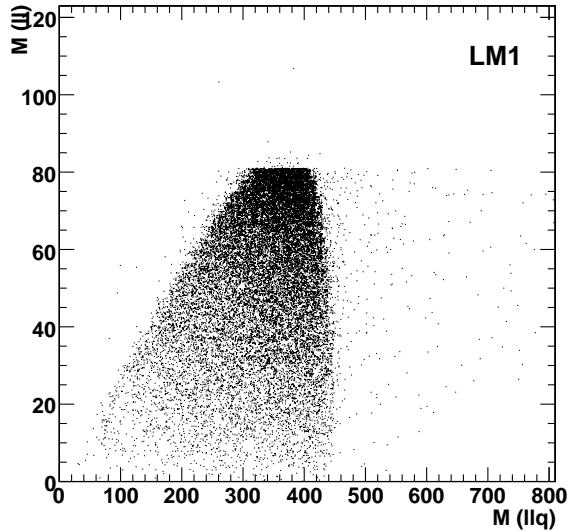


Figure 6.17: *The correlation of $M_{\ell\ell q}$ distribution with $M_{\ell\ell}$.*

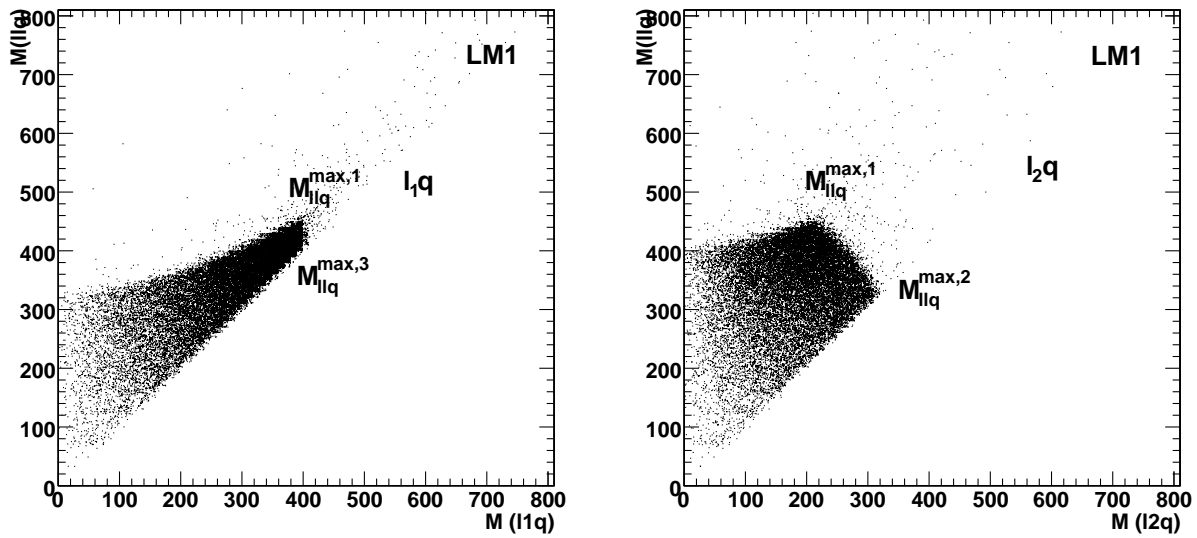


Figure 6.18: *The correlation of $M_{\ell_1 q}$ (left) and $M_{\ell_2 q}$ (right) distributions with $M_{\ell\ell q}$.*

6.3. INVARIANT MASS DISTRIBUTIONS AT LM1 AND LM6

6.3.4 The $M_{\ell_{1q}} + M_{\ell_{2q}}$ invariant mass

The invariant mass distribution of the sum $M_{\ell_{1q}} + M_{\ell_{2q}}$ is shown on figures 6.19 for both the LM1 and LM6 benchmarks. The endpoint of the distribution comes equal to the sum of $M_{\ell_{1q}}^{\max}$ and the secondary endpoint $M_{\ell_{2q}}^{\max,2}$ (i.e. it is not equal to the sum of $M_{\ell_{1q}}$ and $M_{\ell_{2q}}$ maxima). It can be verified that the upper endpoint is $(M_{\ell_{1q}} + M_{\ell_{2q}})^{\max} = 883.6 \text{ GeV}/c^2$, for the case of LM6.

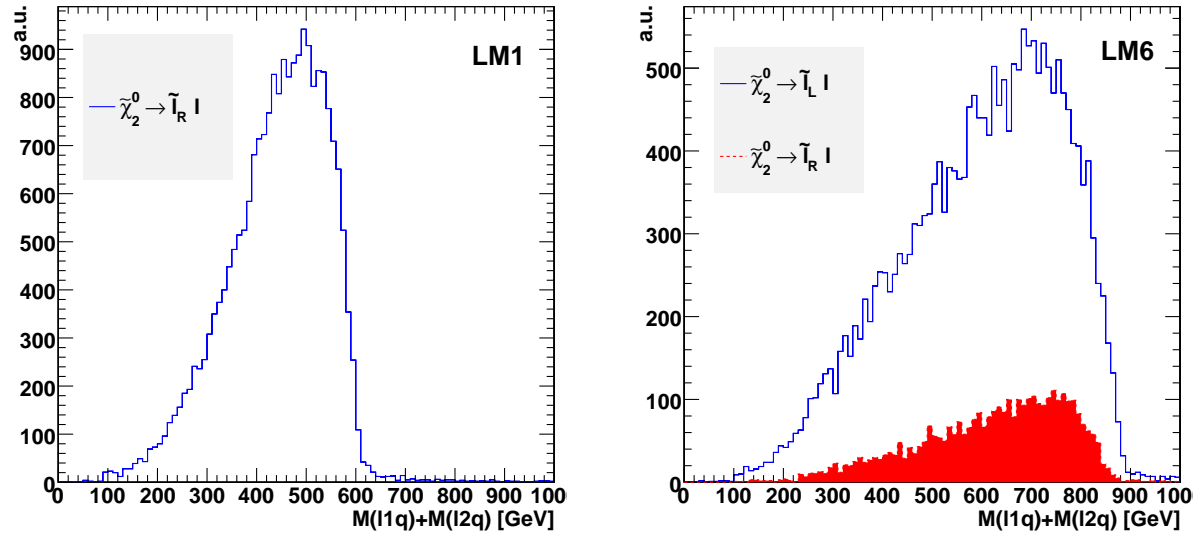


Figure 6.19: $M_{\ell_{1q}} + M_{\ell_{2q}}$ distributions for the LM1 (left) and LM6 (right) benchmark points.

7

Sparticle mass reconstruction

In this chapter, the extraction of the masses of supersymmetric particles from endpoints in mass distributions involving leptons and jets is presented. The mSUGRA benchmark points LM6 and LM1 are used for demonstration. A simple χ^2 fit is performed for the measurement of the endpoint values in the distributions of $M_{\ell\ell}$, $M_{\ell q}$, $M_{\ell\ell q}$ and $M_{\ell_1 q} + M_{\ell_2 q}$. The method of extracting the endpoints is demonstrated assuming a relatively high luminosity¹ in order to unambiguously identify the different sources of difficulties in the reconstruction and fitting procedures.

It is noted that although the $m_{\ell\ell}^{max}$, $m_{q\ell 1}^{max}$ and $m_{q\ell 2}^{max}$ maxima can be identified uniquely, this is not true for the $m_{q\ell\ell}^{max}$ for which the actual value depends on mass ratios between neighbouring particles in the decay chain. The actual shapes of the mass distributions also depend strongly on the SUSY model scenario and the mass hierarchy in it.

Several studies so far have focused on measurements of endpoints based on a fit to the mass distributions only around the region of the edges. Another approach is to exploit the shape of the mass distributions [55]. The shapes are directly related to the masses of the sparticles and an attempt to fit the full mass spectra can, in principle, provide more information than just the endpoints. It will be shown that a direct measurement of mass ratios is, in fact, feasible. In both approaches the difficulty is that, depending on the ratios of the sparticle masses, different configurations and hence different formulae are valid for the masses or their endpoints at a given model. Throughout the analysis, a possible identification of the correct mass hierarchy (and therefore expression of the mass) to be used is investigated, based on correlations between different effective mass distributions.

Finally, a global fit to the endpoints results in the extraction of the supersymmetric masses involved in the $\tilde{\chi}_2^0$ decay chain.

7.1 Event selection

For the supersymmetric signal, generator-level data were produced with the PYTHIA Monte Carlo which was interfaced with ISAJET 7.69 to account for mass spectra and branching ratios calculations. 100 k ntuple events were then simulated with OSCAR/ORCA_8.7.1 [42, 43] and officially

¹The sample statistics will correspond to 15fb^{-1} for LM1 and 300fb^{-1} of integrated luminosity for LM6.

CHAPTER 7. SPARTICLE MASS RECONSTRUCTION

published as Digi/DSTs. The analysis was performed accessing the LM6/LM1 Digi using the CMS Object-oriented framework for reconstruction and analysis, ORCA, version 8_7_4. The offline analysis was carried out with the ExRootAnalysis dedicated package of ORCA. During the analysis studies, the susy signal samples were privately reproduced in order to increase the statistics available in the official production. Such samples were further processed with fast simulation, using FAMOS_1_4_0. Comparisons between the FAMOS and ORCA physics objects reconstruction performance were carried out in order to tune and validate the analysis in the fast simulation mode.

The analysis study used collections of offline objects that were stored in the form of ROOT trees. For the leptons, only electrons or muons with $p_T > 10$ GeV and $|\eta| < 2.4$ (acceptance cuts) are selected. Electrons and muons are reconstructed with the *OfflineElectronCandidate* and *GlobalMuonReconstructor* algorithms respectively. Lepton clean-up has been applied by requiring that the ΔR between any electron or muon pair to be greater than 0.1. An additional cut on the electron likelihood, $\text{EleID} > 0.55$, is applied in order to distinguish between real and fake electrons. Additional isolation requirements are then applied to electrons and muons as per analysis requirements: prompt electrons/muons coming from SUSY particles are expected to be isolated as opposed to hadron electrons or muons arising from inside jets. The isolation variable used is formed as $\text{EleIso} = \sum_{\text{tracks}} p_T^{\text{track}} / E_T^{\text{SC}}$ for the electrons and $\text{MuCaloIso} = \text{Calorimeter isolation}$ for the muons. For electrons, a cut $\text{EleIso} < 0.1$ accepts susy electrons with 98% efficiency while it rejects $\approx 82\%$ of electrons from heavy flavors and jets (“hadron electrons”). For muons, the calorimeter isolation requirement $\text{MuCaloIso} < 5$, accepts susy muons again with 98% efficiency and rejects $\approx 90\%$ of the hadron-muons.

Jets reconstructed with the Iterative Cone 0.5 algorithm were used and required to have $E_T^j > 30$ GeV and $|\eta| < 3$. The reconstructed jets were corrected using the standard Monte Carlo jet correction [45, 46]. Additional isolation cuts were applied to jets to account for lepton-jet separation. First, the electromagnetic fraction (EMF) of jets was checked and a cut $\text{EMF} < 0.9$ was chosen in order to reject fake jets from electrons. In addition, a jet is required to be separate from an offline electron within $\Delta R(\text{jet} - e) > 0.5$, unless the ratio of the electron energy divided by the jet energy is less than 0.5 ($E^e/E^{\text{jet}} < 0.5$). No b-tagging was applied. The reason is that for the LM6 sample, the production cross section for final states involving $\tilde{b}_{1,2}$ has been shown to be negligible compared to the \tilde{q}/\tilde{g} final states (see table 6.3). Throughout the analysis, it was therefore considered that the supersymmetric signal decay chain arises only in the \tilde{q} of \tilde{g} cascades involving \tilde{q} ’s of the first two families. Certainly, in other parts of SUSY space, b-tagging can be very effective. This subject, however, will not be investigated in the current analysis.

The analysis selection requirements that were used in order to eliminate the background processes are:

- At least two Opposite Sign (OS) and isolated leptons (e or μ) with $p_T^\ell > 10$ GeV and $|\eta^\ell| < 2.4$. Both Same Flavor (SF) and Different Flavor (DF) di-lepton events were included.
- At least two jets with $E_T^{\text{jet}} > 30$ GeV and $|\eta^{\text{jet}}| < 3$. The E_T requirement was applied to the corrected jets.
- Two hardest jets E_T cut: $E_T^{j1,j2} > 150, 100$ GeV for the LM6 case and $E_T^{j1,j2} > 100, 60$ GeV

7.2. RECONSTRUCTION OF (DI)LEPTON-JET MASSES

for LM1. A different set of E_T -jet cuts were used for the two endpoints due to the harder jet spectrum observed as a result of the higher sparticle masses in LM6.

- Missing E_T cut: $E_T^{miss} > 200$ GeV.

Given the above requirements, as well as the method of the different-flavor ($e\mu$) subtraction of the background presented in chapter 5, the analysis assumes that SM background processes can be totally suppressed for higher values ($>> 1\text{fb}^{-1}$) of integrated luminosity². The reconstruction therefore proceeds without the inclusion of the SM processes, focusing instead in the demonstration of the endpoint technique using primarily the example of the LM6 benchmark point.

7.2 Reconstruction of (di)lepton-jet masses

In this section we proceed with forming the mass distributions of combinations of the observed particles in the decay chain $\tilde{q}_L \rightarrow q\tilde{\chi}_2^0 \rightarrow q\ell\bar{\ell} \rightarrow q\ell\ell\tilde{\chi}_1^0$, namely two leptons with a quark.

7.2.1 Combinatorial background

In every supersymmetric event, sparticles are produced in pairs and therefore two supersymmetric cascade decays evolve in parallel. As a consequence, the reconstruction of the signal decay chain requires the identification of particles which belong to the same cascade. The reconstruction of the dilepton coming from the signal $\tilde{\chi}_2^0$ decay chain involved the selection of two Opposite-Sign and Same-Flavor (OSSF) leptons. With the addition of the quark to combine with the dilepton, several other quarks belonging to the same or the other leg of the susy cascade have to be distinguished (fig. 7.1).

A parton-level analysis of the MC SUSY sample has shown that the quark which is assigned to the signal decay chain is among the two highest-pt quarks in $\approx 92\%$ of the cases. Selecting the two highest- E_T jets in the event, the probability of including the correct quark among the two is maximized. The statement is true over a wide region of the mSUGRA parameter space where the $\tilde{q}\tilde{g}$ production rates dominate the total SUSY cross section. The squark which matches the signal decay can be selected wrongly in two cases: the decay of a \tilde{g} ($\rightarrow \tilde{q}q$) or the decay of a \tilde{q} ($\rightarrow \tilde{\chi}q$) in the other leg of the susy cascades than the signal one. Under some certain conditions which are discussed next, the quark emitted by the gluino is very unlikely to be among the two most energetic quarks in a supersymmetric event³.

There are arguments supporting the above assumption. In the restrict mSUGRA scenario for example there are specific lower bounds which constrain the sfermion to gaugino/gluino mass ratios,

$$0.8 \leq \frac{m_{\tilde{u}_L, \tilde{d}_L}(500\text{GeV})}{|M_3(500\text{GeV})|} \quad (7.1)$$

²In any case, the background can be estimated reliably (and therefore subtracted).

³Leaving therefore the case for only the signal quark or the quark emitted by an initially decayed squark on the other leg of the SUSY cascade, to be found among the two highest- E_T quarks.

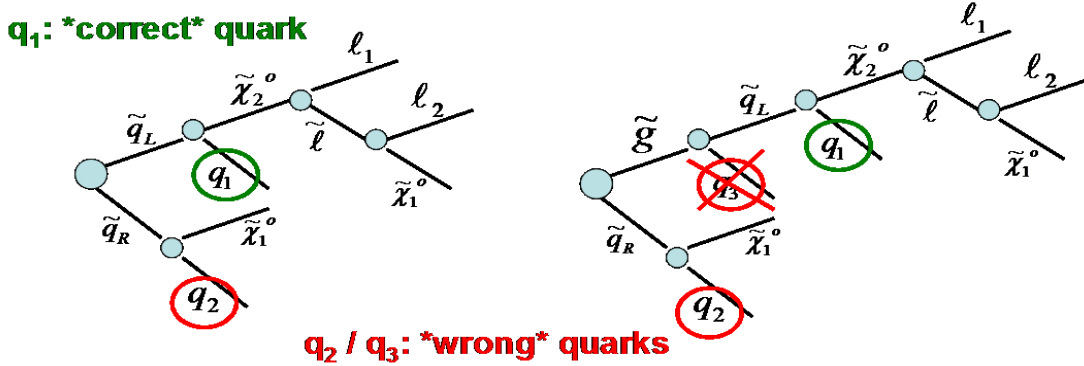


Figure 7.1: Two typical SUSY di-lepton events leading to the supersymmetric signal of a di-lepton coming from the $\tilde{\chi}_2^0$. The pictures demonstrate the sources of combinatorial background arising from the selection between a di-lepton pair ($\ell_1 - \ell_2$ pair) and a quark-jet – will call “correct” quark (q_1) the one matching the same leg with SUSY signal di-lepton, and “wrong” quark (q_2 or q_3) the one matching the other leg of the SUSY cascade. Selecting the two highest- E_T jets in the event, the probability of including the correct one among the two is highly maximized.

which is valid to a scale $Q = 500\text{GeV}$. One can therefore very roughly assign a maximum splitting between the gluino and the squark mass according to $m_{\tilde{q}} \geq 0.8m_{\tilde{g}}$. Additionally, recalling the general relation (2.69) at the weak scale, a minimum mass splitting between the gluino and the neutralinos is implied from the inequality $m_{\tilde{g}} \geq 3m_{\tilde{\chi}_2^0}$. Overall, it leads to the conclusion that

$$(m_{\tilde{g}} - m_{\tilde{q}}) < (m_{\tilde{q}} - m_{\tilde{\chi}_2^0}) \quad (7.2)$$

Therefore, the quark emitted in the gluino decay is on average less energetic than the quark emitted in the squark decay.

Given these expectations, the two hardest jets in the event are considered and their combinations with the two OS leptons are used to reconstruct the invariant masses⁴.

On an event by event basis, the selection will involve either a “signal” dilepton object coming from the $\tilde{\chi}_2^0$ decay, or a “background” dilepton coming from uncorrelated sources. The dilepton is then combined with the two jets, which can be either a signal and an incorrect jet or both incorrect jets. Putting it all together, the following sources of combinatoric background - labelled as B_i - are therefore inevitably introduced:

- a signal dilepton object assigned with an incorrect jet (B_1),
- a non-signal dilepton object assigned with a correct jet (B_2) or,
- a non-signal dilepton assigned with an incorrect jet (B_3).

⁴Assuming that the probability to combine the signal dilepton with a non-correct quark is close to the level of $\sim 50\%$.

7.2. RECONSTRUCTION OF (DI)LEPTON-JET MASSES

Together with the combinations where all objects were to be the true ones (S), the total number of entries N in the (di)lepton-jet invariant mass histogram will be

$$\begin{aligned} N &= S + B_1 + B_2 + B_3 \\ &= S + (B_{11} + B_{12}) + B_2 + (B_{31} + B_{32}) \end{aligned} \quad (7.3)$$

where the numbers of combinations B_1 and B_3 have been each split in two in order to label the entries corresponding to an event where the two hardest jets were a correct-wrong pair (B_{11} and B_{31}) or a wrong-wrong pair (B_{12} and B_{32}).

The estimate of the background from the wrong selection of the dilepton, i.e. cases B_2 and B_3 , is explained in chapter 5. This is going to be handled with the Different-Flavor (DF) subtraction in the OSSF invariant mass distributions in order to remove SF leptons coming from background sources. The combinations B_1 of the wrongly selected jet, although a signal dilepton is reassured, is on the other hand a more involved issue. A study has been performed in order to discriminate between the two combination of the (signal) di-lepton with the two jets (quarks). It has been shown that the di-lepton with the quark belonging to the different decay chain are only weakly correlated and there is no discriminating variable that might be easily used to resolve the correct combination.

The usage of consistency cuts

The rejection of the wrong jet assignments has been treated in several ways in the literature. The most sophisticated one suggests the usage of “consistency” cuts so that to purify the event selection. This method assumes the prior measurement of some quantities and requires that only combinations found consistent with that measurement are kept. This has been proven to work well in for both the $M_{\ell q}$ and $M_{\ell\ell q}$ masses.

In this method, a first attempt to measure the $M_{\ell\ell q}^{\max}$ endpoint consists in plotting only the combination of the dilepton with the jet that gave the minimum value of $M_{\ell q}$ (referred to as $M_{\ell q}^{\min}$). These combinations cannot, by definition, exceed the true $M_{\ell\ell q}$ endpoint and therefore an endpoint value can be extracted from the end point of the $M_{\ell\ell q}^{\min}$ distribution. With a rough estimate of the $M_{\ell q}$ endpoint, only combinations of a lepton with a jet consistent with a value of the $M_{\ell q}$ mass below the measured endpoint are considered. If in addition the dilepton with the second jet in the event forms an $M_{\ell\ell q}$ mass above the measured edge, then the combination is kept; otherwise it is discarded. In this way one ensures that only correct lepton-jet combinations enter in the $M_{\ell q}$ distribution. Still, a small component of wrong assignments are present; these are shown to come from the events where both selected jets are not assigned to the correct quark in the signal chain. As we argued in the beginning of the section, this component is expected to give in general a very small contribution.

The weakness of the method is that the number of events satisfying the criteria above are significantly reduced. In fact, all combinations that were truly correct assignments but their second combination gave an inconsistent result are not used in the final reconstruction histogram. The method should therefore apply to high lumisosity periods of the LHC running.

The mixed event technique

Another approach which could be used is the modeling of the combinatoric background using other lepton-jet combinations. This refers to the method that is known as the “mixed event technique” and was originally used by the ATLAS collaboration [49]. The method has the advantage of a “data-driven technique” to be modeling the background. In the present analysis however, this method is used in a complementary fashion with other approaches as it is not considered as an established reliable method (yet) for the estimate of the combinatorial background under discussion.

The mixed event technique makes use of leptons and jet objects that are taken from different events. Through a random procedure, the leptons found in one event are combined with jets found in another event (satisfying the same selection criteria). The jet is always selected among the two highest- E_T jets with equal probability for both. A problem that arises is the choice of the reference frame in which the four vectors are computed. It is not obvious whether this should be the laboratory frame or the rest frame of the dilepton object for example. Although the latter choice conserves the energy and momentum of the “mixed” event, the laboratory frame is chosen in this case since no significant differences in the resulting mass distributions were observed.

The mixed-event technique proceeds with forming the invariant mass distributions of the randomly chosen dilepton and the jet. Both same-flavor as well as different-flavor dilepton objects are used and two separate distributions are kept. The mixed combinations are therefore used not only to model the combinatorics coming from category B_1 but also to model the ones in B_2 and B_3 corresponding to the background dilepton events. Subtracting the different-flavor mixed-event distribution from the same-flavor one, leads to a distribution which can then be considered to be modeling the B_1 combinatorics.

A comparison of the lepton-jet combination mass shapes predicted with the mixed-event technique (ME) and the true background mass shapes taken from the MC in shown in figures 7.2. The two distributions are shown on the left, whereas the right plot shows their asymmetry which is defined as:

$$\text{Asymmetry} = \frac{\text{MC} - \text{ME}}{\text{MC} + \text{ME}} \quad (7.4)$$

with MC being the Monte Carlo truth distributions formed by the truly wrong lepton-jet assignments, and ME being the lepton-jet mass distribution produced with the mixed-event technique. The agreement between the ME modeling distribution and the true distribution comes fairly good, at least for high mass values and the regions around the first edge of $M_{\ell q}$ (around 240 GeV). However, an asymmetry, at the level of up to $\sim 10\%$ can be noticed with increasing the mass (and around the second edge, at 680 GeV). Along the same lines, fig. 7.3 shows the shape comparison of the $\cos \theta_{[\ell\ell]-q}$ distribution between the di-lepton system and the jet, for the cases forming “truly” wrong di-lepton - jet assignments and the cases formed by the “mixed-event” technique. While the mixed-event result shows a flat distribution in $\cos \theta$ as expected from uncorrelated sources between the dilepton and the jet, the MC truth result shows a (weak) correlation of the two systems, tending to small opening angle between them. It is then obvious that the “mixed-event” technique cannot precisely reproduce the kinematics of the wrong dilepton-jet assignments.

The above comparisons indicate that the mixed-event invariant mass distributions should be used

7.2. RECONSTRUCTION OF (DI)LEPTON-JET MASSES

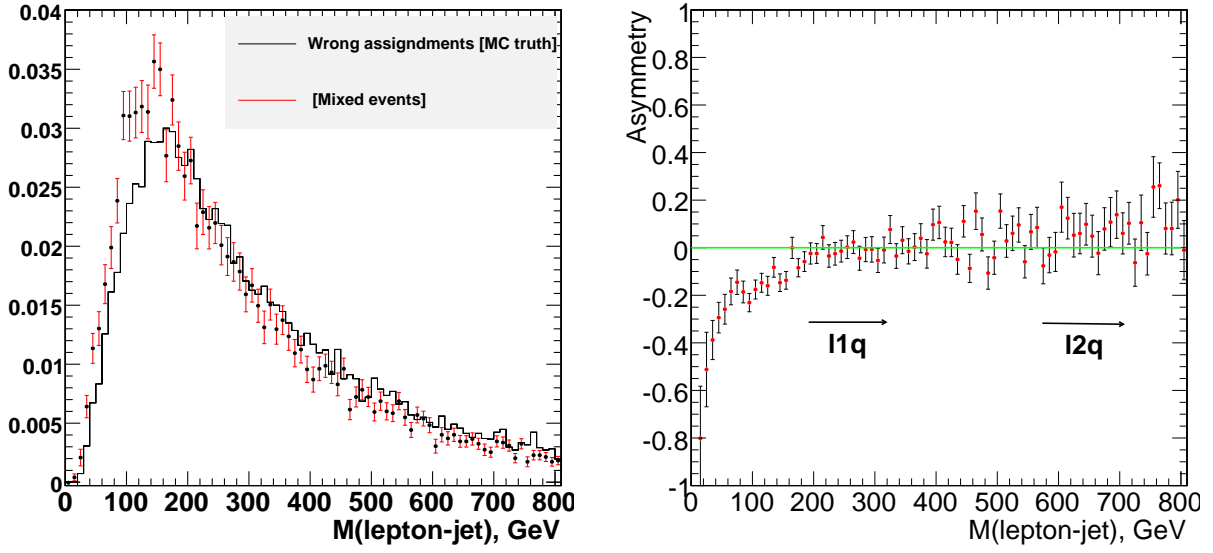


Figure 7.2: Comparison between the “true” $M_{\ell q}$ background coming from combinations of a signal lepton with a wrongly assigned quark (shaded histogram) and the modeling distribution obtained with the mixed-event technique. The right hand plot shows the asymmetry between the two shapes.

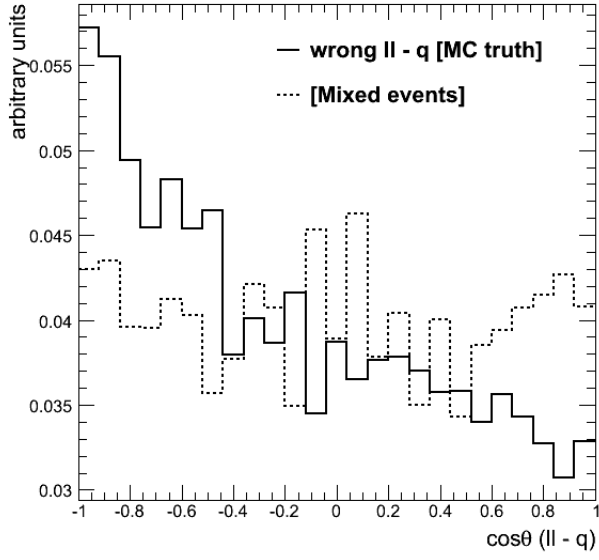


Figure 7.3: Shape comparison of the $\cos\theta$ distribution between the di-lepton system and the quark, for combinations with wrong dilepton-quark assignments (in solid black) and for “mixed-event” combinations (in dashed black).

in a conservative manner, mostly for qualitative analysis purposes, when modeling the combinatorial background sources. First of all, it cannot be safely considered to represent the full shape

of the background and therefore a subtraction from the full mass distribution will not reproduce the original shape of the $M_{\ell q}$ mass. Moreover, the absolute normalization to be used in the subtraction cannot be known. If the number of B_1 combinations were exactly equal to the number of combinations corresponding to a signal dilepton and a correctly assigned jet, then the normalization factor would be indeed 0.5. However, a careful study shows that combinations B_1 result not only from events in which the two highest- E_T jets corresponded to a correct and non-correct jet (B_{11} case), but also to events where both jets were originally selected incorrectly (B_{12} case). As a consequence, the normalization of the background will depend on the SUSY model.

In what follows, the mixed-event technique will be used assuming a normalization factor of 50%, in some cases, in order to provide a rough estimate of the shapes of the background distributions. The technique, however, will not be used in the direct measurement of the endpoints.

7.3 Jet calibration performance

The invariant mass distributions constructed by one lepton and one jet ($M_{\ell q}$) will be fitted over the full mass range in order to extract the endpoints in the distribution. The likelihood function will consist of the convolution of the true shape of the $M_{\ell q}$ with a mass resolution model which is used to describe the smearing of the shape due to the lepton/jet resolutions. The parametrization of the resolution effects is described next.

The mass resolution is dominated by the resolution of the jet energy. The MCJet calibration used to correct the energy of the jets at particle-level⁵. The performance of the calibration procedure was studied in terms of the linearity of the jet response and the jet energy resolution. For this study, particle-level (generated) jets as well as reconstructed jets formed with the same jet algorithm were matched in (η, ϕ) space within a cone of size 0.2. Figure 7.4 shows the average response and the jet energy resolution⁶ as a function of the generated jet E_T using the MCJet calibration method.

The particle-level corrections extracted⁷ from a QCD jet sample, and their application to the supersymmetric sample was shown to restore fairly well the linearity of the Jets. On the other hand, they do not restore well the equality between partons and reconstructed jets for the full range of values of E_T of the parton as shown in fig. 7.5. In this figure, partons (light flavor quarks, b-quarks and gluons) are matched with reconstructed jets within $\Delta R < 0.2$. The resulting response suffers both in terms of the asymptotic value (above 1) and in terms of the rise of the response as a function of the parton p_T .

The effect is known to come from the fact that individual jet flavors (uds, c, b, gluon) need different corrections. This leads to an over- or undercorrection if the MCjet corrections are applied to jets with a flavor composition different than that of QCD jets. In the present case, jets from the decays of \tilde{q}/\tilde{g} of the supersymmetric sample consist mainly of uds and c quarks, which have a higher energy response than b and gluon jets. Consequently, applying MCJet corrections to these

⁵i.e. the method applies scale factors to the energy of the jet in order to correct back to the generator level particle-jet

⁶The plots have been made using a private code to perform the closure test of the correction function and resolution, and do not represent the actual tests of the jet calibration development group.

⁷versus the jet E_T and η

7.3. JET CALIBRATION PERFORMANCE

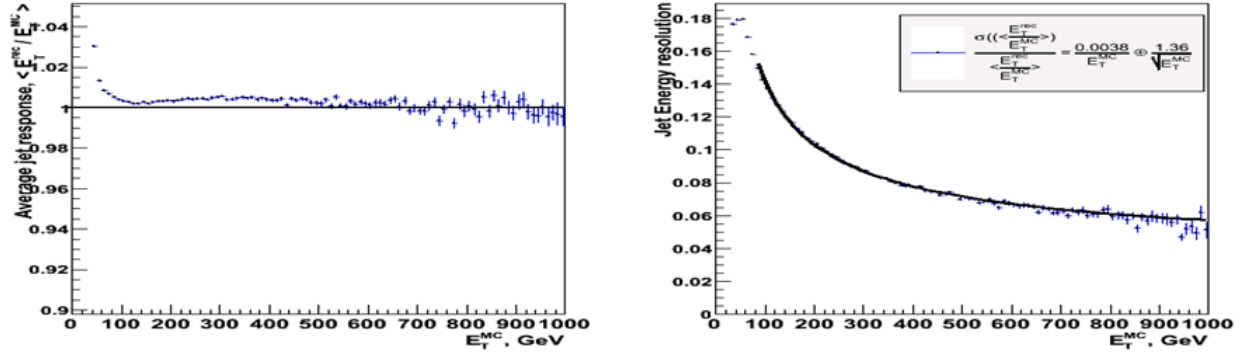


Figure 7.4: Performance of jets reconstructed with the iterative cone 0.5 algorithm and calibrated with the MCJet method. Left plot shows the average response $\langle E_T^{RECO}/E_T^{MC} \rangle$ as a function of the MC jet E_T – Right plot shows the jet resolution, $\sigma(\langle E_T^{RECO}/E_T^{MC} \rangle)/\langle E_T^{RECO}/E_T^{MC} \rangle$, as a function of the MC jet E_T .

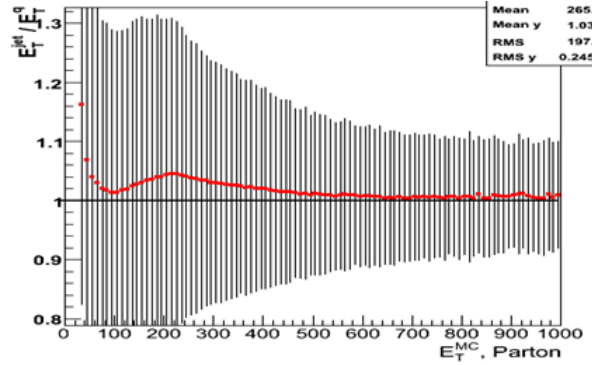


Figure 7.5: Average response (linearity) $\langle E_T^{jet}/E_T^{parton} \rangle$ as a function of the parton energy E_T^{parton} , for MCJet calibrated jets.

jets results in an overcorrection.

Dedicated parton-level corrections have not been applied in what follows, but the effect is taken into account in terms of the results (this will be addressed in section 7.4.3).

7.3.1 Lepton - jet mass resolution

The mass resolution of one lepton with one jet depends on the lepton and jet energies resolutions according to the following formula

$$\frac{\sigma(M_{\ell j})}{M_{\ell j}} = \frac{\sigma(M_{\ell j}^2)}{M_{\ell j}^2} = \frac{1}{2} \sqrt{\left(\frac{\sigma(E_\ell)}{E_\ell} \right)^2 + \left(\frac{\sigma(E_j)}{E_j} \right)^2} \quad (7.5)$$

CHAPTER 7. SPARTICLE MASS RECONSTRUCTION

The mass resolution is dominated by the jet resolution, and the above formula can be simplified to

$$\frac{\sigma(M_{\ell j})}{M_{\ell j}} = \frac{1}{2} \frac{\sigma(E_j)}{E_j} \approx \frac{1}{2} \frac{1.36}{\sqrt{E_j}} \quad (7.6)$$

where the factor 1.36 (see fig. 7.4 - right) accounts for the stochastic term in the jet resolution formula. The result represents a very rough estimate of the lepton-jet resolution and will be considered with some care, since the lepton energy resolution in some cases gives a non-negligible contribution (especially over a large range of the lepton momenta).

The lepton-jet mass resolution formula has been derived from the MC (supersymmetric) sample. A matching between the reconstructed lepton and jet objects with the MC truth has been performed according to requirements that have been described in previous sections. The $\Delta M = M_{\ell j}^{\text{RECO}} - M_{\ell q}^{\text{MC}}$ distributions were plotted in bins of the $M_{\ell q}^{\text{MC}}$ mass; figure 7.6 shows the distributions for four mass regions (100-200 GeV, 200-300 GeV, 300-400 GeV, 400-500 GeV). The distributions are fitted with a resolution model with the form of the sum of two gaussians; the first one to describe the gaussian of minimum sigma and the second one, the gaussian with the maximum sigma:

$$\begin{aligned} \text{ResModel}(M_{\ell j}) &= \alpha \cdot \text{Gauss}_1(M_{\ell j}; \mu_1, \sigma_{\min}) \\ &+ (1 - \alpha) \cdot \text{Gauss}_2(M_{\ell j}; \mu_2, \sigma_{\max}) \end{aligned} \quad (7.7)$$

The parametrization of the mass resolution as a function of the $M_{\ell q}$ mass is shown in fig. 7.7. The parameters of the first gaussian, the coefficient α , the shift μ_1 and σ_{\min} are plotted versus the entire lepton-jet mass spectrum. The outstanding effect is the shift of the gaussian mean in the ΔM distributions away from the centre (zero). This is an indirect effect from the particle-level jet energy corrections and the overcorrection which is observed at parton level. An average shift therefore appears of the ΔM distributions, which varies from $\sim 6 - 10$ GeV over the whole mass range. This is foreseen to affect the endpoint measurements, by exhibiting small shifts from their expected values.

For what concerns the actual sigma of the resolution model, this is shown to depend almost linearly with mass with the form

$$\frac{\sigma(M_{\ell q})}{M_{\ell q}} = 0.03 + \frac{5}{M_{\ell q}} \quad (7.8)$$

The lepton-jet mass resolution should be measurable with real data as well, although not directly. As an example, high statistics sample of $Z + \text{jets}$ events may be used to reconstruct the mass of one lepton tagged from the Z and a jet. A comparison between the data distribution and the one obtained from the MC, can lead to the extraction of the resolution model⁸. It may therefore be kept fixed in the likelihood function used to fit the reconstructed masses.

⁸Assuming of course that the kinematics of the $Z + \text{jets}$ events are correctly reproduced with Monte Carlo.

7.4. ENDPOINT MEASUREMENTS AT LM6

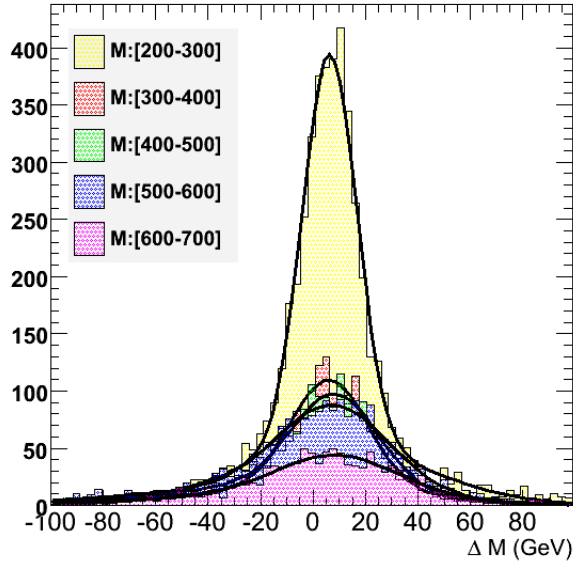


Figure 7.6: $\Delta M = M_{\ell j}^{RECO} - M_{\ell q}^{MC}$ distributions in four mass $M_{\ell q}^{MC}$ bins – The distributions are fitted with the sum of two Gaussians.

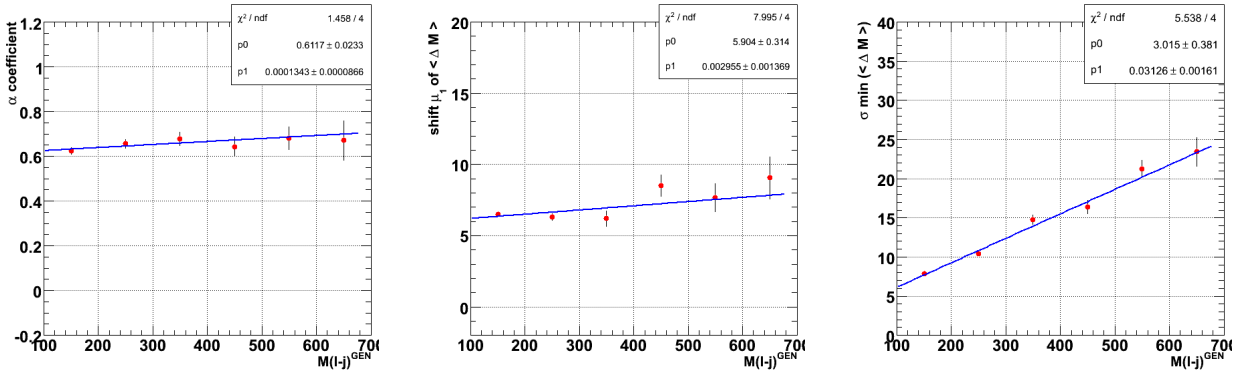


Figure 7.7: The two-gaussian (lepton - jet) mass resolution model as a function of the mass $M_{\ell q}$. Left: the coefficient of the first Gaussian. Middle: the average mean μ_1 showing a shift of $\sim 6 - 10$ GeV from the centre. Right: the minimum sigma, σ_{\min} , of the gaussian model showing a non-constant behavior with mass.

7.4 Endpoint measurements at LM6

7.4.1 Dilepton edge(s)

The extraction of the endpoint in the dilepton $M_{\ell\ell}$ invariant mass is performed along the lines described in the fifth chapter. Opposite-sign and same-flavor dilepton (ee or $\mu\mu$) events are selected

and used to fill a histogram of the invariant mass.

Figure 7.8, on the left, shows the total OSSF dilepton distribution in black superimposed with the OSDF distribution in error bars. The number of events with uncorrelated leptons appears to be more than half of the events which form the total mass. This was expected due to the relatively small branching ratio to the signal decay chain involving the χ_2^0 compared to the other leptonic sources in the supersymmetric events at LM6. The subtraction of the DF distribution from the full dilepton mass distribution is shown on the right plot of the same figure. A structure is already visible in the distribution, indicating the presence of an edge around $M_{\ell\ell} = 75$ GeV; this comes from the decay chain involving a left-handed slepton ($\tilde{\ell}_L$) in the $\tilde{\chi}_2^0$ two-body decay. The edge coming through a right-handed slepton ($\tilde{\ell}_R$) is hardly visible due to its significantly reduced branching ratio. On the other hand there is a Z-peak appearing: this was shown to come from the decays of heavier gauginos to $Z\tilde{\chi}_1^0$ and is responsible for 40% of the peak in a mass window $86 < M_{\ell\ell} < 96$ GeV. The Z-peak lies beyond the first dilepton edge but still quite close.

$M_{\ell\ell}^{\max}$ measurement

The OSDF distribution has been subtracted bin-by-bin from the total distribution. The subtracted distribution is fitted with a χ^2 function which is the sum of three different contributions: a triangular function in the region of the first edge (around 76 GeV), a gaussian function around the Z-peak, and a second triangle to describe the other dilepton edge (around 110 GeV). According to eq.(6.4), the triangular shape of the di-lepton mass distribution can be written in the form:

$$M_{\ell\ell}^{\max} \sqrt{\frac{1+z}{2}} dz, \quad -1 < z < 1 \quad (7.9)$$

where $M_{\ell\ell}^{\max}$ is the endpoint of the distribution and $z = \cos \theta^*$ is the cosine of the decay angle of the slepton in its rest frame. The triangular fit function component is then formed by the convolution of the triangle above with the dilepton mass resolution model,

$$T(M) = \int_{-1}^{+1} dz p_0 \exp \left[\frac{1}{2p_2^2} \left(M - p_1 \sqrt{\frac{1+z}{2}} \right)^2 \right] \quad (7.10)$$

with parameters $p_0 = N$, $p_1 = M_{\ell\ell}^{\max,1}$ and $p_2 = \sigma$ which is the gaussian resolution smearing of the dilepton mass in the region around the first endpoint p_1 . The second edge is parametrized by the same function with parameters corresponding to $p_3 = N'$, $p_4 = M_{\ell\ell}^{\max,2}$ and $p_5 = \sigma'$ (the resolution smearing around the second endpoint p_4). Finally, the component from Z decays is described by a simple Gaussian of fixed mean and sigma, leaving only the normalization (parameter p_6) to float in the fit.

For an integrated luminosity of 300 fb^{-1} , the measurement of the endpoint in the first edge of the dilepton mass yields:

$$M_{\ell\ell}^{\max} = 75.26 \pm 0.25 \text{ (stat)}, \quad \text{GeV}/c^2 \quad (7.11)$$

to be compared with the nominal value at $M_{\ell\ell}^{\max,TH} = 76 \text{ GeV}/c^2$.

7.4. ENDPOINT MEASUREMENTS AT LM6

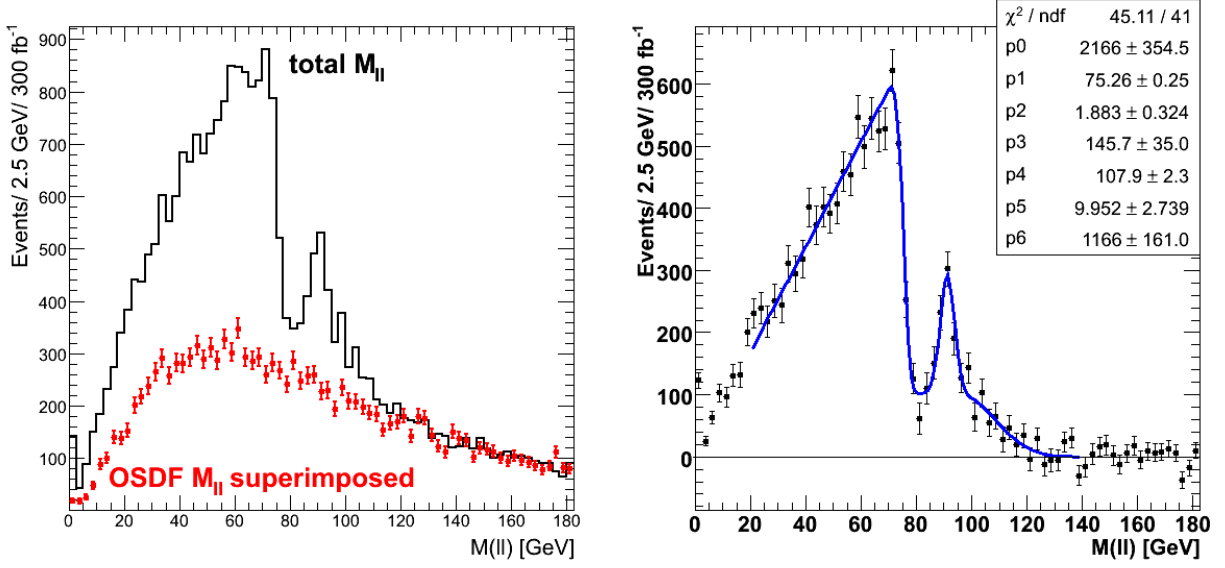


Figure 7.8: Left: the total $M_{\ell\ell}$ distribution (in black) formed by two OSSF leptons superimposed with the OSOF distribution (in error bars). Right: the $M_{\ell\ell}$ distribution after the OSOF background distribution has been subtracted. A fit to the distribution using the sum of three PDF contributions (two triangles and a gaussian Z-peak), is performed in order to extract the endpoint value(s), $M_{\ell\ell}^{\max}$.

The reconstruction of the endpoints in the invariant mass distributions involving the (di)lepton and jets are described in the next sections. The requirement of the dilepton mass to be below the measured endpoint in (7.11),

$$M_{\ell\ell} \leq 80. \text{ GeV}/c^2 \quad (7.12)$$

is applied to all distributions, in order to avoid the interference of the second edge ($\tilde{\ell}_R$ -mediated decay contribution) in the endpoint measurement.

7.4.2 $M_{\ell\ell q}^{\max}$ first measurement

A first estimation of the maximum in the distribution of the dilepton-jet mass, $M_{\ell\ell q}$, can be obtained from the smallest of the two combinations of the dilepton with the two highest- E_T jets. The minimum mass from the two combinations should not exceed the true endpoint of $M_{\ell\ell q}$ - in limits of the resolution. Figure 7.9 (left) shows the minimum mass of $M_{\ell\ell q}$ - in black - superimposed with the distribution obtained by the DF dilepton events respectively (points with error bars). On the right hand side of the figure, the $M_{\ell\ell q}^{\min}$ distribution is shown with the DF combinations subtracted.

To first order, one can ignore the resolution smearing effects around the endpoint and fit the invariant mass distribution with a straight line [56], in order to get a rough estimate of the endpoint.

The fitting function is simply of the form

$$f(M) = p_1 \cdot (p_0 - M) \quad [7.13]$$

where the parameter $p_0 = M_{\ell\ell q}^{\max}$ is used to extract the endpoint value. The fit results in

$$M_{\ell\ell q}^{\max} = 753.5 \pm 3.1 \text{ (stat.)} \pm 1. \text{ (syst.) GeV/c}^2 \quad [7.14]$$

where the systematic uncertainty coming from the variation of the fit range is very small, and at the level of 0.1%. The above result gives a maximum for $M_{\ell\ell q}$ which is almost 50 GeV shifted to higher values from the nominal endpoint. Nevertheless, it may be worthwhile to use this result as a requirement that should be fulfilled in subsequent endpoint measurements.

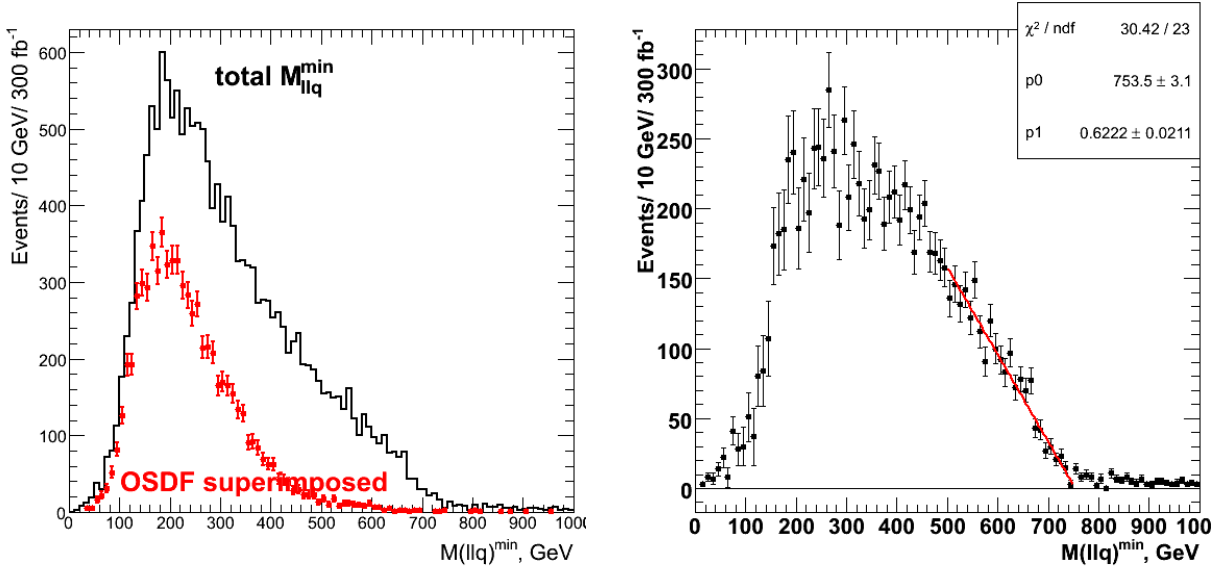


Figure 7.9: *Left:* the total $M_{\ell\ell q}^{\min}$ distribution (in black) formed by combinations of the OSSF dilepton with the two highest- E_T jets. The OSOF distribution (in error bars) is shown superimposed. *Right:* the $M_{\ell\ell q}^{\min}$ distribution after the OSOF background distribution has been subtracted. A fit in the region of the edge using a straight line is performed in order to extract a first estimate of the endpoint value, $M_{\ell\ell q}^{\max}$.

7.4.3 $M_{\ell_1 q}^{\max}$ and $M_{\ell_2 q}^{\max}$ measurements

The endpoints of $M_{\ell_1 q}^{\max}$ and $M_{\ell_2 q}^{\max}$ are measured directly from one distribution, the lepton-jet invariant mass, $M_{\ell j}$. This method is motivated by the fact that mass correlations between the $M_{\ell q}$ mass and the $M_{\ell\ell}$ or $M_{\ell\ell q}$ mass distributions could aid in the identification of two separate distributions in $M_{\ell q}$. Assuming the experimental feasibility of this method, a direct fit of the $M_{\ell j}$ mass would allow the measurement of two endpoints. A nice feature of this distribution is that the $M_{\ell_1 q}$ and $M_{\ell_2 q}$ shapes are uniquely represented independently of the model and the mass hierarchy; and therefore the actual shapes can be unambiguously used to construct a likelihood function.

7.4. ENDPOINT MEASUREMENTS AT LM6

The two OS leptons (ℓ_1 and ℓ_2) are combined with the two hardest jets (j_1 and j_2). On an event-by-event basis, this makes four possible combinations of a lepton with a jet, namely the $(\ell_1 j_1)$, $(\ell_2 j_1)$, $(\ell_1 j_2)$ and $(\ell_2 j_2)$, which enter the $M_{\ell j}$ distribution. Each of them belongs to one of the categories S , B_1 , B_2 and B_3 depicted in equation (7.3), with B_i representing the various sources of combinatorial background.

The subtraction of the B_2 and B_3 components proceeds reliably with the OSDF subtraction like in the previous measurements. On the other hand, the B_1 component requires a more careful treatment. In fact, B_1 is decomposed in B_{11} and B_{12} , depending on the kind of event in which the lepton-jet combination was found; B_{11} represents the combinations coming from events with a correct-wrong jet pair, and B_{12} the ones from events with both wrong jets. The B_{12} component is expected to be small and an attempt to model the combinatorics of B_{11} was attempted first using the mixed-event technique.

Figure 7.10, left, shows the total $M_{\ell j}$ distribution - in black - where it has been filled with all possible combinations and the DF modeling distribution has been subtracted. The mixed event distribution obtained by consecutively combining in pairs lepton and jet objects from randomly selected events (see also fig. 7.2), is shown superimposed in error bars. The mixed event distribution is fitted with the functional form

$$B(M) = (\alpha M)^i \exp[-\beta(\gamma M)^j] \quad (7.15)$$

which is shown in blue on the same plot. In the limit where $B_{12} \rightarrow 0$, the total entries N in the $M_{\ell j}$ histogram are equal to $N = S + B_{11}$, with $S = B_{11} = N/2$. Taking a normalization factor of $N/2$, the mixed-event modeling function is subtracted from the total $M_{\ell j}$ distribution and the resulting histogram is shown on the right of fig. 7.10. The bin errors of this histogram correspond to the errors of the original $M_{\ell j}$ distribution, i.e. before the subtraction. The structure of the resulting histogram already shows the position of two edges, the first around ~ 250 GeV and the second one around ~ 650 GeV. What remains is the assignment of the two edges to the $M_{\ell_1 q}^{\max}$ or the $M_{\ell_2 q}^{\max}$ endpoints.

To this end, the correlation of the $M_{\ell j}$ mass with $M_{\ell \ell j}$ can be used. A two-dimensional plot of the two quantities is constructed with combinations of lepton-jet on the x-axis and dilepton-jet on the y-axis. All sources of combinatorics are modeled in the way described above and subtracted in the two dimensions. Figure 7.11 shows the remaining correlation histogram. In the region where a first edge appears in $M_{\ell j}$ (around 250 GeV), a wide range of $M_{\ell \ell j}$ masses are reached, whereas in the region of the other edge (around 650 GeV), the correlation converges towards one endpoint in $M_{\ell \ell j}$. According to subsection 6.3.3, the first $M_{\ell j}$ region (< 250 GeV) should correspond to the $M_{\ell_1 q}$ distribution, for which the $M_{\ell_1 q}^{\max}$ lies between two endpoint values in $M_{\ell \ell q}$. The second region of $M_{\ell j}$ (> 250 GeV) corresponds to the $M_{\ell_2 q}$ distribution, whose maximum, $M_{\ell_2 q}^{\max}$, comes only for one endpoint in $M_{\ell \ell q}$.

With this in hand, an attempt to fit the full mass distribution, and not just the region of the edges, is now plausible. A likelihood function can be constructed from the convolution of the true shape f^{true} of $M_{\ell q}$ mass smeared by the appropriate resolution model,

$$f(M; \sigma) = \int dx \cdot f^{\text{true}}(x) \cdot \text{ResModel}(M; x, \sigma) \quad (7.16)$$

CHAPTER 7. SPARTICLE MASS RECONSTRUCTION

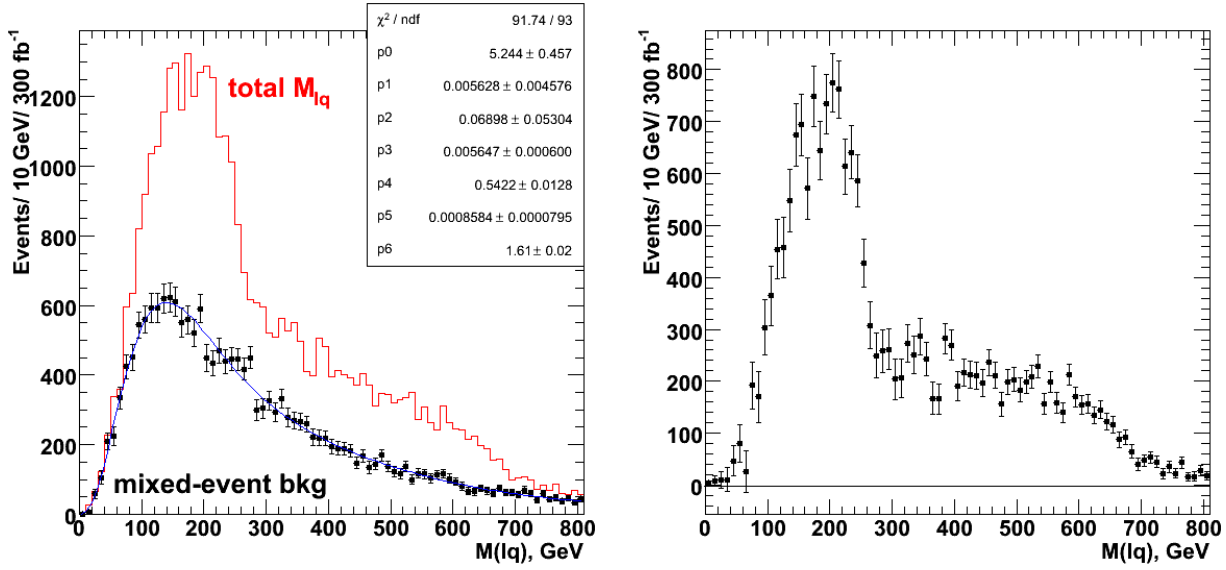


Figure 7.10: Left: the total M_{lq} distribution (in red) formed by combinations of leptons with the two highest- E_T jets. The mixed event background (in error bars), which is used to model the combinations of a wrong assignment between a lepton and a quark, is shown superimposed. Right: the M_{lq} distribution after the mixed-event modeled background shape has been subtracted.

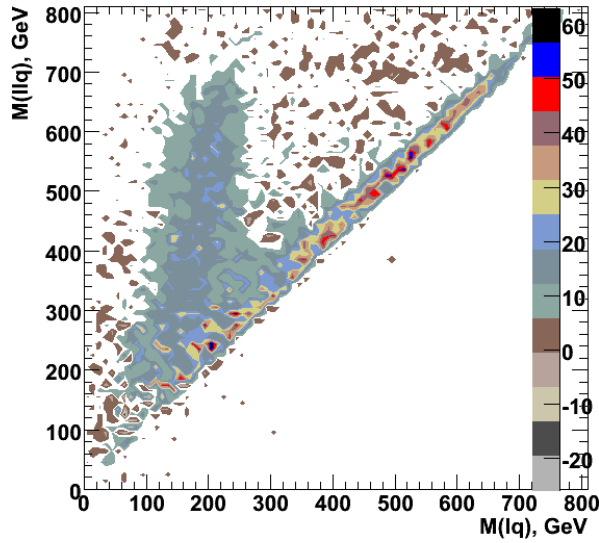


Figure 7.11: The correlation of M_{lq} distribution with M_{llq} at reconstruction level. The OS $\ell\ell - q$ combinations as well as combinations from the mixed events have been subtracted from the total two-dimensional histogram. An indicative structure appears: in the region of the first edge in M_{lq} (around 250 GeV), a wide range of M_{lq} masses are reached, whereas in the region of the other edge in M_{lq} (around 650 GeV), the correlation converges towards one endpoint in the M_{llq} .

7.4. ENDPOINT MEASUREMENTS AT LM6

representing the convolution of the two. The shape of f^{true} is given by (the sum of) the formulae (6.8) and (6.11), each corresponding to the distinct $M_{\ell_1 q}$ and $M_{\ell_2 q}$ distributions. The formulae can be re-written in terms of the endpoints and mass ratios, $r = M_{R/L}/M_X$, as

$$f_{\ell_1 q}^{\text{true}}(M) = \frac{2}{(M_{\ell_1 q}^{\max})^2} \cdot M \quad (7.17)$$

$$f_{\ell_2 q}^{\text{true}}(M) = \frac{4}{(M_{\ell_2 q}^{\max})^2} \cdot \frac{1}{(1 - r^2)} \cdot \begin{cases} \ln(\frac{1}{r}) \cdot M & \text{for } 0 \leq M \leq rM_{\ell_2 q}^{\max} \\ M \cdot \ln\left(\frac{M_{\ell_2 q}^{\max}}{M}\right) & \text{for } rM_{\ell_2 q}^{\max} \leq M \leq M_{\ell_2 q}^{\max} \end{cases} \quad (7.18)$$

This is actually an important fact: the fitting of the $M_{\ell q}$ distribution using the nominal shape, will not only allow the extraction of the endpoint values themselves, but also will provide information on ratios of the SUSY particle masses. In the case of LM6, the mass ratio involved is the ratio of the mass of the left-handed slepton ($\tilde{\ell}_L$), M_L , to the mass of the second neutralino ($\tilde{\chi}_2^0$), M_X , and will be denoted as $r = M_L/M_X$.

The resolution function which accounts for the lepton-jet mass smearing is the same as the one described in subsection 7.3.1. A parametrization of the model is performed by assuming a non-constant behavior of the gaussian sigma with the lepton-jet mass (see fig. 7.7):

$$\begin{aligned} \text{ResModel}(M_{\ell j}) &= \alpha \cdot \text{Gauss}_1(M_{\ell j}; M_{\ell j}^{\text{true}} + \mu_1, \sigma_{\min} = s_i \cdot M_{\ell j} + \text{const.}) \\ &\quad + (1 - \alpha) \cdot \text{Gauss}_2(M_{\ell j}; M_{\ell j}^{\text{true}} + \mu_2, \sigma_{\max} = \text{const.}) \end{aligned} \quad (7.19)$$

which assumes that the quantity $(M_{\ell j} - M_{\ell j}^{\text{true}} - \mu)/\sigma$ is distributed according to Gaussian₁ of mean $\mu_1 = 0$ and $\sigma_{\min} = 1$ with probability α , and according to Gaussian₂ of mean $\mu_2 = 0$ and $\sigma_{\max} = 1$ with probability $1 - \alpha$. The likelihood function is constructed by numerically integrating the true shapes with the resolution function, i.e. the integral in (7.16). The reason for this is that there is no analytic solution to the convolution integral between the gaussian in the resolution function and the second leg of $f_{\ell_2 q}^{\text{true}}$ (logarithmic part)⁹. The sum of two likelihood (PDF) functions, each assigned a different normalization factor N_1 for $f_{\ell_1 q}$ and N_2 for $f_{\ell_2 q}$, is then constructed as

$$f(M; \sigma) = N_1 \cdot f_{\ell_1 q}(M; \sigma) + N_2 \cdot f_{\ell_2 q}(M; \sigma) \quad (7.20)$$

and used in the following fits.

A first attempt to fit the $M_{\ell j}$ mass has been made using the distribution of the right plot in fig. 7.10. This fit is hampered by the fact that the mixed-event model underestimates the true background in the $M_{\ell q}$ distribution. The main reason for this is that the contribution of the B_{12} is in principle non-negligible (and $B_{11} + B_{12} > N/2$), and the modeling background function has been subtracted with the wrong normalization. Therefore, the shape of $M_{\ell j}$ cannot be safely reproduced and the fit results on the endpoints may not be easily disentangled.

Another approach of reproducing safely the $M_{\ell j}$ distribution follows with the usage of the “consistency” requirements. The method uses the earlier measurement of $M_{\ell q}^{\max}$ denoted in eq. (7.14). On an event-by-event basis, the correct jet is selected as the one for which the mass combination

$$M_{\ell \ell j} < 750 \text{ GeV/c}^2 \quad (7.21)$$

⁹Another reason for this will be prominent when it comes to the issue of the Acceptance correction.

CHAPTER 7. SPARTICLE MASS RECONSTRUCTION

with the other jet giving $M_{\ell\ell j} > 750$ GeV. If at least one of the two requirements is not fulfilled the lepton-jet combination is discarded. With some loss of statistics, the combinations entering the mass histogram should be free of any combinatorics coming from the wrongly selected jet (either from B_{11} or B_{12}). The resulting $M_{\ell j}$ distribution is shown on the left of fig. 7.12, superimposed with the DF distribution which has been constructed in a similar fashion. The subtraction of the DF distribution results in the histogram shown on the right of the same figure.

A fit to the newly formed $M_{\ell j}$ distribution is performed next using the likelihood function in 7.20¹⁰. Two different resolution models (i.e. two different values for σ) have been imposed in the $f_{\ell_1 q}$ and $f_{\ell_2 q}$ likelihood functions, since the kinematics of the $(\ell_1 q)$ and $(\ell_2 q)$ objects are quite different.

The parameters of the two endpoints as well as the ratio of the masses $r = M_L/M_X$ were free to float during the fitting procedure. The measurement of the two endpoints, $M_{\ell_1 q}^{\max}$ and $M_{\ell_2 q}^{\max}$, is extracted from the fit as

$$M_{\ell_1 q}^{\max} = 237.3 \pm 1.7(\text{stat.}) \text{ GeV}/c^2 \quad (7.22)$$

$$M_{\ell_2 q}^{\max} = 703.3 \pm 5.8(\text{stat.}) \text{ GeV}/c^2 \quad (7.23)$$

whereas the ratio r measurement comes out to be

$$r = 0.86 \pm 0.02 \quad (7.24)$$

to be compared with the theory values of $M_{\ell_1 q}^{\max, \text{TH}} = 239.1 \text{ GeV}/c^2$, $M_{\ell_2 q}^{\max, \text{TH}} = 675. \text{ GeV}/c^2$ and $r = 0.95$.

The results from the fit are not consistent with the true values of the parameters: a significant shift, of the order of $\sim 30 \text{ GeV}/c^2$, to higher values is observed for the case of the $M_{\ell_2 q}^{\max}$. In addition, a shifted value for the ratio r (by -0.1) is obtained as well. The origin of the effect has been found to be a problematic behavior of the PDF function, when the values of r are close to 1. The fit is repeated keeping the parameter r fixed to its nominal value, as shown in fig. 7.13. In this case, both endpoint values are obtained in good agreement with the nominal ones:

$$M_{\ell_1 q}^{\max} = 237.6 \pm 1.6(\text{stat.}) \text{ GeV}/c^2 \quad (7.25)$$

$$M_{\ell_2 q}^{\max} = 679.5 \pm 2.5(\text{stat.}) \text{ GeV}/c^2 \quad (7.26)$$

Up to this point, one cannot assume knowledge of r -value and therefore the measurements in (7.25 -7.26) are not possible. Moreover, the $M_{\ell_2 q}^{\max}$ measurement in (7.23) cannot be used in the extraction of the supersymmetric masses (because of the observed shift). It will be shown however that a complete set of endpoint measurements can still be achieved and a first estimate of the masses is feasible. After that step, and with the value of r determined by the mass measurements, the $M_{\ell_2 q}^{\max}$ fit can be repeated to yield the result in (7.25 -7.26).

A detailed investigation of the $M_{\ell_2 q}$ fit properties is presented in the next section in order to resolve the issue on the endpoint extraction.

¹⁰Exceptionally in the $M_{\ell j}$ fit, we use a binned likelihood fit performed with RooFit.

7.4. ENDPOINT MEASUREMENTS AT LM6

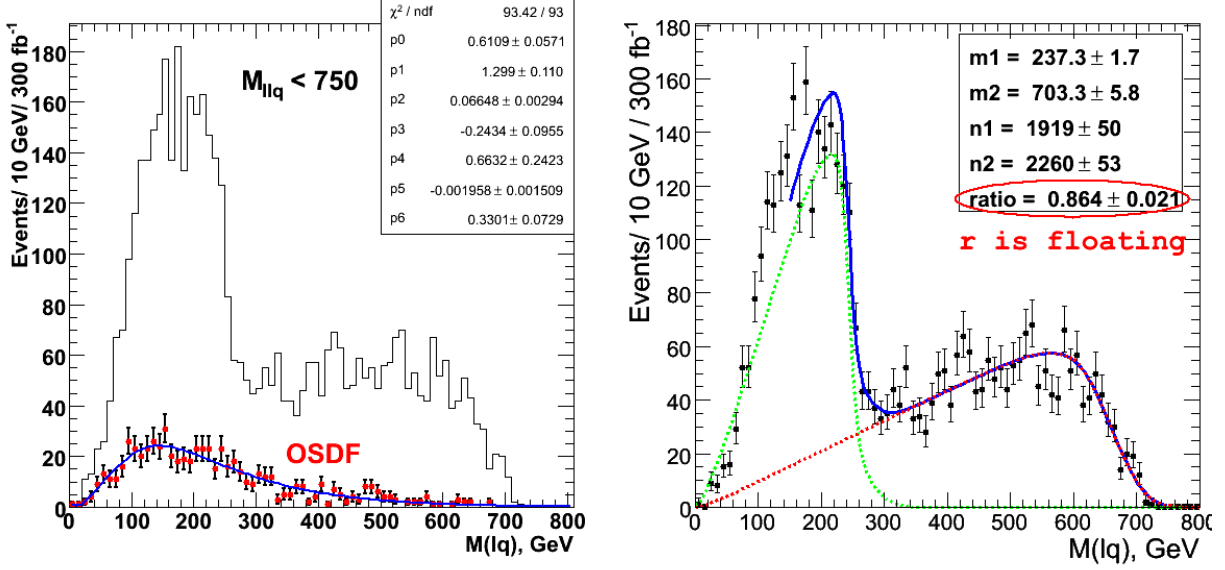


Figure 7.12: *Left:* the total M_{lq} distribution (in red) formed by combinations of lepton-jet found consistent with a cut on $M_{\ell\ell q} < 750 \text{ GeV}/c^2$. The OSDF distribution (in error bars) is shown superimposed. *Right:* the M_{lq} distribution after the OSDF background has been subtracted. A fit to the distribution using the nominal M_{lq} shape is used to directly extract the two endpoint values, $M_{\ell_1 q}^{\max}$ and $M_{\ell_2 q}^{\max}$, as well as the value of the mass ratio, r .

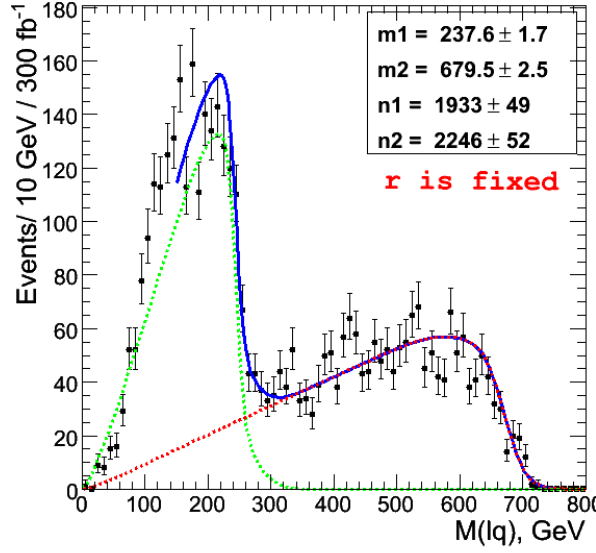


Figure 7.13: The M_{lq} fit repeated - in blue - using the nominal shape of the M_{lq} distribution. The fit function uses exceptionally the parameter $r = M_L/M_X = 0.95$ fixed in the fit in order to cross-check the results with the previous fit (when r is floating). The actual fit results cannot be valid before a first estimate of the supersymmetric mass spectrum is achieved (and consequently a value of r is determined).

7.4.4 The $M_{\ell_2 q}$ fit properties

In what follows, the $f_{\ell_2 q}$ true shape of the $M_{\ell_2 q}$ distribution is overviewed. Figure 7.14 shows a schematic representation of the functional form of $f_{\ell_2 q}$, with point $x_r = r \cdot x_{\max}$ representing the limit between the two functions in (7.18). This point corresponds to the secondary endpoint of $M_{\ell_2 q}$. As can be noticed, r is equal to:

$$r = \frac{x_r}{x_{\max}} = \frac{M_{\ell_2 q}^{\max,2}}{M_{\ell_2 q}^{\max}} \quad \text{or} \quad r = \frac{M_L}{M_X} \quad (7.27)$$

In other words, the ratio of the two masses, M_L and M_X , determines the ratio of the two endpoints in $M_{\ell_2 q}$.

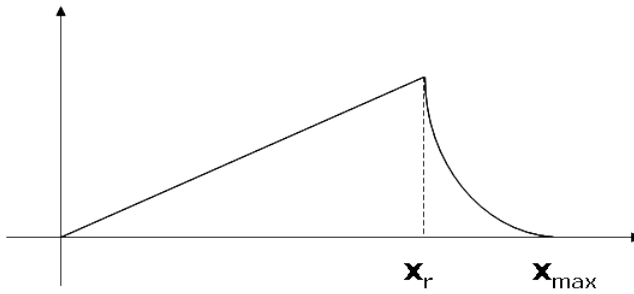


Figure 7.14: Schematic view of the $f_{\ell_2 q}^{true}$ shape: i) a triangular part evolves from 0 to x_r and ii) a logarithmically falling part, from x_r to x_{\max} . The point x_r corresponds to $r \cdot x_{\max}$.

The $M_{\ell_2 q}$ fit uses a likelihood function which is the convolution of $f_{\ell_2 q}$ with a resolution model as described in the previous section. In order to establish the correctness of the fitter, a toy MC study has been performed. Thousands of events were generated, distributed according to the ($\ell_2 q$) PDF. Running for 1000 experiments, the distributions were fitted with the same (generator) PDF and the distributions of the parameters r and x_{\max} , their errors and their pulls of mean were computed.

Using the example of the mSUGRA point LM6, with values of $r = 0.95$ and $x_{\max} = 675$., the fit results for r and x_{\max} are shown in figures 7.15 and 7.16. The first figure shows that the pull distributions of the extracted parameters are not consistent with a gaussian of mean 0 and sigma 1; indicating the fact that the parameter values as well as their errors show an anomalous behavior in the fitter. The second figure shows in addition an anti-correlation of the two parameters, with lower values of r resulting in higher values of x_{\max} and vice versa. The problem is shown to arise from values of r close to 1, or equivalently to x_r being very close to x_{\max} . In these cases, the fitter cannot distinguish the distance between them, due to the smearing caused by the resolution function, and the fit does not converge to the correct values.

In order to cross-check the above result, a similar toy MC study was performed using nominal values for the parameters r and x_{\max} , corresponding to a “test” point in mSUGRA with the same $x_{\max} = 675$. as at LM6 but a value of $r = 0.70$ away from 1. Figures 7.17 and 7.18 show indeed that the fitter works reliably over thousands of experiments, for the case-models where x_r is not too close to x_{\max} . In the opposite cases (like at LM6), the $M_{\ell_2 q}$ fit will suffer from ambiguities and likely will fail.

7.4. ENDPOINT MEASUREMENTS AT LM6

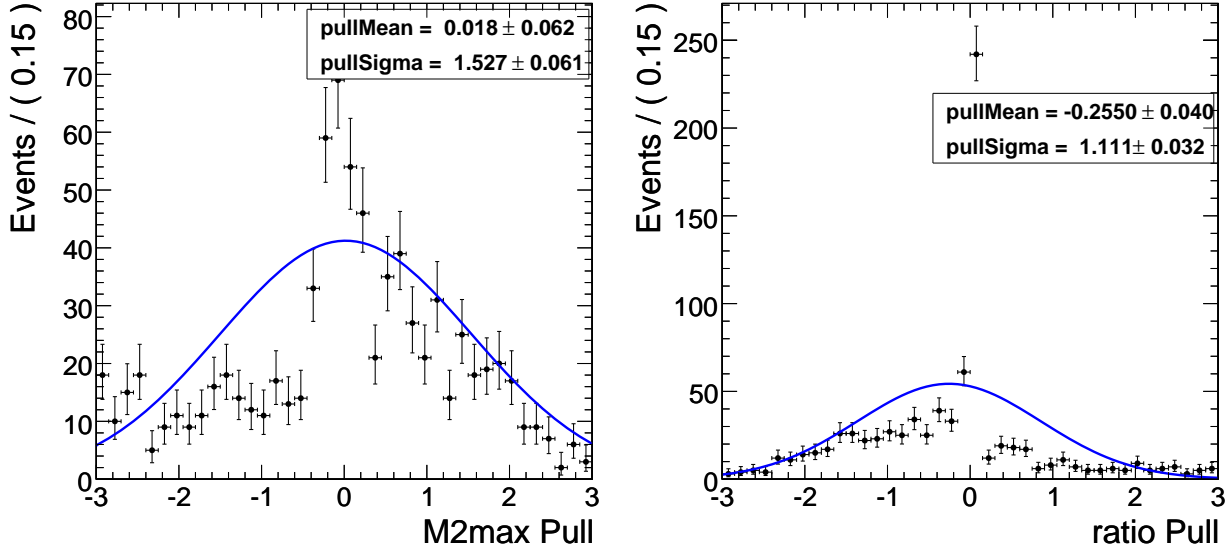


Figure 7.15: The pull distributions of parameters $M_{\ell_2q}^{\max}$ (left) and $r = M_L/M_X$ (right), in a toy MC M_{ℓ_2q} fit. The nominal values of the parameters correspond to the LM6 mSUGRA point: $M_{\ell_2q}^{\max} = 675 \text{ GeV}/c^2$ and $r = 0.95$. The fit results indicate a problematic behavior of the fit for values of $r \rightarrow 1$.

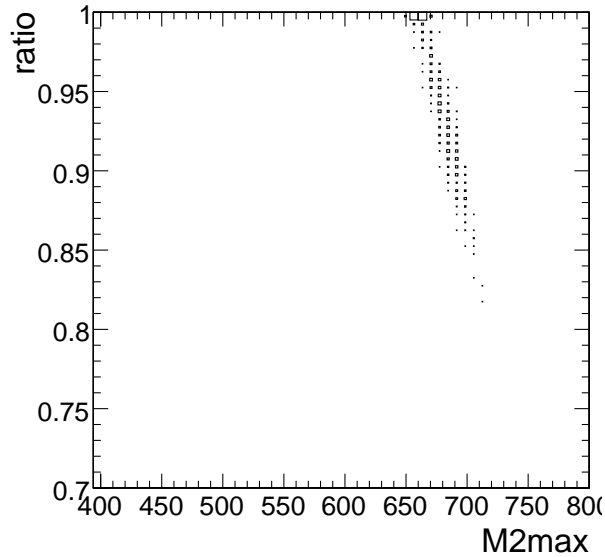


Figure 7.16: Correlation of parameters $M_{\ell_2q}^{\max}$ versus $r = M_L/M_X$, in a toy MC M_{ℓ_2q} fit. The nominal values of the parameters correspond to the LM6 mSUGRA point: $M_{\ell_2q}^{\max} = 675 \text{ GeV}/c^2$ and $r = 0.95$.

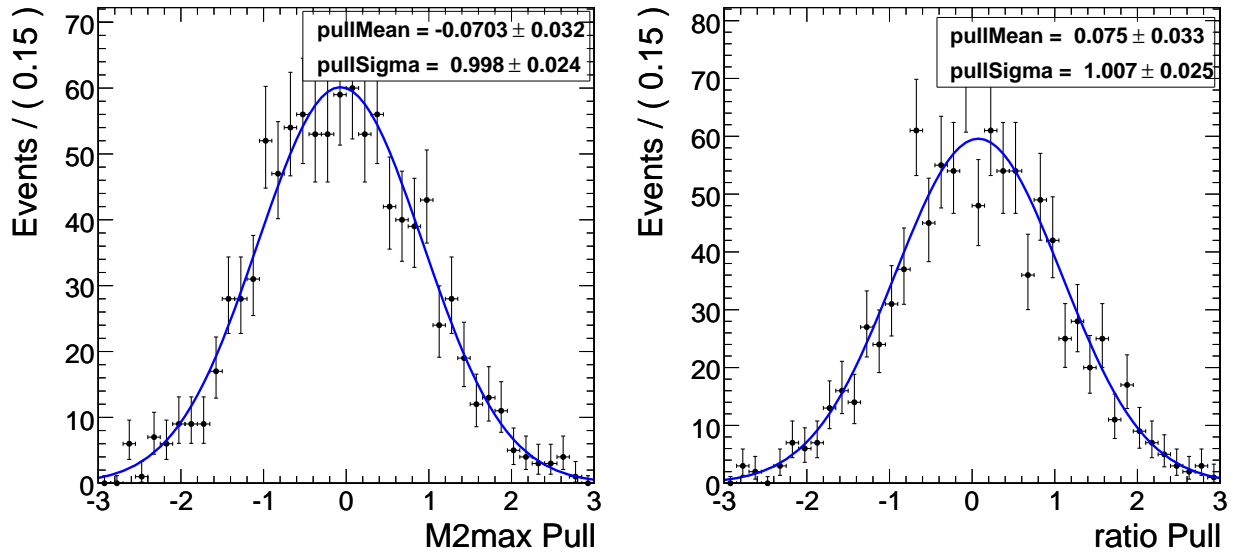


Figure 7.17: The pull distributions of parameters $M_{\ell_{2q}}^{\max}$ (left) and $r = M_L/M_X$ (right), in a toy MC $M_{\ell_{2q}}$ fit. The nominal values of the parameters correspond to a “test” point in mSUGRA, with: $M_{\ell_{2q}}^{\max} = 675 \text{ GeV}/c^2$ and $r = 0.70$. The fit results indicate a healthy behavior of the fit for values of $r \ll 1$.

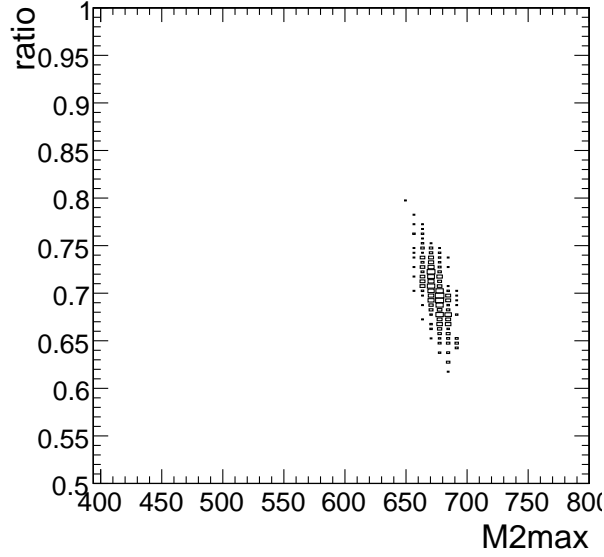


Figure 7.18: Correlation of parameters $M_{\ell_{2q}}^{\max}$ versus $r = M_L/M_X$, in a toy MC $M_{\ell_{2q}}$ fit. The nominal values of the parameters correspond to a “test” point in mSUGRA, with: $M_{\ell_{2q}}^{\max} = 675 \text{ GeV}/c^2$ and $r = 0.70$.

7.4.5 $M_{\ell\ell q}^{\max}$ measurement revisited

With the $M_{\ell j}$ measurement in hand, the dilepton-jet fit is retried in order to obtain a maximum endpoint in the $M_{\ell\ell j}$ distribution. The effect of smearing of the edge structure (due to the resolution in $M_{\ell\ell j}$) can be taken into account.

At this point, it is not possible to know which of the three endpoints in the $M_{\ell\ell q}$ distribution corresponds to the true endpoint that is measured. Consequently, the actual shape of the distribution cannot be used in the fitting formula; otherwise, the knowledge of a particular mass hierarchy of the SUSY model would be implied. The fit function is chosen, instead, to have an empirical form proposed in [56]. It is constructed by the numerical convolution of a second degree polynomial with a mass resolution model, namely:

$$f(M) = \int_0^{p_2} dz \left(p_0 \cdot (p_2 - z) + p_1 \cdot (p_2 - z)^2 \right) \text{Res}[(M - z); \sigma_{\min}, \sigma_{\max}] + p_4 + p_5 \cdot M \quad (7.28)$$

where $\text{Res}[(M - z); \sigma_{\min}, \sigma_{\max}]$ is of the same form as in eq. (7.20). A linear term, $p_4 + p_5 \cdot M$, has been added in the PDF to account for the structure visible beyond the edge.

The parameter p_2 corresponds to the endpoint $M_{\ell\ell q}^{\max}$. The resolution model introduces two parameters, the σ 's of the two gaussians, and affects both the error as well as the position of the endpoint. A first estimate of the gaussian sigmas is taken from the actual $M_{\ell\ell j}$ resolution as measured by the Monte Carlo. This leads to $\sigma_{\min} \sim 8 \text{ GeV}$ and $\sigma_{\max} \sim 25 \text{ GeV}$ for the region around the endpoint, which are used as fixed parameters in the fit. The fit result on the measurement of the endpoint is

$$M_{\ell\ell q}^{\max} = 720.1 \pm 7.5 \text{ (stat.) GeV/c}^2 \quad (7.29)$$

to be compared with the theory value of $M_{\ell\ell q}^{\max,1} = 687.4 \text{ GeV/c}^2$.

An attempt to identify the true endpoint measured with the above result is presented next. From the correlation plot of $M_{\ell j}$ versus $M_{\ell\ell j}$ (fig. 7.11), it can be seen that selecting combinations of dilepton-jet pairs consistent with $M_{\ell j} < 245 \text{ GeV}$, the $(\ell_1 q)$ region can be isolated. Reversely, selecting combinations consistent with $M_{\ell j} > 245 \text{ GeV}$ the $(\ell_2 q)$ region is enhanced. The corresponding $M_{\ell\ell j}$ distributions are shown in fig. 7.20.

Recalling the discussion on fig. 6.16, the following results can be concluded: the left plot of $M_{\ell\ell j}$ ($\ell_1 q$ region), involves the $M_{\ell\ell q}^{\max,1}$ and $M_{\ell\ell q}^{\max,3}$ endpoints. The lower edge around $\sim 250 \text{ GeV/c}^2$ can only be assigned to $M_{\ell\ell q}^{\max,3}$, since the latter comes together with the minimum in the $M_{\ell_2 q}$ distribution. The right plot of $M_{\ell\ell j}$ ($\ell_2 q$ region), involves the $M_{\ell\ell q}^{\max,1}$ and $M_{\ell\ell q}^{\max,2}$ endpoints. Which of the two is the true endpoint cannot be determined from the plot. Instead one can determine that the two endpoints lie very close to each other, since $M_{\ell\ell q}^{\max,2}$ comes together with the minimum in the $M_{\ell_1 q}$ distribution. It is also obvious that the distance between them is smeared out by the resolution effects; as a consequence the ambiguity between $M_{\ell\ell q}^{\max,1}$ and $M_{\ell\ell q}^{\max,2}$ hampers the identification of the endpoint in (7.29).

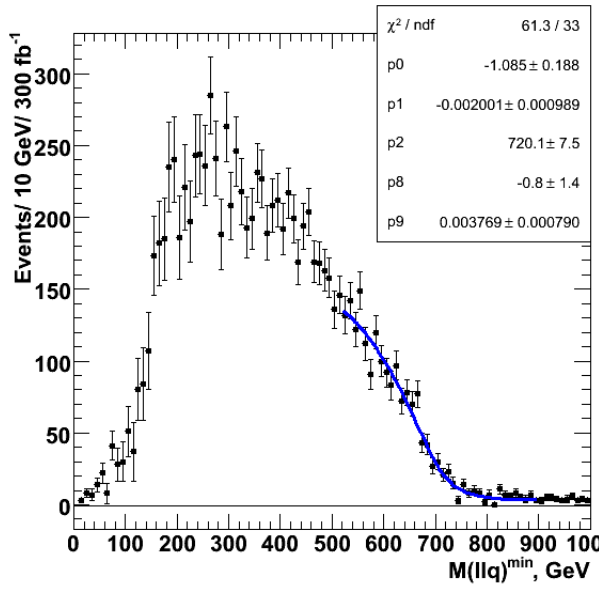


Figure 7.19: The fit of the $M_{\ell\ell q}^{\min}$ distribution using a second degree polynomial smeared with a gaussian resolution model; the fit results are used to quote the final estimate of the $M_{\ell\ell q}^{\max}$ endpoint.

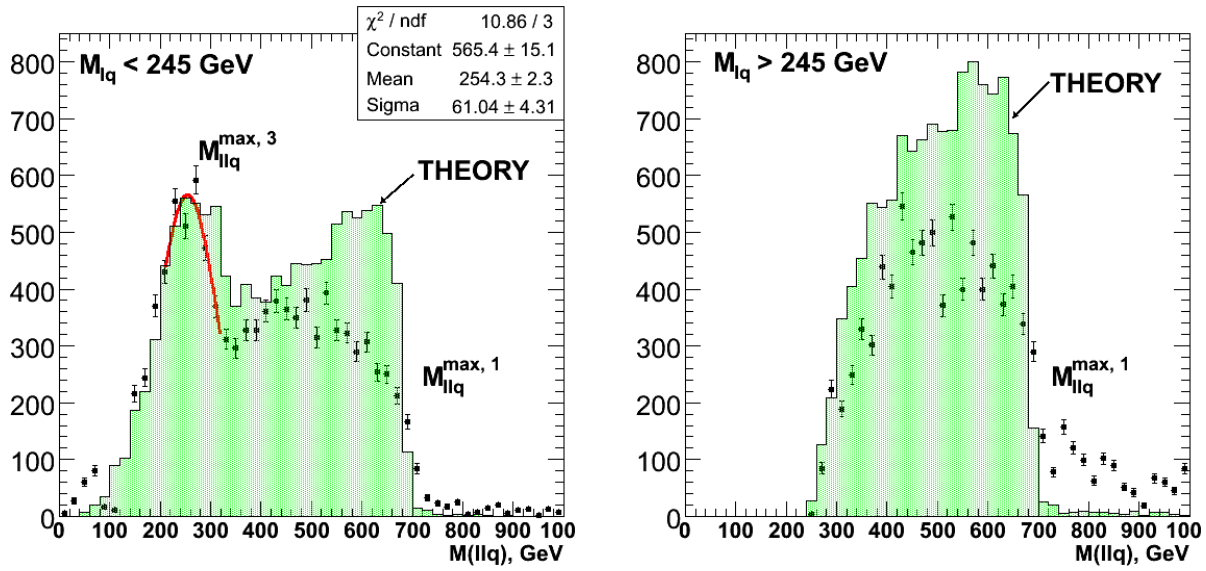


Figure 7.20: Left: the $M_{\ell\ell q}$ distribution using only combinations of dilepton-jets consistent with a cut on $M_{\ell q} < 245 \text{ GeV}$ ($\ell_1 q$ region). Two maxima can be recognized: $M_{\ell\ell q}^{\max,1}$ (true endpoint) and $M_{\ell\ell q}^{\max,3}$ - the latter is determined with a gaussian peak. Right: the $M_{\ell\ell q}$ distribution using only combinations of dilepton-jets consistent with a cut on $M_{\ell q} > 245 \text{ GeV}$ ($\ell_2 q$ region). Two maxima are involved: $M_{\ell\ell q}^{\max,1}$ (true endpoint) and $M_{\ell\ell q}^{\max,2}$, which are almost overlapping.

7.4. ENDPOINT MEASUREMENTS AT LM6

7.4.6 $(M_{\ell_1q} + M_{\ell_2q})^{\max}$ measurement

Up to this point, the SUSY particle masses cannot be determined from the endpoints measured, since the true endpoint of $(\ell\ell j)$ mass distribution has not been identified among the ones in (6.14), (6.15), (6.16) and (6.18). According to section 6.1.4, an additional endpoint measurement is provided by the $(M_{\ell_1j} + M_{\ell_2j})$ mass distribution. Figure 7.21 shows this distribution obtained after imposing the consistency requirements to the lepton-jet combinations, similar to ones in (7.21).

A χ^2 fit in the region around the edge of the distribution is performed using the same formula of Eq. (7.28)¹¹ as in the case of the $M_{\ell\ell j}$. The same resolution model extracted for the $M_{\ell j}$ mass is used for the smearing. Since $(M_{\ell_1j} + M_{\ell_2j})^{\max}$ is reached for the same kinematic configuration as the $M_{\ell_1j}^{\max}$ and $M_{\ell_2j}^{\max}$ ² endpoints and it is equal to their sum, it is plausible that their smearing (and shift) can be used here as well and impose this same model to the $(M_{\ell_1j} + M_{\ell_2j})$ fit. With this procedure, a sigma of the order of $\sigma = 45$ GeV is used for the region around $(M_{\ell_1j} + M_{\ell_2j})^{\max}$.

The endpoint of the distribution is extracted with a larger statistical uncertainty than all other endpoints, and it comes out to be:

$$(M_{\ell_1j} + M_{\ell_2j})^{\max} = 903.4 \pm 27.7 \text{ (stat.) GeV/c}^2 \quad (7.30)$$

to be compared with the theory value $(M_{\ell_1j} + M_{\ell_2j})^{\max, TH} = 883.6 \text{ GeV/c}^2$.

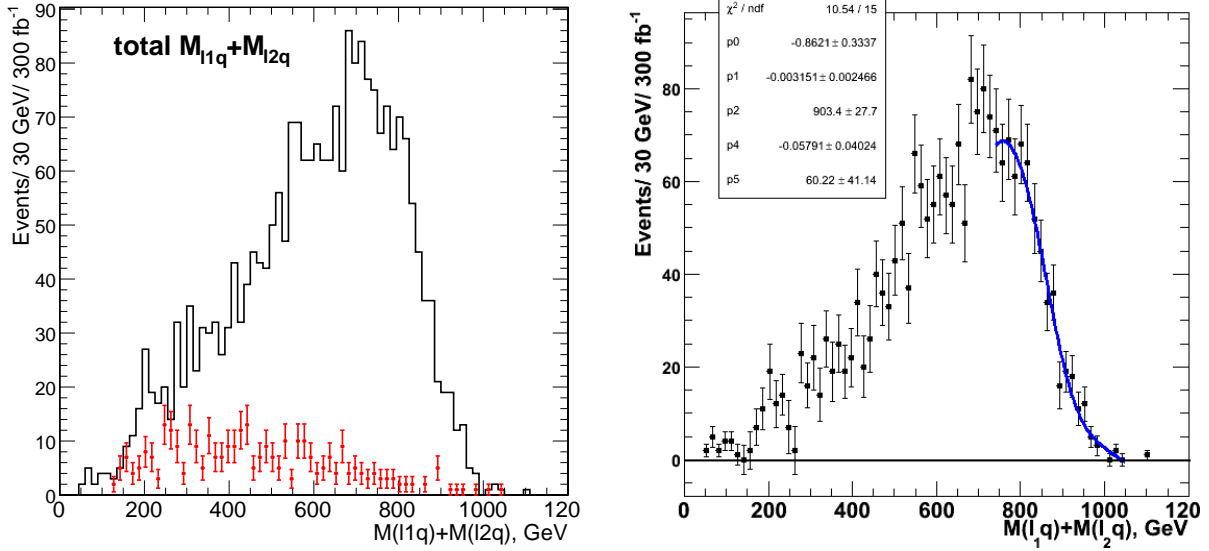


Figure 7.21: Left: The $M_{\ell_1q} + M_{\ell_2q}$ distribution obtained when imposing consistency requirements on lepton-jet combinations . Right: the $M_{\ell_1q} + M_{\ell_2q}$ distribution after the opposite-sign different-flavor (OSDF) background shape has been subtracted. A fit in the region around the edge, using a polynomial smeared by a Gaussian, is used to extract the endpoint value, $(M_{\ell_1q} + M_{\ell_2q})^{\max}$.

¹¹Alternatively, one may have used the nominal shape of the $(M_{\ell_1q} + M_{\ell_2q})$ distribution to fit for the endpoint. It is not tried in this scope since the analytic formula is not found in the literature so far.

7.5 Endpoint measurements at LM1

A brief presentation of the endpoint measurements at the mSUGRA benchmark point LM1 is presented next. The procedure is the same as the one at LM6, so only the final results are quoted. The LM1 sample used corresponds to statistics equivalent to 15fb^{-1} , i.e. it is much lower than the 300fb^{-1} of LM6. The LM1 model is considered to be a rather optimistic SUSY scenario in the search of the di-leptons due to its high cross sections and large branching ratio to the signal decay chain. For this reason, the measurements at LM1 are used to demonstrate the effectiveness of the endpoint method with better precision in the endpoints extraction.

In this context, specific analysis settings relevant to LM1 have been applied. These involved relaxing the jet E_T cuts, to $E_T^{j1,j2} > 100, 60\text{GeV}$, to account for the lower squark/gluino masses. In addition, a b-tagging jet veto has been imposed among the 2 highest- E_T jets in order to minimize the contributions of the \tilde{b} 's in the signal decay chain ¹². The p_T cuts on the leptons remained unchanged, due to the generally low lepton p_T spectrum expected in SUSY models.

Invariant mass distributions at LM1

The invariant mass distributions of the two OS highest- p_T leptons in SUSY events, before and after the different-flavor di-lepton subtraction, are shown in fig. 7.22. A di-lepton triangular shape, due to a $\tilde{\ell}_R$ -mediated two-body decay of the $\tilde{\chi}_2^0$, is prominent. The $\tilde{\ell}_L$ -mediated decay is in this case suppressed for kinematical reasons. A Z-peak approximately 10GeV higher than the SUSY endpoint is visible. The di-lepton mass distribution is fitted with a combined PDF and the endpoint measurement is extracted as:

$$M_{\ell\ell}^{\max} = 80.49 \pm 0.21 \text{ (stat), } \text{GeV}/c^2 \quad [7.31]$$

to be compared with its theoretical value at $M_{\ell\ell}^{\max, \text{TH}} = 81.0 \text{ GeV}/c^2$. Similarly as for LM6, a cut at $M_{\ell\ell} < 85.\text{GeV}/c^2$ is applied in the rest of the analysis, so as to remove di-lepton sources from Z boson decays.

The $M_{\ell\ell q}$ distribution is shown in fig. 7.23. The plots show the minimum mass of the two combinations of the di-lepton with the two highest- E_T jets, before (left) and after (right plot) the subtraction of the OSDF dilepton-jet histogram which is shown in red. The extraction of the endpoint proceeds with a fit in the mass region around the endpoint and results in:

$$M_{\ell\ell q}^{\max} = 453.3 \pm 2.1 \text{ (stat.) GeV}/c^2 \quad [7.32]$$

to be compared with the nominal true endpoint value $M_{\ell\ell q}^{\max, \text{TH}} = 449.1 \text{ GeV}/c^2$. The $M_{\ell\ell q}$ endpoint is extracted with a much better precision in the case of LM1 than of LM6, despite the significantly lower amount of integrated luminosity assumed for LM1. This is due to both the higher cross section that is predicted for the LM1 point, as well as the fact that the endpoint lies at lower $M_{\ell\ell q}$ values and thus the mass measurement has a better resolution.

The formation of the $M_{\ell q}$ (lepton-jet) masses follows the considerations of the previous section. Among the two leptons and the two jets, only combinations of one lepton with a jet giving an $M_{\ell q}$

¹²Nevertheless, even without a b-tagging veto, the results are not expected to be significantly different. The reason is that the \tilde{b} -squark decay chain form endpoints in the lepton-jet distributions which lie well below the endpoint regions of that of the squarks in the first 2 families ($m_{\tilde{b}} < m_{\tilde{q}}$).

7.5. ENDPOINT MEASUREMENTS AT LM1

value below $500\text{GeV}/c^2$ enter the histogram. The resulting distribution is shown in fig. 7.24, on the left. The distribution on the right is obtained after the OSDF subtraction and a likelihood fit is used to extract the two endpoint values - each corresponding to the $(\ell_1 q)$ and $(\ell_2 q)$ distributions - and the ratio r . It is a characteristic of the LM1 point that the value of the ratio is 0.66 which is significantly smaller than 1. Nevertheless, a discrepancy in the $M_{\ell q}$ endpoints is also observed here: significant shifts in the $M_{\ell_2 q}^{\max}$ and r fit values are observed:

$$M_{\ell_1 q}^{\max} = 405.3 \pm 2.9(\text{stat.}) \text{ GeV}/c^2 \quad (7.33)$$

$$M_{\ell_2 q}^{\max} = 331.7 \pm 9.0(\text{stat.}) \text{ GeV}/c^2 \quad (7.34)$$

$$r = 0.58 \pm 0.04 \quad (7.35)$$

The effect has been disentangled using toy MC studies with the $M_{\ell q}$ fit using various values of the $(\ell_1 q)$ and $(\ell_2 q)$ endpoint values. The bottom line was that highly overlapping $M_{\ell_1 q}$ and $M_{\ell_2 q}$ distributions also hamper the performance of the fitter, preventing a reliable fit with the ratio r floating in the fit (fig. 7.24 left). At the LM1 point, the two endpoints are quite close to each other. Due to this overlap, the fitter cannot reliably distinguish between the two when also a third endpoint - the one of $M_{\ell_2 q}^{\max,2}$ secondary endpoint of $(\ell_2 q)$ ¹³ - has to be determined.

The performance of the fit improves significantly when taking the value of r fixed to its nominal value. This is shown in fig. 7.25. The fit results in this case come out in better agreement with the theoretical expectations:

$$M_{\ell_1 q}^{\max} = 404.6 \pm 2.8(\text{stat.}) \text{ GeV}/c^2 \quad (7.36)$$

$$M_{\ell_2 q}^{\max} = 318.2 \pm 6.4(\text{stat.}) \text{ GeV}/c^2 \quad (7.37)$$

Finally, a measurement of an endpoint in the invariant mass distribution of the sum $M_{\ell_1 q} + M_{\ell_2 q}$ is performed. Requiring that the $(M_{\ell q})$ mass values entering the histogram are consistent with an $M_{\ell\ell q} < 500\text{GeV}/c^2$, the distribution of the sum was formed and fitted as in the case of LM6 (see figure 7.26). The smearing of the fit function was accounted with a factor of $\sigma = 30\text{GeV}$, as derived from the lepton-jet resolution modeling around the position of the endpoint in the distribution of the sum. The resulting endpoint measurement came out to be:

$$(M_{\ell_1 q} + M_{\ell_2 q})^{\max} = 698.7 \pm 17.4(\text{stat.}) \text{ GeV}/c^2 \quad (7.38)$$

which is to be compared with the nominal value of the endpoint at $(M_{\ell_1 q} + M_{\ell_2 q})^{\max, \text{TH}} = 610 \text{ GeV}/c^2$. The large shift in the central value of the measured endpoint which is observed is mainly due to the uncertainty on the shape used to model the mass distribution around the edge. Nevertheless, the usage of the true shape in the fitting procedure is expected to improve for the central value of the endpoint, but leave the error at the same level¹⁴.

The extraction of the endpoint value in the $M_{\ell_1 q} + M_{\ell_2 q}$ distribution is crucial, because it will help to solve ambiguities in the identification of the $M_{\ell\ell q}^{\max}$ endpoint among three possible options. As one can recall from the previous chapter, the endpoint of the sum is directly related to the $M_{\ell\ell q}^{\max,1}$ endpoint and can thus offer an additional constraint on the extraction of the SUSY masses, when $M_{\ell\ell q}^{\max,1}$ is missing. The relevant issue will be addressed in the next section.

¹³which is directly related to the ratio r as $r = M_{\ell_2 q}^{\max,2}/M_{\ell_2 q}^{\max}$.

¹⁴Since the error on the endpoint is mainly determined by the mass resolution model imposed.

CHAPTER 7. SPARTICLE MASS RECONSTRUCTION

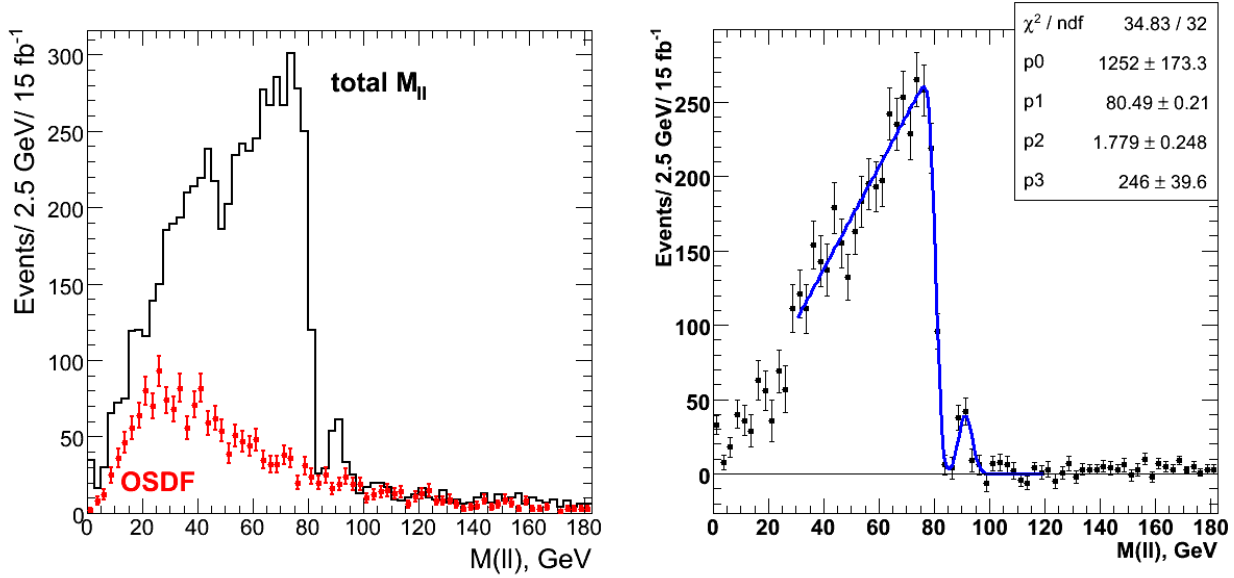


Figure 7.22: *Left:* the total M_{ll} distribution (in black) formed by two OSSF leptons superimposed with the OSOF distribution (in error bars). *Right:* the M_{ll} distribution after the OSOF background distribution has been subtracted. A fit to the distribution using the sum of three PDF contributions (two triangles and a gaussian Z-peak), is performed in order to extract the endpoint value(s), M_{ll}^{max} .

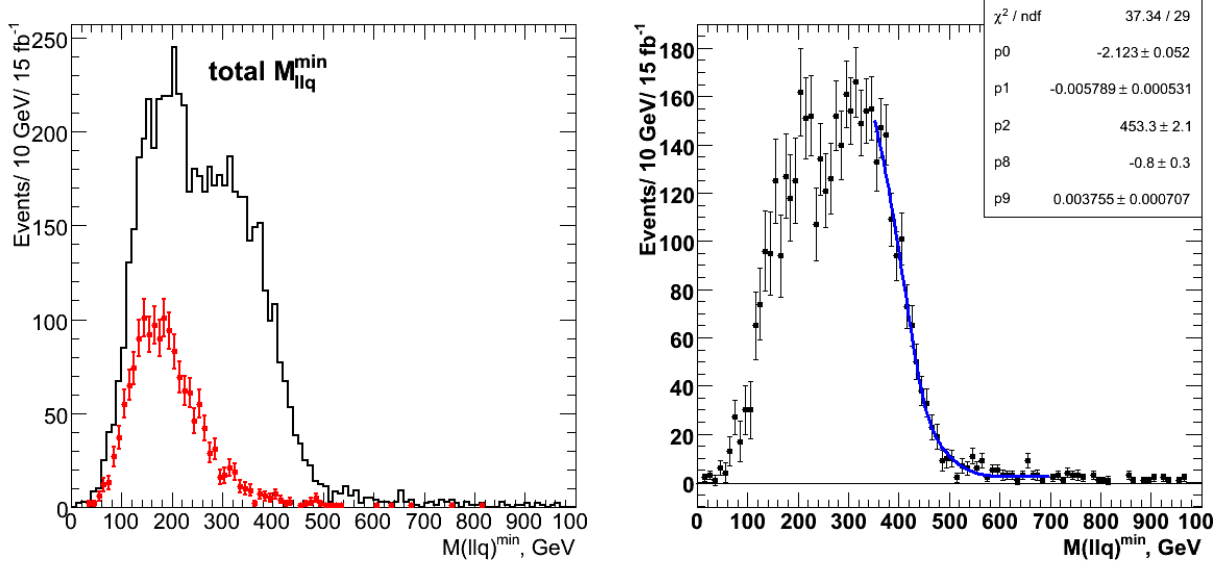


Figure 7.23: *Left:* the total M_{llq}^{min} distribution (in black) formed by combinations of the OSSF dilepton with the two highest- E_T jets. The OSDF distribution (in error bars) is shown superimposed. *Right:* the M_{llq}^{min} distribution after the OSOF background distribution has been subtracted. A fit of the M_{llq}^{min} distribution using a second degree polynomial smeared with a gaussian resolution model is used to quote the final estimate of the M_{llq}^{max} endpoint.

7.5. ENDPOINT MEASUREMENTS AT LM1

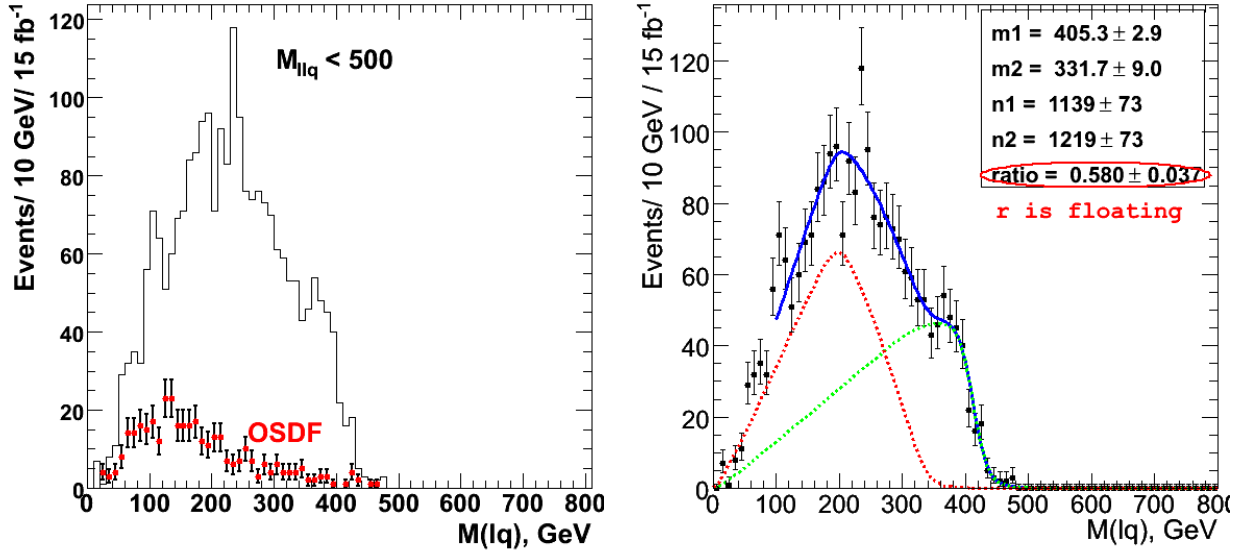


Figure 7.24: *Left:* the total M_{llq} distribution (in red) formed by lepton-jet combinations found consistent with a cut on $M_{llq} < 500 \text{ GeV}/c^2$. The OSDF distribution (in error bars) is shown superimposed. *Right:* the M_{llq} distribution after the OSDF background has been subtracted. A fit to the distribution using the nominal M_{llq} shape is used to directly extract the two endpoint values, $M_{\ell_1 q}^{max}$ and $M_{\ell_2 q}^{max}$, as well as the value of the mass ratio, r .

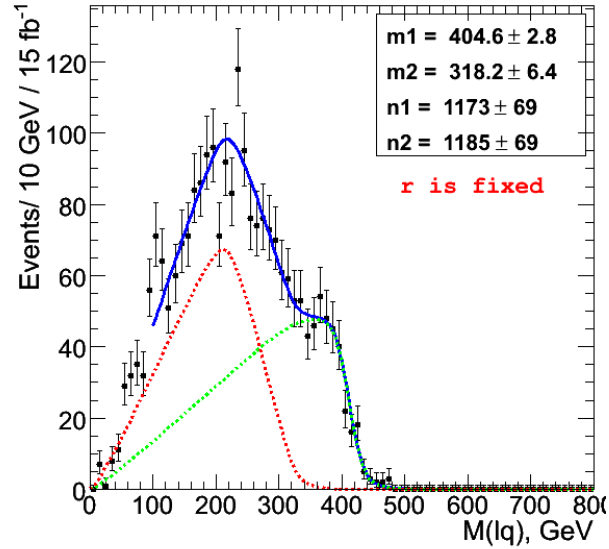


Figure 7.25: The M_{llq} fit repeated - in blue - using the nominal shape of the M_{llq} distribution. The fit function uses exceptionally the parameter $r = M_R/M_X = 0.66$ fixed in the fit in order to cross-check the results with the previous fit (when r is floating). The actual fit results cannot be valid before a first estimate of the supersymmetric mass spectrum is achieved (and consequently a value of r is determined).

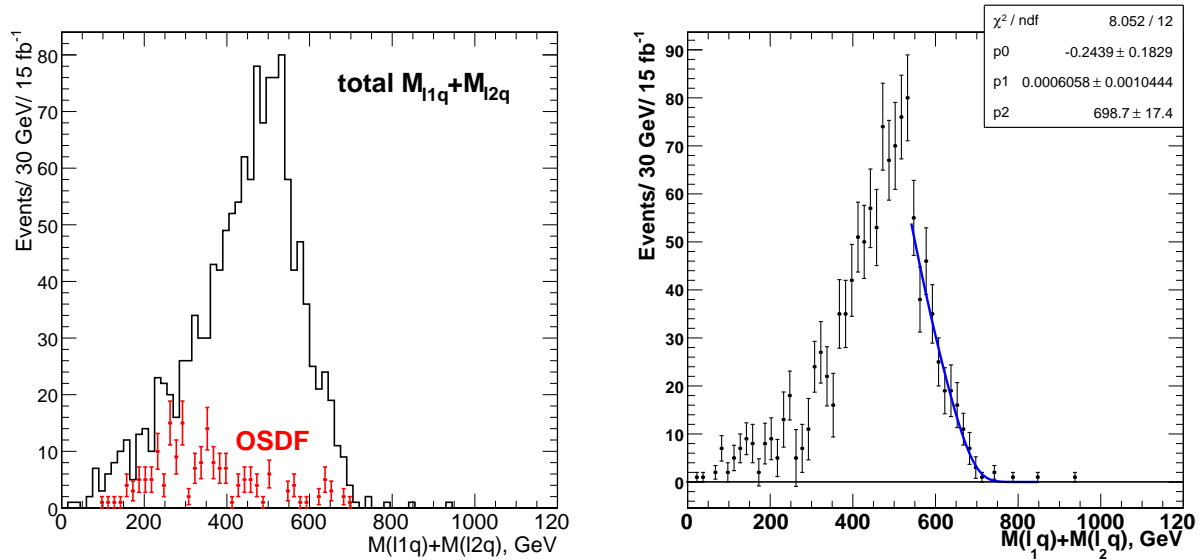


Figure 7.26: Left: The $M_{\ell 1q} + M_{\ell 2q}$ distribution obtained when imposing consistency requirements on lepton-jet combinations. Right: the $M_{\ell 1q} + M_{\ell 2q}$ distribution after the opposite-sign different-flavor (OSDF) background shape has been subtracted. A fit in the region around the edge, using a second degree polynomial smeared by a Gaussian, is performed in order to extract the endpoint value, $(M_{\ell 1q} + M_{\ell 2q})^{\max}$.

7.6. THE GLOBAL FIT TO EXTRACT THE MASSES

7.6 The global fit to extract the masses

The values of four supersymmetric particle masses ($\tilde{\chi}_1^0, \tilde{\ell}_L, \tilde{\chi}_2^0, \tilde{q}_L$) can be extracted from the measurement of (at least) four endpoints in the invariant mass distributions of the previous section. Analytical solutions of the inversion formulae stating the supersymmetric masses as a function of the (measured) endpoints, have been used as derived in [54].

A first set of SUSY masses were obtained by using the explicit solutions above. A value of the ratio r , representing the ratio of the masses $M_{\tilde{\ell}}/M_{\tilde{\chi}}$, is derived and is then used to iterate the fitting procedure and improve the $M_{\ell q}$ fit and the extraction of the $M_{\ell_2 q}^{\max}$ endpoint. The set of endpoint measurements used, are presented in tables 7.1 and 7.2, for the LM1 and LM6 mSUGRA points respectively.

Table 7.1: *The set of LM1 endpoint measurements used in the global fit to extract the supersymmetric particle masses, assuming 15fb^{-1} of integrated luminosity.*

Endpoint	Measured value (GeV/c^2)	Theory value (GeV/c^2)
$M_{\ell\ell}^{\max}$	80.5 ± 0.2	81.0
$M_{\ell_1 q}^{\max}$	404.7 ± 2.8	$\tilde{u} : 396.5 \ (\tilde{d} : 400.7)$
$M_{\ell_2 q}^{\max}$	318.3 ± 6.4	$\tilde{u} : 318.5 \ (\tilde{d} : 322.1)$
$M_{\ell\ell q}^{\max,1}$	453.3 ± 2.1	$\tilde{u} : 449.1 \ (\tilde{d} : 453.9)$
$(M_{\ell_1 q} + M_{\ell_2 q})^{\max}$	698.7 ± 17.4	$\tilde{u} : 610.0 \ (\tilde{d} : 613.9)$

Table 7.2: *The set of LM6 endpoint measurements used in the global fit to extract the supersymmetric particle masses, assuming 300fb^{-1} of integrated luminosity.*

Endpoint	Measured value (GeV/c^2)	Theory value (GeV/c^2)
$M_{\ell\ell}^{\max}$	75.3 ± 0.2	76.1
$M_{\ell_1 q}^{\max}$	237.6 ± 1.7	$\tilde{u} : 239.1 \ (\tilde{d} : 240.5)$
$M_{\ell_2 q}^{\max}$	679.5 ± 2.5	$\tilde{u} : 675.0 \ (\tilde{d} : 678.6)$
$M_{\ell\ell q}^{\max,1}$	720.1 ± 7.5	$\tilde{u} : 687.4 \ (\tilde{d} : 691.1)$
$(M_{\ell_1 q} + M_{\ell_2 q})^{\max}$	903.4 ± 27.7	$\tilde{u} : 883.6 \ (\tilde{d} : 888.4)$

The uncertainties on the endpoints listed so far involve only the statistical ones assuming a certain

amount of integrated luminosity. The systematic uncertainties are considered next as follows: first, systematic biases on the endpoint values are expected to originate from the fitting procedure of the invariant mass distributions. There are different kinds of such sources, the “fit range” variation, the uncertainty in the resolution model, as well as any acceptance effect on the shapes of the invariant mass distributions¹⁵. These types of sources of systematics are expected to be well understood and improved in the future, but are not considered in the scope of this thesis. The systematic uncertainties due to the jet energy scale are included as follows: opposite to the previous ones, they do refer to the potential of the CMS experiment in measuring endpoints in lepton-jet mass distributions. Only the systematics from the jet energy scale are then taken into account in the following discussion.

At a first stage, the arithmetic solutions of the sparticle masses in terms of endpoints were used to explicitly derive the SUSY mass values according to the expected errors on the endpoints. A set of 1000 CMS experiments was performed, considering that the measured endpoint values are distributed with a gaussian of mean equal to the central endpoint value and sigma equal to the measured error, as:

$$E_i^{\text{meas}} = E_i^{\text{nom}} + A_i \sigma_i^{\text{stat}} (+B_i \sigma_i^{\text{syst}}) \quad 7.39$$

where E_i accounts for the position of the i^{th} endpoint, coefficient A_i is picked from a gaussian of mean 0 and sigma 1, and σ_i corresponds to the statistical error of the relevant endpoint. The last term in parenthesis of the above expression describes a systematic term due to the electron and jet energy scale uncertainties (σ^{syst})¹⁶. This term is taken into account later, at the end of the section.

The ensemble distributions of the SUSY masses obtained in this way are shown in figure 7.27, both for the mSUGRA points LM1 (left) and LM6 (right). For LM1, the sparticle mass distributions are shown symmetric around their nominal value, despite the non-linear relationship of the endpoints with the masses. However, for LM6, the endpoint fluctuations are larger, and an asymmetric propagation to the sparticle masses grew stronger, resulting in long tails to higher mass values. In this case, an average shift of $\approx 20\text{GeV}$ is observed for the means of the ensemble distributions with respect to the nominal SUSY masses at LM6.

In practise, however, one uses a fit to find the best estimate of the SUSY masses which corresponds to a set of measured endpoints. We therefore performed a least-squared fit to all the information as follows: the inversion formulae as well as the measured endpoints and their errors are inserted in a χ^2 function of the form

$$\chi^2 = \sum_i \left[\frac{M_i^{\text{th}}(M_Q, M_X, M_L, M_0) - M_i^{\text{exp}}}{\delta M_i} \right]^2 \quad 7.40$$

where M_i^{th} is the nominal value for the measured endpoint i , M_i^{exp} is the experimental value and δM_i the experimental error. The function was minimized using the method MIGRAD from the Minuit2 package. A global fit to extract the supersymmetric particle spectrum is performed using

¹⁵The Acceptance has been shown to be a negligible source of systematic uncertainty as will be addressed in the next subsection.

¹⁶The coefficient B_i is picked up in the same way as the A_i one.

7.6. THE GLOBAL FIT TO EXTRACT THE MASSES

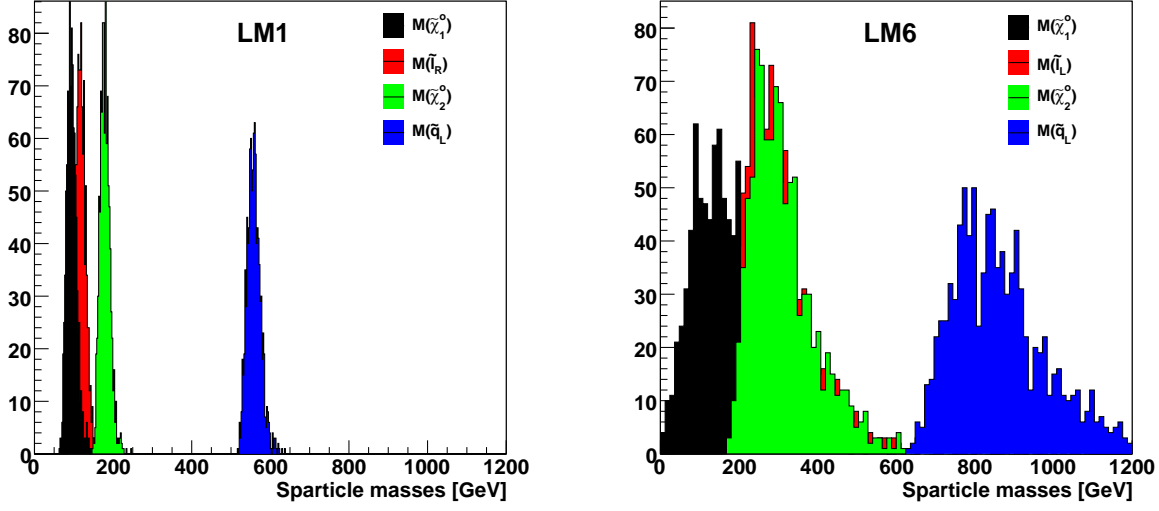


Figure 7.27: Supersymmetric particle masses at LM1 (left) and LM6 (right). The masses are obtained from solutions of the inverted equations which relate the sparticle masses with the complete set of endpoints, including propagation of the statistical endpoint fluctuations.

sets of endpoint values according to eq. (7.39), where the statistical uncertainties are taken as quoted in tables 7.1 and 7.2. Overall, 1000 CMS experiments are repeated, and the results are quoted in terms of the ensemble means on the endpoints and their errors.

The ambiguity in the selection of the correct formula for the $M_{\ell\ell q}^{\max}$ endpoint, implies that one has to test two plus one (for the non-collinear (NC)) hypotheses: either the endpoint corresponds to $M_{\ell\ell q}^{\max,1}$ or $M_{\ell\ell q}^{\max,2}$, and the hypothesis of the non-collinear endpoint $M_{\ell\ell q}^{\max, \text{NC}} = (M_Q - M_O)$. For both the LM1 and LM6 SUSY models, the hypothesis of $M_{\ell\ell q}^{\max}$ being the $M_{\ell\ell q}^{\max,3}$ can be excluded in advance, since this third endpoint has been identified earlier, studying correlations with the $M_{\ell q}$ mass, and cannot correspond to a true endpoint in the $M_{\ell\ell q}$ ¹⁷. It is also important to note that, in what follows, the hypotheses where the $M_{\ell\ell q}^{\max}$ is other than the $M_{\ell\ell q}^{\max,1}$, do not involve a complete set of (independent)¹⁸ endpoint measurements. For these, the $(M_{\ell 1q} + M_{\ell 2q})^{\max}$ measurement is provided as an additional information to adequately constrain the system.

Results at LM1

The results extracted for LM1 are shown in table 7.3. The initial two hypotheses refer to the case where $M_{\ell\ell q}^{\max}(\text{meas})$ is $M_{\ell\ell q}^{\max,1}$, which is actually the “true” case. The fit has been tried with either the inclusion of the $(M_{\ell 1q} + M_{\ell 2q})^{\max}$ - although not mandatory - or not, and it converges well and as expected, almost in the same way, in both cases. The third hypothesis refers to $M_{\ell\ell q}^{\max}(\text{meas})$ being the $M_{\ell\ell q}^{\max,2}$ endpoint; in this case, the extracted mass values come out significantly different

¹⁷See section 7.4.5

¹⁸The endpoints $M_{\ell\ell q}^{\max,2}$ and $M_{\ell\ell q}^{\max,3}$ are not orthogonal to any other available endpoint.

CHAPTER 7. SPARTICLE MASS RECONSTRUCTION

from the nominal ones and a “bad” χ^2 (of ≈ 3000) implies a failure of the fit. However, it can be seen that the last hypothesis, with $M_{\ell\ell q}^{\max}(\text{meas}) = M_{\ell\ell q}^{\max}(\text{NC})$, can be acceptable (i.e. the global fit converges) although the mass values diverge significantly from the theory. A possible way of rejecting this hypothesis in favor of the first one, is the large χ^2 value of the fit.

Table 7.3: *Supersymmetric particle mass values at LM1, extracted from the global fit of a complete set of endpoint measurements. The fit tests three hypotheses for the identification of the $M_{\ell\ell q}^{\max}(\text{measured})$ endpoint, taking also into account the measurement of the endpoint $(M_{\ell_1 q} + M_{\ell_2 q})^{\max}$. The fit converges preferably to hypothesis “ $M_{\ell\ell q}^{\max} = M_{\ell\ell q}^{\max,1}$ ”, which is the true endpoint of the $(\ell\ell q)$ mass.*

HYPOTHESIS	$(M_{\ell\ell q}^{\max})^{\text{meas}}$ $= M_{\ell\ell q}^{\max,1}$	$(M_{\ell\ell q}^{\max})^{\text{meas}}$ $= M_{\ell\ell q}^{\max,1}$ $+(M_{\ell_1 q} + M_{\ell_2 q})^{\max}$	$(M_{\ell\ell q}^{\max})^{\text{meas}}$ $= M_{\ell\ell q}^{\max,2}$ $+(M_{\ell_1 q} + M_{\ell_2 q})^{\max}$	$(M_{\ell\ell q}^{\max})^{\text{meas}}$ $= M_{\ell\ell q}^{\text{NC}}$ $+(M_{\ell_1 q} + M_{\ell_2 q})^{\max}$
$M_{\tilde{\chi}_1^0}$ [GeV/c ²]	94.9 ± 12.1	95.3 ± 12.0	17.5 ± 7.6	74.2 ± 6.0
$M_{\tilde{\ell}_R}$ [GeV/c ²]	118.8 ± 12.5	119.3 ± 12.3	45.0 ± 8.6	96.6 ± 6.2
$M_{\tilde{\chi}_2^0}$ [GeV/c ²]	179.5 ± 12.3	179.9 ± 12.1	99.9 ± 6.9	159.2 ± 6.3
$M_{\tilde{q}_L}$ [GeV/c ²]	558.5 ± 16.8	559.2 ± 16.4	468.3 ± 16.7	523.6 ± 7.2
χ^2 fit, value	4.1	5.1	3324	50.5

Overall, the fit results converge preferably to the hypothesis $M_{\ell\ell q}^{\max}(\text{meas}) = M_{\ell\ell q}^{\max,1}$. The extraction of the supersymmetric spectrum is in excellent agreement with the theoretical predictions.

The global fit to the supersymmetric masses has been repeated next considering also systematic uncertainties from the electron and jet energy scales (ElecES and JES). For an integrated luminosity of 15fb^{-1} , the uncertainty on the ElecES was taken as 0.1% and the uncertainty on the JES, as 2%. The measured endpoint values were additionally smeared according to a σ^{syst} by adding a third term in eq. (7.39). Using the preferred hypothesis $M_{\ell\ell q}^{\max} = M_{\ell\ell q}^{\max,1}$, and re-running the χ^2 fit, the supersymmetric mass spectrum of the particles $\tilde{\chi}_1^0, \tilde{\ell}_R, \tilde{\chi}_2^0, \tilde{q}_L$ was extracted. The final results were inspected in terms of the ensemble distributions of fig. 7.28, that are the distributions of the four masses, the distributions of the statistical as well as the systematic errors. The mean values on these distributions are reported in table 7.4.

7.6. THE GLOBAL FIT TO EXTRACT THE MASSES

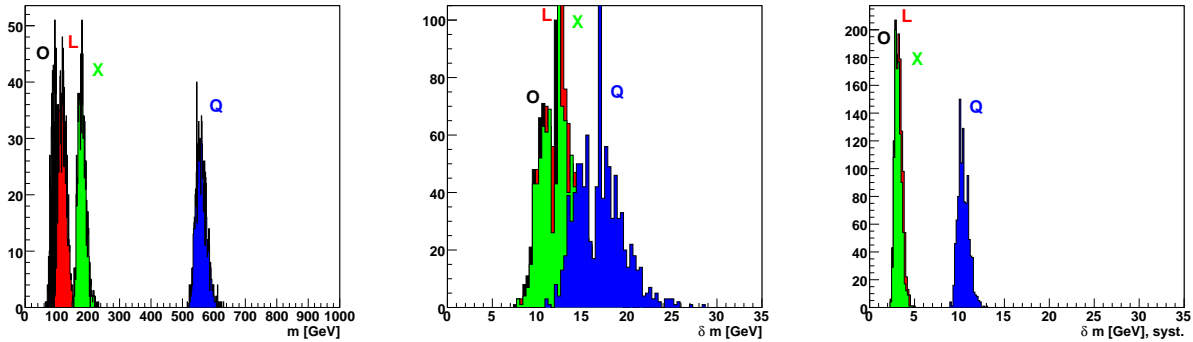


Figure 7.28: *The ensemble distributions of the global fit to the SUSY masses for the mSUGRA point LM1. Left: sparticle mass distributions – Middle: distributions of the errors on the sparticle masses – Right: distributions of the systematic errors on the sparticle masses.*

Table 7.4: *Fitted masses of the SUSY particles at the mSUGRA point LM1. Table shows the fit results of an ensemble of 1000 CMS experiments : the mean values of the ensemble distributions, for the fitted masses, the extracted statistical as well as systematic errors.*

Sparticle	Nominal mass (GeV/c ²)	Fitted mass (GeV/c ²)	Statistical error (GeV/c ²)	Systematic error (GeV/c ²)
$M_{\tilde{\chi}_1^0}$	94.9	96.0	12.7	3.4
$M_{\tilde{e}_R}$	118.8	119.9	12.3	3.1
$M_{\tilde{\chi}_2^0}$	179.6	180.7	12.5	3.2
$M_{\tilde{q}_L}$	558.0	560.2	17.0	10.4

Results at LM6

The same procedure was followed for the LM6 mSUGRA point. First, the measured endpoint values were smeared according to the statistical uncertainty quoted in table 7.2. Feeding them back to the global fit, all hypotheses for the $M_{\ell\ell q}^{\max}$ endpoint were similarly tested and the results were checked in terms of the performance of the fitter.

Figure 7.29 shows the ensemble distributions obtained out of 1000 CMS experiments with the global fit at LM6. The distributions of the SUSY masses along with their statistical uncertainties do not show a smooth behavior, whereas the performance of the pull distributions verifies that the fitter did not converge. The failure of the global fit to the supersymmetric particle masses at LM6, shows that the precision with which the endpoints were measured is not adequate to determine the

masses, despite the high luminosity scenario of 300fb^{-1} that has been assumed. In this work, only the results obtained by the arithmetic solutions of the masses are reported for LM6. Following the toy experiments of fig. 7.27, table 7.5 shows that the average SUSY mass values are shifted by $\approx 20\text{GeV}/c^2$ but also the standard deviations are rather large. Unless additional endpoint measurements are found, that might lead to stringent constraints on the masses, the SUSY mass determination at LM6-like scenarios may not be eventually feasible.

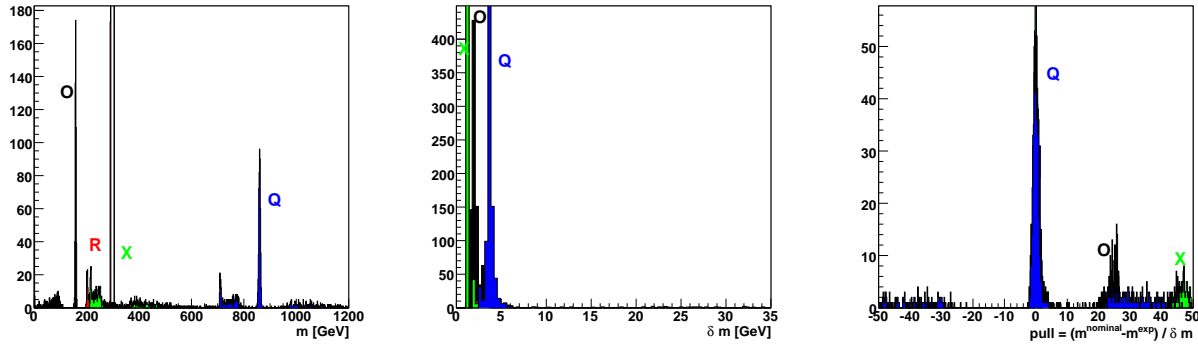


Figure 7.29: The ensemble distributions of the global fit to the SUSY masses for the mSUGRA point LM6. Left: sparticle mass distributions , Middle: distributions of the errors on the sparticle masses and Right: the pull distributions of the fitted sparticle masses.

Table 7.5: Extracted masses of the SUSY particles at the mSUGRA point LM6. Table shows the results of an ensemble of 1000 CMS experiments : the mean values and standard deviations of the ensemble mass distributions.

Sparticle	Nominal mass (GeV/c^2)	Average mass (GeV/c^2)	RMS (GeV/c^2)
$M_{\tilde{\chi}_1^0}$	158.1	183.0	123.3
$M_{\tilde{\ell}_L}$	291.0	309.5	110.1
$M_{\tilde{\chi}_2^0}$	304.8	323.3	110.0
$M_{\tilde{q}_L}$	859.9	861.6	116.0

7.7 The Acceptance effect

During the investigation of the $M_{\ell_2 q}$ fit issue, a study on the kinematics of the $(\ell_2 q)$ system has been performed. It has been seen that the acceptance cuts on the leptons p_T may affect the shape

7.7. THE ACCEPTANCE EFFECT

of the mass distributions and particularly the one of $M_{\ell_2 q}$.

The shape of the $M_{\ell_2 q}$ distribution exhibits two end-points: the first endpoint has been denoted as x_{\max} and corresponds to the true endpoint of the distribution, $M_{\ell_2 q}^{\max}$ (configuration depicted in fig. 6.4). A secondary endpoint lies at the position denoted as x_r and is related with the $M_{\ell_2 q}^{\max,2}$ (configuration depicted in fig. 6.5). The two kinematic configurations leading to the two maxima of the distribution have been both seen at the rest frame of the $Q = \tilde{q}$. In the configuration corresponding to the $M_{\ell_2 q}^{\max,2}(x_r)$, the ℓ_1 which is emitted in the $\tilde{\chi}_2^0$ decay, goes in the opposite direction to the quark (+z direction). In the configuration of $M_{\ell_2 q}^{\max}(x_{\max})$, the ℓ_1 goes together with the quark (-z direction). It follows that, on the way from $M_{\ell_2 q}^{\max,2}$ to $M_{\ell_2 q}^{\max}$, the ℓ_1 needs to flip its direction.

Approaching $M_{\ell_2 q}^{\max}$, the ℓ_1 is forced to go in the minus z direction resulting to a decrease of its energy and momentum, while on the opposite side, the $\tilde{\ell}$ increases its energy and momentum. Figures 7.31 and 7.32 show the energy and longitudinal momentum respectively of the ℓ_1 and $\tilde{\ell}$ ($X = \tilde{\chi}_2^0$ decay products) as a function of the $M_{\ell_2 q}$ mass, in the rest frame of the $Q = \tilde{q}$. The green lines on the plots limit the regions between the two endpoints in $M_{\ell_2 q}$, where the momentum of ℓ_1 starts decreasing to reach its minimum value right upon the true endpoint $M_{\ell_2 q}^{\max}$. There, the lepton momentum points in the negative direction of z.

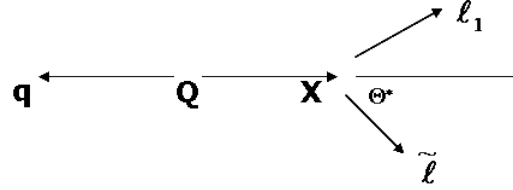


Figure 7.30: Schematic view of the decay of $X = \tilde{\chi}_2^0$ in the $Q = \tilde{q}$ rest frame. θ^* is the decay angle in the rest frame of $X = \tilde{\chi}_2^0$.

The above picture can be understood by some simple kinematic analysis. Figure 7.30 shows a schematic view of the decay starting from the $Q = \tilde{q}$. Choosing the +z-axis to be in the direction of the $X = \tilde{\chi}_2^0$, and θ^* to be the decay angle of $R = \tilde{\ell}$ in the rest frame of $X = \tilde{\chi}_2^0$, then it can be easily shown that the energy of ℓ_1 and $\tilde{\ell}$ in the rest frame of $X = \tilde{\chi}_2^0$ are:

$$E^*(\ell_1) = \frac{M_X^2 - M_{\tilde{\ell}}^2}{2M_X} = p^*(\ell_1) = p^*(\tilde{\ell}) \quad [7.41]$$

$$E^*(\tilde{\ell}) = \sqrt{p^*(\tilde{\ell})^2 + M_{\tilde{\ell}}^2} > E^*(\ell_1) \quad [7.42]$$

With a boost to the $Q = \tilde{q}$ frame, the energy-momentum equations for the $X = \tilde{\chi}_2^0$ products become:

$$E(\tilde{\ell}) = \gamma E^*(\tilde{\ell})(1 + \beta \cos \theta^*) \quad \text{and} \quad E(\ell_1) = \gamma E^*(\ell_1)(1 - \beta \cos \theta^*) \quad [7.43]$$

$$p_L(\tilde{\ell}) = \gamma E^*(\tilde{\ell})(\beta + \cos \theta^*) \quad \text{and} \quad p_L(\ell_1) = \gamma E^*(\ell_1)(\beta - \cos \theta^*) \quad [7.44]$$

with $\gamma = E_X/M_X$ and $\beta = p_X/E_X$ the parameters of the boost from the $X = \tilde{\chi}_2^0$ frame to the $Q = \tilde{q}$ rest frame.

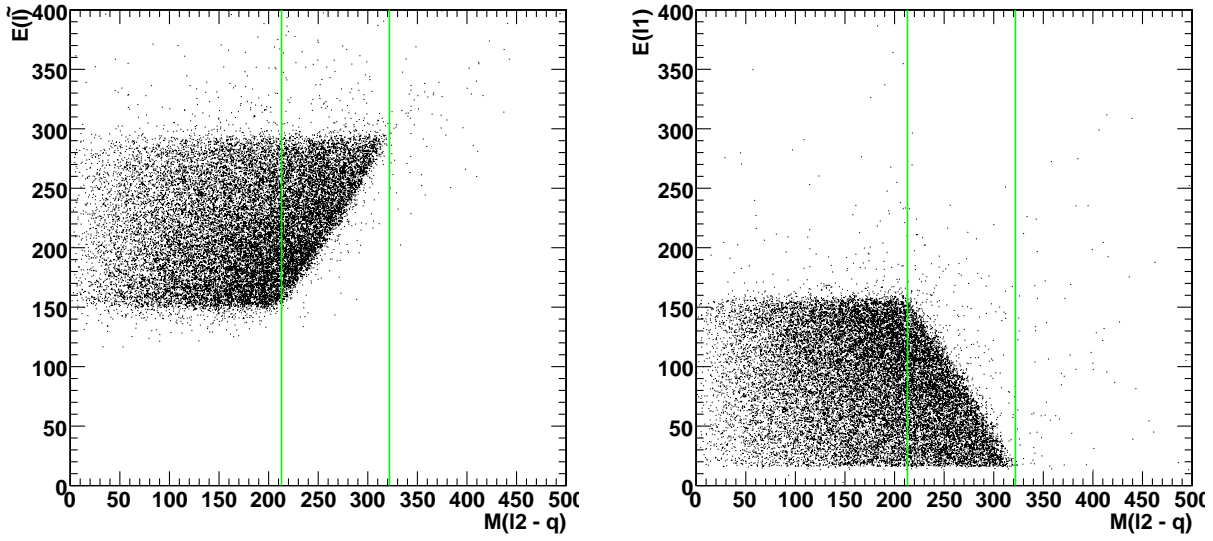


Figure 7.31: The energy of $\tilde{\ell}$ (left) and ℓ_1 (right) versus the $M_{\ell_2 q}$ mass, in the $Q = \tilde{q}$ rest frame. The green lines limit the region between the secondary maximum, $M_{\ell_2 q}^{\max,2}$, and the true maximum $M_{\ell_2 q}^{\max}$.

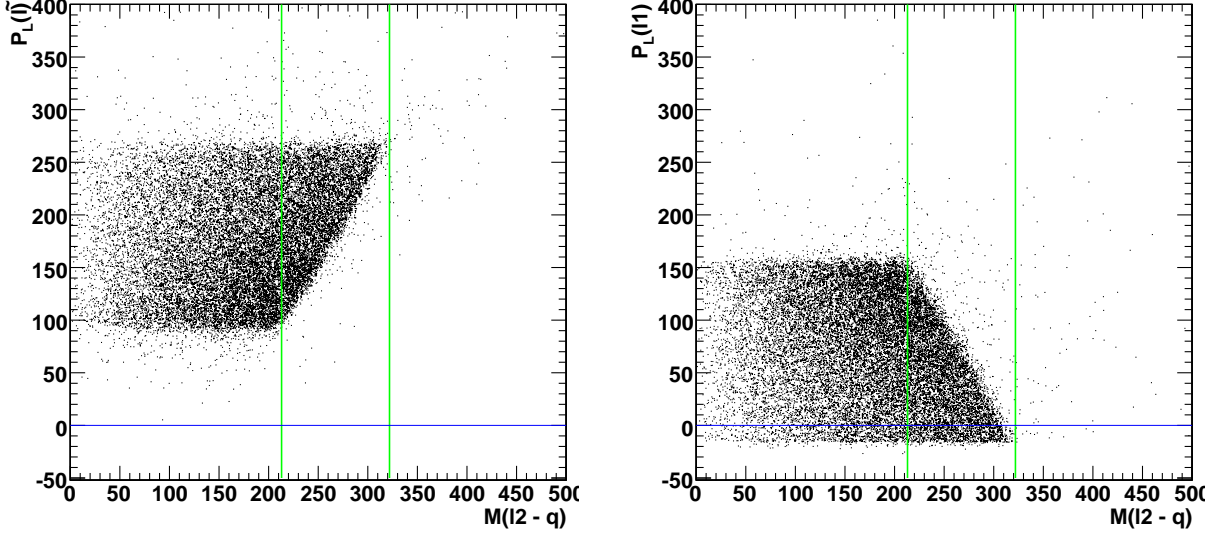


Figure 7.32: The longitudinal momentum of $\tilde{\ell}$ (left) and ℓ_1 (right) versus the $M_{\ell_2 q}$ mass, in the $Q = \tilde{q}$ rest frame. The z -axis is defined along the direction of $X = \tilde{\chi}_2^0$. The green lines limit the region between the secondary maximum, $M_{\ell_2 q}^{\max,2}$, and the true maximum $M_{\ell_2 q}^{\max}$.

It follows from equations (7.44) that the ℓ_1 goes in the $+z$ direction, i.e. the direction of $X = \tilde{\chi}_2^0$, unless $\beta < \cos \theta^*$. It is interesting to look at the behavior of the energy and longitudinal momentum of ℓ_1 and $\tilde{\ell}$ as a function of the $\cos \theta^*$. Figures 7.33 and 7.34 show that the energy and momentum

7.7. THE ACCEPTANCE EFFECT

of the $\tilde{\ell}$ increase linearly with the $\cos \theta^*$. With the opposite behavior, the energy and momentum of ℓ_1 decrease linearly with $\cos \theta^*$. In the cases, in addition, where $\cos \theta^* > \beta$, the ℓ_1 goes to the negative (-z) direction, as shown in red on the plots, minimizing its momentum.

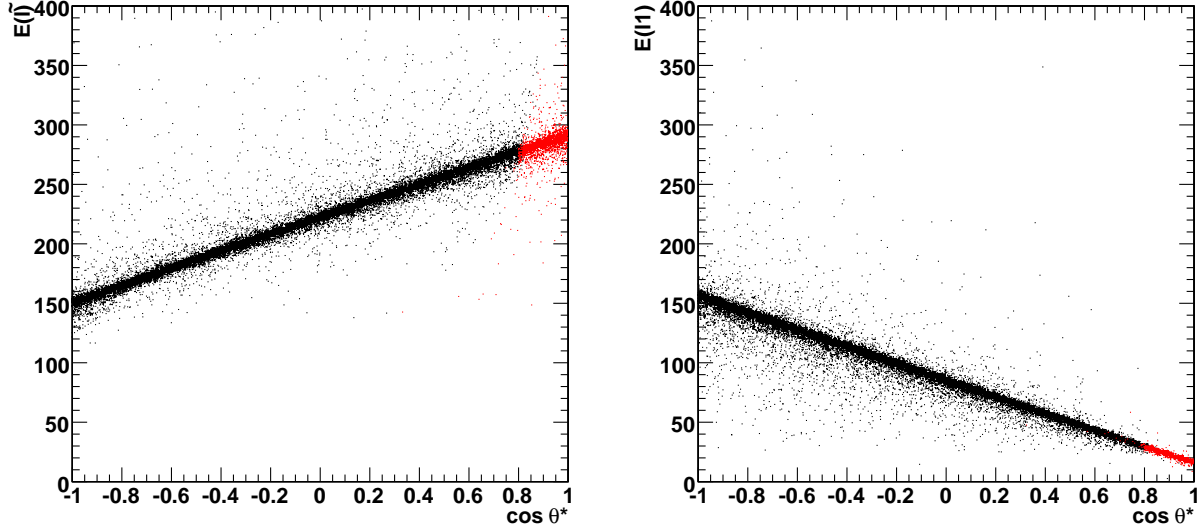


Figure 7.33: The energy of $\tilde{\ell}$ (left) and ℓ_1 (right) versus the decay angle θ^* (in the rest frame of $X = \tilde{\chi}_2^0$), in the $Q = \tilde{q}$ rest frame. In red: cases where $\cos \theta^* > \beta$, with $\beta = p_X/E_X$.

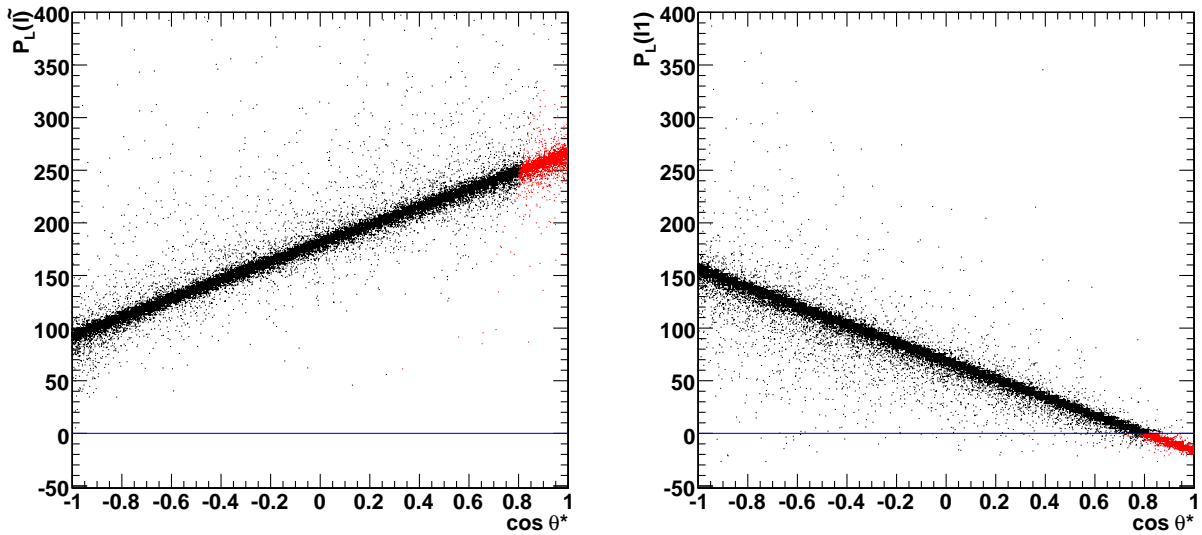


Figure 7.34: The longitudinal momentum of $\tilde{\ell}$ (left) and ℓ_1 (right) versus the decay angle θ^* (in the rest frame of $X = \tilde{\chi}_2^0$), in the $Q = \tilde{q}$ rest frame. In red: cases where $\cos \theta^* > \beta$, with $\beta = p_X/E_X$.

The overall picture is next propagating to the laboratory frame. Figures 7.35 and 7.36 show the average p_T of ℓ_1 and ℓ_2 respectively as a function of the $M_{\ell_{1q}}$ and $M_{\ell_{2q}}$ masses, at LM1. It can be seen that the p_T of ℓ_1 is decreasing on the way from $M_{\ell_{2q}}^{\max,2}$ to $M_{\ell_{2q}}^{\max}$.

CHAPTER 7. SPARTICLE MASS RECONSTRUCTION

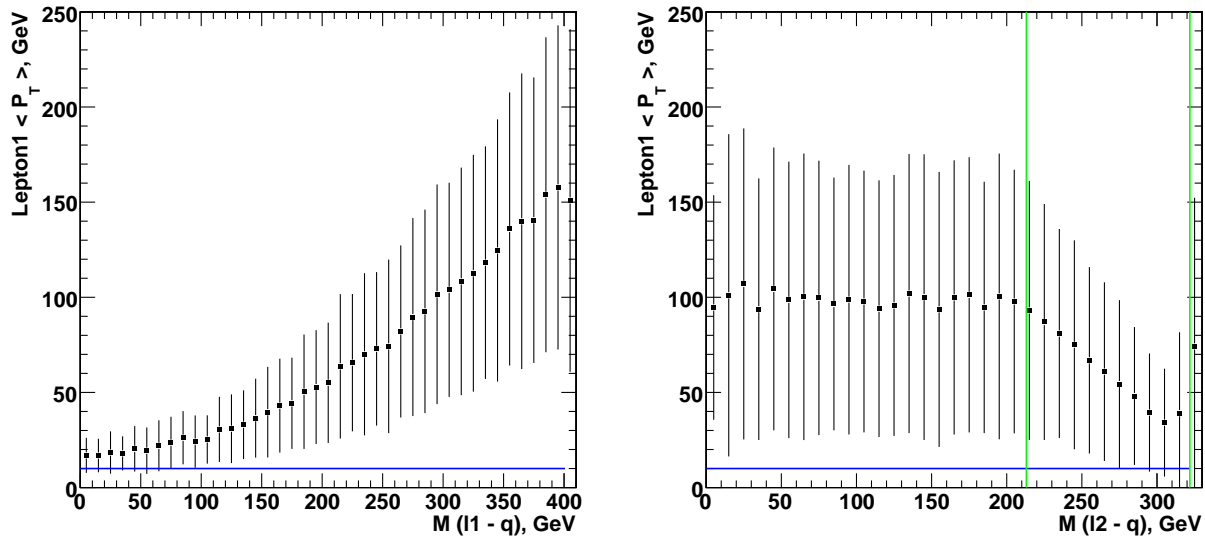


Figure 7.35: Average p_T of the lepton ℓ_1 versus $M_{\ell_1 q}$ (left) and $M_{\ell_2 q}$ (right), in the laboratory frame. A drop of the p_T is visible within the region in $M_{\ell_2 q}$ limited by the $M_{\ell_2 q}^{\max,2}$ and $M_{\ell_2 q}^{\max}$ maxima (green lines).

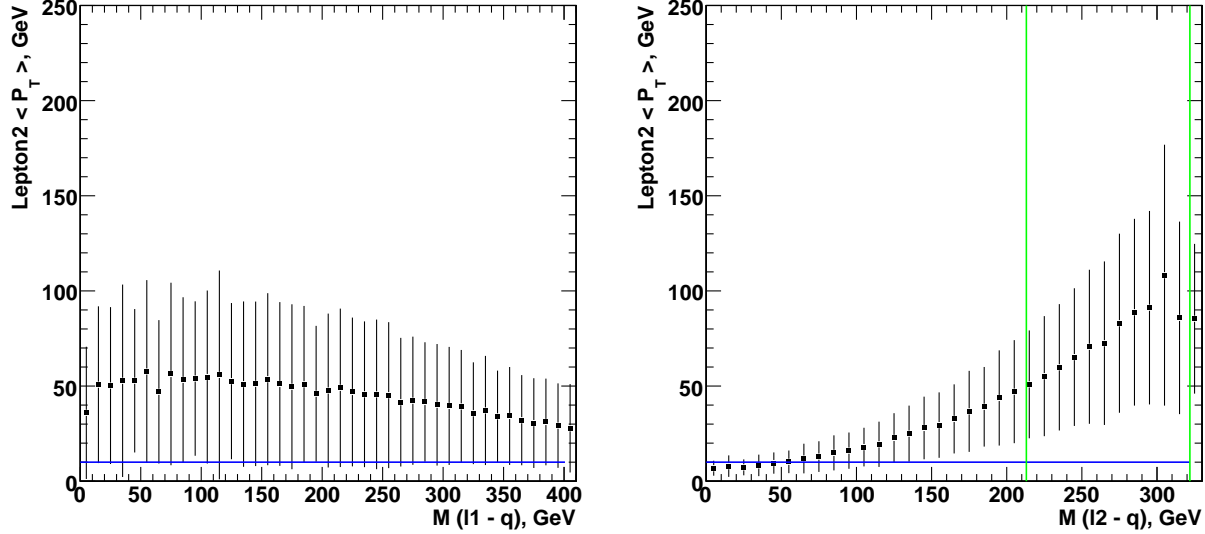


Figure 7.36: Average p_T of the lepton ℓ_2 versus $M_{\ell_1 q}$ (left) and $M_{\ell_2 q}$ (right), in the laboratory frame.

The effect can be explained by the fact that it is the momentum of ℓ_1 which decreases in the rest frame of $Q = \tilde{q}$, and due to the weak boost ($M_{\tilde{q}}$ is large), the picture is visible also in the laboratory frame. It becomes more prominent in the case of LM6, where the average p_T of ℓ_1 reaches very low values (~ 10 GeV) right upon the $M_{\ell_2 q}^{\max}$ (see figures 7.37 and 7.38).

7.7. THE ACCEPTANCE EFFECT

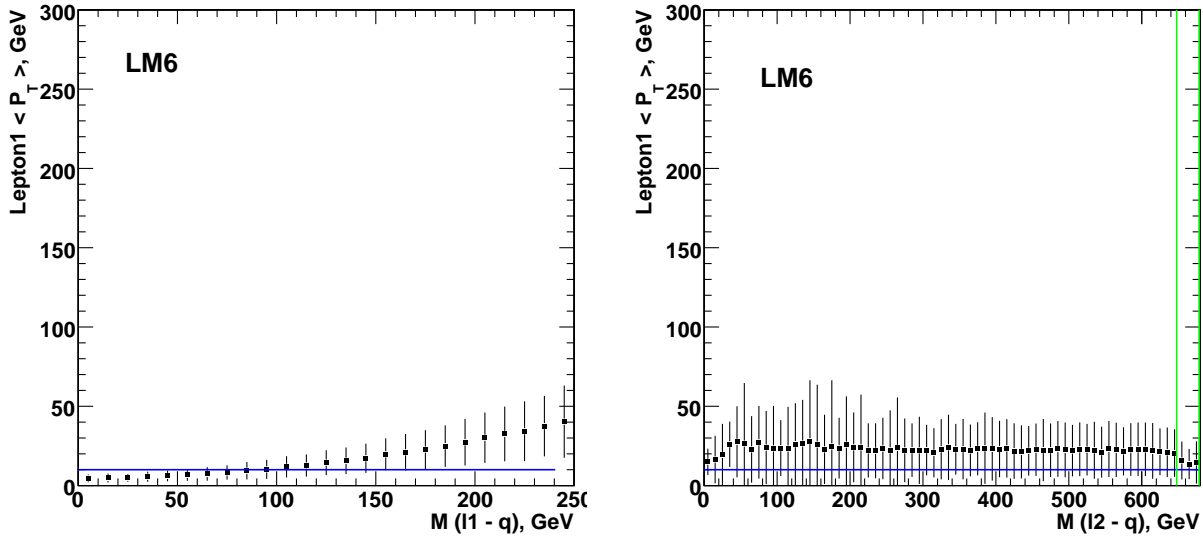


Figure 7.37: Average p_T of the lepton ℓ_1 versus $M_{\ell_1 q}$ (left) and $M_{\ell_2 q}$ (right), in the laboratory frame. A drop of the p_T is visible within the region in $M_{\ell_2 q}$ limited by the $M_{\ell_2 q}^{\max,2}$ and $M_{\ell_2 q}^{\max}$ maxima (green lines).

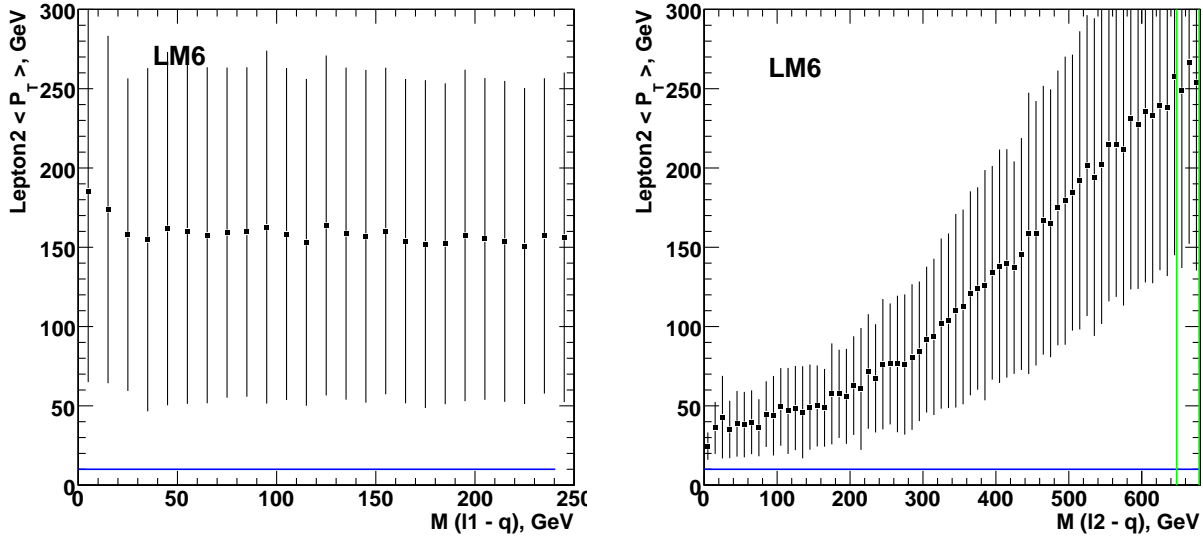


Figure 7.38: Average p_T of the lepton ℓ_2 versus $M_{\ell_1 q}$ (left) and $M_{\ell_2 q}$ (right), in the laboratory frame.

The above results rendered the study of the effect of the lepton p_T cuts imposed in the analysis upon the actual shapes of the mass distributions and particularly the one of $M_{\ell_2 q}$. Due to the fact that the latter distribution has been fitted using the nominal shape of the distribution, a possible bias on the extraction of the $M_{\ell_2 q}^{\max}$ has been investigated. Using a toy SUSY MC generator, the $M_{\ell_2 q}$ distributions before and after the acceptance cuts applied were obtained and an acceptance

CHAPTER 7. SPARTICLE MASS RECONSTRUCTION

histogram was plotted as shown in fig. 7.39. A fit to the $M_{\ell_2 q}$ showed a shift to lower values, by ~ 2 GeV, on the extraction of the $M_{\ell_2 q}^{\max}$ (see fig. 7.40, left). As a closure test, an acceptance correction function was included in the fit function and the fit was repeated as shown on the right side of fig. 7.40. In this case, the $M_{\ell_2 q}^{\max}$ value was indeed restored in its nominal value, proving that a bias on the endpoint can be induced due to the acceptance p_T cuts on the leptons. However, the effect becomes negligible compared to the smearing of the distributions due to detector effects.

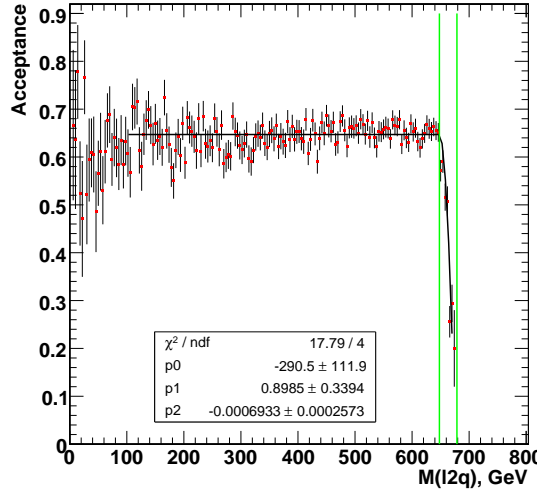


Figure 7.39: *A fit to the $M_{\ell_2 q}$ acceptance is performed in order to be used as a correction to the $M_{\ell_2 q}$ fit function.*

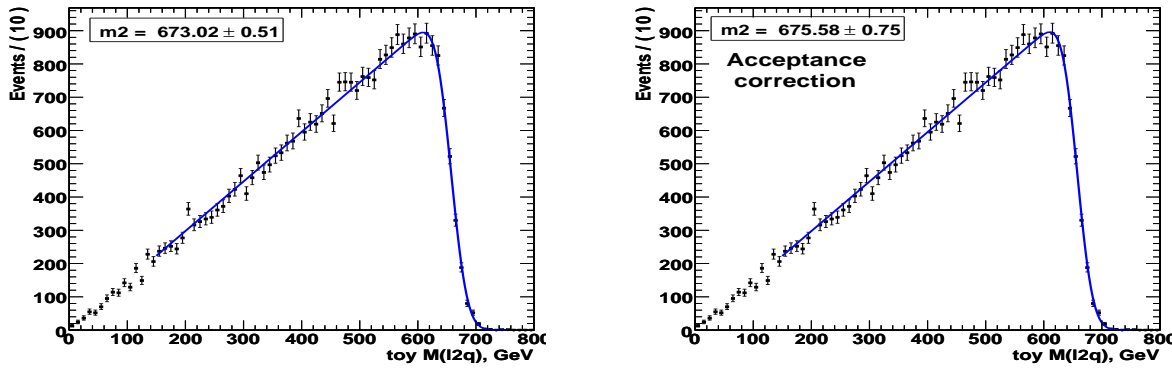


Figure 7.40: *Left: the fit to the toy $M_{\ell_2 q}$ data generated by a toy MC SUSY generator. A shift on the endpoint, of ~ 2 GeV to lower values, is observed which is due to the acceptance cuts effect. Right: the same fit including the acceptance correction function in the fitting PDF, restoring for the shift on the endpoint.*

8

Conclusion

In this thesis, a study of the observation and the measurement of the characteristics of the supersymmetric decay

$$\tilde{q} \rightarrow \tilde{\chi}_2^0 q \rightarrow \tilde{\ell}^\pm \ell^\mp q \rightarrow \tilde{\chi}_1^0 \ell^\pm \ell^\mp q \quad (\ell = e \text{ or } \mu) \quad (8.1)$$

with the CMS detector, has been presented. The experimental signature consists of two opposite-sign and same-flavor leptons, hadronic jets with large transverse momentum, as well as significant missing transverse energy. To enable a detailed simulation of the signature, the mSUGRA theoretical framework is utilized. Using one benchmark point in the mSUGRA parameter space, LM1, the study has developed a set of selection criteria which enhance the supersymmetric signature over other background processes coming from the detector or from physics from the Standard Model. The analysis has targeted an integrated luminosity of 1fb^{-1} and, assuming the earlier observation of an excess of this type of events over the Standard Model expectation, has been optimized for the observation and the measurement of the endpoint in the dilepton invariant mass distribution. This endpoint value can then provide a first constraint to be used for supersymmetric particle mass measurements.

The optimal trigger path for this analysis, has been shown to come from the hadronic related algorithms of the High Level Trigger, particularly the ones which require missing E_T (MET). MET triggers are proven to recover the relatively low p_T leptons (below the leptonic triggers p_T thresholds) present in the SUSY cascades, while maintaining a high efficiency for the signal above the offline MET requirement. The trigger path chosen here was the HT+MET¹ path, which has a signal efficiency of 98% with respect to the offline analysis cuts.

The main sources of physics background are uncorrelated supersymmetric decays and high- p_T SM processes: $t\bar{t}$, di-bosons (WW , WZ and ZZ) as well as the associated production of W/Z bosons and jets. The strategy developed to eliminate these background processes is “data-driven” and makes use of different-flavor di-lepton ($e\mu$) pairs in order to estimate the background in the ee and $\mu\mu$ combinations. The procedure requires knowledge of the electron to muon reconstruction efficiencies (ϵ^e/ϵ^μ) which can be obtained in real data by the “tag-and-probe” method using $Z \rightarrow ee/\mu\mu$ events. It has been demonstrated that the background estimate is reliable for background processes which are symmetric in flavor, i.e. which have equal probabilities for yielding electron and muon signatures. A small but negligible asymmetry has been observed in events where at least one or both leptons are fakes or coming from heavy-flavor quark (b/c) decays.

¹In real data, it may be replaced by the MHT trigger which is expected to be a more robust measurement than MET in the online trigger decision.

CHAPTER 8. CONCLUSION

The position of the endpoint in the invariant mass distribution of the two leptons is then extracted via an unbinned maximum likelihood fit with components describing the background (flavor-symmetric processes and the Z events) and the characteristic triangular shape of the supersymmetric signal. The measurement is performed separately on the dielectron and dimuon mass distributions. The reason for this is the application of two different resolution models for the di-electron or di-muon mass smearing taken into account in the likelihood function. The fitting procedure is tested with a toy MC study which simulates the final distributions from thousands of similar toy experiments. The statistical uncertainty of the endpoint-parameters measurements are quoted according to the pull distributions obtained from this study. Finally, the following sources of systematic uncertainties in the measurement of the position of the edge are considered: the resolution model imposed, the Electron and Jet Energy Scales, the $e\mu$ shape uncertainty due to fake leptons as well as the acceptance effect on the triangular shape of the signal distribution.

The analysis concludes with the measurement of the position of the di-electron and di-muon edges (for an integrated luminosity of 1fb^{-1}) :

$$\Delta m_{ee}^{max} = \pm 1.07 \text{ (stat.)} \pm 0.36 \text{ (syst.)} \text{ GeV/c}^2$$

$$\Delta m_{\mu\mu}^{max} = \pm 0.75 \text{ (stat.)} \pm 0.18 \text{ (syst.)} \text{ GeV/c}^2$$

The systematic uncertainties on the endpoints are found to be small and this measurement is thus placed among the most precise measurements that can be achieved at LHC.

The thesis also presents a study of the feasibility of determining the masses of the supersymmetric particles appearing in chain 8.1, i.e. the four masses $M_{\tilde{q}}$, $M_{\tilde{\chi}_2^0}$, $M_{\tilde{\ell}}$ and $M_{\tilde{\chi}_1^0}$. This is achieved with the measurement of upper endpoints in the invariant mass distributions $M_{\ell_1 q}$, $M_{\ell_2 q}$, $M_{\ell\ell q}$ and $M_{\ell_1 q} + M_{\ell_2 q}$. The method followed is known as the “endpoint technique” and is applied in two benchmark points in mSUGRA, LM1 and LM6, where the \tilde{q}/\tilde{g} cascade decays and the leptonically decaying $\tilde{\chi}_2^0$ appear with large production rates.

The reconstruction of the invariant mass distributions involves now a quark which must be matched with the two leptons. The selection of the quark (jet) is based on the selection of the two highest- p_T jets in the event, which, according to simulation, has a high probability of correctness. Since in every supersymmetric event there are two different decay chains, the invariant mass distributions constructed by the dilepton with two jets are subject to large combinatorial background due to wrong dilepton-jet associations. To reduce this background two methods are investigated: the first one makes use of the so-called “mixed-event technique”, which assumes that for a given event, the di-lepton and the quark belonging to a different SUSY decay chain are correlated (kinematically) only weakly. The lepton sector of one event is thus combined with the jet sector of another randomly selected event and pairs of lepton-jet combinations are used to model the combinatorial background. It is shown that the shape of the background distributions can be reproduced fairly well, at least in the regions around the edges, with a small discrepancy towards high mass values. For this reason, the technique is used conservatively and only when a rough estimate of the shape is needed. A second, more robust, method makes use of certain kinematic constraints that must be fulfilled by the combination of two leptons with a jet, so as to be consistent with endpoint measurements. A drawback of this method is, however, that the statistics are significantly reduced and therefore the measurements are feasible only in high luminosity scenarios.

A novel aspect of the analysis is the usage of the theoretical shape in the likelihood function to fit (almost all) of the mass distributions. The methodology has the advantage of the extraction of additional kinematic constraints, beyond the endpoint values themselves, which are directly related with the masses of the supersymmetric particles (in particular, the extraction of ratios of supersymmetric particle masses). A weakness of the method is that depending on the mass hierarchy, different kinematic configurations and hence different mass formulae are valid for a given SUSY model. That is the case for the $M_{\ell\ell q}$ distribution, in which the shape depends on the actual true endpoint of the distribution among the four possible ones ($M_{\ell\ell q}^{\max,1}$, $M_{\ell\ell q}^{\max,2}$, $M_{\ell\ell q}^{\max,3}$, or $M_{\ell\ell q}^{\text{NC}}$) depending on the SUSY particle masses. In the example of the LM6 point, the effect is met in the measurement of the endpoint in the $M_{\ell\ell q}$ mass, where an ambiguity between two endpoints in the distribution ($M_{\ell\ell q}^{\max,1}$ or $M_{\ell\ell q}^{\max,2}$) hampers the usage of the actual shape in the likelihood function. On the other hand, the shape of the $M_{\ell q}$ distribution is uniquely represented in any SUSY particle mass hierarchy and a direct fit to the distribution is possible. Still, a distinction between the $(\ell_1 q)$ and $(\ell_2 q)$ regions has to be established.

It is shown that the observation of correlations among particular effective mass distributions enables the identification of the correct mass formula to be used in the fitting procedure. This is particularly advantageous in the identification of the $M_{\ell_1 q}$ and $M_{\ell_2 q}$ endpoint regions when these are plotted as a function of the $M_{\ell\ell q}$ distribution. It is proven that the $M_{\ell_1 q}^{\max}$ endpoint is reached over a wide range of $M_{\ell\ell q}$ values whereas the $M_{\ell_2 q}^{\max}$ endpoint is projecting towards one endpoint in $M_{\ell\ell q}$. This also restricts the number of hypotheses for the $M_{\ell\ell q}$ true endpoint measured. A difficulty on the direct measurement of the $M_{\ell_2 q}$ upper endpoint has been observed in the case of the LM6 point. It is shown that in any given SUSY model where the mass ratio of $M_{\tilde{\ell}}$ to $M_{\tilde{\chi}_2^0}$ is close to 1, the fitting procedure of the $M_{\ell_2 q}$ mass, using the nominal shape of the distribution, does not reliably converge to the correct values for the endpoint and for the ratio of the masses $r = M_{\tilde{\ell}}/M_{\tilde{\chi}_2^0}$, simultaneously. The problem is resolved by iteratively solving the endpoint-mass relations, obtaining a first estimate for the ratio r and finally correcting the fitting results.

Table 8.1: *The full set of endpoint measurement uncertainties at LM1 and LM6.*

Endpoint measurement uncertainties		
	LM1 @15fb ⁻¹	LM6 @300fb ⁻¹
$\Delta M_{\ell\ell}^{\max}$	~ 0.2 GeV/c ²	~ 0.2 GeV/c ²
$\Delta M_{\ell_1 q}^{\max}$	~ 2.8 GeV/c ²	~ 1.7 GeV/c ²
$\Delta M_{\ell_2 q}^{\max}$	~ 6.4 GeV/c ²	~ 2.5 GeV/c ²
$\Delta M_{\ell\ell q}^{\max}$	~ 2.1 GeV/c ²	~ 7.5 GeV/c ²
$\Delta(M_{\ell_1 q} + M_{\ell_2 q})^{\max}$	~ 17.5 GeV/c ²	~ 28.0 GeV/c ²

Overall, a complete set of endpoint measurements has been obtained assuming an integrated luminosity of 15fb⁻¹ and 300fb⁻¹, for both the mSUGRA models LM1 and LM6. The statistical

CHAPTER 8. CONCLUSION

uncertainties on the positions of the endpoints vary among the different (di)lepton-jet combinations as shown in table 8.1.

As for the systematic uncertainties, the following sources have been investigated: (i) the fitting procedure including the fit range variation and the lepton-jet mass resolution model imposed, (ii) the acceptance effect from the lepton p_T cuts imposed and (iii) the variation of the electron and jet energy scale uncertainties. The systematics arising from the fitting procedure have been assumed to be well understood and controlled by the time the analysis will be performed on real data. The systematics from the acceptance on the leptons were shown to be at lower levels than the statistical uncertainties. Finally, the systematic effect arising from the electron and jet energy scale variation, assuming the “knowledge” of the lepton and the jet energy scales with a precision of 0.1% and 2% respectively, are calculated and reported here.

With at least four endpoint measurements made, a global fit is performed in order to extract the values of supersymmetric particle masses. For the LM1 point, the following SUSY mass measurements were shown to be feasible at 15 fb^{-1} of integrated luminosity:

$$\begin{aligned} M_{\tilde{\chi}_1^0} &= 96.0 \pm 12.7 \text{ (stat.)} \pm 3.4 \text{ (syst.)} \text{ GeV/c}^2 \\ M_{\tilde{\ell}_R} &= 119.9 \pm 12.3 \text{ (stat.)} \pm 3.1 \text{ (syst.)} \text{ GeV/c}^2 \\ M_{\tilde{\chi}_2^0} &= 180.7 \pm 12.5 \text{ (stat.)} \pm 3.2 \text{ (syst.)} \text{ GeV/c}^2 \\ M_{\tilde{q}_L} &= 560.2 \pm 17.0 \text{ (stat.)} \pm 10.4 \text{ (syst.)} \text{ GeV/c}^2 \end{aligned}$$

This analysis has thus demonstrated a possible method to measure the masses of the four sparticles involved in the decay chain 8.1, once the first dilepton edge is established and measured (as demonstrated in this thesis) at lower integrated luminosities. Whereas only two points in mSUGRA space has been investigated, the methodology developed applies also to general mass hierarchies for the four sparticles in the decay chain. The results are encouraging: it seems that with significant luminosities, the LHC, and CMS in particular, may well obtain good estimates of the masses of the low-lying sleptons, neutralinos and squarks.

Appendix A

A toy MC study with the di-lepton mass

Figures 8.1 and 8.2 show the distributions of the dielectron endpoint, its error as well as the pull distribution respectively.

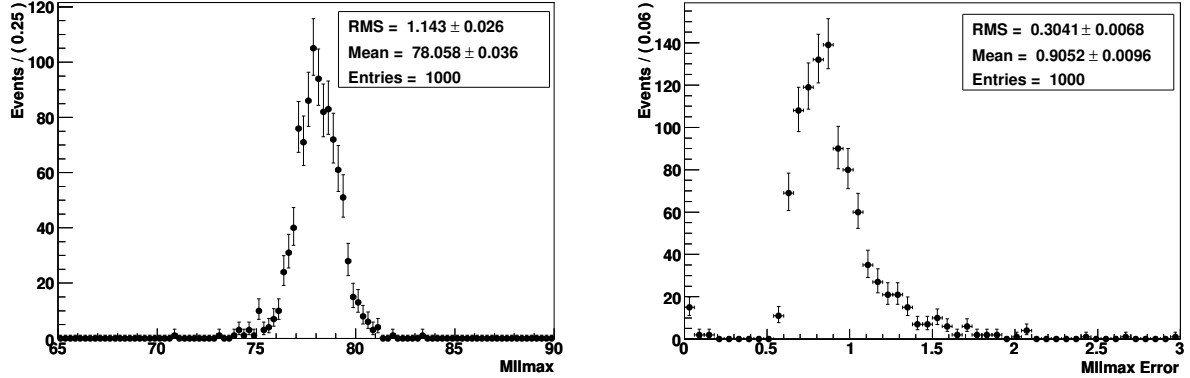


Figure 8.1: Toy MC fit result of the distribution of the dielectron endpoint (left) and its error (right).

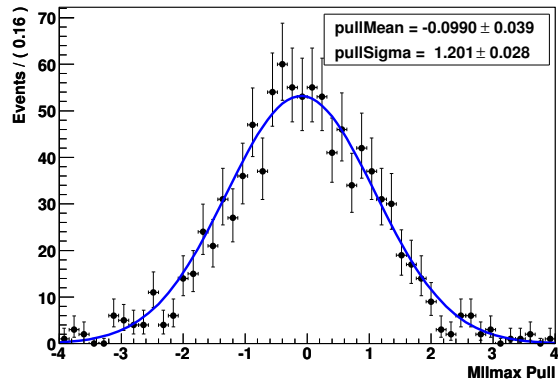


Figure 8.2: Toy MC fit result for the pull distribution of the dielectron endpoint.

Appendix A

Figures 8.3 and 8.4 show the distributions of the dimuon endpoint, its error as well as the pull distribution respectively.

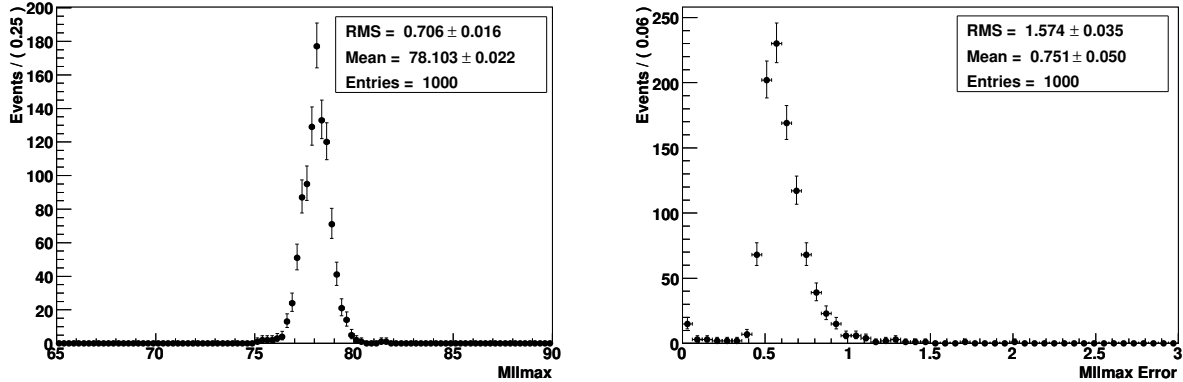


Figure 8.3: *Toy MC fit result of the distribution of the dimuon endpoint (left) and its error (right).*

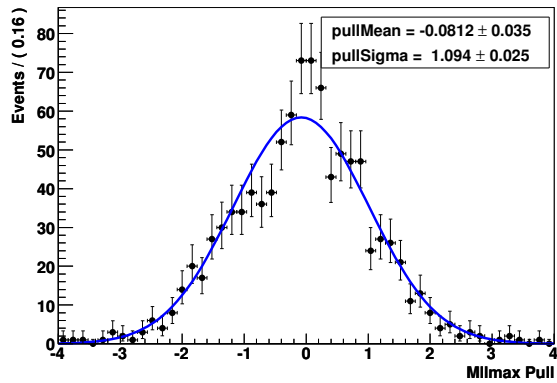


Figure 8.4: *Toy MC fit result for the pull distribution of the dimuon endpoint.*

Acknowledgements

The work of my PhD thesis has been done during my doctoral studentship at CERN and evolved to an exciting experience due to the collaboration of several people that I would like here to acknowledge.

Foremost, I would like to thank my supervisor, Prof. Paris Sphicas, whose immense knowledge and ethos have held the steering motivation to the completion of this thesis. I am deeply grateful for his valuable scientific insight, his constant guidance and support. I am also especially grateful to Luc Pape, who has been tirelessly guiding and supporting me. His ideas and comments have been always inspiring and valuable.

I would like then to thank my colleagues Filip Moortgat, Jens Rehn, Joanna Weng and Ulrich Felzmann, for all the fruitful discussions and the enjoyable time we spent together. I thank all members of the CERN CMS Physics (CMG) group and especially Maria Spiropulu, Albert De Roeck, Patrick Janot, Christos Leonidopoulos and Florian Beaudette for contributing to my work in various ways. Their assistance has been much appreciated. I am also very grateful to Oliver Buchmuller for giving useful and friendly advices during my work.

Further thanks go to Peter Kreuzer and Nancy Marinelli who have been keeping track of my work and advising me. I thank the members of the CRAB team, Daniele Spiga, Stefano Lacaprara, Marco Corvo and Federica Fanzago for their friendly collaboration in the context of the computing activities. Many thanks I also owe to the members of the CERN CMS Computing (CMC) group, and especially Ian Willars, Nick Sinanis, Zhechka Toteva and Gilles Raymond for their support and for inviting me to their group dinners.

I also wish to acknowledge the members of my thesis committee for their contribution. Prof. Christina Kourkoumelis and Prof. Athanasios Lahanas of the Physics Department at the University of Athens, read carefully my thesis and their detailed comments improved significantly its content.

Finally I would like to individually thank the friends who have joined me through the time of my PhD years: Dimitrios Tsirigkas and Anna Sfyrla for keeping a long-lasting friendship, as well as Konstantinos Kousouris, Konstantinos Theofilatos and Fabian Stoeckly for the enjoyable discussion evenings we spent at CERN.

Last but not least, I would like to express my endless appreciation to my parents and sisters for their constant encouragement and love.

Bibliography

- [1] M. Herrero, “The standard model,” arXiv:hep-ph/9812242.
- [2] A. Pich, “The Standard Model of Electroweak Interactions,” arXiv:0705.4264 [hep-ph].
- [3] L. H. Ryder. Quantum Field Theory. Cambridge University Press, 1996.
- [4] S. Weinberg J. Goldstone, A. Salam. Broken Symmetries. Phys. Rev. 127, 965 - 970, 1962.
- [5] M. Drees, “An introduction to supersymmetry,” arXiv:hep-ph/9611409.
- [6] M. E. Peskin, “Beyond the standard model,” arXiv:hep-ph/9705479.
- [7] J. Wess and B. Zumino, “Supergauge transformations in four dimensions”. Nucl. Phys. B70 (1974) 39-50, 1974
- [8] Julius Wess and Jonathan Bagger, “Supersymmetry and Supergravity”. Princeton University Press, Princeton, New Jersey, 1992
- [9] S. P. Martin, “A supersymmetry primer,” arXiv:hep-ph/9709356.
- [10] S. Dimopoulos and D. Sutter, “The Supersymmetric Flavour Problem”. arXiv:hepph/9504415v1, 1995
- [11] W. Beenakker, R. Hopker, M. Spira, and P.M. Zerwas. Squark and gluino production at hadron colliders. Nucl. Phys. B, 492, 197.
- [12] W. Beenakker, M. Klasen, M. Kramer, T. Plehn, M. Spira, P.M. Zerwas. The Production of Charginos/Neutralinos and Sleptons at Hadron Colliders. Phys. Rev. Lett., 83, 1999.
- [13] B. C. Allanach, J. P. Conlon and C. G. Lester, “Measuring Smuon-Selectron Mass Splitting at the CERN LHC and Patterns of Supersymmetry Breaking,” Phys. Rev. D **77** (2008) 076006 [arXiv:0801.3666 [hep-ph]].
- [14] Particle Data Group, Particle Physics Booklet. <http://pdg.lbl.gov>, 2004.
- [15] D.J. Gross and F. Wilczek, “Ultraviolet Behavior of Non-Abelian Gauge Theories”. Phys. Rev. Lett. 30, 1973
- [16] U. Amaldi, W. de Boer, and H. Fuerstenau, “Comparison of Grand Unified Theories with electroweak ans strong Coupling Constants measured at LEP”. CERN-PPE/ 91-44, 1991.
- [17] D. Hooper and Lian-Tao Wang, “Direct and Indirect Detection of Neutralino Dark Matter In Selected Supersymmetry Breaking Scenarios”. arXiv:hep-ph/0309036v1, 2003
- [18] U.Chattopadhyay and P. Nath A. Corsetti, “WMAP Constrains, SUSY Dark Matter and Implications for the Direct Detection of SUSY”. arXiv:hep-ph/0303201, 2003
- [19] CMS Collaboration. The CMS experiment at the CERN LHC. Submitted to Journal of Instrumentation, 2008.
- [20] CMS Collaboration, “Detector Performance and Software, Physical Technical Design Report, Volume I”, CERN/LHCC 2006-001 (2006).

BIBLIOGRAPHY

- [21] CMS Collaboration, “Physics Performance, Physical Technical Design Report, Volume II”, CERN-LHCC-2006-021, 2006 J. Phys. G **34** 995.
- [22] CMS Collaboration. The Tracker Project Technical Design Report. CERN/LHCC 98-006, 1998.
- [23] CMS Collaboration. CMS ECAL Technical Design Report. CERN/LHCC 97-33, 1997.
- [24] CMS Collaboration. The Hadron Calorimeter Project, Technical Design Report. CERN/LHCC 97-31, 1997.
- [25] CMS Collaboration. CMS MUON Technical Design Report. CERN/LHCC 97-32, 1997.
- [26] CMS Collaboration. The Trigger Systems, Technical Design Report. CERNLHCC, 38, 2000.
- [27] CSA07 TWiki. <https://twiki.cern.ch/twiki/bin/view/CMS/CSA07>. 2007.
- [28] SusyAnalyzer webpage, <https://twiki.cern.ch/twiki/bin/view/CMS/SusyAnalyzer>, October 2007.
- [29] S. Baffioni et. al., “Electron reconstruction in CMS”, CMS NOTE-2006/040.
- [30] EGamma POG ,“An Update on electron isolation”
<http://indico.cern.ch/getFile.py/access?contribId=1&resId=0&materialId=slides&confId=29233>.
- [31] E. James et al. “Muon Identification in CMS”. CMS Note 010, 2006.
- [32] P. Schieferdecker et. al., “Performance of Jet Algorithms in CMS”, CMS AN-2008/001.
- [33] CMS AN-2007/055, “Plans for Jet Energy Corrections at CMS”.
- [34] T. Sjostrand, S. Mrenna and P. Skands. PYTHIA 6.4 Physics and Manual. JHEP, 0605, 2006.
- [35] B. C. Allanach, “SOFTSUSY: A C++ program for calculating supersymmetric spectra,” Comput. Phys. Commun. **143** (2002) 305 [arXiv:hep-ph/0104145].
- [36] M.L. Mangano, M.Moretti, F.Piccinini, R.Pittau, and A.D.Polosa, “ALPGEN, a generator for hard multi-parton processes in hadronic collisions”, JHEP 07 (2003) 001, arXiv:hep-ph/0206293.
- [37] R. Brun et al. ROOT - an object oriented data analysis framework. Nucl. Instrum. Meth. A, 389(81-86), 1997.
- [38] “The RooFit toolkit for Data Modeling”, <http://roofit.sourceforge.net/>.
- [39] G. Cowan. Statistical Data Analysis. Oxford University Press, 1998.
- [40] B. C. Allanach *et al.*, “The Snowmass points and slopes: Benchmarks for SUSY searches,” in *Proc. of the APS/DPF/DPB Summer Study on the Future of Particle Physics (Snowmass 2001)* ed. N. Graf, *In the Proceedings of APS / DPF / DPB Summer Study on the Future of Particle Physics (Snowmass 2001), Snowmass, Colorado, 30 Jun - 21 Jul 2001, pp P125* [arXiv:hep-ph/0202233].

BIBLIOGRAPHY

- [41] GEANT4 Collaboration, S. Agostinelli et al., “GEANT4: A simulation toolkit,” Nucl. Instrum. and Methods A506 (2003) 250303. doi:10.1016/S0168-9002(03)01368-8.
- [42] “OSCAR: CMS Simulation Package Home Page.” <http://cmsdoc.cern.ch/oscar>.
- [43] “ORCA: CMS Reconstruction Package.” Site located at <http://cmsdoc.cern.ch/orca>.
- [44] H. Baer, F. Paige, S. Protopescu, and X. Tata. ISAJET 7.69: A Monte Carlo Event Generator for pp, p-bar p and e+e- Reactions. arXiv:hep-ph/0312045v1, 2003.
- [45] A. Heister et al., “Measurement of Jets with the CMS Detector at the LHC,” CMS Note 2006/036 (2006).
- [46] O. Kodolova, “Jet Energy Measurements in CMS,” CMS CR 2005-019 (2005). Presented at HCP 2005, Hadron Collider Physics Symposium, Les Diablerets, Switzerland, 46 July
- [47] M.Chiorboli, A.Tricomi, “Squark and gluino reconstruction with the CMS detector”, CMS Note RN 2003-002.
- [48] M.Chiorboli, M.Galanti, A.Tricomi , “Leptons+Jets+Missing Energy analysis at LM1”, CMS NOTE 2006/133.
- [49] D. J. Miller, P. Osland and A. R. Raklev, “Invariant mass distributions in cascade decays,” JHEP **0603** (2006) 034 [arXiv:hep-ph/0510356].
- [50] B. K. Gjelsten, D. J. Miller and P. Osland, “Measurement of SUSY masses via cascade decays for SPS 1a,” JHEP **0412** (2004) 003 [arXiv:hep-ph/0410303].]
- [51] B. K. Gjelsten, D. J. Miller and P. Osland, “Measurement of the gluino mass via cascade decays for SPS 1a,” JHEP **0506** (2005) 015 [arXiv:hep-ph/0501033].
- [52] B. C. Allanach, C. G. Lester, M. A. Parker and B. R. Webber, “Measuring sparticle masses in non-universal string inspired models at the JHEP **0009** (2000) 004 [arXiv:hep-ph/0007009].
- [53] B. K. Gjelsten, D. J. Miller and P. Osland, “Resolving ambiguities in mass determinations at future colliders,” [arXiv:hep-ph/0507232].
- [54] L. Pape, “Reconsruction of sparticle masses from endpoints at LHC”, CMS IN-2006/012.
- [55] B. K. Gjelsten, D. J. Miller, P. Osland and A. R. Raklev, “Mass determination in cascade decays using shape formulas,” AIP Conf. Proc. **903** (2007) 257 [arXiv:hep-ph/0611259].
- [56] H. Bachacou, I. Hinchliffe and F. E. Paige, “Measurements of masses in SUGRA models at LHC,” Phys. Rev. D **62** (2000) 015009 [arXiv:hep-ph/9907518].
- [57] I. Hinchliffe, F. E. Paige, M. D. Shapiro, J. Soderqvist and W. Yao, “Precision SUSY measurements at LHC,” Phys. Rev. D **55** (1997) 5520 [arXiv:hep-ph/9610544].
- [58] C. G. Lester, M. A. Parker and M. J. White, “Three body kinematic endpoints in SUSY models with non-universal Higgs masses,” JHEP **0710** (2007) 051 [arXiv:hep-ph/0609298].
- [59] C. G. Lester, M. A. Parker and M. J. White, “Determining SUSY model parameters and masses at the LHC using cross-sections, kinematic edges and other observables,” JHEP **0601** (2006) 080 [arXiv:hep-ph/0508143].